UNIVERSITÉ DU QUÉBEC À CHICOUTIMI

THÉSE PRÉSENTÉ À

L' UNIVERSITÉ DU QUÉBEC À CHICOUTIMI

COMME EXIGENCE PARTIELLE

DU DOCTORAT EN INGÉNIERIE

PAR

WALEED KHALIFA

RÔLE DES INCLUSIONS DANS LA GERMINATION DE LA PHASE α-ALUMINIUM ET DES INTERMÉTALLIQUES CONTENANT DU FER DANS LE COIN RICHE EN ALUMINIUM DU SYSTÈME TERNAIRE Al-Si-Fe

NOVEMBRE 2003

Bibliothèque
Paul-Émile-Boulet

UQAC
Université du Québec
à Chicoutimi

Mise en garde/Advice

Afin de rendre accessible au plus grand nombre le résultat des travaux de recherche menés par ses étudiants gradués et dans l'esprit des règles qui régissent le dépôt et la diffusion des mémoires et thèses produits dans cette Institution, **l'Université du Québec à Chicoutimi (UQAC)** est fière de rendre accessible une version complète et gratuite de cette œuvre.

Motivated by a desire to make the results of its graduate students' research accessible to all, and in accordance with the rules governing the acceptation and diffusion of dissertations and theses in this Institution, the **Université du Québec à Chicoutimi (UQAC)** is proud to make a complete version of this work available at no cost to the reader.

L'auteur conserve néanmoins la propriété du droit d'auteur qui protège ce mémoire ou cette thèse. Ni le mémoire ou la thèse ni des extraits substantiels de ceux-ci ne peuvent être imprimés ou autrement reproduits sans son autorisation.

The author retains ownership of the copyright of this dissertation or thesis. Neither the dissertation or thesis, nor substantial extracts from it, may be printed or otherwise reproduced without the author's permission.

Dedicated to my parents,
Shimaa and my little ones, Abdo and Ahmed

Résumé

Le but de ce travail était d'étudier la germination des intermétalliques du fer (Fe) et de la phase α-Al à partir des alliages liquides dilués Al-Si-Fe, sur le noyau de particules d'inclusions courantes se trouvant dans les alliages d'aluminium commerciaux. Les inclusions furent introduites dans l'alliage fondu en utilisant une technique d'injection de gaz. Des expérimentations systématiques furent mises au point afin d'étudier l'effet (i) de la composition de l'alliage (Fe et Si), (ii) du taux de refroidissement (de 0.2 °C/s à 15 °C/s, similaire à ceux rencontrés dans la plupart des procédés de fonderie des alliages commerciaux), et (iii) du type d'inclusions (où une variété d'inclusions, dont les plus courants des oxydes, carbures et borures, furent utilisées). De plus, une analyse en profondeur du système d'injection de gaz fut aussi entreprise, celle-ci s'avérant utile à la compréhension de l'influence des particules solides et des propriétés du métal liquide sur le procédé d'injection de gaz.

Six alliages expérimentaux représentatifs de la partie riche en aluminium du système Al-Si-Fe furent utilisés dans la présente étude. Des expériences d'injection de gaz pour ajouter une variété d'inclusions (α- et γ-Al_2O_3, MgO, CaO, TiC, SiC, Al_4C_3 et TiB_2) aux alliages fondus, furent entreprises en utilisant une technique d'injection de gaz qui a permis d'introduire avec succès les différents oxydes, carbures et borures dans les alliages d'aluminium liquide. Les alliages dans lesquels des inclusions furent injectées ont été coulés dans différents moules afin d'obtenir des taux de refroidissement variés. Plusieurs techniques d'examen furent utilisées pour étudier l'effet de la composition de l'alliage, du taux de refroidissement, et du type d'inclusion, sur la structure des alliages. Ces techniques sont l'analyse thermique, l'analyse d'image, la micro-analyse par sonde électronique équipée avec la cartographie, le rayon X par énergie dispersive et le spectromètre des rayons X par longueur d'onde.

Les résultats ont montré que la fraction volumique des intermétalliques du Fe obtenue augmente avec les quantités de Fe et Si ajoutées, aussi bien qu'avec la baisse du taux de refroidissement. Un taux de refroidissement faible produit des intermétalliques de dimensions plus grandes, alors qu'un taux de refroidissement élevé résulte en une plus grande densité d'intermétalliques. L'ajout de fer seul est plus efficace que des ajouts de Si ou de Fe+Si à produire des intermétalliques. La composition de l'alliage et le taux de refroidissement contrôlent la stabilité des phases intermétalliques: Les phases binaires Al-Fe prédominent à des taux de refroidissement bas et à un ratio Fe/Si élevé; la phase β-Al_5FeSi est dominante à un contenu en Si élevé et à un taux de refroidissement bas; les intermétalliques α-AlFeSi (i.e. α-Al_8Fe_2Si) existent entre ces deux phases; les phases ternaires riches en Si, telles que l'intermétallique δ-Al_4FeSi_2, sont stabilisées à des taux de refroidissement élevés et à des contenus en Si de 0.9 % et plus en poids.

Les calculs des parcours de solidification représentant les ségrégations de Fe et Si dans la partie liquide, basés sur l'équation de Scheil, ne sont pas conformes aux parcours de solidification actuels, en raison du fait que la diffusion du solide n'est pas prise en compte dans l'équation. Les modèles théoriques de Brody et Flemings [1966], et Clyne et Kurz [1981] ne parviennent pas à expliquer l'écart observé avec le comportement de l'équation de Scheil, puisque ces modèles donnent moins de poids à l'effet de la rétro-diffusion du solide. Une section isotherme métastable du diagramme de phase Al-Si-Fe ajustée à 500°C a été proposée (au lieu de celle à l'équilibre), qui prédit correctement les phases intermétalliques formant dans cette partie du système à des taux de refroidissement bas (~0.2 °C/s).

En ce qui a trait à la technique d'injection de gaz utilisée, l'effet des particules d'inclusions sur le développement de la microstructure dans les alliages d'aluminium a démontré la signifiance d'utiliser cette technique dans la conduite d'études systématiques de ce type. Le processus de fluidisation des particules solides fut décrit et discuté en détail. Les équations et diagrammes qui mettent certaines limites sur la vélocité et le débit du gaz sont donnés à titre de guides dans la fluidisation contrôlable. De plus, l'analyse théorique du procédé d'injection de gaz, incluant l'énergétique du transfert des particules de gaz à liquide et l'effet des forces cinétiques, fut utilisée afin de dériver une relation théorique faisant état de la vélocité d'injection minimale requise pour le transfert de particules de gaz à liquide.

La capacité de la technique d'injection s'avère être très restreinte par la dimension des particules. Des particules très petites (< 1-μm) ou grandes (> 100-μm) ne peuvent être introduites dans le métal liquide en utilisant la présente technique d'injection pour plusieurs raisons reliées à la capacité de pourvoir des débits de gaz appropriés pour l'injection et celle d'avoir une fluidisation ne déstabilisant pas le bain de métal.

Alors que la discussion donnée dans ce travail est étroitement reliée au présent système d'injection de gaz, les considérations, particulièrement celles reliées à l'effet des propriétés physiques des particules liquides et solides sur le processus de transfert des particules de gaz à liquide, sont assez générales et devraient être applicables à tout procédé d'injection. Les considérations pratiques générales sont: (i) la mouillabilité a une grande influence sur l'incorporation des particules, une faible mouillabilité nécessitant des vélocités d'injection plus grandes, (ii) la densité du liquide a un effet sur l'incorporation des particules dans le bain de métal, l'incorporation des particules solides dans les liquides plus lourds étant plus difficile et requérant des vélocités d'injection plus grandes, et (iii) plus le type de particules est gros et/ou lourd, plus petite est la vélocité d'injection requise.

Les expérimentations d'inoculation systématique entreprises pour étudier l'influence d'inclusions diverses sur la germination de la phase α-Al dans les alliages Al-Si-Fe à des taux de refroidissement différents, ont montré que dans les alliages dilués

(contenant moins de 1.5% de Si + Fe), presque tous les types d'inclusions ont des pourcentages élevés d'occurrence à l'intérieur de la phase α-Al, indiquant que la germination est promue sur la surface de telles inclusions. Dans un alliage hypoeutectique Al-Si contenant 6.3% en poids de Si, les particules d'inclusions de MgO, TiB_2, TiC, α-Al_2O_3, et SiC deviennent surtout des agents nucléants inactifs repoussés dans les régions interdendritiques à cause de l'effet empoisonnant dominant du Si.

Les résultats présents furent utilisés avec succès afin d'expliquer les différences d'efficacité des affineurs de grain commerciaux dans les alliages Al-Si hypoeutectiques. Le silicium est ségrégé préférentiellement aux interfaces Al liquide/inclusions de façon à réduire leur énergie libre. Une analyse théorique de l'effet empoisonnant du Si a montré que la ségrégation du Si à l'interface liquide/agents nucléants altère le bilan d'énergie interfaciale de manière que l'efficacité catalytique des particules de s est réduite de façon spectaculaire. Une analyse soignée a montré que l'effet empoisonnant du Si dans l'alliage Al-Si hypoeutectique est surmonté lorsque les particules d'agents nucléants ont des caractéristiques de surface actives tel que représenté par les puissances catalytiques élevées des particules de γ-Al_2O_3, CaO et Al_4C_3 dans la germination de la phase α-Al de l'alliage. Bien que certaines inclusions aient des niveaux d'occurrence comparables ou supérieurs à ceux du TiB_2 dans la phase α-Al, elles ne peuvent pas être utilisées comme agents nucléants efficaces en raison de leur faible mouillabilité avec l'aluminium liquide ou de leur réactivité chimique.

La germination des phases intermétalliques contenant du Fe (c'est à dire les phases binaires Al-Fe, α-AlFeSi, β-AlFeSi, δ-AlFeSi et q_1-AlFeSi) sur la surface de différentes inclusions dans les six alliages expérimentaux Al-Si-Fe fut étudiée. Il s'est avéré que la germination de chacune des phases intermétalliques contenant du Fe était généralement promue sur la surface de plusieurs inclusions dans les mêmes conditions de composition d'alliage et de taux de refroidissement. Toutefois, certaines inclusions ont exhibé une haute puissance de germination pour les phases intermétalliques particulières contenant du Fe dans certaines conditions et une faible puissance dans d'autres conditions. Les agents nucléants puissants pour la phase primaire α-Al, tel que γ-Al_2O_3, ont exhibé une faible puissance pour la germination des particules d'intermétalliques contenant du Fe se trouvant à l'intérieur de la phase primaire (particules intragranulaires). Les inclusions réactives telles que CaO et SiC sont des agents nucléants très puissants pour les particules intragranulaires de la phase intermétallique contenant du Fe.

La germination des phases intermétalliques contenant du Fe dans les alliages Al-Si-Fe obéit aux caractéristiques générales de la germination, en particulier, l'effet du taux de refroidissement et de la concentration de soluté sur la puissance des particules d'agents nucléants: (i) Il a été observé que l'augmentation du taux de refroidissement améliore la germination hétérogène des phases intermétalliques contenant du Fe sur la surface de différentes inclusions, et (ii) la puissance de germination des particules d'inclusions dans la phase α-Al et dans les régions interdendritiques s'améliore avec l'augmentation de la

concentration de soluté jusqu'à un certain niveau. Au-dessus de ce niveau, la concentration de soluté empoisonne les sites de germination. La germination des intermétalliques contenant du Fe dans les alliages étudiés ne semble pas être grandement affectée par le type ou la structure cristallographique de la surface nucléante.

Abstract

The aim of this work has been to study the nucleation of iron intermetallics and the α-Al phase on inclusions introduced into dilute liquid Al-Si-Fe alloys. The inclusions studied are those commonly found in commercial aluminum alloys. The inclusions were introduced into the alloy melt using a gas injection technique. Systematic experiments were designed to study the effect of (i) the alloy composition (Fe and Si), (ii) cooling rate (from 0.2 °C/s to 15 °C/s, similar to those encountered in most commercial casting processes), and (iii) inclusion type (where a variety of inclusions covering the most common oxides, carbides, and borides were used). In addition, an in-depth analysis of the gas injection system was also carried out, which was useful in understanding the influence of the solid particle and liquid metal properties on the gas injection process.

Six experimental alloys representative of the Al-rich corner of the Al-Si-Fe system were used in the present study. Gas injection experiments for the addition of a variety of inclusions (α- and γ-Al_2O_3, MgO, CaO, TiC, SiC, Al_4C_3 and TiB_2) to the alloy melts were carried out using a gas injection technique that successfully introduced the different oxides, carbides and borides into the liquid aluminum alloys. The inclusion injected melts were cast into different molds in order to achieve various cooling rates. Several examination techniques were used to study the effect of alloy composition, cooling rate, and inclusion type on the structure of the alloys. These techniques include thermal- and image analysis, scanning electron microscopy, X-ray mapping, electron probe microanalysis (EPMA), and wavelength dispersive spectroscopy (WDS).

The results showed that the volume fraction of iron intermetallics obtained increased with the increase in the amount of Fe and Si added, as well as with the decrease in cooling rate. A low cooling rate produces larger-sized intermetallics, whereas a high cooling rate results in a higher density of intermetallics. Iron addition alone is more effective than either Si or Fe+Si additions in producing intermetallics. The alloy composition and cooling rate control the stability of the intermetallic phases: binary Al-Fe phases predominate at low cooling rates and a high Fe/Si ratio; the β-Al_5FeSi phase is dominant at a high Si content and low cooling rate; the α-AlFeSi intermetallics (*e.g.*, α-Al_8Fe_2Si) exist between these two; Si-rich ternary phases such as the δ-Al_4FeSi_2 intermetallic are stabilized at high cooling rates and Si contents of 0.9 wt% and higher.

Calculations of the solidification paths representing segregations of Fe and Si to the liquid using the Scheil equation did not conform to the actual solidification paths, due to the fact that solid diffusion is not taken into account in the equation. The theoretical models of Brody and Flemings [1966], and Clyne and Kurz [1981] also fail to explain the observed departure from the Scheil behavior, since these models give less weight to the effect of

solid back-diffusion. An adjusted 500°C metastable isothermal section of the Al-Si-Fe phase diagram has been proposed (in place of the equilibrium one), that correctly predicts the intermetallic phases that occur in this part of the system at low cooling rates (~0.2 °C/s).

With respect to the gas injection technique that was used, the effect of inclusion particles on the microstructure development in aluminum alloys showed the significance of using the technique in conducting systematic studies of this type. The fluidization process of the solid particles has been described and discussed in detail. Equations and diagrams that put certain limits on the gas velocity and flow rates are given as guides for controllable fluidization. In addition, theoretical analysis of the gas injection process, including the energetics of particle transfer from gas to liquid and the effect of kinetic forces, was used to derive a theoretical relation for the minimum injection velocity required for successful particle transfer from gas to liquid.

The capability of the injection technique was found to be very much restricted by the size of the particles. Very small (< 1-μm) or large (> 100-μm) particles cannot be introduced into the liquid metal using the present injection technique for several reasons related to the capability of providing the appropriate gas flow rates for injection and fluidization without destabilizing the metal bath.

While the discussion given in this work is closely related to the present gas injection system, the considerations, particularly those related to the effect of physical properties of the liquid and the solid particles on the process of particle transfer from gas to liquid are quite general and should be applicable to any injection process. The general practical considerations are: (i) the wettability has a great influence on the incorporation of particles, poor wettability necessitating higher injection velocities, (ii) the density of the liquid has an important effect on particle incorporation into metal baths, with solid particle incorporation in heavier liquids being more difficult and requiring higher injection velocities, and (iii) the larger and/or heavier the particle type, the smaller the injection velocity required.

The systematic inoculation experiments carried out to study the influence of various inclusions on the nucleation of the α-Al phase in Al-Si-Fe alloys at different cooling rates showed that in the dilute alloys (containing less than 1.5 pct Si+Fe), almost all the inclusion types have high percentages of occurrence within the α-Al phase, indicating that nucleation is promoted on the surface of such inclusions. In a hypoeutectic Al-Si alloy containing 6.3 wt pct Si, the inclusion particles of MgO, TiB_2, TiC, α-Al_2O_3, and SiC become mostly inactive nucleants and are pushed to the interdendritic regions because of the dominant poisoning effect of Si.

The present results were used successfully to explain the efficiency differences between commercial grain refiners in hypoeutectic Al-Si alloys. Silicon is observed to preferentially segregate to the liquid-Al/inclusion interfaces so as to lower their free energy. A theoretical analysis of the poisoning effect of Si showed that Si segregation to the

liquid/nucleant interface alters the interfacial energy balance so that the catalytic efficiency of the nucleant particles is dramatically reduced. Careful analysis showed that the poisoning effect of Si in the hypoeutectic Al-Si alloy is overcome when the nucleant particles have active surface characteristics as represented by the high catalytic potencies of γ-Al_2O_3, CaO and Al_4C_3 particles in nucleating the α-Al phase in the alloy. Although some inclusions have comparable or higher occurrence levels than TiB_2 in the α-Al phase, they cannot be used as efficient nucleants either due to their poor wettability with liquid aluminum or their chemical reactivity.

Nucleation of Fe-intermetallic phases (*i.e.* binary Al-Fe, α-Al_8Fe_2Si, β-Al_5FeSi, δ-Al_4FeSi_2 and q_1-AlFeSi phases) on the surface of different inclusions in the six experimental Al-Si-Fe alloys was studied. It was found that nucleation of each of the Fe-intermetallic phases was generally observed to be promoted on the surface of several inclusions under the same conditions of alloy composition and cooling rate. However, some inclusions exhibited high potency for the nucleation of particular Fe-intermetallic phases under certain conditions and poor potency under other conditions. The potent nucleants for the primary α-Al phase such as γ-Al_2O_3 exhibited poor potency for the nucleation of the Fe-intermetallic particles that lie within the primary phase (intragranular particles). Reactive inclusions such as CaO and SiC are very potent nucleants for the intragranular Fe-intermetallic phase particles.

The nucleation of the Fe-intermetallic phases in Al-Si-Fe alloys obeys the general features of nucleation, in particular, the effect of cooling rate and solute concentration on the potency of the nucleant particles: (i) it was observed that increasing the cooling rate enhances the heterogeneous nucleation of the Fe-intermetallic phases on the surface of different inclusions, and (ii) the nucleation potency of inclusion particles in both α-Al and interdendritic regions improves with increasing solute concentration up to a certain level. Above this level, the solute concentration poisons the nucleation sites. Nucleation of the Fe-intermetallics in the alloys studied does not seem to be largely affected by the type or crystallographic structure of the nucleating surface.

Acknowledgements

I would like to sincerely acknowledge the guidance of my supervisors, Professors F.H. Samuel and J.E. Gruzleski, who gave me the opportunity to undertake this research study. I would also like to thank all members of the TAMLA group for their help and assistance during various stages of my work, in particular, Dr. A.M. Samuel for her critical review of the manuscript, MM. Alain Bérubé and Régis Boucher, technicians, TAMLA-UQAC, for their assistance with the castings, sample preparation and the construction and maintenance of the injection apparatus.

Financial support in the form of scholarships received from the Natural Sciences and Engineering Research Council of Canada (NSERC), the Fondation de l'Université du Québec à Chicoutimi (FUQAC), General Motors Powertrain Group (U.S.A), and Corporativo Nemak (Mexico) is gratefully acknowledged.

Thanks are also due to MM Glenn Poirier and Shi Lang of the Microanalysis Laboratory, Earth and Planetary Science Department, McGill University for carrying out the EPMA work.

Finally, I would like to extend a special acknowledgment to my wife, Shimaa, for her continuous encouragement and support during my work.

Publications

Two research articles have been published, one has been submitted and two others have been prepared for submission from this work. [1,2,3,4,5] The details are provided below.

1. Iron Intermetallic Phases in the Al Corner of the Al-Si-Fe System, W. Khalifa, F. Samuel and J. Gruzleski.
   Light Metals 2002, T.Lewis (Ed.), The Metallurgical Society of the Canadian Institute of Mining, Metallurgy and Petroleum, Montreal, **2002**, pp. 285-303.

2. Iron Intermetallic Phases in the Al Corner of the Al-Si-Fe System, W. Khalifa, F. Samuel and J. Gruzleski.
   Metallurgical and Materials Transactions. A, **2003**, vol. 34A, pp. 807-825.

3. Influence of Inclusions on the Nucleation of the α-Al Phase in the Al-Si-Fe Alloys, W. Khalifa, F. Samuel and J. Gruzleski.
   Submitted for publication in *Metallurgical and Materials Transactions. A*, **2004**.

4. Analysis of the Gas Injection Technique Used for Inclusion Additions to Molten Aluminum Alloys, W. Khalifa, F. Samuel and J. Gruzleski.
   Prepared for publication in *Inter. Journal of Cast Metals Research*, **2004**.

5. Heterogeneous Nucleation of the Fe-Intermetallics in the Al-Si-Fe Alloys: the Role of Inclusions, W. Khalifa, F. Samuel, J. Gruzleski, H. Doty, and S. Valtierra.
   Prepared for publication in *Metallurgical and Materials Transactions*, **2004**.

Conference Presentations

1. Iron Intermetallic Phases in the Al Corner of the Al-Si-Fe System, W. Khalifa, F. Samuel and J. Gruzleski.
   Presented at the *Int. Conf. on Enabling Technologies for Light Metals and Composite Materials and Their End-Products* (COM 2002), Montreal, Aug 11-14, 2002.
   Casting and Solidification II. Session 13B: Paper 13B.2.

Table of Contents

List of Tables

List of Figures

List of Symbols

A	The area of the solid as seen in projection along the direction of motion, surface area of casting, m^2.
d_b	The diameter of the gas bubble, cm.
d_o	The internal diameter of orifice, cm.
d_p	The average particle size, μm.
d_P^*	Dimensionless particle size.
D	Drag force, N.
E_D	Drag energy, J.
E_k	Kinetic energy, J.
f	Friction factor.
f_S	Fraction solid.
g	The gravitational acceleration, $m.s^{-2}$.
I	The nucleation rate.
k	Boltzman constant, $1.35*10^{-23}$Joule.$^oK^{-1}$.
m	Mass, g.
n_{cr}	Number of atoms in a cluster.
q_e	The external heat flux, $W.m^2$.
q_i	The internal heat flux, $W.m^2$.
Q_G	The gas flow rate, $cm^3.s^{-1}$.
r	The particle radius, crystal radius, μm.
r_{cr}	The critical size of a crystal, μm.
R	Gas constant, rate constant, hr^{-1}.
R_{eG}	The gas Reynolds number.
R_{eP}	The particle Reynolds number.
t	Temperature, ^oC, time, hr.
T	Temperature, ^oK.
u	Particle velocity, $cm.s^{-1}$.
u_{mf}	The minimum fluidization velocity, $cm.s^{-1}$.
u_{mi}	The minimum injection velocity, $cm.s^{-1}$.
u_t	The terminal (elutriation) velocity of particles, $cm.s^{-1}$.
u_t^*	Dimensionless terminal velocity of particles.
V	The growth rate, $cm.s^{-1}$, volume of casting, m^3.
V_t	The terminal velocity of gas bubble, $cm.s^{-1}$, the volume percent of sludge at time t, %.
V_i	The sludge initial volume percent, %.

γ_{LG}	Liquid surface tension, dyne.cm^{-1}.
μ_G	Gas viscosity, poise (= g.cm^{-1}.s^{-1}).
μ_L	Liquid Viscosity, poise (= g.cm^{-1}.s^{-1}).
θ	Wetting angle, deg.
ρ_G	Gas density, g.cm^3.
ρ_L	Liquid density, g.cm^3.
ρ_P	Particle density, g.cm^3.
ω	Immersion angle, deg.
ΔE_B	Buoyancy energy, J.
ΔE_P	Potential energy, J.
ΔE_S	Surface energy, J.
ΔE_T	Total free energy change, J.
ΔG	The total Gibbs free energy, J.
ΔH_f	The latent heat of fusion, J.mole^{-1}.
ΔS_f	The entropy of fusion, J.mole^{-1}.^{o}K.
ΔT	The undercooling, ^{o}C.
ΔT_n	The nucleation undercooling, ^{o}C.
ΔT_r	The nucleation undercooling for a crystal size r, ^{o}C.
Γ	Gibbs-Thomson Coefficient, ^{o}K.m.

CHAPTER 1

DEFINITION OF THE PROBLEM

CHAPTER 1

DEFINITION OF THE PROBLEM

1.1. Introduction

Commercial unalloyed aluminums and aluminum base alloys contain a considerable amount of iron and silicon as impurities or alloying additions. Commercial aluminum alloys, which have up to 1 % of iron and silicon, can be considered ternary alloys. As the solid solubility of iron in aluminum is less than 0.05 % at equilibrium, nearly all iron in aluminum alloys forms second-phase particles. Both iron and silicon have partition coefficients less than unity, and accordingly segregate to the liquid between the Al dendrite arms during the course of solidification. Therefore, when considering the solute segregation, primary particles of binary Al-Fe and ternary Al-Fe-Si phases, and even silicon can form during casting of an aluminum-rich alloy.

Certain alloying elements may be added to the aluminum alloys to improve the mechanical properties and/or avoid the effect of some undesirable impurity elements. The most detrimental element in these alloys is iron. The existence of iron in aluminum alloys is increased as a result of the usage of recycled alloys.

Iron forms a number brittle intermetallic phases[6,7] such as β-phase (Al_5FeSi), which leads to degradation of the mechanical properties of the cast products. The volume and size

of Fe-intermetallics depend on the iron and manganese contents,[8,9,10,11] solidification parameters,[11,12,13,14] and the modifier type and amount.[10,15]

In addition, some Fe-intermetallic phases in Al alloys were found to be stabilized by minor elements such as Cr, V, Mo, W and Cu.[16,17,18] Increasing the cooling rate was observed to cause a shift of the as-cast Fe-intermetallics content toward Si-richer particles.[16] An effect of inclusion type (α-alumina and γ-alumina) on the Fe-intermetallic phase selection has been observed.[10] It was proposed that γ-alumina acts as a nucleus for crystallization of β-AlFeSi phase whereas the α-alumina is a poor nucleus. Other authors reported that the addition of grain refiner to dilute Al-Fe-Si alloys increased the presence of the θ-$Al_{13}Fe_4$ phase with respect to the Al_6Fe phase in the solidified microstructure.[19] However, the evaluation of the role of inclusions and the grain refiner particles in the nucleation of the Fe-intermetallics based on direct observations of physical contact has not been carried out yet.

A major part of the examination of nucleation in aluminum-base alloys has been spent in the study of the mechanisms of grain refinement, specifically, those associated with the presence of Al_3Ti, TiB_2, AlB_2, TiC, etc, where the focus was on rationalizing the usefulness of such grain refiners. The actual evidence that any one nucleant may be associated with the initiation of solidification is not extensive. It does not seem to have been clearly established that these proposed nucleants operate singly or in association with each other or other nucleants already existing in the melt. Furthermore, the role and the catalytic activity of inclusions in the solid nucleation (of the Fe-intermetallics and the α-Al

phase) have not been systematically studied because of the difficulty of introducing inclusions to alloy melts in a controllable way.

1.2. Objectives

This work aimed to study the formation of the iron intermetallics and the α-Al phase from liquid Al-Si-Fe alloys on nuclei of the common inclusion particles. The inclusions were introduced to the alloy melts using the gas injection technique.[20] The present inoculation experiments were designed to study the effect of the following parameters:

(1) Alloy composition (Fe and Si),

(2) Cooling rate (from about 0.2 °C/s to 15 °C/s, similar to those encountered in most of the commercial casting processes), and

(3) Effect of inclusion type (α-, γ-Al_2O_3, MgO, CaO, TiC, SiC, Al_4C_3 and TiB_2).

In addition, an in-depth analysis of the gas injection system was carried out in order to understand the effect of the solid particle and liquid metal properties on the gas injection process and how these parameters can be used to estimate the appropriate injection velocity required to conduct successful injection experiments.

CHAPTER 2

LITERATURE REVIEW

CHAPTER 2

LITERATURE REVIEW

2.1. Iron in Aluminum Alloys

Commercial unalloyed aluminum and aluminum base alloys contain a considerable amount of iron and silicon as impurities or alloying additions. Commercial aluminum alloys, which have up to 1% of iron and silicon, can be considered ternary alloys. As the solid solubility of iron in aluminum is less than 0.05% at equilibrium, nearly all iron in aluminum alloys forms second-phase particles. Both iron and silicon have partition coefficients less than unity, and accordingly segregate to the liquid between the Al dendrite arms during the course of solidification. Therefore, when considering the non-equilibrium lever-rule assumption,[21] primary particles of binary Al-Fe and ternary Al-Fe-Si phases, and even silicon can form during casting of an aluminum-rich alloy. The chemical composition and local cooling rate are the controlling factors that determine which phases will form[22,23] and their size.[12,14]

Extensive reviews of the Al-Fe-Si system and the intermetallic phase selection in the 1XXX alloys have been published.[24,25] Several studies by other workers[26,27] have focused upon the Al-rich part of the system, where the θ-Al_3Fe, α-AlFeSi and β-AlFeSi phases have been reported as equilibrium phases.[27,28] In addition, some non-equilibrium phases have been identified, for example, metastable phases such as Al_6Fe,[23,29] Al_mFe[30] and Al_xFe[23,31] instead of the θ-Al_3Fe (or θ-$Al_{13}Fe_4$)[32] equilibrium phase. Structures of various phases, *e.g.*, Al_6Fe[33], Al_3Fe[29,34] and α-AlFeSi[35,36] have been investigated. The complex structure of Al_mFe has also been suggested.[37,38]

A deep understanding of the constitutional and the thermal factors that affect the crystallization of the Fe-intermetallic phases is vital for process control purposes. In this section, a review of the available articles on this subject is presented. The review addresses several topics such as Fe solubility in Al, Fe-intermetallic phases, observation of Fe-intermetallics in dilute Al-alloys, crystallization and neutralization of Fe-intermetallics which include the effect of Fe, cooling rate, Mn, other chemical neutralizers, melt superheat, aluminum oxides transformation, minor impurity elements, and the effect of Mg. The review also explains the subject of sludge formation,

dissolution of Fe-intermetallics through heat treatment, the role of iron in the formation of porosity and finally the quantification of iron intermetallics by thermal analysis.

2.1.1. Iron Solubility in Aluminum

The solubility of iron in liquid aluminum is quite high. At 655°C, it is 1.87 wt%.[39] This high solubility leads to the dissolution of ferrous materials in contact with molten aluminum during handling and processing. As a result, Al diecasters minimize tool wear by keeping the Fe content of the molten Al as high as 0.8%,[40,41] and even up to 2% in order to reduce the tendency of the molten metal to stick to the die components.[42]

In solid Al, the solubility of Fe is very low, only 0.052% at 655°C.[39] The Fe solubility is even less at room temperature or in the presence of alloying elements that form compounds with Fe. The electrical conductor grade of aluminum uses Fe to combine with impurity elements that decrease electrical conductivity and to form insoluble precipitates that moderately increase the elevated temperature strength.[40] This strong phase forming ability of iron reduces its diffusion rate in alloyed aluminum.[43]

2.1.2. Iron Intermetallic Phases

The transition metals –including Fe- often form a succession of intermetallic phases with Al.[39] They also exhibit frequent metastability, in which one phase introduced during fast solidification transforms in the solid state to another, for example, $Al_6Fe \rightarrow Al_3Fe$. This takes place for several non-equilibrium phases as confirmed by Griger and Stefaniay.[6,44] The possible Fe-intermetallics that can form in Al-Si alloys were summarized in the work of Dons [16,45] and Liu *et al.*[17] These phases are listed in Table 1 and illustrated in Figure 1 and Figure 2. It is worth mentioning in this context that Dons[45] observed that the Philips phase diagram given in Figure 1 couldn't be used to predict the Fe-intermetallic phases in her experimental alloys.

In the Al-Si alloys the most important of these are the α-AlFeSi and the β-AlFeSi phases.[39,40,46] In addition, there are two less common phases, δ-Al_4FeSi_2 and p-$Al_8Mg_3FeSi_6$. The Si and Al contents of both the α- and β-phases are high and a lot of Fe is replaced either by Mn or Cr. This leads to the fact that the amount of Fe-intermetallics which form is much greater than that predicted from the actual iron content. According to the density of various Fe-rich phases, it is estimated that 3.3 vol% intermetallics will form for each 1 wt% of the total %Fe+%Mn+%Cr.[40]

Table 1 List of the Fe-intermetallic phase structures that form in the Al-Si-Fe system[16,17,39,45]

Name	Composition	Symmetry
Al_3Fe	$Al_{3.2\text{-}3.6}Fe$	Monoclinic, a=15.487, b=8.0831, c=12.4776Å, β=107°43′
	$Al_{3.6}Fe$	
	$Al_{3.4}Fe$	
	$Al_{3.3\text{-}3.5}FeSi_{0\text{-}0.05}$	
Al_6Fe	$Al_{6.3}Fe$	C-centered Orthorhombic
Al_xFe	--	Monoclinic, a=21.6, b=9.1, c=9.05 Å, β=94°
Al_mFe	--	Body-centered Tetragonal, a=0.884, c=2.160Å
Al_pFe	--	Body-centered Cubic, a=1.03Å
θ-$Al_{13}Fe_4$	--	C-centered Monoclinic, a=15.49, b=0.808, c=1.247Å, β=107°
α-AlFeSi[a]	$Al_{15}Fe_3Si$	Cubic, a=12.54Å, and Body-Centered Cubic, a=12.56 Å.
	$Al_{12}Fe_3Si$	
	$Al_{11.3}Fe_3Si_{1.6}$ -	
	$Al_{10.9}Fe_3Si_{1.9}$	
	$Al_{12.7}Fe_3Si_{1.0}$ -	
	$Al_{12.9}Fe_3Si_{1.5}$	
α′-AlFeSi[a]	$Al_{11.8}Fe_3Si_{1.7}$	Hexagonal, a=12.3, c=26.2 Å.
	$Al_{12}Fe_3Si_2$	
	Al_8Fe2Si	
	$Al_{12.0}Fe_3Si_{2.0}$	
	$Al_{12.6}Fe_3Si_{1.6}$	
α″-AlFeSi	--	Tetragonal, a=12.6, c=37.0,
α_V-AlFeSi	Al_9Fe	Monoclinic, a=8.69, b=6.35, c=6.32 Å, β=93.4°
	$Al_{14.6}Fe_3Si_{1.0}$	
	$Al_{12.4}Fe_3Si_{2.1}$	
α_T-AlFeSi	In the α region	Monoclinic, a=28.1, b=30.8, c=20.8Å, β=97.74
β-AlFeSi	$Al_9Fe_2Si_2$	Monoclinic, a=6.12, b=6.12, c=41.5Å, β=91°
	Al_9FeSi	
	$Al_{13.6}Fe_3Si_{3.05}$ -	
	$Al_{13.3}Fe_3Si_{3.3}$	
	$Al_{13.6}Fe_3Si_{3.4}$	
β′-AlFeSi	--	Monoclinic, a=8.9, b=4.9, c=41.6 Å, β=92°
δ-AlFeSi	Al_4FeSi_2	Tetragonal, a=6.16, b=9.49Å
q_1-AlFeSi	--	C-centered Orthorhombic, a=1.27, b=3.62, c=1.27Å
q_2-AlFeSi	--	Monoclinic, a=1.25, b=1.23, c=1.93Å, β=109°

[a] According to Hatch,[39] the structure of the α-AlFeSi is hexagonal and that of α′-AlFeSi is body-centered cubic.

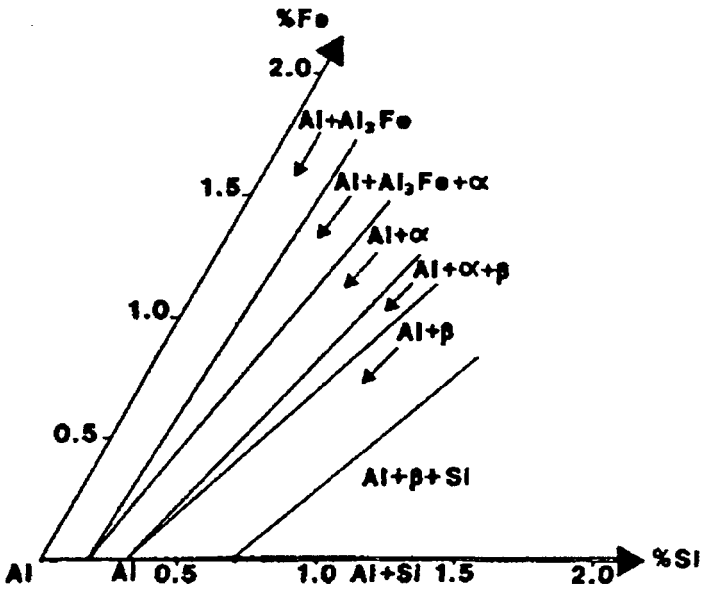

Figure 1 The 500 °C isothermal section of the Al-Si-Fe system.[47]

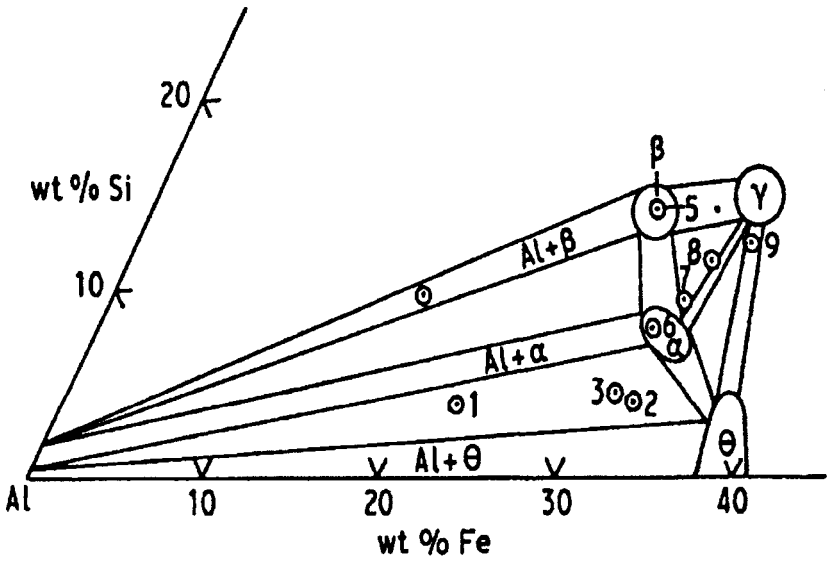

Figure 2 Projection of the 570 to 600 °C section of the Al-corner of the Al-Si-Fe system for heat-treated samples.[48]

2.1.2.1. The α-AlFeSi phase

The α-AlFeSi phase appears like Chinese script in the microstructure (Figure 3 (a)). The Chinese script morphology of the α-AlFeSi occurs during eutectic solidification with the α-Al phase. The α-AlFeSi phase can also appear as polyhedrons if it solidifies before the eutectic reaction (*i.e.,* a primary phase).[40] Usually Mn (and/or perhaps Cr) is added to the melt to promote the formation of the $Al_{15}(Mn, Fe)_3Si_2$ phase. This phase has a compact morphology and does not initiate cracks in the cast material to the same extent as does the β-AlFeSi phase.

(a) (b)

Figure 3 a) Microstructure of a sample from alloy 319.1 cooled at a rate of 0.3 °C/s, showing the [Chinese script $Al_{15}Fe_3Si_2$ - α-Al] eutectic (see arrows).[46] b) Microstructure of a sample from alloy B319.1 cooled at a rate of 0.6 °C/s, showing a β-Al_5FeSi particle formed before the main eutectic reaction (arrowed).[46]

The α-AlFeSi phase shows some variation in composition and quite different morphologies depending on the cooling conditions. For example, the basic formula, $Al_{15}Mn_3Si_2$, should give the atomic percentages of Al = 75, Mn = 15 and Si = 10. The EDX analysis data from a number of particles of different morphologies gives Al = 67.1, Mn = 5.3, Fe = 14.3, Cu = 1.6 and Si = 11.3 atomic %. These data indicate that Mn is partially substituted by Fe, and Cu may partially substitute for Al. In the this case, the formula will correspond to $(Al,Cu)_{15}(Mn,Fe)_3Si_2$.[46]

2.1.2.2. The β-AlFeSi phase

The β-AlFeSi phase is always a primary phase, having a three-dimensional form of a platelet which appears as needles in the micrographic section (Figure 3 (b)). The β-AlFeSi phase is most associated with Fe greater than about 1%, roughly the location of the eutectic point in the Al-Si-Fe phase diagram.[40] However, due to the segregation of Fe during solidification, the β-AlFeSi phase forms even when Fe content is less than 1% (Figure 4).[46] It was also reported that the β-AlFeSi phase forms at Fe levels as low as 0.5%.[40] However, the addition of certain alloying elements and fast cooling increase the Fe content at which the β-AlFeSi phase forms.

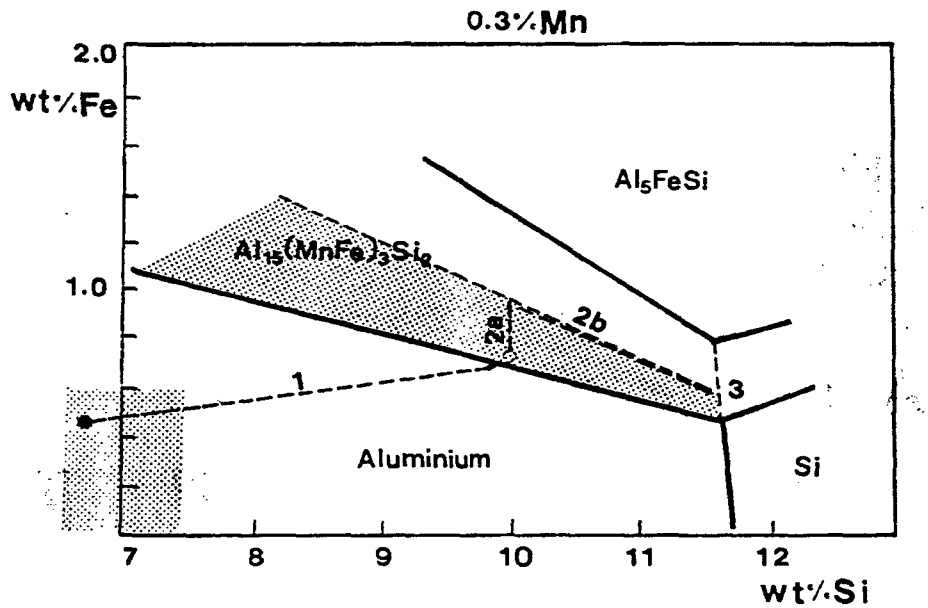

Figure 4 Simplified phase diagram showing the formation of the β-Al_5FeSi phase in a 356.0 alloy sample through the segregation paths (1-2a-2b-3).[46]

The β-AlFeSi phase only has a detrimental influence on the alloy properties when it is a primary phase. Its effect may be negligible when it is part of the eutectic. The detrimental effect of Fe can be minimized by various techniques: (1) rapid solidification, (2) manganese addition, and (3) melt superheating.[10] All these techniques basically convert the crystallization of the needle-like β-AlFeSi phase to the less harmful dendritic (Chinese script) form, *i.e.*, α-AlFeSi phase.

2.1.3. Observation of Fe-Intermetallics in Dilute Al-Alloys

In commercial unalloyed aluminum up to 1% of Fe and Si are usually present. Small amounts of other elements also occur but Fe and Si are the main ones that form particles together with aluminum. To some extent commercial aluminum may therefore be regarded as ternary Al-Si-Fe alloys.

Dones[16] sorted out the different α-AlFeSi phases (*i.e.*, phases in the composition range $Al_{12\text{-}15}Fe_3Si_{1\text{-}2}$),[a] that can form in industrially cast Al-alloys according to the rate of cooling (from 0.1 to 500 K/s) at which they formed as follows:

Heat treatment	α, α', α'', α_T
DC cast, inner zone	α, α_V, α_T
DC cast, outer zone	α, α''
Strip cast	α

The α′-AlFeSi phase, which is generally believed to be an equilibrium phase, was only observed in heat-treated materials. This indicates that it is difficult to nucleate this phase. It forms in pure Al-Si-Fe alloys after extremely slow cooling.

---

[a] Refer to Table 1.

The α-AlFeSi phase (bcc) does not from in pure Al-Si-Fe alloys. Since the α-AlFeSi phase is less ordered than the α′-AlFeSi phase, it is expected to be favored by rapid cooling. Thus, it becomes increasingly important as the rate of cooling increases. The α″- and α_T-AlFeSi phases (superstructure phases) form at intermediate cooling rates. The α_V-AlFeSi phase is found only in the inner part of DC cast billets, so it may form as a result of the presence or absence of some minor elements similar to the α-AlFeSi phase which is stabilized by the presence of certain elements as Mn, Cr, V, Mo, W and Cu.

There is also an observed shift toward Si-richer particles with increasing cooling rate. Dons[16] has also proposed a particle diagram for the middle of strip cast sheets (at about 500°C). It seems useful to construct diagrams in order to facilitate the prediction of what phases can form in different alloy compositions.

Liu *et al.*[17] investigated the formation of Fe-intermetallic phases such as θ-$Al_{13}Fe_4$, α-Al_8Fe_2Si and β-Al_5FeSi and others during solidification of dilute Al-Si-Fe alloys. The chemical compositions of these phases were quite similar, and the precipitate morphologies were also often very similar. Thus, the exact identification of phases was possible only by electron diffraction. The average size of precipitates was considerably more dependant upon solidification rate than upon Fe content of the alloy.

Most of the phases were intermediate non-equilibrium precipitates, which transform to more stable variants during subsequent heat treatments. Solidification rate, alloy composition and the presence of trace elements are important factors that determine the dominant phase under particular solidification conditions.

The solidification rates studied by Liu *et al.*[17] were 1 and 10 °K/s. The θ-$Al_{13}Fe_4$ phase was the predominant phase at slow cooling rate (~1 °K/s) for commercial and high purity alloys. At fast cooling rates both the α-AlFeSi and the q_1-AlFeSi phases dominated in the commercial-purity alloys. The q_1-AlFeSi phase transformed to the q_2-AlFeSi phase after annealing for 24 hours at 600°C. In the high purity alloy, the θ-$Al_{13}Fe_4$ and Al_pFe phases formed as well as the dominant α-AlFeSi phase at fast cooling rates. All phases except the α-AlFeSi disappeared on annealing for 24 hours at 600°C. Thus, it is clear that trace elements can play a decisive role in determining the presence of many of these phases under conditions of fairly rapid solidification. These authors also highlighted the fact that the sensitivity of analysis by EDX is not sufficient to detect the presence of the trace elements in the precipitates.[17]

2.1.4. Crystallization and Neutralization of Fe-Intermetallics

2.1.4.1. Effect of Fe Content

Tanihata *et al.*[8] studied the effect of Fe content from 0.1 to 0.5% on the occurrence of Fe-intermetallics in a 6063 alloy in the as-cast condition. They found that with increasing the Fe content in the alloy from 0.1 to 0.2 wt %, the amount of β-AlFeSi phase sharply increased to 80% of all the phases, at the expense of the other phases such as the α- and α′-AlFeSi. In contrast, they found that in a 0.3% Fe alloy the β-AlFeSi phase decreased again to about 25%, while that of the α-AlFeSi phase increased to about 70%. When the Fe content was 0.5%, this tendency became remarkable and no β-AlFeSi particles were observed. Thus, they concluded that a slight change in the Fe content of the 6063 alloy ingots causes considerable changes in the relative frequency of the Fe-intermetallic phases. Murali *et al.*[49] have found that as the Fe content increases the maximum length of the β-AlFeSi plates increases and the continuous presence of the β-plates is observed within interdendritic regions.

2.1.4.2. Effect of Cooling Rate

Cooling rate plays a basic role in stabilizing the different Fe intermetallic phases in Al-alloys, so that some phases are stabilized only at slow cooling rates, such as the binary Al-Fe phases, while others are stabilized at intermediate cooing rates, and still others, such as the δ-AlFeSi and q_1-AlFeSi phases, at only high cooling rates. There are also some phases, *e.g.*, α-AlFeSi, which have high stability over a wide range of cooling rates.

Slow cooling rates result in the formation of stable phases, whilst high cooling rates lead to the precipitation of metastable phases. The intermetallic phases that appear in a microstructure are controlled not only in terms of whether the cooling rate is high or low, but, more accurately, also by the fact that each of these phases is associated with a certain cooling rate range. This fact is indispensable for a proper understanding of the alloy system. In view of this, some studies have specified the occurrence of Al-Fe binary phases to certain cooling rate ranges.[22,50] Young[23] has constructed cooling rate regimes for the formation of different intermetallic precipitates in hypoeutectic Al-Fe alloys.

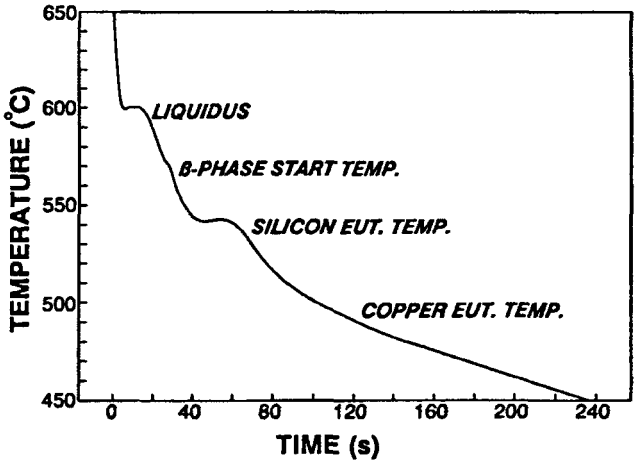

Figure 5 The cooling curve of a 319 alloy (0.3% Mg), cooling rate 2.5 °C/s.[10]

Narayanan *et al.*[10] reported that Fe forms a ternary intermetallic phase with the main components of Al-Si alloys and, in the absence of Mn, crystallizes only in the form of needles (*i.e.*, β-AlFeSi phase) for Si and Fe contents of 6 and 1%, respectively. However, crystallization of the Fe-compounds in the Chinese script form was not observed even at cooling rates of 20°C/s for the 319 alloy, but with addition of 0.3% Mg, the β-AlFeSi phase starts to crystallize at temperatures between the liquidus and the Si-eutectic temperature (572°C at a cooling rate of 2.5°C/s) as shown in Figure 5.

With decreasing temperature or increasing solidification time, the β-AlFeSi phase continues to crystallize until the end of the Si-eutectic reaction. The interesting aspect of the β-AlFeSi phase reaction is that unlike the Si and Cu eutectic temperatures, which are

only slightly affected (less than 7°C) by variations in cooling rate, the β-phase start temperature decreases with decreasing Fe content, increasing cooling rate and increasing melt superheat temperature until it eventually occurs with the Si-eutectic temperature.[10,11,51]

The average length of β-AlFeSi needles decreases with decreasing Fe content, increasing cooling rate and decreasing Mg content. The average maximum length of β-AlFeSi platelets and the β-AlFeSi phase start temperature decrease exponentially with increasing the cooling rate as shown in Figure 6. In addition, the amount of Mn needed to neutralize the Fe varies with the cooling rate during solidification. Mn was found to inhibit the formation of β-AlFeSi phase for Fe contents less than 1.2% in thin chilled sections, and less than 0.75% in sand-cast test bars. The critical Fe content at which the β-AlFeSi phase appeared in terms of cooling rate were 0.75% Fe at 1 °C/s, 0.8% Fe at 5 °C/s and 1.0% Fe at 10 °C/s.[40] It is clear that increasing the cooling rate leads to an increase of the critical Fe content at which β-phase precipitates, thus promoting the formation of (the Fe-richer) Chinese script phase. However, the effect of Mn content is still unclear and needs more explanation.

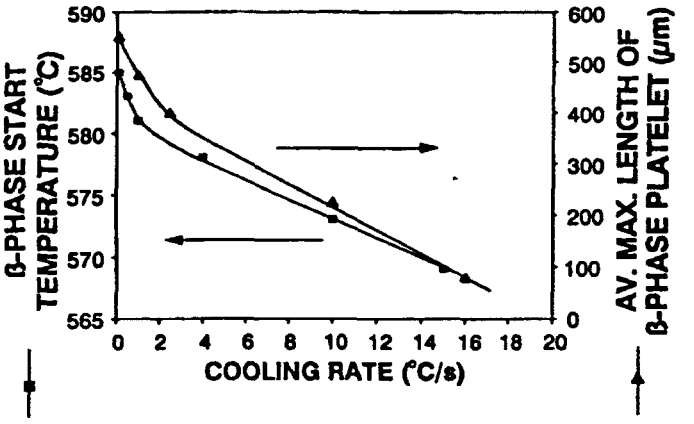

Figure 6 Plots of average maximum length of β-AlFeSi platelets and β-AlFeSi phase start temperature *vs.* cooling rate.[10]

2.1.4.3. Effect of Mn Content

In the presence of Mn, the Fe-compounds crystallize in three distinctly different morphologies, namely: (1) a needle-like form (β-AlFeSi phase), (2) a Chinese script morphology (α-AlFeSi phase), and (3) a starlike or polyhedral morphology (the primary α-AlFeSi phase), depending on the Fe/Mn weight ratio and the cooling rate. At low cooling rates, Fe-compounds form in the primary α-AlFeSi morphology, whereas at high cooling rates, both α- and β-AlFeSi phases crystallize. In the absence of Mn, the Fe-compounds crystallize only in the β-AlFeSi form, which is stable at cooling rates less than 20 °C/s. When the melt is superheated to a high temperature, and solidified under high cooling rates, the Fe-compounds crystallize in the metastable form of the α-AlFeSi phase.[10]

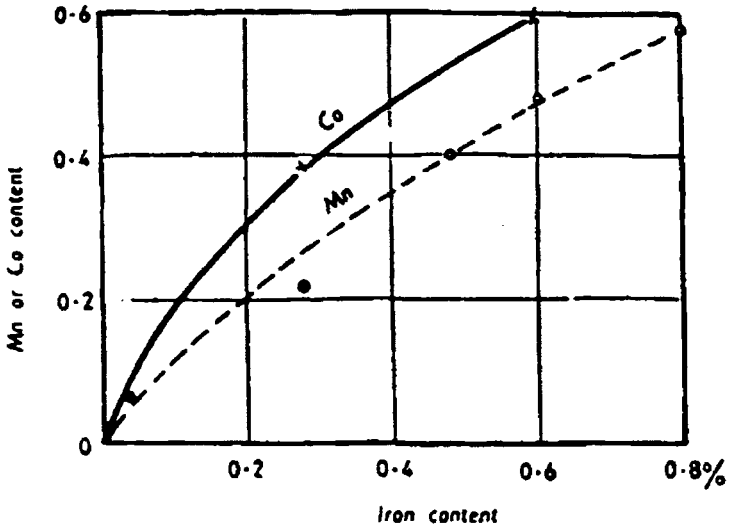

Figure 7 Amount of Co and Mn necessary to suppress the harmful effect of Fe in Al-Si eutectic alloys.[52]

The ratio of Mn to Fe necessary to compensate for the negative effects of Fe-intermetallics has not yet been established. However, in the reviews of Crepeau[40] and Couture[52], this was mentioned to be 0.6 to 0.8:1 depending on the chemistry of the alloy. In other reports, it was mentioned that the Mn content must be > ½ Fe content, or may be given by the relation, Mn = 2 × (%Fe - 0.5), or taken from the chart of Figure 7.

The ASTM B108-95 (standard specification for Al permanent mold casting) and ASTM B26-95 (standard specification for Al-alloy sand castings) set the maximum Fe level in the Al-alloys from very low as 0.15 % in alloy 201.0 to very high as 1.5% in alloy 222.0, while in other alloys such as 355.0 and 356.0 the Fe content was allowed to

reach 0.6 % or more with the comment that if Fe exceeds 0.45 %, Mn content shall not be less than half of the Fe content.

The chemical compositions of the α- and β-AlFeSi phases are given in Table 2. It is clear that the chemical composition of the primary α-AlFeSi phase is almost the same as that of the Chinese script morphology. However, the α-AlFeSi phase, especially in primary crystal form, may dissolve a significant amount of Cu, Cr, Ni, *etc.* Unlike the chemical compositions of Table 2, some authors reported that the β-AlFeSi phase does not dissolve appreciable amount of other alloying elements.[17,40,48] From the analysis in Table 2, it is clear that the ratio of Si to Fe is higher in the β-phase than in the α-phase.

Table 2 Comparison the chemical analysis of the Fe- intermetallic compounds in some Al-Si-Fe alloys.[10,18]

Reference	Phase	Al	Si	Fe	Mn	Cu
Gruzleski[10]	β	46.5	27	20.8	4.2	1.1
Apelian[a]	β	48.5	16	29.3	6.1	--
Shimizu[18]	β	58.5	15.3	24	--	--
Shimizu[18]	β	54.5	17.5	28	--	--
Gruzleski	α	59.6	8.9	18.5	9	3.71
Apelian[a]	α	48.8	9.4	29.7	12.1	--
Shimizu[18]	α	61.5	10.5	28.2	--	--
Shimizu[18]	α	59.8	10.5	28.3	--	--
Gruzleski[10]	1^{ry}-α	60.9	8.2	15.6	13.5	1.5

[a] Apelian *et al.*, Annual workshop 1991, aluminum casting research laboratory, Worcester Polytechnic Institute, MA, p143 [cited by Gruzleski[10]].

In order to obtain the Fe-compounds crystallized in the Chinese script form and to avoid the needle-like and polyhedron crystal morphologies a certain critical ratio of Fe:Mn is required and this ratio depends on the cooling rate as mentioned above.

Xiufang *et al.*[53] used master alloys containing Al-10% Mn-2% Ti, to modify (*i.e.*, spheroidize) the Fe-compounds in the Al-Si, Al-Mg, and Al-Zn alloys. This addition led to the improvement of the room temperature and the 300 °C tensile properties of an Al-Si alloy containing 1.4% Fe.

2.1.4.4. Effect of Other Chemical Neutralizers

Chromium: Various additions of Cr to an Al-7% Si-0.3% Mg alloy caused the coarse β-AlFeSi platelets to be replaced with Chinese script. It was also reported that additions of 0.2 to 0.6% Cr prevented the embrittlement of an Al-13% Si alloy for Fe contents more than 1%. In other cases, Cr was reported to increase the elongation of certain alloys.[40]

Cobalt: It was reported that Co has a neutralizing effect for Fe similar to that of Mn.[40] However, the Co has less tendency to segregate during solidification, and thus offers superiority to Mn. This property supports the observation of Murali *et al.*,[49] where,

in a Co-added alloy, the Fe-intermetallic particles form mostly within the primary α-Al dendrites (*i.e.*, intragranular particles) rather than in the interdendritic regions. It was suggested that the Fe:Co ratio should be 1:2. However, Figure 7 shows that the amounts of Co required to antidote the Fe-compounds and achieve similar results are much lower.

Beryllium: Be can be combined with Fe into compact particles of $Al_4Fe_2Be_5$ provided that the amount of Be is > 0.4%. It was reported[40] that additions of Be caused the Fe-rich intermetallics to form in a round, nodular or spheroidal form, and this increases the tensile strength and elongation. In addition, Murali *et al.*[49] found that the phases formed in all the Be-added alloys were seen only inside the α-Al dendrites. This may provide additional explanation for the observed increase in strength and elongation, because the Fe-intermetallics form in the ductile Al-matrix rather than in the less ductile interdendritic regions. In this case, if cracks initiate in the Be-Fe scripts, they will be arrested within the α-Al dendrites.

Molybdenum, nickel and sulfur were mentioned to be useful neutralizers for Fe as well.[40]

Strontium: Additions of Sr were found very effective to eliminate some morphologies of Fe-intermetallic compounds in both commercial and synthetic alloys.[52]

It was reported that the Sr caused reduction in size, number and volume fraction and transformation of all Fe-intermetallics to spot-like phases in a synthetic 413 alloy and the elimination of all kinds of intermetallics in the A413 and 413P alloys under fast cooling conditions. In this solidification condition, Sr is very effective in reducing the amount and size of the β-AlFeSi needles and changing it to the α-AlFeSi phase morphology (Chinese script).[54] This is probably due to the undercooling at the solidification front caused by Sr additions. Samuel *et al.*[55] proposed that Sr had a poisoning effect on the nucleation sites for β-AlFeSi needles. This reduces the number of sites available for nucleation and, thus, a lower β-AlFeSi phase density is obtained, compared to that in the unmodified alloy.

In another study, it was found that the combined addition of (Mg + Sr) in 1XXX alloys, led to spheroidization of the α-Al_8Fe_2Si particles and fragmentation of the Al_3Fe phase needles.[56] The effect of Sr on the morphology of Fe intermetallics in the 319 alloy was evaluated, Sr tends to dissolve the β-AlFeSi needles within the Al-matrix without transformation into any other type of intermetallic compounds. Samuel and Samuel[56] also concluded that Sr did not nucleate sludge crystals, the star-like particles, in alloy 319.

2.1.4.5. Effect of Melt Superheat

Narayanan *et al.*[10] showed that at a low melt superheating temperature of 750 °C (about 150 °C above the liquidus for alloy 319), the Fe-compounds crystallized in the needle-like form (*i.e.*, β-phase) at all cooling rates, whereas at high melt superheating temperatures of about 850 or 900 °C and at high cooling rates crystallization occurred in both the Chinese script and the needlelike forms. The relative amounts of each phase depend on the Fe, Mg contents and cooling rate. However, the superheating temperature affects the β-AlFeSi phase start temperature, so that the latter decreases as the former increases (Figure 8).

Jiaji *et al.*[57] found that the morphology of the Fe-compounds changes from a long needle-like form to rosettes as the melt-temperature changes from low to high. For example, they found that for an alloy containing 1.2% Fe and melt superheating of 840 °C, the Fe-compounds present in the sample were in the needle-like form. Increasing the pouring temperature to above 920 °C spheroidized the phase morphology. When pouring in the temperature range 840-920 °C most of Fe-compounds appeared as rosettes with only a small portion appearing as needles or spheroids. In the case of 1.8% Fe, poured from below 900 °C, the morphology of the Fe-compounds was revealed as long needles.

When the alloys were heated to 980 °C and then poured into a permanent mould, the needle-like form of Fe-intermetallic phases changed completely into the spheroidal shape. The room-temperature tensile strength of the alloy containing 1.8% Fe increased by 83% and the elongation by 115%. The high-temperature tensile and elongation for the same material increased by 32% and 80%, respectively.

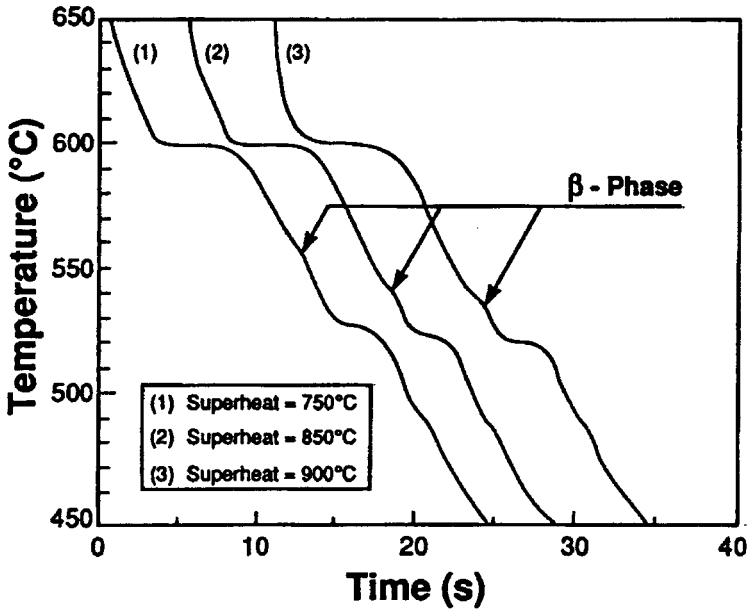

Figure 8 Cooling curves of a high Mg alloy (0.3% Mg) superheated to 750, 850 and 900 °C prior to casting, cooling rate 10 °C/s.[10]

Narayanan *et al.*[10] found that, in the case of high Mg alloys (0.3% Mg), the α-AlFeSi phase did not crystallize even at a high melt superheating temperature (900 °C) and a high cooling rate (25 °C/s). In the case of low Mg content (0.003% Mg), complete

crystallization of the Fe compounds in the α-AlFeSi phase was achieved at a superheating temperature of 850 °C or above, and at cooling rates of 25 °C/s or higher. The same behavior was also reported by Awano and Shimizu,[18] where the superheating temperature inhibited the AlMgFeSi and AlFeSi compounds in Mg alloyed samples to crystallize in a needle-like morphology. However, heating to such high temperatures increased the chance for hydrogen pick up and increased the inclusion content.

2.1.4.6. Effect of Aluminum Oxide Transformation

Through TGA analysis, Narayanan *et al.*[10] noticed that transformation of the γ-Al_2O_3 to α- Al_2O_3 takes place during heating at about 950 °C. The presence of the γ- and α-Al_2O_3 inclusions was also confirmed by XRD analysis at low and high melt superheat temperatures, respectively. This transformation temperature (950 °C) coincides with the critical melt superheat temperature above which iron compounds crystallized in the α-AlFeSi phase rather than the stable β-AlFeSi phase form. Therefore, the change in the crystallization behavior of Fe-compounds by melt superheating can be attributed to the γ-$Al_2O_3 \rightarrow$ α-Al_2O_3 transformation. With increasing melt superheat temperature, a series of

metastable highly porous oxide phases formed before the final conversion to the α-Al_2O_3 phase,[a] according to the following sequence:

$$\gamma -_{(500^\circ C-850^\circ C)} \rightarrow (\gamma + \delta)_{(850^\circ C-900^\circ C)} \rightarrow \delta -_{(900^\circ C-950^\circ C)} \rightarrow (\delta + \theta)_{(950^\circ C-1000^\circ C)} \rightarrow \theta -_{(1000^\circ C-1050^\circ C)} \rightarrow (\theta + \alpha)_{(1050^\circ C-1100^\circ C)} \rightarrow (\alpha - Al_2O_3)_{(>1100^\circ C)} \quad (1)$$

The temperature values given here are only approximate, with the exact transformation temperatures depending on a variety of factors such as impurity content, melt holding time and stirring. The addition of small amounts of Ga, Li, Mn, Si and Cu were reported to have a pronounced effect on the oxidation behavior of aluminum, so that they can decrease or increase the temperature at which the transformation of the γ-Al_2O_3 to the α-Al_2O_3 may occur, especially in commercial purity alloys.

The presence of certain alloying elements such as Mg strongly stabilizes γ-Al_2O_3, since the γ-Al_2O_3 is isomorphous with the spinel phase, $MgAl_2O_4$, and thus increases the γ-$Al_2O_3 \rightarrow \alpha$-$Al_2O_3$ transformation temperature. High Fe seems to have the same effect as Mg.

---

[a] K. Wefers and G. M. Bell: Technical Paper No. 19, Alcoa, Pittsburgh, PA, 1972, p.1 [cited by Narayanan *et al.*[10]].

2.1.4.7. Effect of Minor Impurity Elements

Liu *et al.*[17] and Awano and Shimizu[18] found that trace elements can play a decisive role in stabilizing many of the intermetallic phases under conditions of fairly rapid solidification. Allen *et al.*[58] proposed that there should be a potent catalyst for the nucleation of the $Al_{13}Fe_4$ phase and suggested this to be the primary Al-matrix or an undetected impurity which is present even in the super purity Al-based alloys. In addition, they found that the metastable phase content is largely controlled by the concentration of the solute atoms of V and P. Thus, the constitution of the alloy has a major effect on the intermetallic phase selection. Other workers showed that the Al_mFe phase forms in the grain refined alloys provided that a certain level of V[59,60] or Si[59,61] is attained in the alloy composition.

Liu *et al.*[17] also highlighted that the sensitivity of analysis by EDX is not sufficient to detect the presence of the trace elements in the precipitates. In addition, Awano and Shimizu[18] found that the gas content is not related to the phenomenon of precipitation of the Fe-compounds in the Chinese script morphology because this phase was observed when the melt was vacuum-degassed and, thus, they pointed out the strong effect of impurity elements on the stability of phases. The same phenomenon was

observed by Murali *et al.*[49] They found that trace additions of Be, Cr, Mn, and Co, individually or combined, tied up the Fe in the alloy to form new phases with altered morphology such as Chinese script, polygons, and irregular shapes.

2.1.4.8. Effect of Mg Content

Narayanan *et al.*[10] found that increasing the Mg content depresses the Si-eutectic temperature; this is one of the reasons why it was more difficult to crystallize the α-AlFeSi phase in high Mg alloys even at high melt superheat temperature, 900 °C. This effect was also reported by Awano and Shimizu.[18] However, it is more difficult to force the β-AlFeSi phase start temperature to below the Si-eutectic temperature in high Mg alloys by using either a high melt super heating temperature, a high cooling rate or both. In addition, the plate length and volume fraction of the β-AlFeSi phase increased with Mg content due to the increase in the growth time of the primary β-AlFeSi phase.[10] In contrast, Samuel *et al.*[55] found that the addition of Mg to the 319 type alloys transformed a large proportion of the β-Al_5FeSi needles into the $Al_8Mg_3FeSi_6$ compacted Chinese script phase.

The relationship between superheating temperature and Mg content affecting the change in the shape of the Fe-compounds in Al-6% Si-Mg-0.4% Fe alloy castings is shown in Figure 9. In the Al-6%Si-0.4%Fe alloy superheated to 815 °C, the Fe-compounds almost crystallized in a Chinese script form. However, after adding a small amount of Mg, the change in the shape of the compounds did not occur, and even when the melt was superheated to 950 °C the Fe-intermetallic phases crystallized not only in a Chinese script form but also in a needle-like form.[18] The Chinese script tended to crystallize when the solidification time became shorter even when the superheating temperature was the same.

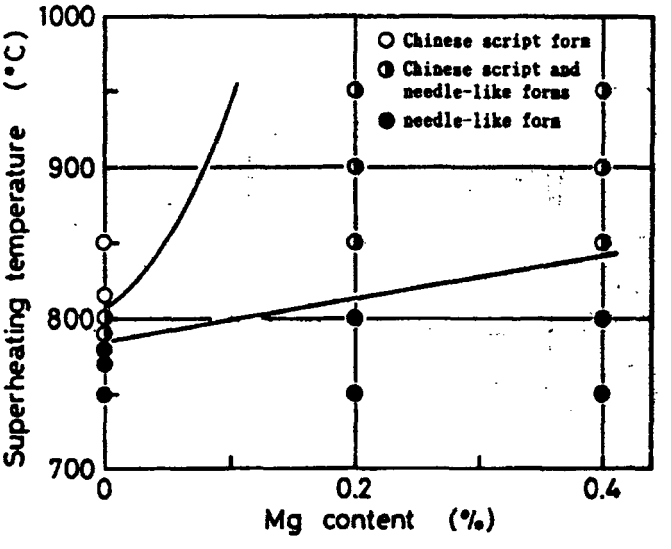

Figure 9 Effect of Mg content on the structure of Fe-compounds in Al-6% Si-Mg-0.4% Fe alloy castings.[18]

In addition, it was confirmed that the compositions of the Fe-compounds in the needle-like and the Chinese script forms were $Al_{4.5-4.6}FeSi_{1.2-1.3}$ and $Al_{5.5-6.6}Fe_{1.3-1.5}Si$, respectively. Moreover, each Fe-compound contained about 0.1% Mg.[18]

2.1.5. Complex Iron Intermetallic Compounds (Sludge)

The $(FeMn)Al_6$ phase is the first phase in the Al-Fe-Mn-Si system to form over a good part of the system where many of the commercial alloys are located. In many alloys, the $(FeMn)Al_6$ phase reacts peritectically with liquid to form the $(FeMn)_3Si_2Al_{15}$ phase. In high Si alloys, the $(FeMn)_3Si_2Al_{15}$ phase may be primary and since its crystals tend to be limited by the (111) faces, it appears as more or less well formed hexagons. These primary phases containing Fe, Mn and Cr are usually called sludge.

The sludge compounds have high melting points and high specific gravity which causes them to settle to the floor of the melt. If stirred into the melt and incorporated into a casting, they act as hard spots and have a detrimental influences on the mechanical and physical properties of the cast parts.

Gruzleski *et al.*[13,41,62] studied the kinetics of formation and growth of the complex intermetallic compounds in the 319 and 413 alloys. They studied alloys containing 3%

Mn, 0.1% Cr and 0.4, 0.8 and 1.2% Fe. According to these studies, the temperature of sludge formation increased with the Fe content of the alloy, about 650, 660 and 690 °C at 0.4, 0.8 and 1.2% Fe, respectively. The Fe-intermetallic phase formed at high temperatures consumed some of the Si present in the alloy, and shifted the local chemical composition of the melt to the Al-side of the phase diagram resulting in the formation of primary Al-dendrites around the intermetallics particles. The volumetric change of intermetallics was directly related to the number of particles nucleated in a unit area. Thus, the process of volumetric growth is nucleation controlled. The data curves have an exponential shape, so, a first-order reaction model was proposed as follows:

$$V_t = V_i \exp(Rt) \quad (2)$$

Where, V_t is the volume percent of sludge at time t, V_i is the initial volume percent, R is a rate constant (hr^{-1}) and t is the time (hr).

The constants of this relationship are given in Table 3.

Table 3 Reaction constants for the volumetric change of sludge.[41]

Alloy	600°C		630°C		660°C		690°C	
	R	V_i	R	V_i	R	V_i	R	V_i
0.4% Fe	0.68	0.08	0.82	0.07	-0.80	0.08	-6.21	0.06
0.8% Fe	0.57	0.32	0.39	0.34	-1.61	1.31	-6.55	0.08
1.2% Fe	0.4	1.70	0.40	1.93	0.22	2.16	0.27	2.82

An empirical formula called the "sludge factor" has been suggested by Gobrecht[a] and Jorstad[b]. The sludge factor in Al-Si-Cu is used to determine how much Fe, Mn, and Cr can cause sludge to form, and so it serves as a guide but not as a guarantee to avoid sludging. This factor is calculated from:

$$\text{Sludge Factor} = (\text{wt\% Fe}) + 2(\text{wt\% Mn}) + 3(\text{wt\% Cr}) \quad (3)$$

A sludge factor of 1.8 will normally result in sludge formation if a casting temperature of 650 °C or more is maintained, for example, in die casting alloys. However, for lower holding temperatures a sludge factor of 1.4 or less may hold. For the 319 and 413 alloys the critical sludge factor is estimated to be 2.1.[13]

The effect of Mn and Fe contents on the formation of sludge is shown in Figure 10. Sludge formed at a high Fe content, *e.g.*, 1.2% Fe, or at high concentrations of Mn and Cr with low contents of Fe, *e.g.*, 0.4% Fe. More than 0.2% Mn and 0.1% Cr were needed to convert all Fe platelets to the star-like form.[62] According to Osame,[63] in an alloy containing Cr, the critical Fe and Mn concentrations for sludge deposition in the molten metal at a holding temperature of "t °C" are given by:

---

[a] J. Gobrecht, Fonderie, 1977, pp.171-173 [cited by Gruzleski[13]]

[b] J. L. Jorstad, Die Casting Engineer Nov/Dec 1986 [cited by Gruzleski[13]]

$$\%Fe + \{3.34 - (t - 630)/714\}\%Mn = 2.39 + (t - 630)/152 \quad (4)$$

The critical concentrations of Mn and Cr in alloys containing 1.0% Fe at a temperature of "t °C" are determined from:

$$\%Mn + \{4.00 + (t - 630)/333\}\%Cr = 0.40 + (t - 630)/500 \quad (5)$$

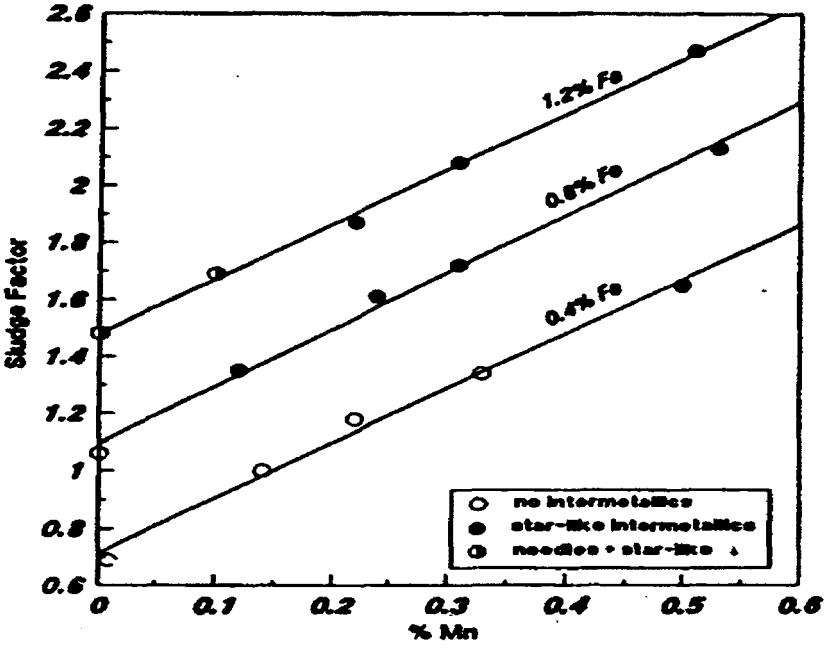

Figure 10 Effect of Mn and Fe on the sludge factor of the Al-12.7% Si-0.1% Cr alloy.[62]

It was found that holding the melt at a temperature of 800-850 °C for 1.5 hours was sufficient to dissolve the intermetallics completely. The sludge formation temperature varies with the Fe content as shown in Figure 11. Sludge is thermodynamically unstable at temperatures above this value, which, as seen from Figure

11, increased with the Fe content of the alloy. The sludge formation temperature as a function of the Fe content is given by the power equation:[62]

$$Temperature(^{\circ}C) = 645.7 + 34.2(\%Fe)^2 \quad (6)$$

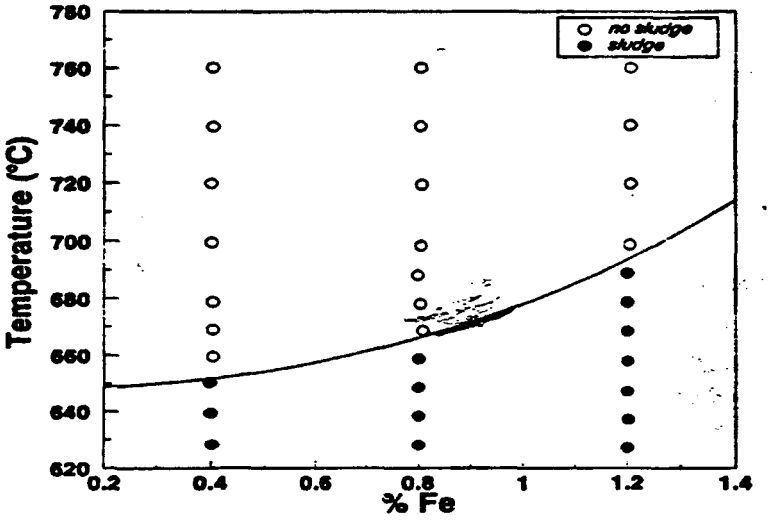

Figure 11 Temperature of sludge formation in alloys containing 12.7% Si and three different Fe levels, 0.4, 0.8 and 1.2%.[41]

However, this temperature depends on the sludge factor as presented in the work of Gruzleski *et al.*[13] The critical temperature was found to be 800 and 690°C for the 319 alloy with a sludge factor of 2.4 and the 413 alloy with a sludge factor of 2.1, respectively.

The effect of cooling rate on the total volume percent of intermetallics formed is shown in Figure 12. The total amount of intermetallic compounds increased with

decreasing cooling rate in all the alloys studied, the maximum was observed at 0.1 °C/s.[62] While the total volume percent of intermetallics increased with decreasing cooling rate, the number of particles of each phase per unit area decreased and the size of each morphology increased.

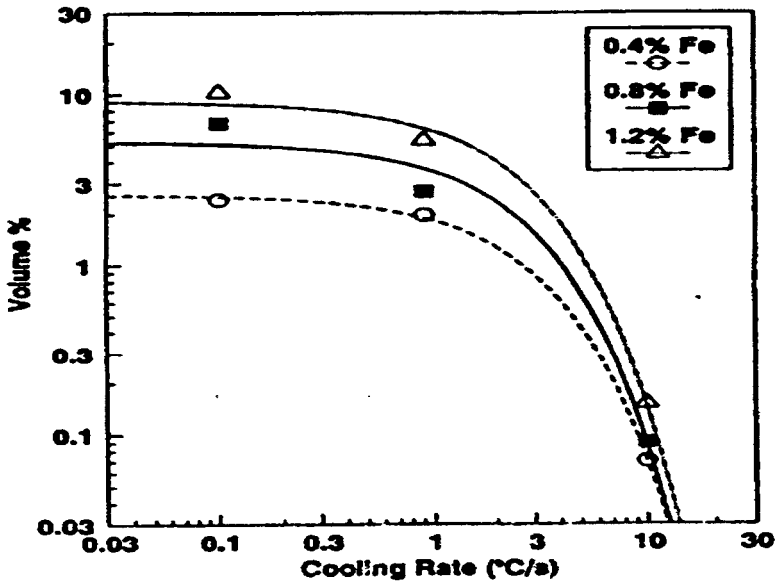

Figure 12 Effect of cooling rate on the total volume percent of intermetallic compounds formed in the alloys.[62]

2.1.6. Dissolution of Fe-Intermetallics by Heat Treatment

Narayanan *et al.*[64] investigated the dissolution of iron intermetallics through non-equilibrium heat treatments for alloy Al-6% Si-3.5% Cu-0.3% Mg-1% Fe, by means of microstructure and mechanical properties. Their conclusions are summarized below.

With increasing solution temperature, the β-phase platelets dissolved slowly through concurrent fragmentation along plate width and dissolution at plate tips (Figure 13). Addition of Mn hindered the dissolution of Fe-intermetallics (Figure 14 and Figure 15); the β-AlFeSi phase underwent a substantial dissolution, whereas the α-AlFeSi phase did not undergo any dissolution. The solution temperature plays a much more important role than does the solution time. Non-equilibrium heat treatment increased the strength properties of the high Fe alloys matching those of the low Fe alloys.

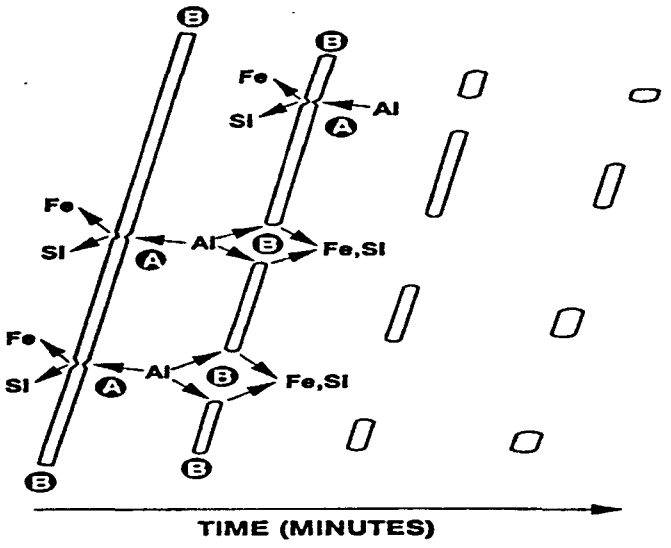

Figure 13 Schematic illustration of the mechanism of the β-AlFeSi phase fragmentation and dissolution process.[64]

The optimum solution treatment temperature was found to be between 515 and 520 °C. At this temperature range, the maximum amount of Fe-intermetallics would

dissolve in the Al-matrix. If this temperature range is exceeded, the amount of liquid phase increased drastically and causes premature failure of the alloy. It was also found by fractography that the α-AlFeSi phase is more fracture resistant than the β-AlFeSi phase. They also showed that the fragmentation of the β-phase should play a beneficial role on the alloy tensile properties provided that the maximum percentage of porosity does not exceed 0.1%.

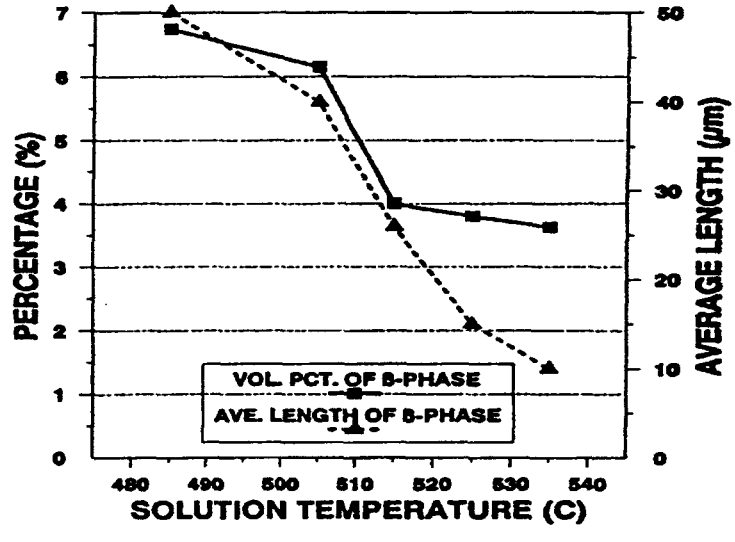

Figure 14 Plot of volume percent and average length of β-AlFeSi particles *vs.* solution temperature for Mn-free alloy samples initially solidified at 10 °C/s.[64]

Awano and Shimizu[18] have suggested that applying a solutioning temperature slightly higher than the temperature of final solidification for the Al-7% Si-3% Cu alloy is expected to lead to a complete dissolution of the Cu-intermetallics.

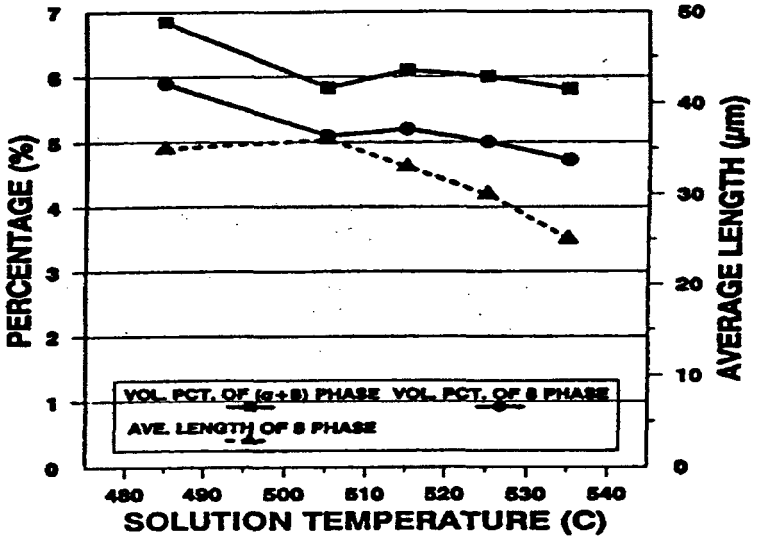

Figure 15 Plot of volume percent and average length of β-AlFeSi particles *vs.* solution temperature for Mn-containing alloy samples initially solidified at 10 °C/s. [64]

More recently, Villeneuve and Samuel[65] investigated the effect of the solution treatment duration on the fragmentation rate of the β-Al_5FeSi phase in Al-Si-Mg alloys, and the impact of this process on the alloy tensile properties. They also studied the effect of modification by Sr on the β-phase dissolution. They found that the presence of a sufficiently high concentration of Sr (~350ppm) led to a breakdown of the β-needles into small thin fragments via two mechanisms:

(1) Splitting of needle into two halves through the formation of longitudinal cracks.

(2) Fragmentation through Si rejection. The process proceeds by the decomposition of the β-AlFeSi phase which takes place by the rejection of Si solute atoms at crevice

sites. This mechanism is schematically represented in Figure 16 and the decomposition can be expressed by the following reaction:

$$Al + Al_5FeSi \rightarrow Al_6Fe + Si \quad (7)$$

Villeneuve and Samuel[65] found that the solution treatment of Fe-containing alloys accelerated the dissolution of the β-phase. The fragmentation of the β-phase led to an improvement in the Young's modulus of the alloy. The addition of Sr and the solution treatment affected only the small β-needles, resulting in a noticeable decrease in the average needle length.

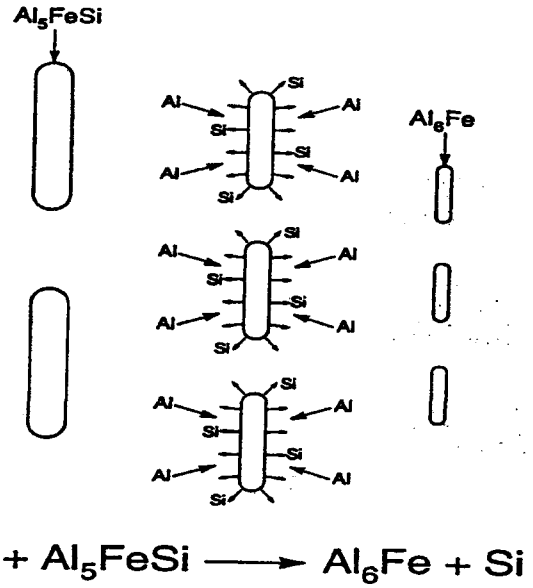

Figure 16 Schematic representation of β-Al_5FeSi decomposition during solution heat treatment.[65]

2.1.7. Role of Fe-Intermetallics in the Porosity Formation[a]

Two basic theories have been proposed in the literature to account for the role of Fe in the porosity formation in Al-alloys, these are the "restricted feeding theory" and the "pore nucleation theory".

The first theory suggests that the β-Al_5FeSi intermetallic platelets restrict feeding. Since the platelets form in the interdendritic channels during solidification, they cause physical restrictions to the movement of the compensatory feed liquid. Regions undergoing shrinkage cannot be fed adequately and porosity is likely to form as a result. For the Al-6.8% Si-3.2% Cu alloy, the limiting temperature[b] was found to be constant at 570 °C, up to Fe levels of 0.5%, and no increase was observed thereafter with increasing Fe content. This theory suggests that it is the origin of the β-AlFeSi phase, rather than the nature of and/or the quantity and size of which, that likely influences the formation of porosity.

The second theory suggests that the β-AlFeSi phase platelets are active pore nucleation sites and also physically constrain the growth of the pores and, so, influence

---

[a] This section is based mainly on the three-part article of Taylor *et al.*[66]

[b] It is the temperature below which feeding is restricted and shrinkage defects arise.

the ultimate pore shapes. The primary objection on the pore nucleation theory is the observation that, at least up to Fe levels of 0.4%, there does not appear to be an increase in actual number of pores observed in any given area.[66] Moreover, the presence of large clusters of the β-platelets within a particular area of microstructure does not lead to the formation of more pores.

Taylor *et al.*[66] found that Fe exhibits a strong threefold influence on porosity and shrinkage-defect formation in the AA309 alloy (in the unmodified, nongrain-refined condition). The aspects of this Fe-porosity effect are given below.

The development of a localized shrinkage-porosity defect, at Fe contents above approximately 0.4%, was observed in castings produced under poor cooling and feeding conditions. The occurrence of configuration-independent minimum total porosity and minimum background porosity values were found at the same critical Fe content. A change in pore morphology from discrete isolated pores of rounded and elongated shapes to regions of spongy interdendritic porosity at Fe contents above 0.1% was observed as well.

Taylor *et al.*[66] showed that the highly localized porosity formation during the solidification of an Al-5% Si alloy (AA309) only occurs at Fe levels greater than 0.4%.

For an alloy containing 10% Si, this defect onset composition was shifted to 0.7% Fe. They explained this in terms of the solidification sequence; based on segregation lines calculated using the Scheil equation, see Figure 17. This shows the calculated line (bold) that defines the compositions at which the solidification sequence, according to the Scheil equation, proceeds directly from Al-dendrite formation to the ternary eutectic troughs (either AT or BT). To ensure that serious Fe-related shrinkage porosity defects do not occur, it was suggested that compositions below the bold line be chosen.

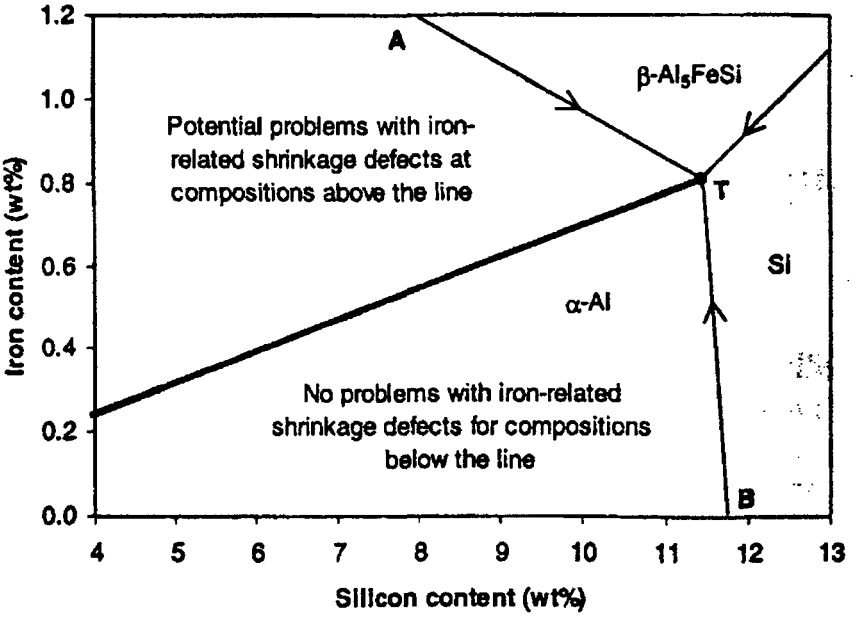

Figure 17 A portion of the liquidus projection of the Al-Si-Fe ternary phase diagram showing the relation between porosity formation and Scheil solidification paths.[66]

The casting is optimmal when solidification proceeds directly to the ternary Al-Si-Al_5FeSi eutectic point, whereas the casting outcome is poor when solidification proceeds via the binary Al-Al_5FeSi eutectic region. They have also found that the critical Fe content, at which the minimum porosity occurred, was a function of the Si content of the alloy. The relation is given by:

$$Fe_{crit} \approx 0.075 \times Si\% - 0.05 \tag{8}$$

This Fe content was proposed to allow the maximum possible amount of ternary eutectic to form.

Taylor *et al.*[66] explained that at these Fe_{crit} compositions the alloy solidifies with the most open and permeable dendritic network and, possibly, with the most mobile interdendritic feed liquid. As a consequence, feeding is optimized at these compositions and the lowest porosity values exist. At Fe contents on either side of the Fe_{crit}, there would be a smaller proportion of ternary eutectic formation and, hence, porosity formation increased as the situation became dominated by the increasing amounts of either Al-Si or Al-β binary eutectic; both of them reduce permeability. Moreover the Al-β eutectic is the more detrimental of the two eutectics. The formation of major shrinkage

porosity defects occurred more frequently and more severely as the proportion of the (Al-β-AlFeSi) eutectic increased.

2.1.8. Identification of Fe-Intermetallics by Thermal Analysis

Thermal analysis of aluminum silicon alloys, including the identification of Fe-intermetallics, was used by several workers (see for example Ref 46,51 and 67). The most extensive thermal analysis of wrought and cast Al-alloys can be found in the work of Backreud *et al.*[46] Sparkerman and Kearney[67] used the second derivative to signal the presence of Al_5FeSi in the 319 alloys. Mackay and Gruzleski[51] used the same technique to quantify the Fe content in Al-Si alloys. They showed that both time duration and resolvable formation temperature of Al_5FeSi could be used to quantify the Fe content in the melt.

2.2. Nucleation Kinetics and Energetics

Nucleation during solidification is a thermally activated process involving a fluctuational growth in sizes of solid clusters. It is inherently difficult to observe the process of nucleation because it involves such a small clusters of atoms. Consequently, only extremely careful comparison of theoretical models and experimental results can clarify the first stages of solidification. During the first stage of equiaxed solidification, which is essentially nucleation controlled, the volume fraction of solid is still very small. Changes in cluster size are considered to occur by a single atom addition or by removal exchange between the cluster and the surrounding undercooled liquid.

After some time, the temperature of the system has risen above the nucleation temperature and the second stage of solidifications starts, which is growth controlled. At this stage, the number of grains present remains essentially constant and solidification proceeds via the lengthening of dendrites, and dendrite arm thickening. At small cluster sizes, the energetics of cluster formation reveal that the interfacial energy is dominant as can be observed by noting that the ratio of surface area to volume of a sphere is 3/r. For the smallest sizes, clusters are called embryos; these are more likely to dissolve than

grow to macroscopic crystals. In fact, the excess interfacial energy due to the curvature of small clusters is the main contribution to the activation barrier for solid nucleation. This accounts for the kinetic resistance of liquids to recrystalization and is manifested in the frequent observation of undercooling effects during solidification.

It is possible to deduce that the nucleation is the dominant process at the beginning of solidification and leads very rapidly to the establishment of the final grain population, with each nucleus forming one equiaxed grain (except if there is dendrite fragmentation). Note that even in the case of columnar solidification, the very first solid in a casting always appears in the form of equiaxed grains. The conditions leading to nucleation are therefore of utmost importance in determining the characteristics of any cast microstructure.

2.2.1. Conditions for Nucleation

As demonstrated in Figure 18 for the case of a hypothetical metal, nucleation begins at some degree of undercooling, $\Delta T = \Delta T_n$,[a] which is very small in practical

[a] The undercooling, ΔT, is usually defined as the temperature difference between the equilibrium temperature of a system and its actual temperature. The latter is lower than the equilibrium temperature

situations. The usual cooling curve Figure 18(a) begins to deviate slightly at the undercooling where nucleation occurs, ΔT_n. At this point, the first fraction of solid, f_s, appears Figure 18(d). With further cooling, the nucleation rate, I, rapidly increases to a maximum value, Figure 18(e), which correspond to the minimum in the cooling curve, Figure 18(a). At this point, the growth rate, V, of the grains is at its highest. The subsequent increase in temperature is due to the high internal heat flux, q_i, arising from the rate of transformation, $\dot{f}_s (= df_s / dt)$, and the latent heat released, Figure 18(c). The final solidification takes place after impingement of grains involving dendrite arm coarsening at a tip growth rate, V, equal to zero. During this time interval, the number of grains, N, remains constant.

The initially small number of grains, which begin to grow, does not appreciably modify the cooling rate imposed by the external heat flux, q_e. Increasing the undercooling has the effect of markedly increasing the nucleation rate, I, and also the growth rate, V. The solidification rate approaches a maximum value when the internal heat flux, q_i,

---

when the melt is undercooled. In this case, ΔT is greater than zero. The term, supercooling, is often used interchangeably with undercooling in the literature.

which is proportional to the latent heat of fusion and the volume rate of transformation, $\dot{f}_s (= df_s / dt)$, is equal to the external heat flux, q_e,[68] as follows:

$$q_e\left(\frac{A}{V}\right) = -C\left(\frac{dT}{dt}\right) + \Delta h_f\left(\frac{df_s}{dt}\right) \tag{9}$$

so that:

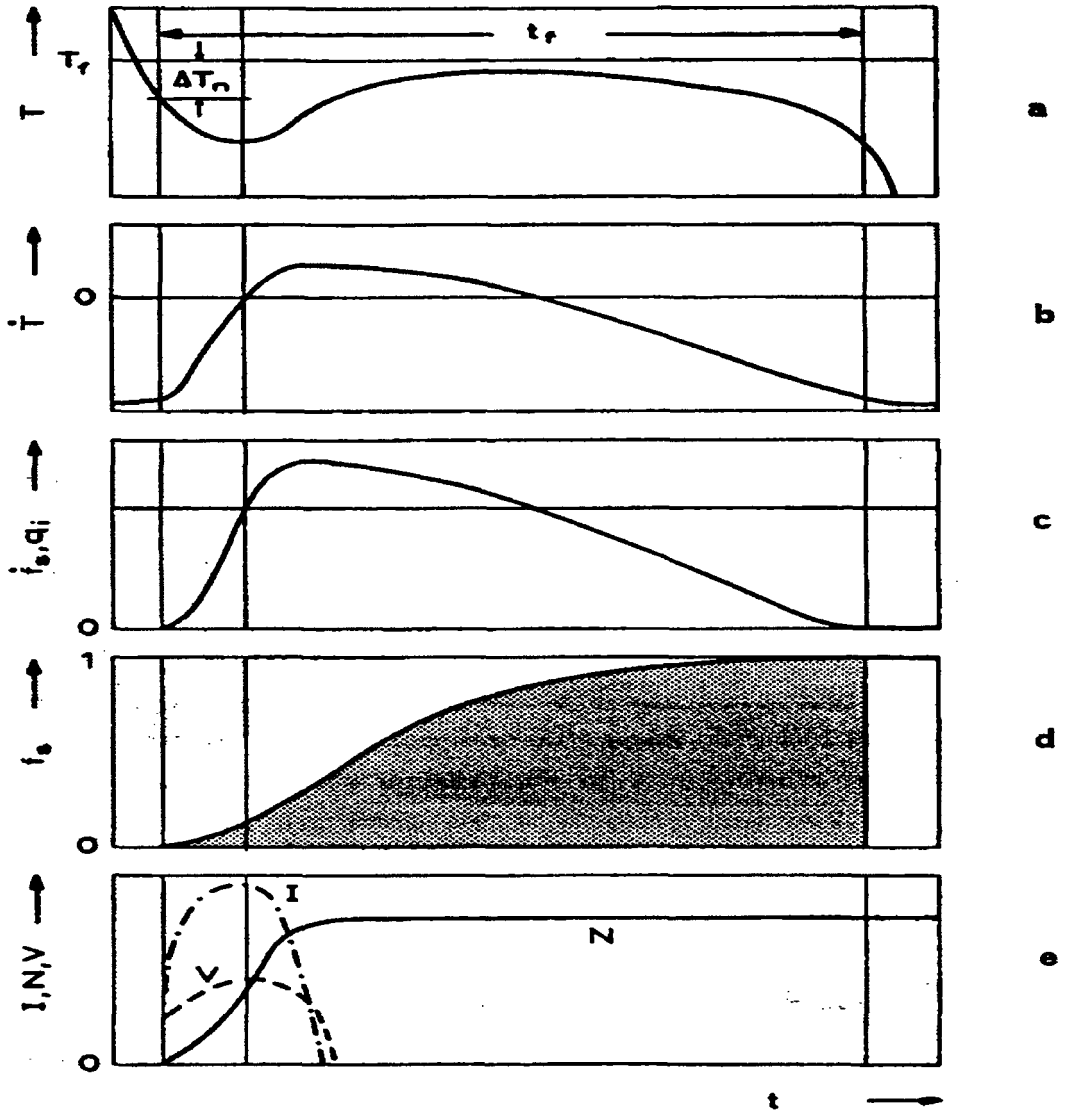

Figure 18 Thermal history of equiaxed dendritic solidification.[68]

$$\dot{T} = \frac{dT}{dt} = -q_e\left(\frac{A}{VC}\right) + \left(\frac{df_s}{dt}\right)\left(\frac{\Delta h_f}{C}\right) \tag{10}$$

The first term on the right hand side (RHS) of Eq (10) reflects the effect of casting geometry (ratio of surface area of casting, A, to its volume, V) upon the extraction of heat, while the second term takes account of the continuing evolution of latent heat of fusion during solidification. It can be seen from this equation that, during solidification, heating will occur if the second term of RHS becomes greater that the first one. This phenomenon is known as *recalescence.* For an alloy, where solidification occurs over a range of temperatures, the variation of fraction of solid as a function of time must be calculated from:

$$\frac{df_s}{dt} = \left(\frac{dT}{dt}\right)\left(\frac{df_s}{dT}\right) \tag{11}$$

Since f_s is a function of temperature, in this case:

$$\dot{T} = \frac{-q_e\left(\frac{A}{V}\right)}{1-\left(\frac{\Delta h_f}{C}\right)\cdot\left(\frac{df_s}{dT}\right)} \tag{12}$$

It is seen that solidification decreases the cooling rate since df_s/dT is negative.

In phase changes such as solidification, which are discontinuous, the transformation process cannot occur at any arbitrary small undercooling. The reason for

this arises from the large curvature associated with a crystal of atomic dimensions. This curvature markedly lowers the equilibrium temperature, so that the smaller the crystal, the lower is its melting point. This occurs because the small radius of curvature creates a pressure difference between the two phases, which is of the order of 100 Mpa for a crystal radius of 1 nm.[68] The equilibrium melting point of the system is thus lowered by an amount, ΔT_r. The critical size, r_{cr}, of a crystal, *i.e.*, the size which allows equilibrium between the curved crystal and its melt, can be calculated. For a sphere this is:

$$\Delta T_r = \Gamma K = \frac{2\Gamma}{r_{cr}} \tag{13}$$

and,

$$r_{cr} = \frac{2\Gamma}{\Delta T_r} = \frac{2\sigma}{\Delta T_r \Delta s_f} \tag{14}$$

This relationship indicates that, the smaller the difference between the melting point and the temperature of the melt (*i.e.*, undercooling), the larger will be the size of the equilibrium crystal.

2.2.2. Homogeneous Nucleation

Homogeneous nucleation is the process in which solid formation occurs without the involvement of any external impurity atoms, or other surface sites in contact with the

melt. The energetics of cluster formation for a spherical geometry can be expressed in terms of a surface and a volume contribution as:

$$\Delta G(r) = 4\pi r^2\sigma + \frac{4}{3}\pi r^3 \Delta G_V \qquad (15)$$

where, $\Delta G(r)$ is the free energy change to form a cluster of size r; σ is the interfacial energy which is always positive; ΔG_V is the Gibbs free energy difference between the liquid and the solid per unit volume. ΔG_V is proportional to ΔT as:[68,69]

$$\Delta G_V = -\Delta s_f \Delta T \qquad (16)$$

with the result that ΔG_V is negative if ΔT is positive.

Thompson and Spaepen[70] have proposed an approximate method for calculating ΔG_V in binary alloy systems, as a function of liquid composition and temperature. These calculations are based on the assumption of regular solution behavior for the liquid and ideal solution behavior for the solid. The calculations require knowledge of the equilibrium phase diagram and the entropies of fusion of the pure components.

The behavior expressed in Eq (15) leads to the occurrence of a maximum in the value of $\Delta G(r)$ when the melt is undercooled, *i.e.*, when ΔT is positive, as shown in Figure 19. It is also shown in the figure that an activation barrier for nucleation, ΔG_{cr}, is reached at a critical size, r_{cr}, (that is, $d\Delta G(r)/dr = 0$), as given by:

$$r_{cr} = \frac{-2\sigma}{\Delta G_V} = \frac{-2\sigma T_f V_m}{\Delta H_f \cdot \Delta T} \tag{17}$$

Here, $\Delta H_f/T_f V_m = \Delta s_f$ (entropy of fusion per unit volume), which makes this equation similar to Eq. (14), and:

$$\Delta G_{cr} = \frac{16\pi\sigma^3}{3\Delta G_V^2} = \frac{16\pi\sigma^3 T_f^2 V_{m,}^2}{3\Delta H_f^2 \Delta T^2} \tag{18}$$

At increasing values of undercooling, r_{cr} is reduced ($r_{cr} \propto \Delta T^{-1}$)[71,72] and G_{cr} is reduced more rapidly ($\Delta G_{cr} \propto \Delta T^{-2}$).[71,72] A cluster is often considered to reach a stage of nucleus capable of continued growth with decreasing free energy when the size r_{cr} is achieved, but in fact stable nucleus growth ensues when the cluster size exceeds r_{cr} by an amount corresponding to (ΔG_{cr}-kT), as shown in Figure 19, where k is the Boltzman constant.[a] The relationship between cluster size and the number of atoms in a cluster, n_{cr}, is expressed by $(n_{cr}V_a) = 4/3\pi r_{cr}^3$, where V_a is the atomic volume.

[a] Boltzman constant is equal to; 1.98 cal/mol °K; $8.62*10^{-5}$eV/°K; or $1.35*10^{-23}$Joule/°K

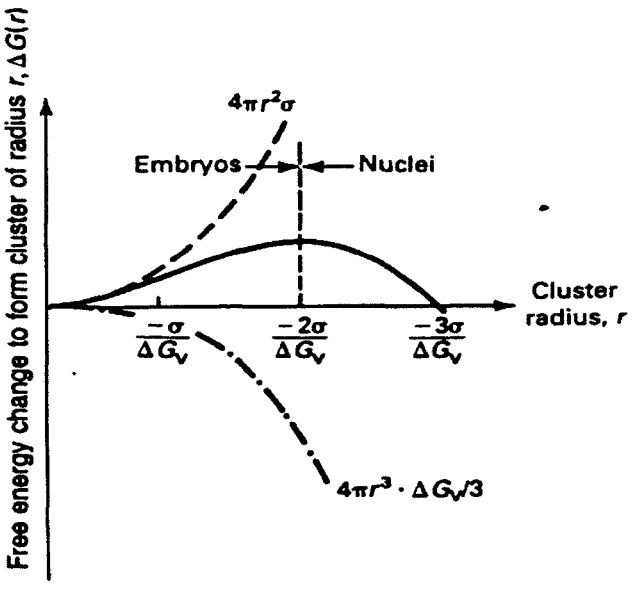

Figure 19 Free energy change for cluster formation as a function of cluster size. The surface contribution to $\Delta G(r)$ is $4\pi r^2\sigma$; and the volume contribution is $4\pi r^3\Delta G_v/3$; r_{cr} occurs at $-2\sigma/\Delta G_v$.

To relate cluster energetics and fluctuational growth to the rate of nucleation, it is necessary to describe the cluster population distribution. Because the mixture of clusters in an undercooled melt is a dilute solution, the entropy of mixing can be described in terms of an ideal solution. The metastable equilibrium concentration of clusters of a given size, C(n), is then given by:[68,71]

$$C(n) = C_\ell \cdot \exp\left(-\frac{\Delta G(n)}{kT}\right) \tag{19}$$

where, C is the number of atoms per cubic meter in the liquid and $\Delta G(n)$ is given by Eq (15), where r is converted to n, as noted above. Equation (19) shows that there are always crystal clusters in a melt, although they are not necessarily stable. Their numbers increase

with decreasing value of $\Delta G(n)$. If the melt is superheated, $d(\Delta G(n))/dn$ is always positive and the equilibrium concentration of crystal nuclei is zero. In an undercooled melt, a maximum in $\Delta G(n)$, as a function of n exists, over which clusters can escape and form the flux of nuclei, I.

If solid nucleation is regarded as the growth of clusters past the critical size, then the resulting cluster flux or the nucleation rate I (in $m^3.s^{-1}$) can be represented kinetically by the product:

$$I = \upsilon_{SL} S_{cr} C(n_{cr}) \tag{20}$$

where, υ_{SL} is the jump frequency associated with atom jumps from the liquid to join the cluster and can be estimated from the liquid diffusivity, D_L, and jump distance, a, as in (D_L/a^2); S_{cr} is the number of atoms surrounding a cluster that is roughly $(4\pi r_{cr}^2/a^2)$; and $C(n_{cr})$ is the concentration of critical clusters.

The full expression for steady state nucleation rate is then:[71]

$$I = \left(\frac{D_L}{a^2}\right)\left(\frac{4\pi r_{cr}^2}{a^2}\right) C_\ell \exp\left(-\frac{\Delta G_{cr}}{kT}\right) = I_o \cdot \exp\left(-\frac{\Delta G(n)}{kT}\right) \tag{21}$$

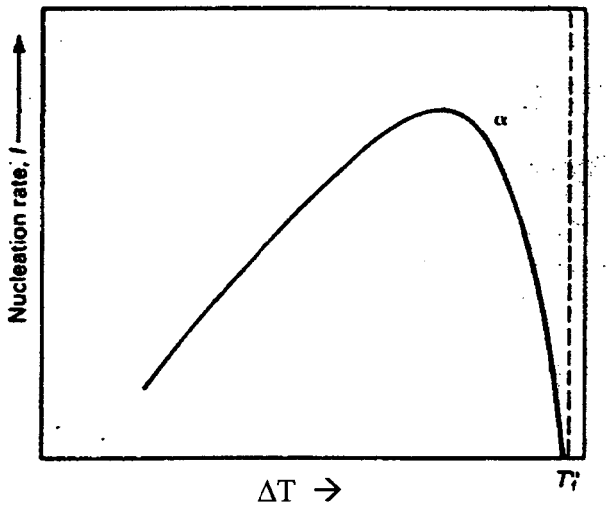

Figure 20 Steady-state nucleation rate as a function of undercooling below the melting point.

For typical metals, C $\sim 10^{28}m^{-3}$, $D_L \sim 10^{-9}m^2/s$, and $a_o \sim 0.3\times10^{-9}m$, so that:[71,73]

$$I \approx 10^{40} \exp\left(-\frac{16\pi\sigma^3 T_f^2 V_m^2}{3k \cdot \Delta H_f^2 T \cdot \Delta T^2}\right) \tag{22}$$

This relation shows a rather steep temperature dependence as illustrated in Figure 20. At low undercooling, the nucleation rate is primarily controlled by the driving free energy; at high undercooling, nucleation is limited by the diffusional mobility. At high temperature, the temperature dependence of I is dominated by the driving free energy term, which is contained within the exponential dependence on the activation barrier, and I can vary by a factor of about five per degree Celsius.

2.2.3. Heterogeneous Nucleation

Homogeneous nucleation is the most difficult kinetic path to crystal formation, because of the relatively large activation barrier for nucleus development (ΔG_{cr}). To overcome this barrier, classical theory predicts that large undercooling values are required, but in practice, undercooling values of only a few degrees or less are the common observation with most castings. This behavior is accounted for by the operation of heterogeneous nucleation, in which foreign bodies such as impurity inclusions, oxide films, or crucible walls act to promote crystallization by lowering (ΔG_{cr}).

A purely geometrical calculation shows that when the solid/liquid interface of the substance is partly replaced by an area of low-energy solid/solid interface between the crystal and a foreign solid, nucleation can be greatly facilitated. In addition, because only a single nucleation event is required for the freezing of liquid volumes, the likelihood of finding a heterogeneous nucleation site in contact with a bulk liquid is great. Indeed it has been established that even in a sample of high-purity liquid metal there is a nucleant particle concentration of the order of about $10^{12}m^{-3}$.[71] Only by using special sample preparation methods to isolate the melt from internal and external nucleation sites, by

subdivision into a fine droplet dispersion has it been possible to achieve undercoolings in the range of 0.3 to 0.4 T_f.

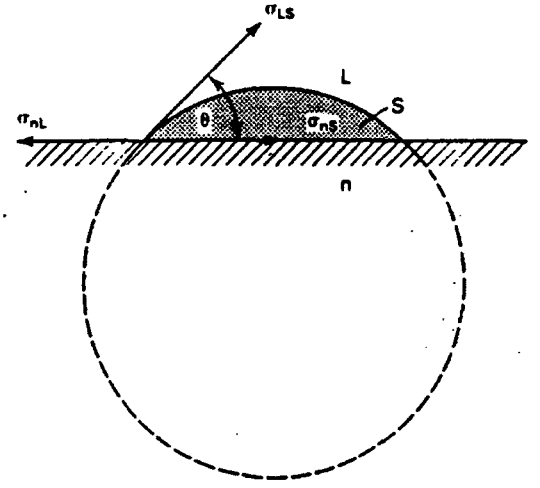

Figure 21 The interfacial energy relationships among a planar nucleant substrate (n), a spherical sector solid (S), and the liquid (L).

The action of heterogeneous nucleation in promoting crystallization can be visualized in terms of the nucleus volume that is substituted by the existing nucleant, as illustrated schematically in Figure 21. For a nucleus that wets a heterogeneous nucleation site with a contact angle, θ, the degree of wetting is obtained from the condition of static equilibrium and is expressed in terms of $\cos\theta = (\sigma_{nL} - \sigma_{nS})/\sigma_{LS}$, where the interfacial energies are defined in Figure 21. As θ approaches 0°, complete wetting develops; as θ approaches 180°, there is no wetting between the nucleus and the nucleant (which is inert), and the conditions approach homogeneous nucleation. When θ lies outside the

stated limits, there can be no equilibrium of the surface tension forces,[74] and either the liquid or the solid phase will spread over the catalyst surface.

The energetics of heterogeneous nucleation can be described by a modification of Eq (15) to account for different interfaces and the modified cluster volume involved in nucleus formation. In terms of the cluster formation shown in Figure 21, the free energy change during heterogeneous nucleation is expressed by:

$$\Delta G(r)_{het} = V_{SC}\Delta G_V + A_{SL}\sigma_{SL} + A_{nS}\sigma_{nS} - A_{nL}\sigma_{nL} \qquad (23)$$

where, V_{SC} is the spherical cap volume and A_{SL}, A_{nS} and A_{nL} are the solid-liquid, nucleant-solid and nucleant-liquid interfacial areas, respectively.

When the volume and relevant interfacial areas are expressed in terms of the geometry of Figure 21, the evaluation of ΔG_{cr} for heterogeneous nucleation yields:

$$\Delta G_{cr}(het) = \frac{16\pi\sigma_{SL}^3}{3\Delta G_V^2}\left[\frac{2-3\cos\theta+\cos^3\theta}{4}\right] = \Delta G_{cr}(\text{hom})[f(\theta)] \qquad (24)$$

Thus, the barrier for homogeneous nucleation is modified by $f(\theta)$, the shape factor,[a] during heterogeneous nucleation. This heterogeneity factor responsible for

[a] $f(\theta)$ may be termed as the catalytic efficiency, as defined by Maxwell and Hellawell.[69]

nucleation has a composition independent potency.[70] The physically maximum nucleation rate occurs with the nucleus composition that minimizes $\sigma_{SL}^3 f(\theta)/\Delta G_V^2$.[69]

Table 4 Critical dimensions and activation energy for the nucleation of a spherical nucleus in a pure melt ($\Delta G_V = \Delta s_f \Delta T$).[68]

	Homogeneous Nucleation	Heterogeneous Nucleation
critical dimension r_{cr}	$-\frac{2\sigma}{\Delta G_V}$	$-\frac{2\sigma}{\Delta G_V}$
n_{cr}	$-\left(\frac{32\pi}{3V_a}\right)\left(\frac{\sigma}{\Delta G}\right)^3$	$-\left(\frac{32\pi}{3V_a}\right)\left(\frac{\sigma}{\Delta G}\right)^3 f(\theta)$
activation energy $\Delta G(n_{cr})$	$\left(\frac{16\pi}{3}\right)\left(\frac{\sigma^3}{\Delta G_V^2}\right)$	$\left(\frac{16\pi}{3}\right)\left(\frac{\sigma^3}{\Delta G_V^2}\right) f(\theta)$

The critical parameters of homogeneous and heterogeneous nucleation are given in Table 4. Over the variation of θ ranging from complete wetting (θ = 0) to nonwetting (θ = 180°), $f(\theta)$ or $[\Delta G_{cr}(het)/\Delta G_{cr}(hom)]$ various from 0 to 1.0, as illustrated in Figure 22 and tabulated in Table 5. It is important to note that the value of r_{cr} for the curvature of the critical nucleus does not change in the classical analysis of heterogeneous nucleation, but the reduction in activation barrier (Figure 22) has a significant influence on nucleation rate. This feature is also described in Figure 22, in which the spherical cap size as measured by the ratio (h/r) is shown as a function of θ. The dimension, h, is the height above the substrate.

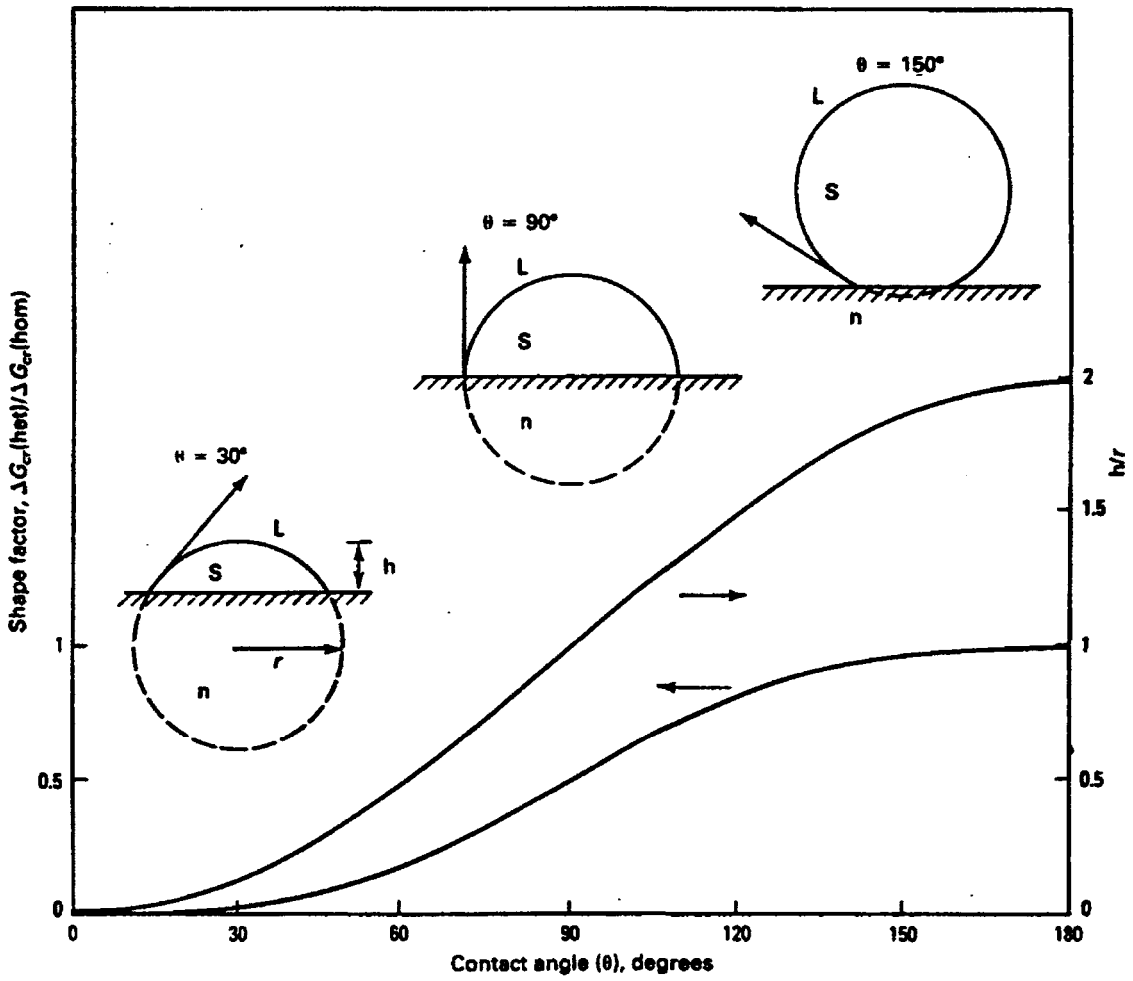

Figure 22 The variation of shape factor $f(\theta)$ and spherical cap size, h/r as a function of the contact angle, θ.[71]

The rate of heterogeneous nucleation I_{het} ($m^{-3} \cdot s^{-1}$) is given by:

$$I_{het} = \left(\frac{D_L}{a^2}\right)\left(\frac{2\pi r_{cr}^2(1-\cos\theta)}{a^2}\right)C_a \exp\left[\left(-\frac{\Delta G_{cr}(\text{hom})}{kT}\right)f(\theta)\right] \qquad (25)$$

where, $2\pi r_{cr}^2(1-\cos\theta)/a^2$ is the value of surface area for spherical cap geometry, C_a is the concentration of critical clusters, represented in terms of the number of surface atoms of

the nucleation site per unit volume of liquid, which is in the order of 10^{20}. The rate of heterogeneous nucleation for typical metals is given by:[71,73]

$$I_{het} = 10^{30} \exp\left[-\frac{16\pi\sigma_{LS}^{3} T_f^2 V_m^2 f(\theta)}{3k \cdot \Delta H_f^2 \cdot T \cdot \Delta T^2}\right] \tag{26}$$

Table 5 Values of the expression: $f(\theta)=(1/4)(2+\cos\theta)(1-\cos\theta)^2$.[68]

θ(°)	Type of nucleation	f(θ)
0 complete wetting	No nucleation barrier	0
10		0.00017
25		0.0027
30		0.013
50		0.084
70	Heterogeneous	0.25
90		0.5
110		0.75
130		0.92
150		0.99
170		0.9998
180 no wetting	Homogeneous	1

2.2.4. Nucleation from Coherent and Semi-coherent Interfaces

For coherent nucleation, the total strain energy of the interface is the dominant term,[75] and probably the one of importance in nucleation calculations. Christian[74] gives the value of the free energy for nucleation in the coherent case as:

$$\Delta G_{cr} = \frac{\mu \upsilon^{\beta} \delta^{2}}{1-\nu} \tag{27}$$

where, μ is the shear modulus, δ[a] is the disregistry between the nucleant and the nucleus, ν is the Poisson ratio, and υ^{β} is the specific volume of atoms on the β phase.

For semicoherent interfaces,[b] the free energy for nucleation varies with δ. When δ is small, the strain energy is small. As δ increases, the strain energy term increases parabolically while the contribution of dislocations to the energy is approximately linear with δ. At small δ, coherency is favored since strain energy is small and the free energy for nucleation has its smallest value. As δ increases, dislocation geometries become more favorable for taking up the misfit at the interface. The critical free energy for nucleation then becomes dependent on this term.

2.2.5. Inclusions and Their Role in the Solidification of Al-Alloys

It is well established that a large variety of inclusions are present in small quantities in commercial aluminum and aluminum alloys. The common types of inclusions in aluminum are: oxides, carbides, borides, nitrides, chlorides, and fluorides.[76,77,78,79] Commercial aluminum contains 6 to 16 ppm oxides. These are mainly

---

[a] The disregisrty between the two phase α and β, with lattice parameters, a_1 and a_2 respectively is equal to: $\delta = (a_1 - a_2)/a_2$

[b] For semi-coherent interfaces the interface energy is composed of strain energy and dislocation energy.

α-Al_2O_3 and γ-Al_2O_3 in addition to some dispersed amorphous aluminum oxide particles. The dominant oxides in aluminum-magnesium alloys are Al_2MgO_4 and MgO. The common carbide in aluminum is Al_4C_3. Material obtained from electrolysis cells normally contains 10 to 35 ppm Al_4C_3. A few very small TiC particles have also been detected in aluminum alloys. Ordinary aluminum contains less than 1 ppm borides and grain-refined material 10 to 100 ppm borides. The common borides are TiB_2 and VB_2. In addition, in aluminum matrix composites, reinforcing phases (particulates or fibers) such as Al_2O_3, graphite, mica, SiO_2, zircon, MgO, sand, TiC, ZrO_2, TiO_2 and lead are commonly used, to provide different characteristics to the composite properties.[80,81,82]

These inclusions and dispersed particles play an important and indispensable role in facilitating the crystal nucleation process of the matrix phase and other primary phases,[83] since the high-energy crystal-liquid interface is partly replaced by an area of low-energy crystal-inclusion interface.[68] Several observations have confirmed the nucleation of different phases on the surface of inclusions. For example, carbon, alumina and silicon carbide particles were shown to be preferential nucleation sites for the primary silicon particles in Al-Si alloys.[84] It was also observed that certain inclusions act as potential nucleation sites for some iron-bearing phases.[10] Other authors[19] reported that

the addition of grain refiner to dilute Al-Fe-Si alloys increased the presence of the θ-$Al_{13}Fe_4$ phase with respect to the Al_6Fe phase in the solidified microstructure. More recently, it was found that in casting practice, if pushed to solute rich interdendritic regions, boride particles could nucleate intermetallics with a well-defined orientation relationship.[85]

However, a major part of the examination of nucleation in aluminum-base alloys has been spent in the study of the mechanisms of grain refinement, specifically, those associated with the presence of Al_3Ti, TiB_2, AlB_2, TiC, *etc*, where the focus was on rationalizing the usefulness of such grain refiners.[71] The actual evidence that any one nucleant may be associated with the initiation of solidification is not extensive. It does not seem to have been clearly established that these proposed nucleants operate singly or in association with each other or other nucleants already existing in the melt. Furthermore, the role and the catalytic activity of the inclusions in the solid nucleation process have not been systematically studied.

Considering how inclusions (or dispersed particles) can affect the structure of engineering alloys, systematic studies of their role during solidification have to be carried

out, in order to rule out the possibility of generalization. Such generalizations usually result from single observations and may lead to incorrect conclusions.

2.2.6. Introducing Particles to Alloy Melts

To conduct these systematic studies, appropriate amounts of the solid particles must be introduced into the molten alloys. There are different techniques for introducing particles into a melt, a review of which can be found in Ref [86]. A suitable technique that allows the introduction of different particles irrespective of their wettability and chemical reactivity must be used. In addition, the incorporation of undesirable surface oxides or gas bubbles has to be minimized, or even avoided, if possible. The gas injection technique was found to satisfy these requirements.[87]

In order to predict particle transfer behavior during gas-to-liquid transfer, approximate thermodynamic and kinetic models have been proposed. The engulfment of particles by an electromagnetic stirred melt was studied by Ilegbusi and Szekely.[88] The balance among surface forces, the force of gravity, and the drag force exerted on the particles was established; hence, the melt velocity was estimated based on the system variables. The Neumann's[89] thermodynamic approach ignores the effect of buoyancy

forces acting on the particle. According to this model, the total free energy change involved in the transfer of particle from gas to liquid must be negative for spontaneous transfer. In comparison, the work of Rohatgi and coworkers[90,91] is more exact as it takes into account the buoyancy forces. The spontaneity of particle transfer can be predicted from an analysis of the energy path involved.

2.2.7. Inoculation Practice

There is a wide commercial application of cast alloy treatments that modify the initial solidification characteristics to provide a means for effective control of grain size and morphology. Inoculation is the common approach to grain refinement, and it involves the introduction of nucleating agents to a melt either externally in the form of fine dispersions or through internal means by phase[92] or chemical reactions[93,94] (segregation process at the melt-nucleant interface) that result in the formation of a solid reaction product.

The basic requirements[71,95] of an efficient nucleant can be assessed from consideration of the nucleation theory. To promote the formation of crystals on a nucleant, the interface between the nucleant and the liquid should be of higher energy

than that between the nucleant and the solid crystal. A means of maximizing this condition is to provide a nucleant crystal relationship that is associated with a good crystallographic fit between the respective crystal lattices. In fact the potency of a given crystal is believed to increase with decreasing lattice disregisrty.[71,95]

According to Turnbull and Vonnegut,[96] the heterogeneous nucleation of crystals on a catalyst is enhanced by good lattice disregistry across the nucleation interface. This theoretical approach, which was adopted as a basis for the prediction of useful inoculants, failed in practice. Some workers reported experimental results in full disagreement with the Turnbull and Vonnegut[96] crystallographic theory of crystal nucleation (see for example the work of Zhang and Cantor[97]). Others proved that the physical and chemical characteristics of the nucleant surface are more important for nucleation than the lattice disregistry,[98] while Porter and Easterling[99] concluded that the lattice disregistry is unable to account for the effectiveness of nucleants. In their review, Cantor and O'Reilly[100] showed that catalysis is dominated by chemical rather than structural compatibility at the nucleating interface. As a result, the nucleation theory based on the theoretical model of lattice registry, has failed in the prediction of efficient nucleants and, therefore, it has been primarily used to rationalize the identification of useful nucleants.[71]

For effective nucleation, the melt should tend to wet the surface of the nucleant,[a] and for a uniform refining; the solid nucleant should remain widely dispersed in the liquid. Nakao *et al.*[101] showed that the very effective agents for grain refining were obtained when the carbides were under the following conditions at the same time: large free energy for formation; small density; crystal structure of NaCl-type and small size factor for aluminum.

Within the basic requirements of effective nucleantion, there appear to be two general classes of compounds that are effective in aluminum base alloys. The first group includes Al_3Ti, Al_3Zr and Al_7Cr and can be considered to be associated with a peritectic reaction. The second group comprises compounds such as TiC, TiB_2 and AlB_2, which are added either intentionally or which result from a chemical reaction in the melt with residual impurities. It is useful to note that the undercooling required to activate solidification is usually less than 5°C. Despite the rather extensive discussion concerning the mechanism of action and the activity of these proposed nucleants, the strongest

---

[a] Maxwell and Hellawell[69] clarified that the catalytic efficiency, $f(\theta)$, is not necessary to relate to the physical contact angel, but can be considered as the efficiency of the inoculant.

evidence for the operation of compound nucleants is derived from the observed orientation relationships.

The crystallographic relationships that have been observed involve planes of relatively close packing between the nucleant and the aluminum with disregistries of usually less than about 10%. The issue of specific nucleant identity is not significant considering that in commercial melts the rather broad spectrum of background catalysts may often result in solidification at undercoolings of about 5°C. Indeed, only 1 to 2% of all the potential nucleant particles in a master alloy addition result in the formation of grains.[71] Furthermore, it has not been clearly established that these proposed nucleants operate singly or in association with each other or with background nucleants in the melt.

Grain Refinement

According to Maxwell and Hellawell,[69] the ranking of the various particles in terms of their catalytic activity for nucleation is not an absolute measure that can be reflected in the degree of grain refining unless the cooling rate and alloy constitution are also considered. In addition, it has been reported that not all the particles in a given nucleant addition are of equal effectiveness in promoting grain refining.[95] Therefore, a

certain proportion of the added grain refiner particles is responsible for nucleation and for the final grain size attained.

In aluminum alloys, it is generally viewed that Al_3Ti crystals are mainly responsible for grain refinement at alloy compositions above 0.15% Ti, that is within the peritectic range. For compositions outside the peritectic ranges, where the Al_3Ti is not stable under equilibrium conditions,[a] there are basically two interpretations of the grain refinement effect: the carbide-boride view and the peritectic reaction theory.

2.2.7.1. The Carbide Boride Model

This model suggests that a compound such as AlB_2, TiB_2, or TiC is responsible for the nucleation of aluminum crystals, because the Al_3Ti particles that are introduced into the master alloy are expected to dissolve rapidly. The borides are hexagonal structures, and the carbide is cubic structure with a relatively close fit with the aluminum lattice. Although it is considered that a boride or carbide is the site of nucleation, the Al_3Ti particles do play a role in the overall grain refinement process. The dissolution of Al_3Ti is required, for example, to provide excess titanium to rapid crystal growth. With

---

[a] Maxwell and Hellawell[69] mentioned that it is not necessary for the nucleant to be an equilibrium phase.

this viewpoint, the establishment of an optimum contact time can be related to the initial dissolution of Al_3Ti and to the possible conditioning of the nucleant surface.

The subsequent fading reaction is related to the agglomeration and settling of the nucleant particles. Although there is evidence of stability of boride or carbide particles in aluminum melts and reports of observations of these particles in ingots, other observation indicated a number of problems in attributing nucleation solely to the action of boride or carbide particles. For example a consistent relationship between Al_3Ti and aluminum can be found; however, no consistent relationship between TiB_2 and aluminum was detected even though the orientations detected for AlB_2 would be expected to develop for TiB_2 with a lattice disregisrty of –5.9 and -5.8%, respectively, in a and b directions.[71] Excess Ti helps to form $TiAl_3$ at TiB_2/melt interface,[102] which helps the formation of α-aluminum. In addition boride particles have been often observed to be located at grain boundaries, indicating that the borides were present as insoluble material and inactive particles for nucleation during freezing.[103]

2.2.7.2. Peritectic Reaction Theory

The alternative viewpoint of nucleation behavior during grain refinement was originally developed on the basis of a peritectic reaction. Although many types of particles are believed to be active in the nucleation of aluminum crystals at undercoolings less than 5 °C, the presence of Al_3Ti is believed to offer a more active catalyst requiring little or no undercooling. Thus, Al_3Ti crystals when present, will dominate in the grain refinement nucleation. For peritectic alloys, it is clear that Al_3Ti can form upon cooling below the liquidus and can promote the formation of aluminum crystals at the peritectic temperature, T_p. At alloy compositions below the peritectic range the grain refinement effect is expected to be reduced by the loss of Al_3Ti particles, which are added externally in master alloy form. Indeed, independent Al_3Ti particles in liquid aluminum that is not saturated with titanium dissolve within several minutes. On the other hand boride particles, that is, TiB_2 or (Al, Ti)B_2 are observed to be reasonably stable in melts and offer a fine particulate dispersion.

To account for the beneficial effect of incorporating boron into the master alloy compositions and also the observation of the interaction between TiB_2 and Al_3Ti, it appears likely that TiB_2 particles may provide an effective substrate for the nucleation of

Al_3Ti for compositions spanning the peritectic reaction. During cooling of the melt or holding (the contact time period), the TiB_2 particles will react slowly with liquid aluminum to form an $(Al,Ti)B_2$ solution, with appropriate[104] and high[105] Ti/B ratio and liberate excess titanium locally to provide for the formation of a sheath of Al_3Ti as a coating on $(Al,Ti)B_2$ particles. In this way the boride particle is believed to act as a substrate for the formation of the Al_3Ti particles at low titanium levels, that is, even in alloys with composition below the peritectic range.

2.2.8. Master Alloys and Their Processing

Wrought or primary aluminum alloys can be readily grain-refined, while cast alloys, containing large amounts of Si, Cu or Zn, exhibit some difficulty in attaining an acceptable level of grain refinement using the conventional grain refiners designed for wrought alloys. The alloying additions hinder the effect of Al-Ti-B grain refinement. The master alloys used to refine the grains in wrought alloys are not equally efficient when used in cast alloys.[106] For example, the Al-5Ti-1B master alloy, which is a foolproof grain refiner in wrought alloys, cannot provide an acceptable level of refining in cast alloys. However, other master alloys such as Al-2.5Ti-2.5B and Al-4B have been

developed in order to provide powerful grain refining in cast alloys. The latter alloys also operate using the grain refinement effect of Al-Ti-B or Al-B. Why they are more powerful than the Al-5Ti-1B master alloy is still an open debate.

The effectiveness of the nucleant particles in promoting formation of the solid phase may be affected by the morphology of the nucleating particles. Thus this relates to the preparation conditions during master alloy processing. For example, it was observed that Al_3Ti particles may appear with different morphologies and may exhibit several possible crystallographic relationships with the aluminum crystals. The degree of refinement is observed to be dependant on the Al_3Ti morphology.[71,107] In addition, the observation of different morphologies and twining for Al_3Ti crystals may account for the variety of orientation relationships that have been observed between Al_3Ti and aluminum. Other particles such as TiB_2, TiC, TiN, ZrB_2 and TaB_2, have been examined, but undercooling required to initiate solidification was minimized when Al_3Ti particles were present.

2.2.9. Effect of Inclusions, Trace Elements and Grain Refiner Additions on the Nucleation of Fe-Intermetallics

Inclusions and dispersed particles play an important and indispensable role in facilitating the crystal nucleation process of the matrix phase and other primary phases,[83] since the high-energy crystal-liquid interface is partly replaced by an area of low-energy crystal-inclusion interface.[68] Several observations have confirmed the nucleation of different Fe-intermetallic phases on the surface of inclusions. It was observed that certain inclusions act as potential nucleation sites for some iron-bearing phases.[10] Others demonstrated that Sr has a poisoning effect on the nucleation sites for β-AlFeSi needles. This reduces the number of sites available for nucleation and a lower β-AlFeSi phase density is obtained, compared to that in the unmodified alloy.[55]

Other authors reported that the addition of grain refiner to dilute Al-Fe-Si alloys increased the presence of the θ-$Al_{13}Fe_4$ phase with respect to the Al_6Fe phase in the solidified microstructure.[19] More recently, it was found that in casting practice, if pushed to solute rich interdendritic regions, boride particles could nucleate intermetallics with a well-defined orientation relationship.[85]

In addition, Evans *et al.*[108] have observed the appearance of Al_mFe at a solidification velocity of 1.33 – 2 mm/s in unidirectionally solidified Al–0.3 wt% Fe–0.1

wt% Si, but only in the presence of Ti : B grain refiner addition. Al_mFe is not, however, promoted in the absence of Si.[61] In the same alloy with or without grain refiner addition, $Al_{13}Fe_4$ and Al_6Fe were seen to coexist over the solidification velocity range 0.17 – 1.33 mm/s. It seems that impurity particles present in the alloy or grain refiner additions made during casting may provide nucleation sites for phases.[25] Kosage[109] and Griger *et al.*[110] have also proposed that Al-Ti-B grain refiner addition increases the number density of nucleation sites for Al_mFe in 1XXX series alloys, whereas Tesuka and Kamio[111] noted that Al-Ti-B addition to Al–0.3–0.5 wt% Fe–0.1–0.15 wt% Si promoted both Al_mFe and α-AlFeSi. Maggs *et al.*[112] has proposed that there may be a small lattice mismatch between the hexagonal lattice of TiB_2 and phases with orthogonal crystal axes such as cubic α-AlFeSi and Al_mFe.

Recent work by Allen *et al.*[59,60] has shown that the nucleation of Al_mFe can be promoted by both V impurity (< 100 ppm) and Al-Ti-B grain refiner addition with or without an excess of Ti at cooling rates as low as 0.03 $^oK/s$. The Al_mFe promotion also occurs on the addition of Al-B or Al-Ti-C grain refiners to alloy Al–0.3 wt% Fe–0.1 wt% Si containing ~ 100 ppm V. This suggests that although it is the TiB_2 present in the Al-Ti-B added to commercial alloys that is involved in the promotion of Al_mFe, this

promotion is not grain refiner specific. Also this promotion does not require an excess level of Ti, which rules out the adsorbed layer of Al_3Ti on TiB_2 as being responsible for the nucleation of Al_mFe.

According to Allen *et al.*,[25] grain refiner additions are proposed to affect the intermetallic phase selection in three ways. Firstly, TiB_2 and TiC particles that do not nucleate the α-Al may be partitioned into the interdendritic spaces, where they may affect the solidification of the second phase particles.[109,110] The local chemistry of these interdendritic spaces (*i.e.*, solute element and impurity levels) may be as important for second-phase selection as it is in determining the effect of grain refiner. Secondly, primary grain refinement may result in a greater number density of the interdendritic liquid spaces towards the final stages of solidification. With increasing division of the liquid volume, nucleation and hence impurities play a more important role in influencing second-phase selection.[58] Thirdly, primary grain refinement may change the shape of the interdendritic liquid channels (*e.g.*, from long channels between columnar dendrites to more convoluted shapes between equiaxed grains), forcing the second-phase particles that form in these spaces to change their growth morphology. This may influence which is the preferred second-phase under given solidification conditions.[61]

Meredith *et al.*[19] reported that the addition of grain refiner to dilute Al-Fe-Si alloys increased the presence of the $Al_{13}Fe_4$ phase with respect to the Al_6Fe phase in the solidified microstructure. They attributed this to the effect of Si and Al-Ti-B grain refiner on the temperature interval between the dendrite and the eutectic growth fronts from ~ 9 to ~ 16 °K. More recently, Mckay *et al.*[85] found that in casting practice, if pushed to solute rich interdendritic regions, boride particles could nucleate intermetallics with a well-defined orientation relationship.

Flores *et al.*[113] have given the following empirical equation for the nucleation rate of $Al_8FeMnSi_2$ crystals, formed from supersaturated liquid solution of Al-Si-Fe-Mn:

$$I = K_N \exp\left(-\frac{\Delta G_{cr}}{RT}\right)\left(C_i - C_{eq}\right)^{r1}\left(T_f - T\right)^{r2} \tag{28}$$

where, K_N is the rate coefficient, ΔG_{cr} is the nucleation activation energy, R is the gas constant, r1 is the rate of reaction with respect to supersaturation and r2 is the rate of reaction with respect to undercooling, C_i and C_{eq} are the actual and equilibrium concentrations of solute, Mn.

Wang *et al.*[114] have discussed the nucleation behavior of precipitation in aluminum. They provide a summary of possible nucleation mechanisms in the Al matrix. The modeling of microsegregation and nucleation of intermetallic precipitates was

carried out. Lacaze and Lesoult[115] and Tromborg *et al.*[116] presented models for the precipitation of intermetallic phases from the multi-component system (Al-Cu-Mg-Si and Al-Fe-Si-Mn-Mg) depending on the phase diagrams, solid state diffusion and solidification paths. The output from these solidification models includes types, amounts, chemical compositions, number of particles per unit area and size distribution for all the intermetallic particles.

CHAPTER 3

MATERIALS AND EXPERIMENTAL PROCEDURE

CHAPTER 3

MATERIALS AND EXPERIMENTAL PROCEDURE

3.1. Materials and Melt Preparation

The chemical compositions of the six alloys investigated are shown in Table 6 (each composition representing the average of three spectro-analyses). About 25 Kg of each alloy was prepared by melting in an electric resistance furnace. This amount of metal was prepared to be sufficient for all required tests and castings. In addition, three samples were taken from each melt to perform spectro-chemical analysis. The first sample was taken before the start of casting, the second after casting of one third of the melt, and the last one before pouring the last third of the metal. The overall chemical analysis is taken by averaging analyses of the three samples.

The alloys were poured into metallic moulds. The resulting ingots were cut into smaller pieces, between 200-300 g each. These alloy pieces were used to carry out the thermal analysis, intermetallic phase identification and the inclusion injection experiments of the current work.

This group of experimental alloys is representative of the Al-rich corner of the Al-Si-Fe system. The alloys were prepared from high purity components to avoid any contamination that could arise from the use of commercial purity materials.

Table 6 Compositions of alloys used in the present study.*

Alloy	Element, wt %								
	Si	Fe	Cu	Mn	Mg	Bi	La	V	Ga
1	0.35	0.23	.0033	<.0005	.0015	<.0025	.0094	.0041	.0087
2	0.49	0.23	.0057	<.0005	.0017	<.0025	.0094	.0042	.0086
3	0.62	0.55	.0040	<.0005	.0009	<.0025	.0091	.0038	.0088
4	0.90	0.56	.0035	.0006	.0014	<.0025	.0091	.0040	.0089
5	0.62	1.03	.0043	.0032	.0013	<.0025	.0088	.0042	.0091
6	6.32	0.52	.0030	.0007	.0011	<.0025	.0090	.0045	.0082

* The other elements found in very small quantities are not shown in the table.

Alloys 1 and 2, with the same iron level (0.23 wt %) but different silicon levels, were proposed in order to study the effect of Si content when the Fe level is low. Alloys 3 and 4 are the analogs of alloys 1 and 2, with nearly double concentrations of iron and silicon. These compositions enable us to study the effect of a higher Fe content and an increase in Si content. Only alloy 5 has higher iron than silicon (1.03% and 0.62%, respectively), and was proposed in order to evaluate the effect of a very high Fe level such as those often encountered in commercial alloys. Alloy 6, with its high Si level (6.32%) and Fe level of 0.52% was selected as being representative of commercial Al-Si alloys. These compositions were selected very carefully, with a view to investigating the occurrence of the different iron intermetallic phases which can form in dilute aluminum alloys. The total Fe+Si alloying (or impurity element) content increases gradually from alloy 1 through alloy 6. This group of experimental alloys is representative of the Al-rich corner of the Al-Si-Fe system, and was selected precisely for this reason.

Table 7 List of inclusions used in the present study.

Type	Chemical Analysis, wt pct	Powder Size, μm	Supply Source
α-Al_2O_3	Al_2O3=99	< 20	Norton, USA
γ-Al_2O_3	Al_2O3=99.997	<50	Alfa Aesar, USA
MgO	MgO=96 min.	< 70	Alfa Aesar, USA
CaO	CaO=99	< 10	Alfa Aesar, USA
Al_4C_3	Al_4C_3=99	< 10	Alfa Aesar, USA
SiC	SiC=99	< 20	Norton, USA
TiC	TiC=99.5	Av. ~2	Alfa Aesar, USA
TiB_2	TiB_2=99	< 10	Strem Chemicals, USA

Gas injection experiments for a variety of inclusions covering the most common oxides, carbides and borides found in commercial aluminum alloys were carried out in this work. The chemical analysis and particle size of each inclusion (powder), according to the supplier, are given in Table 7. High purity argon, min. of 99.998% Ar, was used as a carrier gas in the experiments. Each inclusion was injected into separate melts of the six experimental aluminum alloys.

3.2. Experimental Procedure

3.2.1. Thermal Analysis

Thermal analysis tests were performed for the six alloys over a wide range of cooling rates (*i.e.*, solidification times) as follows. Alloy melts were poured into (i) a graphite mold preheated to ~ 600 °C, which provided the lowest cooling rates (0.16-0.21 °C/s, depending on the alloy), and (ii) a cylindrical metallic mold with decreasing wall thickness, kept at room temperature that provided high cooling rates (10-15 °C/s). When the ingots temperature reached 500 °C, the ingots were brought to the ambient temperature by

forced cooling in running water. Hereafter, the terms "metallic mold" and "graphite mold" will be taken to represent the high cooling and low cooling conditions, respectively. Figure 23 (a, b) shows the schematic diagram for the two molds.

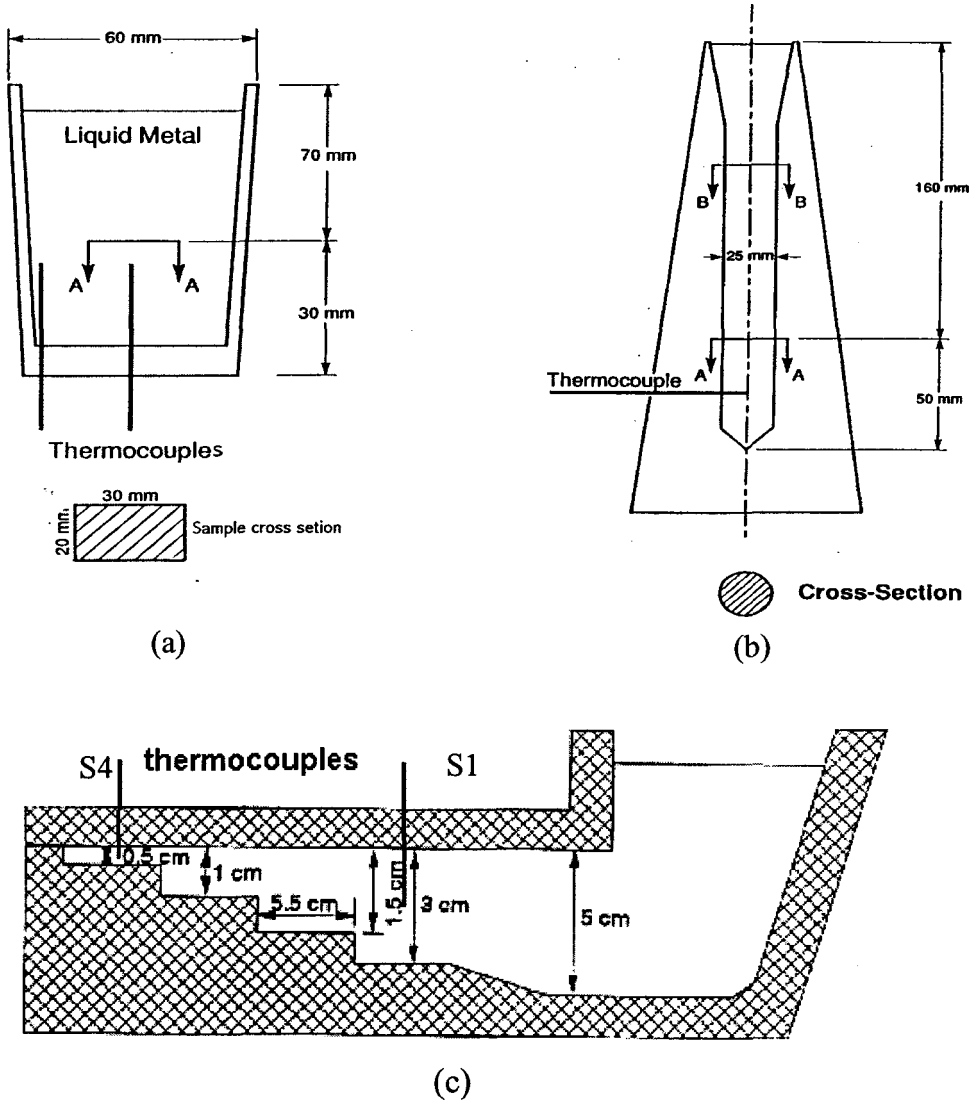

Figure 23 Schematic diagram of the (a) graphite [G], (b) metallic [C], and (c) step-like [S1, S4] molds used to prepare alloy castings.

The thermal analysis was carried out using chromel-alumel type K thermocouples and Strawberry Tree software to obtain the cooling curves corresponding to each alloy and mold system. In the case of the graphite mold, a two-thermocouple system similar to that used by Backerud et al.[46] was employed for accuracy (see Figure 23 (a)). The starting and termination points of a reaction were also determined according to the definitions given by Backerud et al.[46]

3.2.2. Injection of Inclusions

The technique used here to introduce inclusions into the aluminum alloy melts was developed by our group.[87] Although the injection of powders into molten metal is not a new process, different techniques were used previously. The principle of the current method is to heat a sufficient quantity of solid particles (powder) in an inert atmosphere (argon), and then to blow a continuous stream of these particles (carried by the inert gas) into the melt. In the melt, the gas bubbles are continuously broken with the help of an impeller.

The injection process can be viewed as follows: during the journey through the bath, the buoyant forces slow down the gas bubbles without affecting the velocity of the particles. Subsequently, the solid particles contact the gas-liquid interface. A larger particle, having sufficient kinetic energy, is able to penetrate the gas-liquid interface and enter the bath; a smaller particle cannot penetrate the barrier and is carried to the surface of the bath.

A General view and a schematic of the inclusion addition system are shown in Figure 24. It consists of (a) a fluidizer tube, (b) a carrier tube and a quartz nozzle, (c) resistance heating coils, (d) an adjustable two-dimensional movable stand, (e) a melting unit with resistance heating, (f) an impeller (stirrer) with adjustable rotation speed, and (g)

flow diversion baffles. The fluidizer unit is a cylindrical quartz tube (45 mm diameter × 300 mm height), heated using electric resistance coils. It has a gas inlet system on one end and a conical outlet fitted to the carrier tube on the other end. The gas inlet system has four nozzles (1 mm diameter each) positioned in a hemispherical dome to avoid dead zone formation (known as channeling phenomenon).[117] The carrier tube, which is also heated by electric resistance coils to compensate for the heat loss during blowing, converges uniformly into an immersion nozzle of 2 mm diameter. The impeller system is comprised of an alumina-coated stainless steel tube with three blades (60 mm diameter) inclined at an angle of 45° to the stock. The impeller system is fitted to the argon cylinder outlet so that it can be used as a degassing system before the injection stage. The injecting part of the system is mounted on a two-dimensional movable stand so that the nozzle position can be adjusted accordingly.

(a)

Figure 24 A general view (a) and a schematic (b) of the injection system.

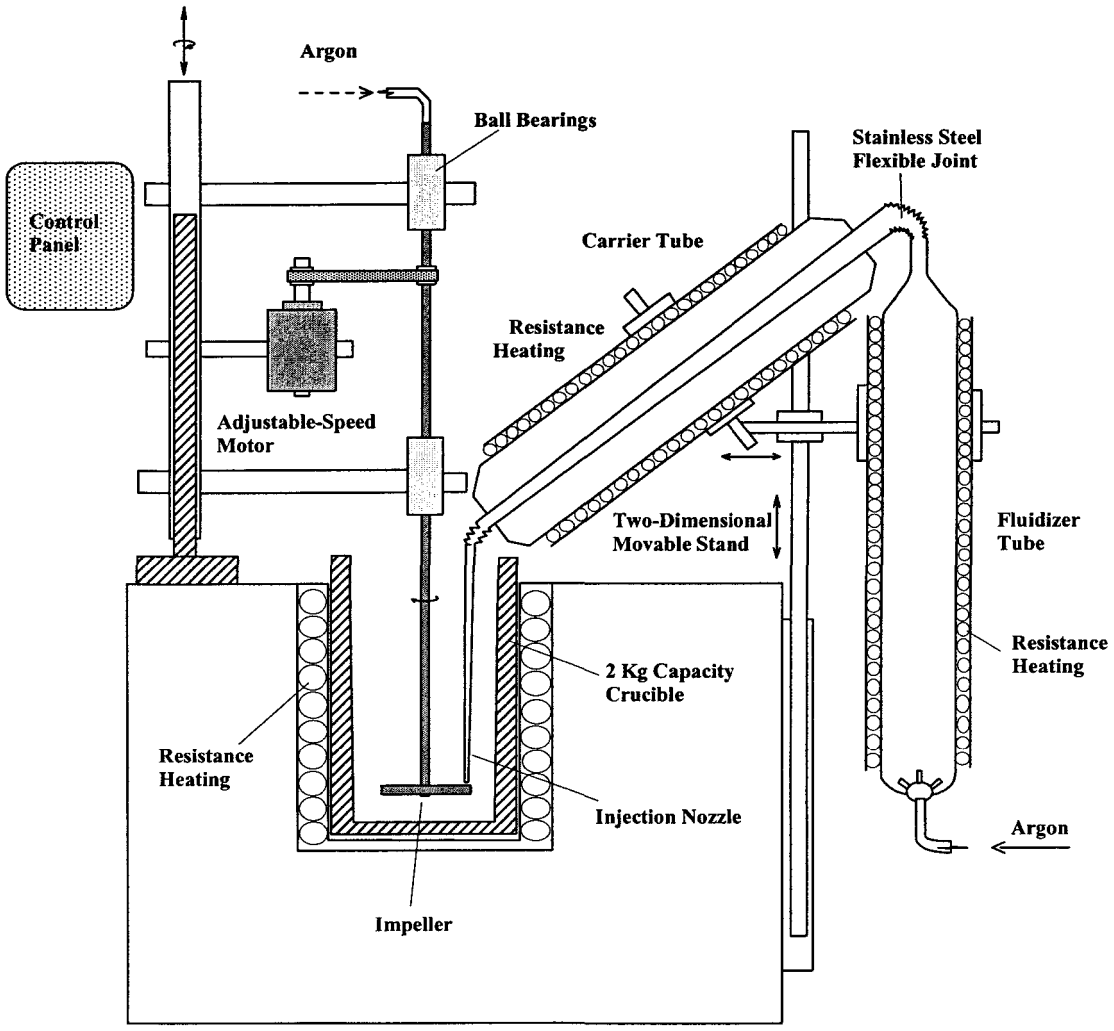

(b)

Figure **24** A general view (a) and a schematic (b) of the injection system.

To inject an inclusion type into the melt, a measured amount of the inclusion powder (*e.g.*, 90 g) is fed into the fluidizer tube. The powder is normally heated for 2 to 3 hours before injection. The prolonged heating is necessary to ensure that the powder is uniformly heated and moisture-free before injection. During preheating (high temperature fluidization), a slow stream of argon is passed through the powder bed, with a flow rate

insufficient to lift the powder out of the fluidizer tube. The argon flow helps to break the sticky particles (clusters) as well. The temperature of the fluidizer tube as measured from the outside is maintained around 500 °C. The heat input to the tube should be increased during the injection to compensate for the heat losses carried away by the argon flow.

According to the calculations of Mortensen *et al.*[118] and the model of Kim and Rohatgi,[83] the time taken for the temperature of the particle to become equal to that of the melt is in the order of microseconds. Mortensen *et al.*[118] found that the time required to achieve thermal equilibrium between 1.9-μm-diameter alumina fibers in contact with aluminum is of the order of a microsecond. Kim and Rohatgi[83] showed that for 10- and 100-μm-sized SiC and graphite particles, thermal equilibrium with the aluminum melt takes less than 6×10^{-6} s. Thus, the loss of the particle temperature during transfer from the fluidizer tube to the melt can be recovered at the onset of contact between the particles and the melt.

In the present work, melting was done using an electric resistance furnace and 2-Kg silicon carbide crucibles. The aluminum alloy bath was approximately 200 mm in depth and 85 mm in diameter. The temperature of the melt was usually around 750°C at the onset of addition. Once the melt reached this temperature, the impeller was lowered into the melt and the flow of argon started. This degassing step took about 20 min, following which skimming of the surface dross was done.

Once the melt was ready, the passage of argon was stopped from the impeller side and started from the injection system side. The flow rate was increased to 10-25 ft^3/hr (or 80-200 cm^3/s). The nozzle was then lowered and immersed in the melt in keeping with the

configuration shown in Figure 25. The position of the submerged nozzle in the melt was very crucial for efficient recovery of the particles[87] since, on blowing, the gas bubbles carrying the inclusions must be delivered directly onto the blades of the impeller. The direction of rotation was kept such that the impeller forced the metal down. The bubbles must remain as long as possible in the melt to increase the probability of powder transfer to the liquid phase. For this purpose, three factors were taken into consideration:

(1) *The bubble size*: the smaller the bubble size the slower it travels through the melt before it escapes to the atmosphere. The impeller rotation speed has a large effect on reducing the size of bubbles liberated after breaking. The rotation speed, therefore, was kept at maximum (~600 rev./min.).

(2) *The position of the nozzle in the melt*: the speed of the metal in contact with the crucible wall is theoretically zero. It is also minimum near the crucible center and maximum in some location between these two positions. Thus, the nozzle was placed in the middle between the wall and the center of the crucible in order to provide the bubbles with a long helical path to the melt surface and, as a result, increase their residence time in the melt.

(3) *The direction of rotation*: it was always kept such that the impeller pushed the metal down. The result was that the liquid streams carried the bubbles to levels lower than the nozzle position, lengthening their travel path to the atmosphere.

To avoid vortex formation, which leads to the incorporation of metal surface oxides (dross) in the melt, ceramic baffles were used. The baffles were immersed so that 50 mm of their length was kept under the melt surface (Figure 25).

Normally, injection continued for approximately 90 min to ensure adequate introduction of inclusion particles. Agitation at the highest speed was also maintained for about 5 min after the injection stage, to assure good mixing.

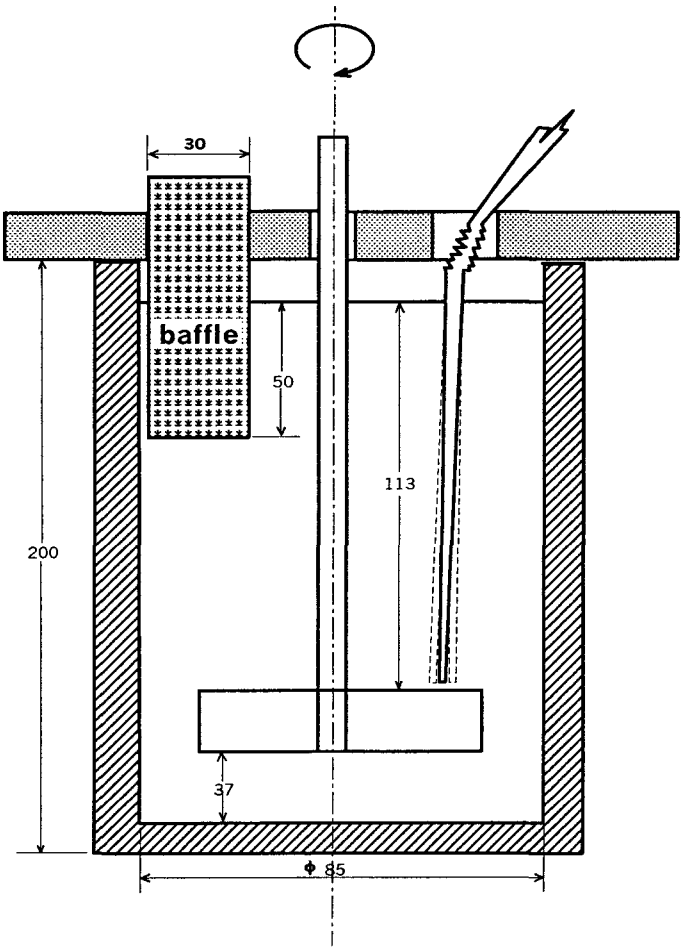

Figure 25 Dimensions (in mm) and positions of the system elements during injection.

The melt was then cast into different molds in order to achieve various cooling rates: (i) a graphite mold preheated to ~ 600 °C, which provided the lowest cooling rates (0.16-0.21 °C/s) and was designated by "G" throughout this thesis, (ii) a metallic step-like mold preheated to ~ 450 °C, which provided the intermediate two cooling rates (0.76-10.3

°C/s) that correspond to the largest and the smallest steps in the mold and were designated by "S1" and "S4", respectively, and (iii) a cylindrical metallic mold with decreasing wall thickness, kept at ambient temperature that provided highest cooling rates (10-15 °C/s) and was designated by "C". Figure 23 shows the schematic diagram for the two molds. The alloy/mold conditions and corresponding cooling rates are listed in Table 8 for the different castings that were prepared.

Table 8 Cooling conditions for the experimental alloys

Condition*	Cooling rate, °C/s	Condition*	Cooling rate, °C/s	Condition*	Cooling rate, °C/s
1G	0.16	3G	0.21	5G	0.19
1S1	0.76	3S1	1.3	5S1	1.2
1S4	8	3S4	10.5	5S4	8
1C	10.7	3C	14.7	5C	14.3
2G	0.16	4G	0.18	6G	0.18
2S1	1.53	4S1	1.4	6S1	0.76
2S4	8	4S4	10.3	6S4	5.1
2C	13.8	4C	12.8	6C	12.8

* The first digit refers to the alloy, and the rest refers to the mold type.

3.2.3. Quantitative Metallography

For the purpose of studying the microstructure and various phases that were obtained corresponding to the different cooling conditions, samples were sectioned near the thermocouple tip (see Figure 23), mounted and polished for metallographic examination.

Quantitative analysis was carried out using an Olympus BH-2UMA optical microscope in conjunction with a LECO 2001 image analyzer. The following features/measurements have been evaluated:

(1) the volume fractions of the various phases and their particle characteristics,

(2) the percentage of particles within the α-Al phase or in the interdendritic regions, and

(3) the percentage of particles associated, *i.e.* in physical contact, with Fe-intermetallic phases within the α-Al phase or in the interdendritic regions.

The volume fraction and characteristics of phases were done using the automatic image analyzer software, while the other measurements including the number of inclusion particles in physical contact with Fe-intermetallic particles within the α-Al or in the interdendritic regions have been performed manually for the different fields in the microsection and for the different metal/inclusion systems studied in this work.

Table 9 is a typical example of the manual image analysis sheets used for evaluating the potency of different inclusions for the nucleation of the α-Al and the Fe-intermetallics. The data of these sheets have been processed using the EXCEL© software. Table 10 is an example of how the image analysis data have been processed to obtain some specific results. The following are the main results obtained (the list numbering given below refers to the table heading numbers):

(1) the inclusion particles observed within the α-Al phase, %,

(2) the overall percentage of inclusions observed in contact with the Fe-intermetallics,

(3) the number of inclusions in contact with Fe-intermetallics in Al to the number of inclusions observed in Al, %,

(4) the number of inclusions in contact with Fe-intermetallics in the interdendritic regions to the number of inclusions observed in the interdendritic regions, %,

---

© Excel is a trademark for the Microsoft Inc.

(5) the ratio of the percentage of inclusion particles in contact with Fe-intermetallics in the interdendritic regions to the total number of inclusions in contact with Fe intermetallics,

(6) the ratio of the percentage of inclusion particles in contact with Fe-intermetallics within the α-Al phase to the total number of inclusions in contact with Fe intermetallics,

(7) the number ratio of the inclusions located in Al to the number located in the interdendritic regions, and

(8) the percentage of inclusion particles in contact with porosity (in TiB_2 alloy samples only).

About 32528 particles were studied over 142 conditions (condition being defined as a particular combination of alloy/cooling rate/inclusion type). The average number of particles studied for each condition was about 229.

3.2.4. Scanning Electron Microscopy and Microanalysis

Scanning electron microscopy was used to examine the microstructure. Mapping of some specific areas of the polished sample surfaces was also done to determine the distribution of alloying elements within phases and around the inclusions. Electron probe microanalysis (EPMA) and wavelength dispersive spectroscopic (WDS) analysis of the intermetallic phases was carried out using a JEOL WD/ED combined microanalyzer (model JXA-8900R), operating at 20 kV and 30 nA (electron beam size of ~ 1 μm).

Table 9 Example for the manual image analysis sheets

Sample: 4S1, TiB_2								Date: 12/6/2002
Field	Total number of inclusions	No of inclusions in contact with			No of inclusions inside the α-Al	Inclusions not in contact with Fe-intermetallics in the interdendritic regions.	Interface reaction?	Comments
		Fe-intermetallics	Porosity	Silicon particles				
1	18	5			17	1	no	
2	18	3			16	0	no	
3	6	2			5	0	no	
4	6	2			4	0	no	
5	6	2			5	0	no	
6	9	0			7	2	no	
7	6	1			4	2	no	
8	17	1			16	0	no	
9	3	2			1	1	no	
10	7	2			5	0	no	
11	16	3			10	3	no	
12	5	3			1	1	no	
13	8	3			5	0	no	
14	9	2			6	1	no	
15	3	1			2	0	no	
16	15	7			10	2	no	
17	9	2			7	0	no	
18	16	6			13	0	no	
19	2	1			1	0	no	
20	2	1			2	0	no	
21	2	1			1	0	no	
22	12	3			10	0	no	
23	31	1			30	0	no	
24	10	4			8	1	no	
25	9	4			8	0	no	
Total	**248**	**63**			**197**	**14**	---	---
Comments:								

Table 10 Example for the processing of the manual image analysis data (the α-Al_2O_3-injected alloys).

Alloy	Alloy Condition	Cooling Rate	Total Number of Inclusions	Number of Inclusions Observed in a-Al	(1)	Number of Inclusions in Interdendritic Regions	Total Number of Inclusions in Contact with Fe-intermetallics	(2)
1	1G	0.16	**515**	**443**	86.01942	72	**49**	9.514563107
	1S	0.76	**302**	**242**	80.13245	60	**55**	18.21192053
	1S	8	**237**	**149**	62.8692	88	**70**	29.53586498
	1C	10.7	**342**	**192**	56.14035	150	**152**	44.44444444
2	2G	0.16	**429**	**364**	84.84848	65	**58**	13.51981352
	2S	1.53	**240**	**199**	82.91667	41	**52**	21.66666667
	2S	8						
	2C	13.8	**318**	**182**	57.2327	136	**129**	40.56603774
3	3G	0.21	**469**	**259**	55.22388	210	**177**	37.73987207
	3S	1.3	**262**	**205**	78.24427	57	**54**	20.61068702
	3S	10.5	**331**	**264**	79.75831	67	**86**	25.98187311
	3C	14.7	**363**	**247**	68.04408	116	**111**	30.5785124
4	4G	0.18	**261**	**171**	65.51724	90	**120**	45.97701149
	4S	1.4	**387**	**318**	82.17054	69	**61**	15.7622739
	4S	10.3	**421**	**299**	71.02138	122	**100**	23.75296912
	4C	12.8	**262**	**164**	62.59542	98	**90**	34.35114504
5	5G	0.19	**353**	**148**	41.92635	205	**199**	56.37393768
	5S	1.2	**194**	**55**	28.35052	139	**138**	71.13402062
	5S	8	**78**	**35**	44.87179	43	**42**	53.84615385
	5C	14.3	**309**	**184**	59.54693	125	**101**	32.68608414
6	6G	0.18	**270**	**38**	14.07407	232	**74**	27.40740741
	6S	0.76	**187**	**124**	66.31016	63	**19**	10.16042781
	6S	5.1	**236**	**14**	5.932203	222	**74**	31.3559322
	6C	12.8	**335**	**87**	25.97015	248	**57**	17.01492537
	Overall Average		308.74					30.96489323

The data in bold letters are taken directly form the image analysis sheets.
The meanings of the table heading numbers are shown in pages 97-98.

Table 10 (continued)

Number of Inclusions Not in Contact with Fe-intermetallics in the Interdendritic Regions	Number of Inclusions in Contact with Fe-intermetallics in Al	(3)	Number of Inclusions in Contact with Fe-intermetallics in the Interdendritic Regions	(4)	(5)	(6)	(7)	(8)
34	11	2.48307	38	52.778	77.55102	22.44898	6.152777778	
19	14	5.785124	41	68.333	74.54545	25.45455	4.033333333	
23	5	3.355705	65	73.864	92.85714	7.142857	1.693181818	
34	36	18.75	116	77.333	76.31579	23.68421	1.28	
15	8	2.197802	50	76.923	86.2069	13.7931	5.6	
12	23	11.55779	29	70.732	55.76923	44.23077	4.853658537	
32	25	13.73626	104	76.471	80.62016	19.37984	1.338235294	
54	21	8.108108	156	74.286	88.13559	11.86441	1.233333333	
15	12	5.853659	42	73.684	77.77778	22.22222	3.596491228	
12	31	11.74242	55	82.09	63.95349	36.04651	3.940298507	
29	24	9.716599	87	75	78.37838	21.62162	2.129310345	
24	54	31.57895	66	73.333	55	45	1.9	
15	7	2.201258	54	78.261	88.52459	11.47541	4.608695652	
42	20	6.688963	80	65.574	80	20	2.450819672	
35	27	16.46341	63	64.286	70	30	1.673469388	
43	37	25	162	79.024	81.40704	18.59296	0.72195122	
19	18	32.72727	120	86.331	86.95652	13.04348	0.395683453	
5	4	11.42857	38	88.372	90.47619	9.52381	0.813953488	
47	23	12.5	78	62.4	77.22772	22.77228	1.472	
165	7	18.42105	67	28.879	90.54054	9.459459	0.163793103	
48	4	3.225806	15	23.81	78.94737	21.05263	1.968253968	
155	7	50	67	30.18	90.54054	9.459459	0.063063063	
196	5	5.747126	52	20.968	91.22807	8.77193	0.350806452	
Overall Average		13.44648		65.344	79.69389		2.279700419	

The data in bold letters are taken directly form the image analysis sheets.
The meanings of the table heading numbers are shown in pages 97-98.

CHAPTER 4

IRON INTERMETALLIC PHASES IN THE Al-CORNER OF THE Al-Si-Fe SYSTEM

CHAPTER 4

IRON INTERMETALLIC PHASES IN THE Al-CORNER OF THE Al-Si-Fe SYSTEM

4.1. Introduction

Commercial unalloyed aluminum and aluminum base alloys contain a considerable amount of iron and silicon as impurities or alloying additions. Commercial aluminum alloys, which have up to 1% of iron and silicon, can be considered ternary alloys. As the solid solubility of iron in aluminum is less than 0.05% at equilibrium, nearly all iron in aluminum alloys forms second-phase particles. Both iron and silicon have partition coefficients less than unity, and accordingly segregate to the liquid between the Al dendrite arms during the course of solidification. Therefore, when considering the non-equilibrium lever-rule assumption,[21] primary particles of binary Al-Fe and ternary Al-Fe-Si phases, and even silicon can form during casting of an aluminum-rich alloy. The chemical composition and local cooling rate are the controlling factors that determine which phases will form[22,23] and their size.[12,14]

Several studies[26,47] have focused upon the Al-rich part of the system, where the θ-Al_3Fe, α-AlFeSi and β-AlFeSi phases have been reported as equilibrium phases.[27,28] In addition, some non-equilibrium phases have been identified, for example, metastable phases such as Al_6Fe,[23,29,119] Al_mFe[30,120] and Al_xFe[23,31] instead of the θ-Al_3Fe (or θ-$Al_{13}Fe_4$)[32,121] equilibrium phase. The structure of various phases, *e.g.*, Al_6Fe,[33,120] Al_3Fe,[29,34] α-AlFeSi[35,122] and Al_mFe[37,38] have been investigated.

Without doubt, the binary Al-Fe and ternary Al-Fe-Si phases constitute an important part of the microstructure in aluminum alloys. Particles formed during casting may influence the material properties during subsequent fabrication steps or in service. For example, the β-AlFeSi plate-like phase has a detrimental influence on the alloy properties. The β-phase platelets act as potential sites for crack initiation that, consequently, results in decohesion failure.[10] Other phases such as Al_3Fe and α-AlFeSi are cathodic to the aluminum matrix, and when present on the surface, promote pitting attack of the surface in conductive liquids.[39] Thus, control of these phases is of considerable technological importance.

In view of the importance of iron intermetallic phases in aluminum alloys, this study was carried out to characterize their precipitation as affected by (i) the chemical composition, through the use of six dilute alloys covering the Al-corner of the Al-Si-Fe

system, and (ii) the cooling rate, where two ranges of cooling rates were employed: a slow cooling rate range (0.16 –0.21 °C/s) resembling the sand casting condition, and a high cooling rate range (10-15 °C/s), similar to the cooling rates observed in pressure die casting processes. Experiments described in this chapter were designed to determine the iron intermetallic phases that might form in the group of alloys, as a first part of the project, which aims to study the nucleation of these phases on the surface of certain inclusions.

4.2. Results and Discussions

As mentioned in Chapter 3, metallographic samples were sectioned from the graphite mold and metallic mold castings close to the thermocouple tip and polished for microstructural examination. The corresponding microstructure may be considered as representative of the solidification conditions recorded by the thermocouples. It should be mentioned here that, although results for all alloys have been described in detail, for the sake of brevity, not all microstructures and cooling curves have been presented.

4.2.1. Optical Microscopy and Image Analysis

The optical micrographs of Figure 26 to Figure 29 show how the microstructure varies with alloy composition. The intermetallic phases that form in this part of the Al-Si-

Fe system are mainly iron-bearing phases (grouped together hereafter as iron intermetallics). The microstructures of alloy 1 shown in Figure 26 reveal that, in general the intermetallic phases form in the interdendritic regions. At a slow cooling rate (0.16 °C/s), the microstructure contains needle-like phases and fine eutectic regions (see arrows in Figure 26 (a)). At a high cooling rate (10.7 °C/s), the microstructure is extremely fine (see arrows in Figure 26 (b)).

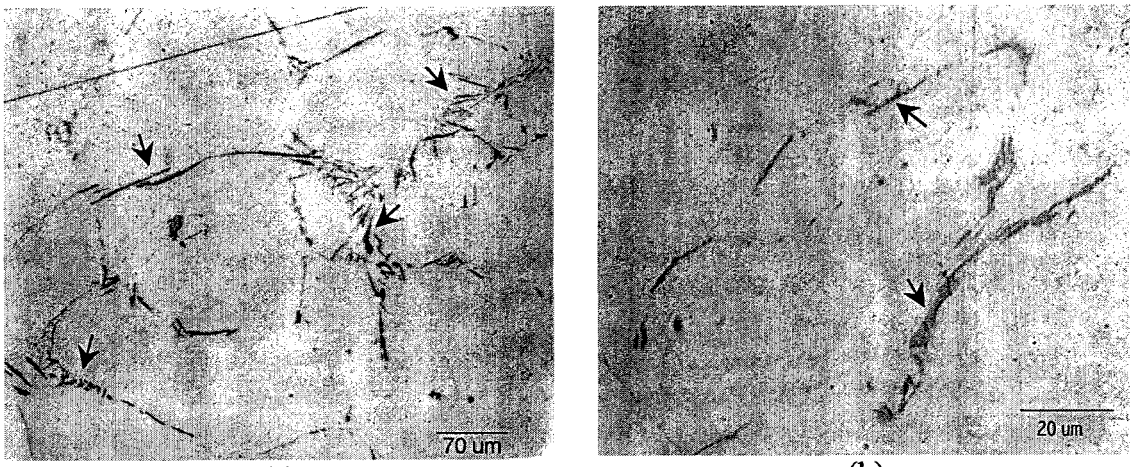

Figure 26 Microstructures of alloy 1 obtained from (a) graphite mold (cooling rate 0.16 °C/s), and (b) metallic mold (cooling rate 10.7 °C/s) castings.

Microstructures of alloys 2 and 3 (not shown) contained almost exclusively iron intermetallic phases with dendritic (or so-called Chinese script) morphologies, in addition to the aluminum matrix, when cooled slowly in the graphite mold (Figure 27 (a)). These phases changed to finer lamellar and plate-like phases when the alloys were cooled in the metallic mold, (see arrows in Figure 27(b)). Two types of intermetallic phases were

observed in the microstructure of the graphite mold-cast alloy 4 sample: a dendritic or Chinese script-like phase (α-AlFeSi), and a plate-like phase (β-AlFeSi). In the fast-cooled sample, however, only the plate-like δ-AlFeSi phase was observed, as is clear from Figure 28.

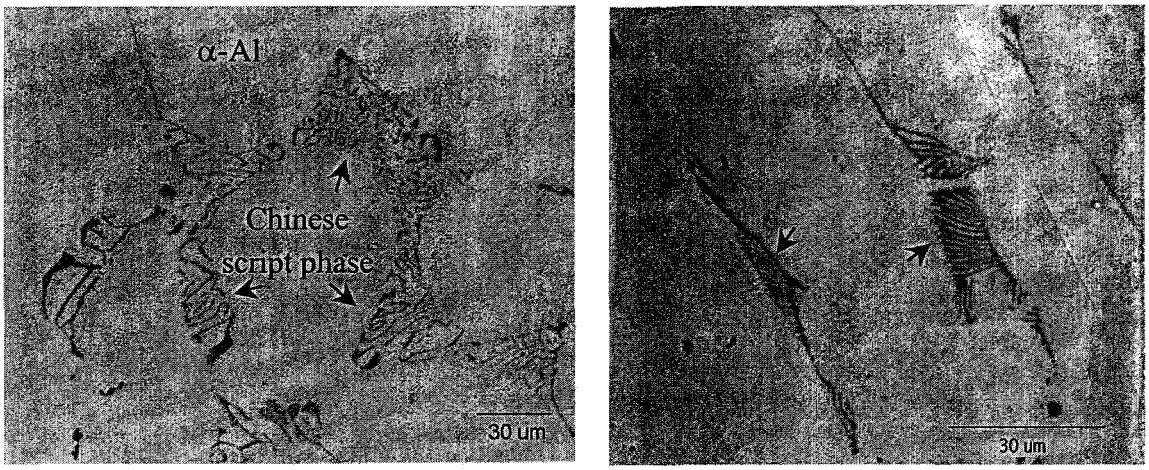

(a) (b)

Figure 27 Microstructures of alloy 2 obtained from (a) graphite mold (cooling rate 0.16 °C/s), and (b) metallic mold (cooling rate 13.8 °C/s) castings.

Alloy 5 exhibits a diversity of phases at slow cooling rate, which could not be differentiated by the image analyzer, because of their similar gray levels, as seen in Figure 29(a). The fast-cooled sample of alloy 5, Figure 29(b), exhibited a fine fibrous phase and a dendritic phase (see arrows). Coarse eutectic silicon and large platelets of β-AlFeSi were observed in alloy 6 after slow cooling, whereas at the high cooling rate (12.8 °C/s), the structure exhibited fine, modified eutectic areas delineating the aluminum dendrites, and a light gray phase (δ-AlFeSi) in the interdendritic regions.

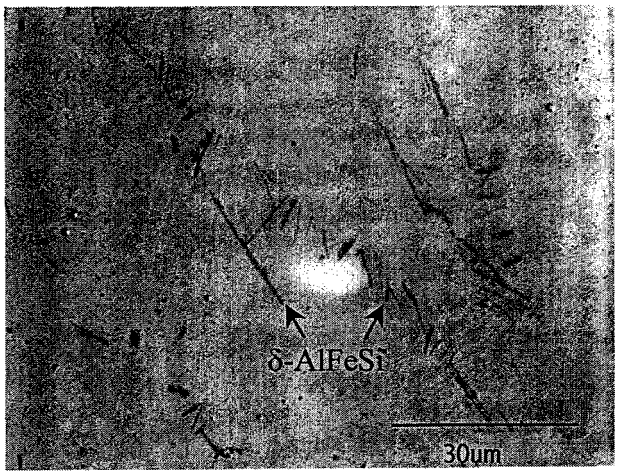

Figure 28 Microstructure of alloy 4 obtained from metallic mold casting (cooling rate 12.8 °C/s).

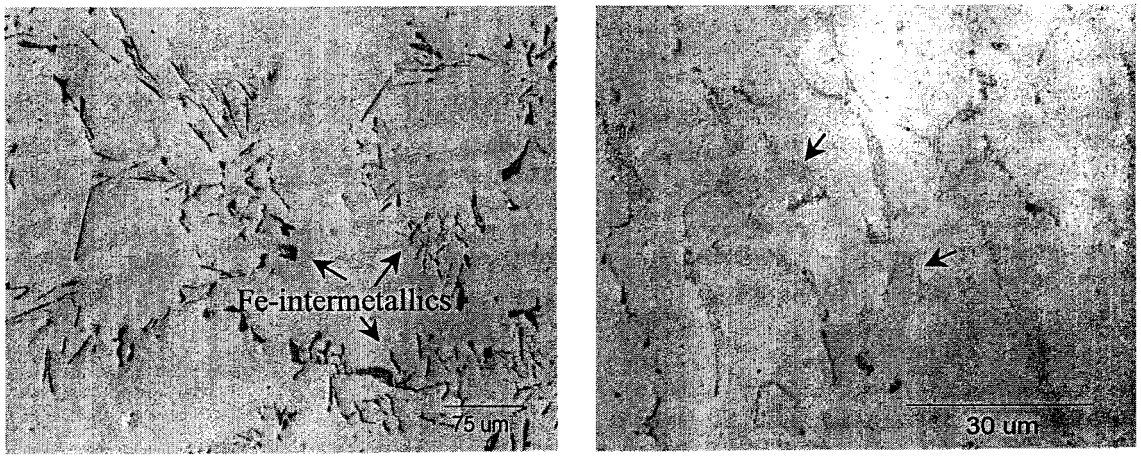

(a) (b)

Figure 29 Microstructures of alloy 5 obtained from (a) graphite mold (cooling rate 0.19 °C/s) and (b) metallic mold (cooling rate 14.3 °C/s) castings.

The similar gray levels of the intermetallic phases impeded their quantitative measurement, as various phases could not be distinguished from each other by the image analysis system. It should be mentioned here that the Leco image analyzer recognizes

various phases depending on their gray level which can range over a scale of 0 to 250 (0 representing the black, and 250 representing the white end of the range). The threshold level for each phase is set by the observer and, once set, the machine measures the volume fraction or other characteristics of the phase based upon these levels. In addition, as there appeared to be no remarkable differences in the morphology of these phases, particularly in alloys 1 and 5, the quantitative analysis was carried out for all the iron intermetallics grouped together.

Volume fractions of all iron intermetallic phases were measured for each alloy condition, and the results are plotted in the histogram shown in Figure 30. As can be seen, the volume fraction of iron intermetallics increases as the Si + Fe content increases, from alloy 1 to alloy 6, for both conditions of cooling. Obviously, solidification in the graphite mold at slow cooling rates/longer solidification times resulted in a larger volume fraction of intermetallics compared to that obtained with the metallic mold-cast samples. The largest volume fraction of intermetallics was recorded for alloy 5, containing 1.03% Fe and 0.62% Si. Analysis of Figure 30 shows that the Fe content is more important than either the Si or the Si + Fe contents in determining the volume fraction of iron intermetallics formed. The effect of silicon is less evident, as demonstrated by the

negligible difference in the volume fractions of iron intermetallics obtained in alloys 1 and 2, and in alloys 3 and 4.

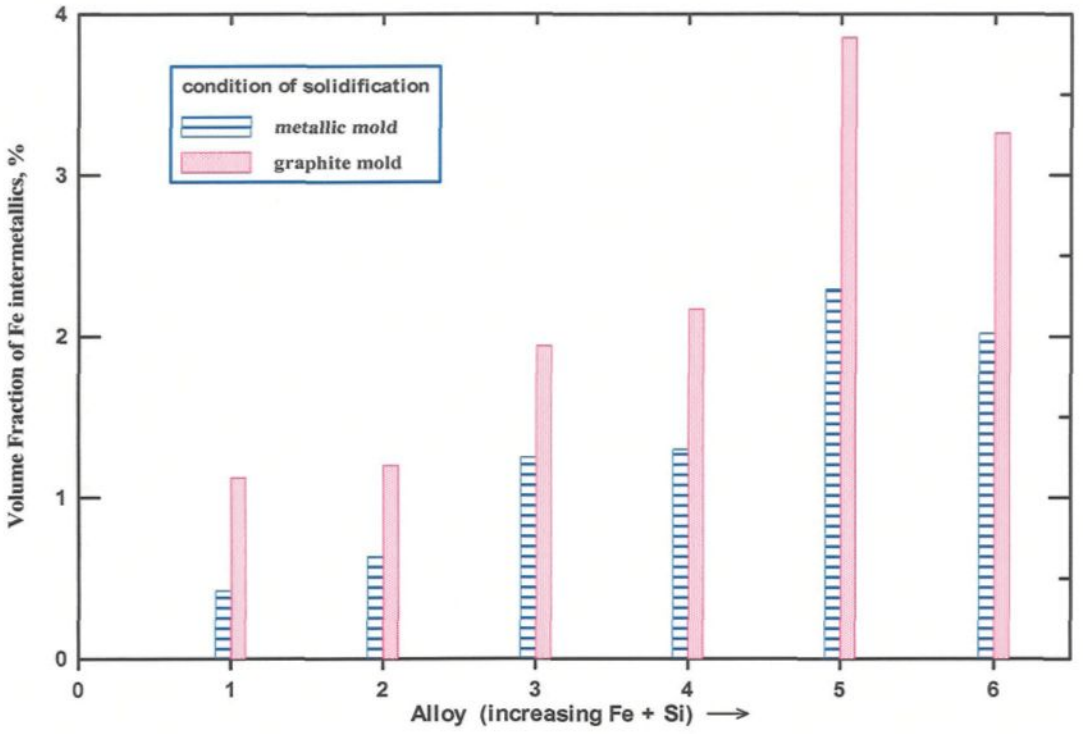

Figure 30 Volume fraction of iron intermetallics observed in the alloys studied, as a function of solidification condition.

Figure 31 shows the plots of (a) average particle lengths and (b) densities obtained from quantitative analysis of the Fe-intermetallics observed in the six alloys. Owing to the fact that slow cooling (*i.e.*, a longer solidification time) enhances the growth of phases during solidification, the lengths of the Fe-intermetallics are longer in the graphite mold-cast samples compared to those obtained from the metallic mold, Figure 31 (a). The latter samples, however, display higher densities, which is in

accordance with the fact that a greater number of smaller sized Fe intermetallics are expected to precipitate at the higher cooling rate, to compensate for the total volume fraction of intermetallics estimated to result in a specified alloy (depending upon its Fe and Si contents). In general, under both cooling conditions, the density is observed to increase with the increase in the Fe + Si content, as one proceeds from alloy 1 to alloy 6.

4.2.2. Scanning Electron Microscopy, WDS Analysis and Thermal Analysis

As mentioned previously, although results for all alloys have been described in detail, for the sake of brevity, not all microstructures and cooling curves have been shown.

4.2.2.1. Observed Phases

4.2.2.1.1. Alloy 1 (0.23 % Fe + 0.35 % Si)

The structure of alloy 1 contains only binary iron intermetallic phases when solidified slowly, but also some ternary phases after rapid cooling. The results of the WDS analysis carried out on these phases are summarized in Table 11, and correspond to the backscattered images shown in Figure 32 for the alloy 1 sample cooled at ~0.16 °C/s. Three binary iron intermetallics were identified namely, Al_mFe, Al_6Fe and Al_xFe.

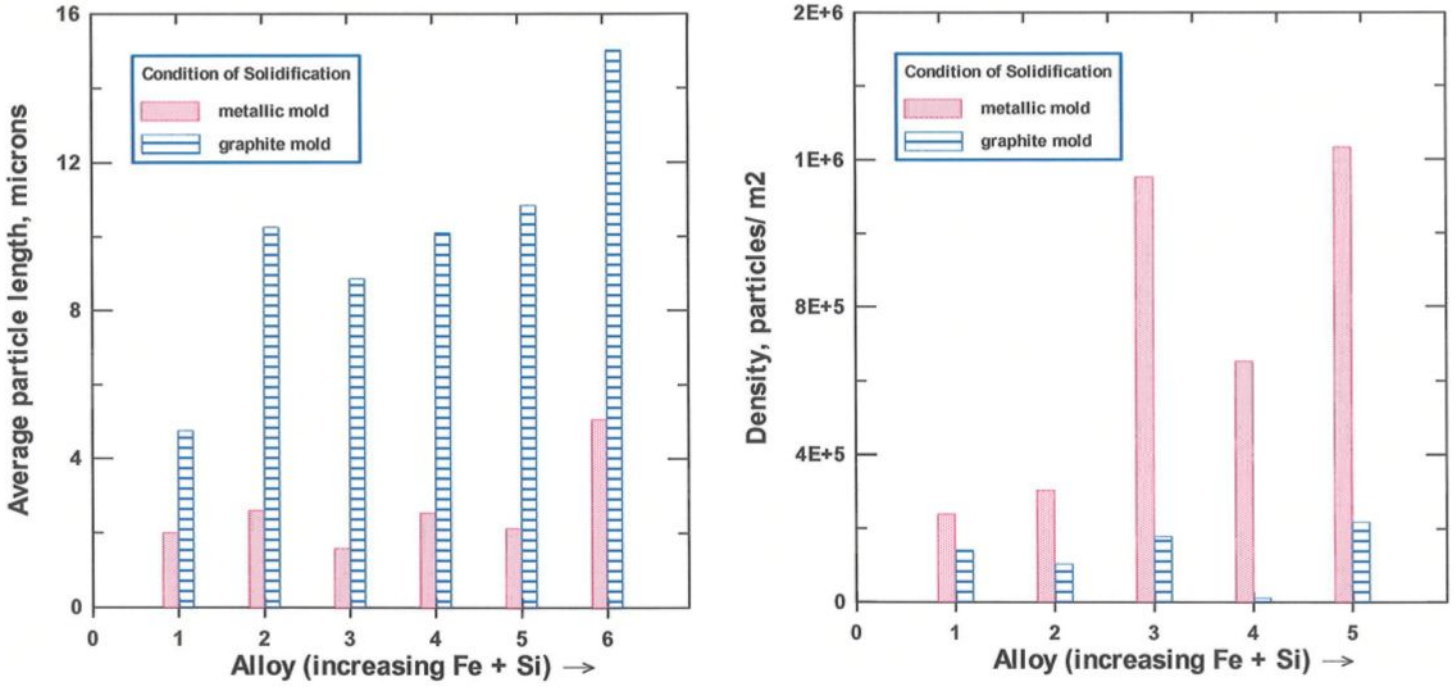

Figure 31 Quantitative analysis of the iron intermetallics observed in different alloy samples obtained from the graphite and metallic mold castings:(a) average particle length, (b) density. The (Fe + Si) increases with the alloy number.

Table 11 WDS analysis of iron intermetallic phases observed in the present study (as shown in Figure 42).

Phase	Composition, wt%					Stoichometry, Fe/Si atomic ratio	Condition	
	Al	Si	Fe	Cu	Mn+Cr		alloy	Cooling rate, °C/s
Al_mFe	63.23	1.53	33.31	.040	0.026	$Al_{3.93}FeSi_{0.091}$	1	0.16
	66.45	1.63	34.20	.0057	0.016	$Al_{4.02}FeSi_{0.095}$		
	65.94	1.72	32.15	0.000	0.045	$Al_{4.25}FeSi_{0.11}$	5	0.19
Al_6Fe	73.44	1.49	25.94	.044	0.02	$Al_{6.05}FeSi_{0.114}$	1	0.16
	73.30	1.59	27.04	.005	0.024	$Al_{6.02}FeSi_{0.117}$		
	73.16	1.76	25.92	0.017	0.033	$Al_{6.10}FeSi_{0.14}$	5	0.19
Al_xFe	70.72	1.69	26.12	.032	0.019	$Al_{5.60}FeSi_{0.128}$	1	0.16
Al_3Fe	61.85	1.45	37.15	0.038	0.044	$Al_{3.43}FeSi_{0.08}$	5	0.19
α-AlFeSi	63.59	7.61	30.45	.050	.025	$Al_{8.7}Fe_{2.0}Si$	2	0.16
	69.12	7.68	26.62	.057	.037	$Al_{11.18}Fe_2Si_{1.15}$		
	69.85	7.65	25.22	.028	.041	$Al_{11.45}Fe_2\ Si_{1.2}$		
	68.78	8.07	25.71	--	--	$Al_{11.08}Fe_2Si_{1.25}$	3	0.21
	74.48	7.38	26.42	--	--	$Al_{11.67}Fe_2Si_{1.11}$		
						Fe : Si = 2 : 1.36	3	14.7
						Fe : Si = 2 : 1.11		
	59.46	8.06	30.37	0.81	0.085	$Al_{8.12}Fe_2Si_{1.06}$	4	0.18
	62.05	7.87	30.07	0.45	0.125	$Al_{8.55}Fe_2Si_{1.04}$		
	62.36	8.61	30.21	0.43	---	$Al_{8.59}Fe_2Si_{1.14}$		
	62.73	9.34	30.28	0.46	---	$Al_{8.60}Fe_2Si_{1.23}$		
	62.91	8.08	30.17	0.32	---	$Al_{8.65}Fe_2Si_{1.06}$		
	66.89	8.38	23.91	0.42	---	$Al_{11.65}Fe_2Si_{1.4}$		
	60.80	9.11	29.71	0.076	0.035	$Al_{8.47}Fe_2Si_{1.2}$	5	0.19
	62.76	9.24	29.48	0.050	0.049	$Al_{8.81}Fe_2Si_{1.25}$		
	67.59	6.71	30.75	0.042	0.053	$Al_{9.1}Fe_2Si_{0.87}$		
	67.46	7.29	26.79	0.039	0.029	$Al_{10.42}Fe_2Si_{1.08}$		
	73.01	6.87	23.88	0.065	0.030	$Al_{12.66}Fe_2Si_{1.14}$		
						Fe:Si= 2 : 1.16	5	14.3
β-AlFeSi	58.97	13.06	26.42	0.042	0.036	$Al_{4.60}FeSi_{0.98}$	4	0.18
	59.04	14.69	26.59	0.059	0.056	$Al_{4.59}FeSi_{1.10}$		
	61.39	14.37	26.41	0.01	---	$Al_{4.84}FeSi_{1.09}$		
	63.52	14.43	26.25	0.02	---	$Al_{4.98}FeSi_{1.09}$		

Table 11 (continued)

β-AlFeSi	55.31	14.79	26.99	0.022	0.061	$Al_{4.24}FeSi_{1.09}$	6	0.18
	55.32	15.25	26.86	0.00	0.097	$Al_{4.20}FeSi_{1.13}$		
	55.57	14.90	26.90	0.00	0.071	$Al_{4.27}FeSi_{1.04}$		
	57.46	14.68	26.47	0.119	0.221	$Al_{4.50}FeSi_{1.10}$		
	56.47	14.61	26.70	0.031	0.213	$Al_{4.38}FeSi_{1.09}$		
	57.27	14.75	26.64	0.099	0.206	$Al_{4.67}FeSi_{1.14}$		
	55.31	14.79	26.99	0.022	0.061	$Al_{4.24}FeSi_{1.09}$		
	55.32	15.25	26.86	0.00	0.097	$Al_{4.20}FeSi_{1.13}$		
						Fe : Si = 1 : 0.91	1	10.7
						Fe : Si = 1 : 1.13	2	13.8
δ-AlFeSi or δ-β composite particles						Fe : Si = 1 : 1.52	1	10.7
						Fe : Si = 1 : 1.31	2	13.8
						Fe : Si = 1 : 1.38		
						Fe : Si = 1 : 1.37	3	14.7
						Fe : Si = 1 : 2.08	4	12.8
						Fe : Si = 1 : 1.53		
						Fe : Si = 1 : 1.50		
						Fe : Si = 1 : 2.50	6	12.8
						Fe : Si = 1 : 3		
						Fe : Si = 1 : 2.23		
Q_1-AlFeSi	86.26	4.77	12.02	---	---	$Al_{14.9}FeSi_{0.79}$	2	13.8
	83.69	4.34	13.03	---	---	$Al_{13.2}FeSi_{0.66}$	5	14.3

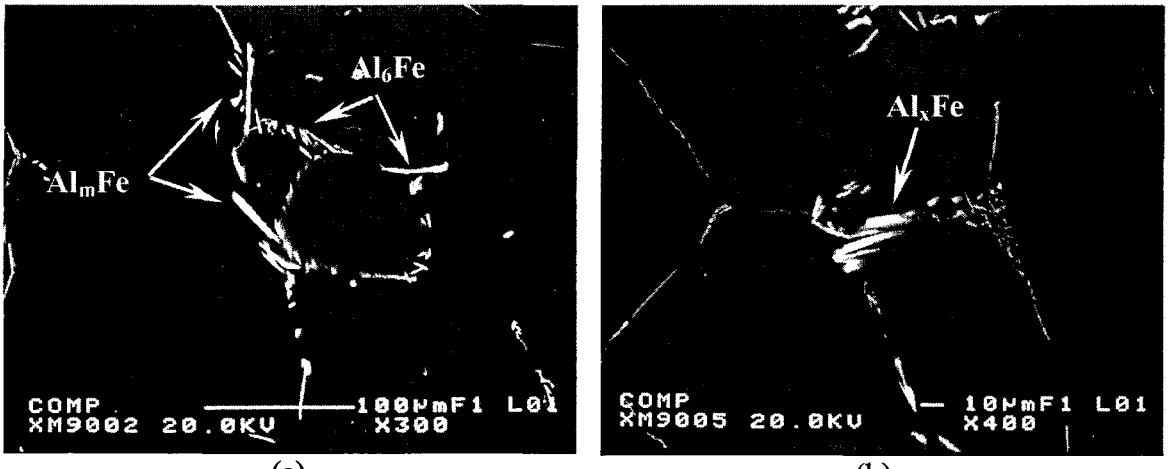

(a) (b)

Figure 32 Backscattered images showing the iron intermetallics in the graphite mold-cast alloy 1 sample (cooling rate 0.16 °C/s).

The composition of Al_mFe was 64.84 wt% Al, 33.8 wt% Fe and 1.6 wt% Si, corresponding to m = 4. Values of m = 4.2[123] and m = 4.4[32] have been ascribed to the phase previously by other workers. The Al_6Fe phase, which has the highest aluminum content among all the iron intermetallic phases, was nearly stoichiometeric, as previously reported by Porter and Westengen.[30,32] Its composition was 73.4 wt% Al, 26.5 wt% Fe and 1.5 wt% Si. It can be seen from Table 11 that the chemical composition of Al_xFe is 70.72 wt% Al, 26.1 wt% Fe and 1.7 wt% Si, which corresponds to x = 5.6. The structure of this phase is not known. It has been reported to have a defective crystal structure, and a chemical composition corresponding to x = 5.8.[32]

The formation of these three metastable phases at a very low cooling rate (0.16 °C/s) is in direct contrast to the findings of Miki *et al.*,[22] Young and Clyne,[23] and Kosuge and Mizukami.[50] According to these studies, the Al_3Fe phase is stable when obtained at cooling rates below 1 °C/s, the Al_xFe phase between 0.5° and 6 °C/s;[23] and the Al_6Fe phase at cooling rates in the ranges 1° – 10 °C/s,[22] 3° – 18 °C/s,[23] or 2° – 20 °C/s.[50] The Al_mFe phase is reported to be stable when obtained at cooling rates above 10 °C/s,[22] 18 °C/s,[23] or 20 °C/s.[50] Apparently, the difference in results between these studies and the present one can be attributed to the commercial grade DC casting alloys used in the former, which contained much higher Fe/Si ratios. In the present study, the Si content is

considerably higher, in fact, higher than that of iron in most cases. For example, Kosuge and Mizukami[50] used an alloy containing 0.58 wt% Fe and 0.01 wt% Si, while Miki *et al.*[22] used Fe/Si ratios close to 10.

From a comparison of these results, it can be deduced that Si stabilizes metastable Al-Fe phases such as Al_mFe, Al_6Fe and Al_xFe at slow cooling rates (0.16 °C/s). In other words, Si shifts the cooling rates that are required for the stability of the binary Al_mFe, Al_6Fe and Al_xFe phases to very low values. In addition, these phases have been reported to contain small amounts of silicon in their composition,[36] a fact that is confirmed in the present work (to be discussed later). From the absence of Al_3Fe in the microstructure of alloy 1, and according to the results of Miki *et al.*[22] and Kosuge and Mizukami[50], it is suggested that silicon stabilizes the metastable Al-Fe binary phases and destabilizes the Al_3Fe phase at slow cooling rates.

When alloy 1 was cast in the metallic mold (cooling rate, 10.7 °C/s), the δ- and β-AlFeSi ternary phases were observed to form. The size of these phases was small compared to the size of the electron beam of the microanalyzer used to identify them. Consequently, due to contamination from the surrounding matrix, chemical analysis showed a higher aluminum content than expected. For this reason, the ratio Fe/Si has

been used for identification of phases in almost all the rapidly-cooled samples in this study.

It is also worth noting in Figure 32 that the binary Al-Fe phases are formed in the interdendritic regions. The formation of these high-Fe phases (26-33 wt% Fe) in a dilute alloy (which contained 0.23 wt% Fe) indicates that as solidification proceeded, the liquid phase was enriched with Fe, resulting finally in very rich interdendritic liquid regions from which the iron-rich phases could precipitate.

Thermal analysis of alloy 1 was carried out for both conditions of solidification (metallic and graphite molds). In the case the of graphite mold, Figure 33 (a), the cooling curve, first derivative, and the corresponding temperature differences between the wall and the center thermocouples (T_w-T_c) are plotted. Two reactions can be distinguished: formation of the α-Al dendrites, and precipitation of Al_6Fe through a eutectic reaction.[23] On the other hand, as a result of the high cooling rate, (*i.e.*, very short solidification time, 3.9 s and, hence, low volume fraction of intermetallics formed (Figure 30)), no thermal arrests apart from the development of the aluminum dendritic network were distinguished in the case of the metallic mold, Figure 33 (b). The solidification range being still wide (42 °C), the formation reactions of these phases had small heat effects. Thus, no noticeable peaks in the first derivative curve could be observed, on account of the high

rate of heat extraction during solidification in the metallic mold. Unlike the microstructure of alloy 1 which contained only binary Al-Fe intermetallic phases, alloy 2 contained no binary phases, as discussed in the next section.

4.2.2.1.2. Alloy 2 (0.23 % Fe + 0.49 % Si)

The data obtained from WDS analysis of the alloy 2 sample is also listed in Table 11. The α-AlFeSi phase with its characteristic dendritic- or Chinese script-like morphology is formed during slow cooling. The average composition of the phase was 27.4 wt% Fe and 7.6 wt% Si. In addition, some traces of Cu and Mn were found in this phase. As the composition of alloy 2 differs from that of alloy 1 only in its higher Si content, this leads to the conclusion that a Si content greater than 0.35 wt% stabilizes the α-AlFeSi phase. By contrast, the high cooling rate of the metallic mold promoted the formation of other phases, such as the β-, δ-, and q_1-AlFeSi phases, which were generally distinguished by their higher silicon contents. As Figure 34 shows, the collective morphology of these phases is feather-like and dendritic-like.

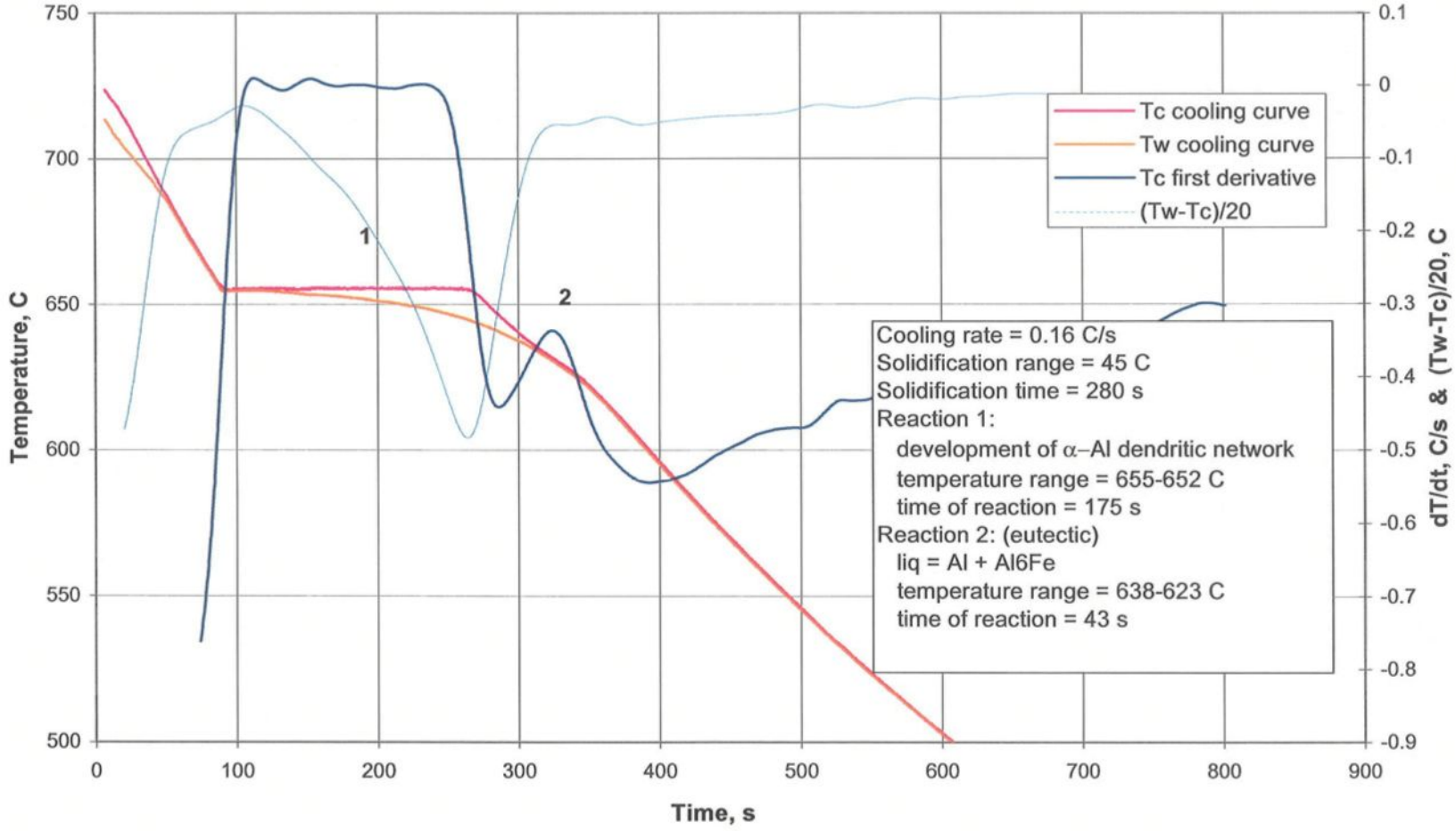

(a)

Figure 33 Plots of thermal analysis data obtained for alloy 1 (Al-0.35 % Si-0.23 % Fe) solidified in (a) graphite, and (b) metallic molds. Tc: temperature corresponding to thermocouple at center of the mold, Tw: temperature corresponding to thermocouple near the wall of the mold.

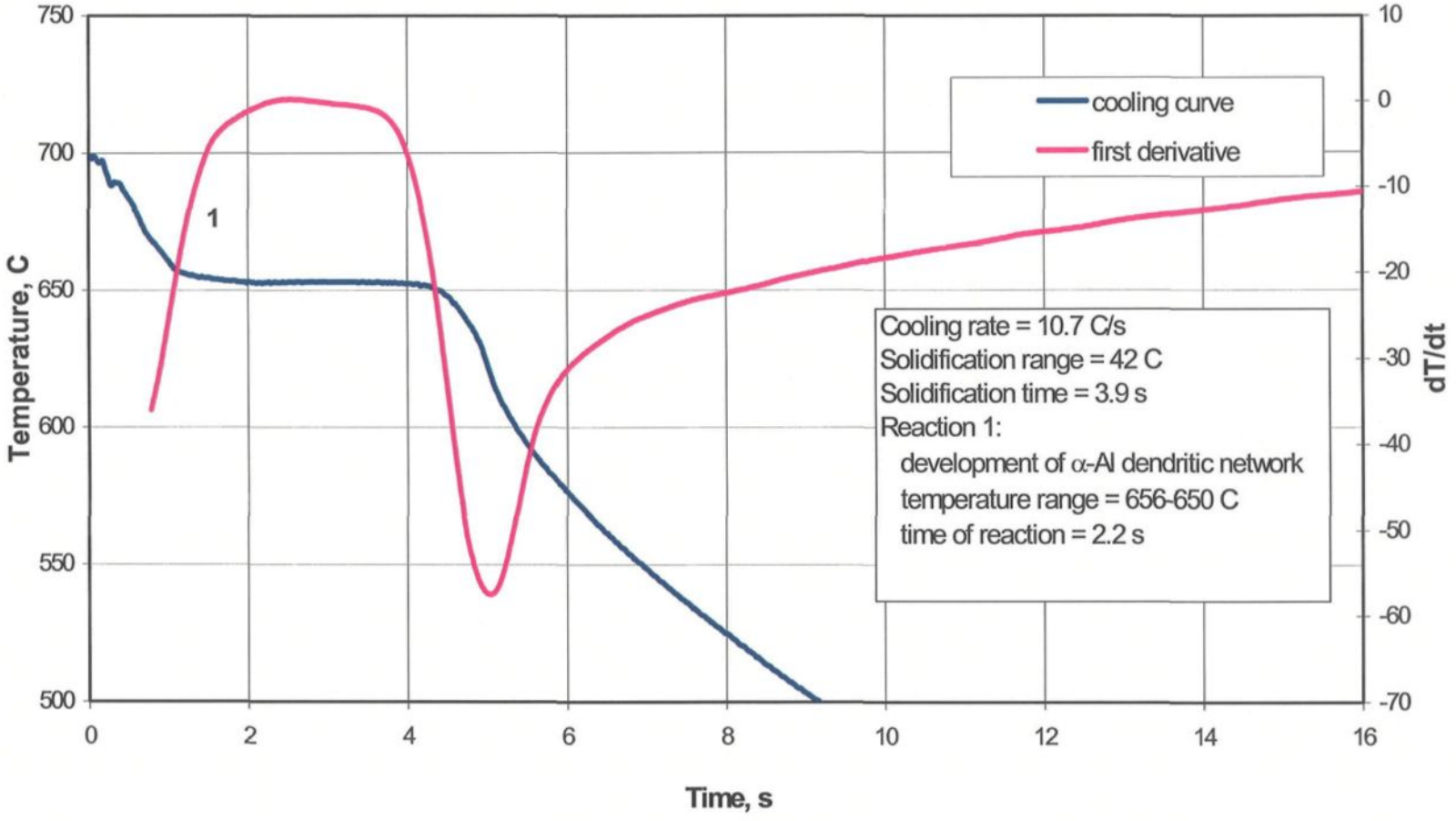

(b)

Figure 33 Plots of thermal analysis data obtained for alloy 1 (Al-0.35 % Si-0.23 % Fe) solidified in (a) graphite, and (b) metallic molds.

The α-AlFeSi phase displayed a noticeable thermal arrest in the cooling curve of alloy 2 cast in the graphite mold, Figure 35. The temperature of formation range was 633-611 °C, with a peak at 624 °C. The starting and termination points of the reaction were determined according to the definitions given by Bäckreud *et al.*[46] Unlike the α-phase, the heats of formation of the β-, and q_1-AlFeSi phases observed in the metallic mold-cast sample of alloy 2 were too weak to be detected, due to (a) the very short period of time over which these phases formed, (b) their very small volume fractions and (c) the high rate of heat extraction of the metallic mold. The exception was the δ-phase. It formed in the temperature range 611-600 °C, with a reaction peak at 604 °C, and a very short time of formation, 0.3 s.

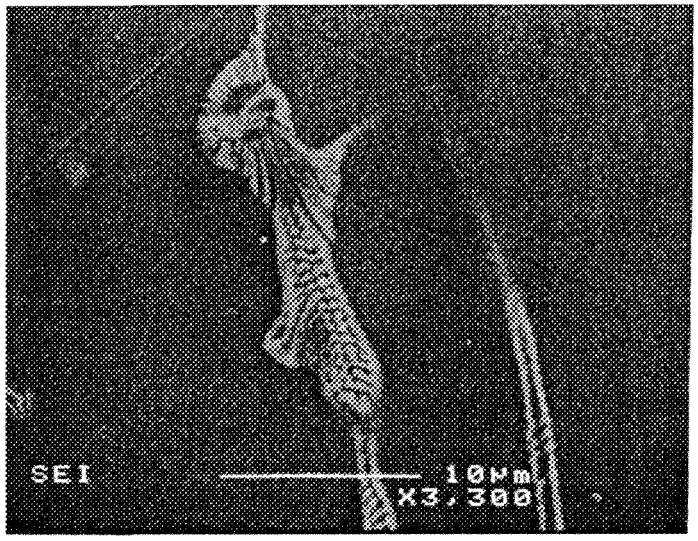

Figure 34 Secondary electron image depicting the morphology of the iron intermetallics observed in the alloy 2 sample obtained from the metallic mold.

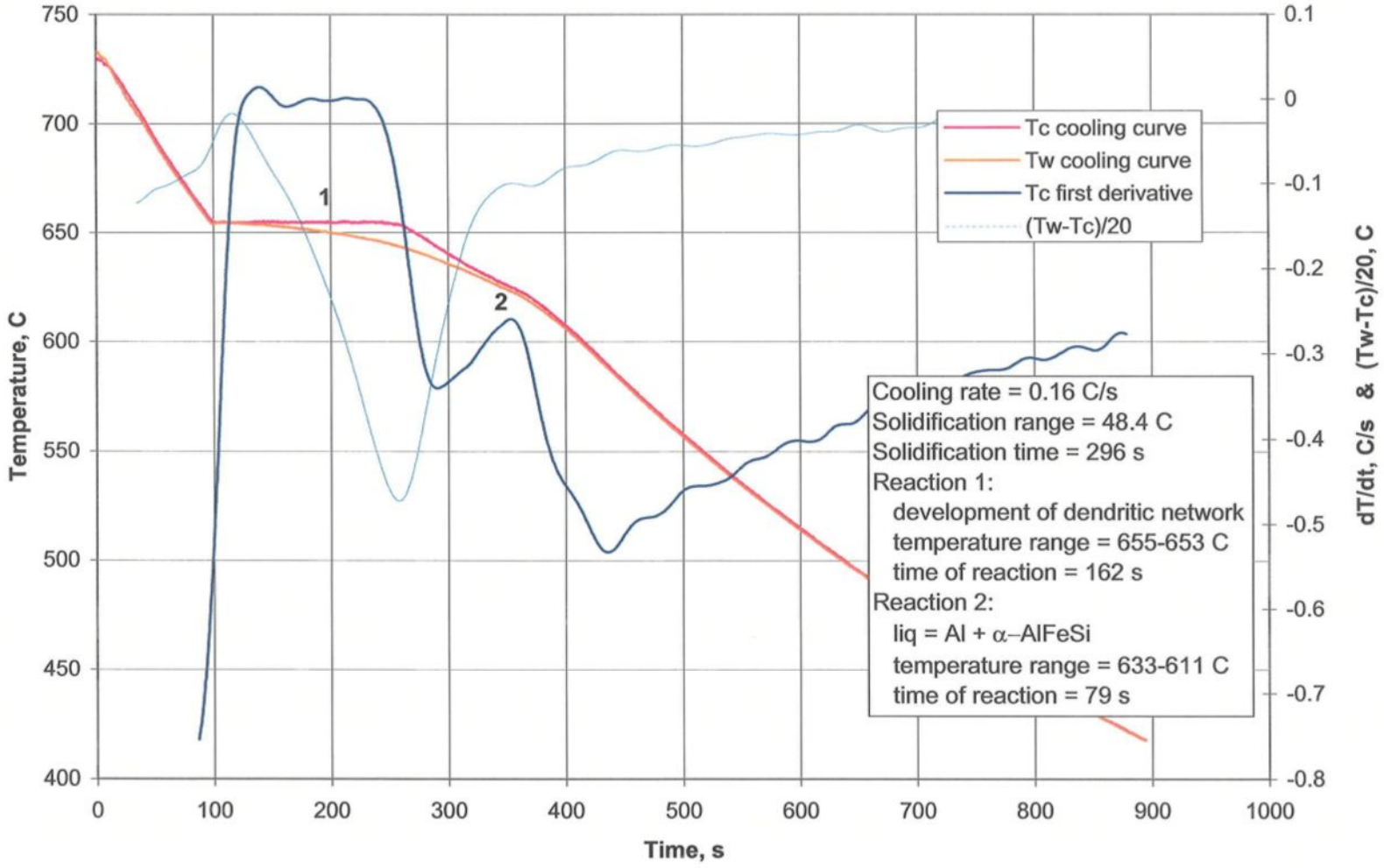

Figure 35 Plot of thermal analysis data obtained for alloy 2 (Al-0.49 % Si-0.23 % Fe) solidified in the graphite mold.

4.2.2.1.3. Alloy 3 (0.55 % Fe + 0.62 % Si)

The graphite mold-cast structure of alloy 3 contained α-AlFeSi and Si-rich spheroids, as shown in Figure 36. The chemical composition of the α-AlFeSi phase lies in the same range as that observed in alloy 2 (Table 11). The Si-rich spheroid is probably a liquid inclusion. At the high cooling rate, both α- and δ-AlFeSi phases were observed to form (Figure 37). The cooling curve for the slowly cooled alloy 3 sample (not shown) shows that the thermal arrest of the α-AlFeSi phase is similar to that observed for alloy 2 when cooled slowly (Figure 35). The temperature of formation range of the α-AlFeSi phase was 631-615 °C, with the reaction taking 40 s. Apparently, the α-AlFeSi phase has a high latent heat of formation.

On the other hand, well-defined peaks of two reactions corresponding to the formation of α- and δ-phases were identified from the thermal analysis curve of alloy 3 cooled in the metallic mold (Figure 37). The first reaction took place between 635 and 625°C, with a temperature peak at 630°C, corresponding to the formation of the α-phase. The other reaction occurred between 617 and 609°C, and reached a maximum at 612°C, corresponding to the formation of δ-AlFeSi.

4.2.2.1.4. Alloy 4 (0.56 % Fe + 0.90 % Si)

The microstructure of alloy 4 obtained from the graphite mold casting contained both β- and α-AlFeSi phases (Table 11), the two major iron intermetallic phases that form in commercial aluminum alloys. The average composition of the β-phase was 60.7 wt% Al, 26.4 wt% Fe and 14.1 wt% Si, (in addition to some trace elements of Cu, Mn and Cr), corresponding to a formula of $Al_{4.75}FeSi$, which lies between those reported previously by Phillips[47] ($Al_9Fe_2Si_2$) and Mondolfo[124] (Al_5FeSi). The α-AlFeSi phase was observed more frequently than the β-AlFeSi phase in alloy 4. The chemical composition of the α-phase corresponded to 62.7 wt% Al, 30.2 wt% Fe, 8.4 wt% Si, and 0.5 wt% Cu with traces of Mn and Cr.

The α-phase shows some variations in chemical composition, as is clear from a comparison of its compositions in alloys 2 and 3. Bäckreud *et al.*[46] have suggested that if Cu partially substitutes for Al, and Mn for Fe, the formula $(Al+Cu)_x(Fe+Mn)_ySi$ may be proposed, where x and y represent the appropriate values. The β-phase, on the other hand, undergoes negligible variation in composition and morphology; it dissolves less trace elements and retains its plate-like morphology.

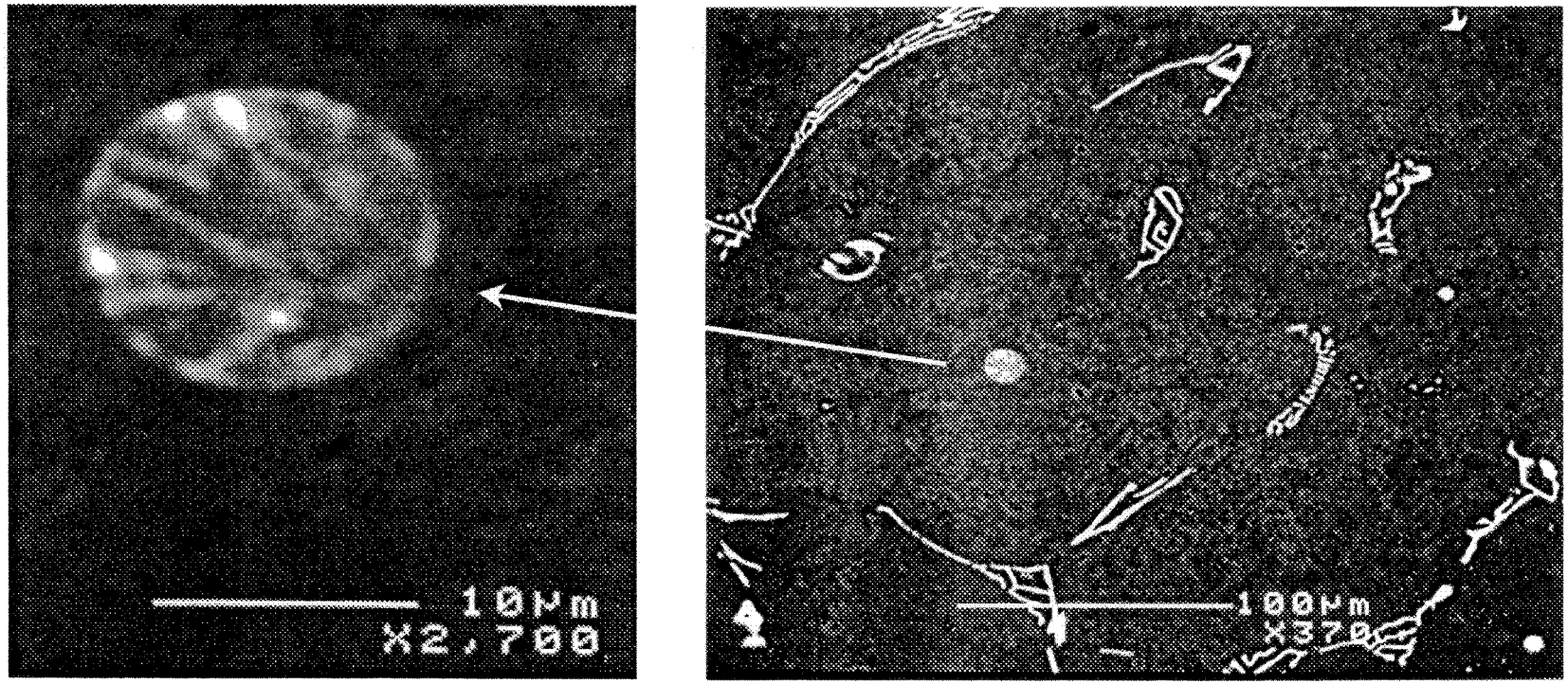

Figure 36 Backscattered images obtained from the alloy 3 sample cast in the graphite mold. The image to the left shows a magnified view of the Si-rich spheroid particle.

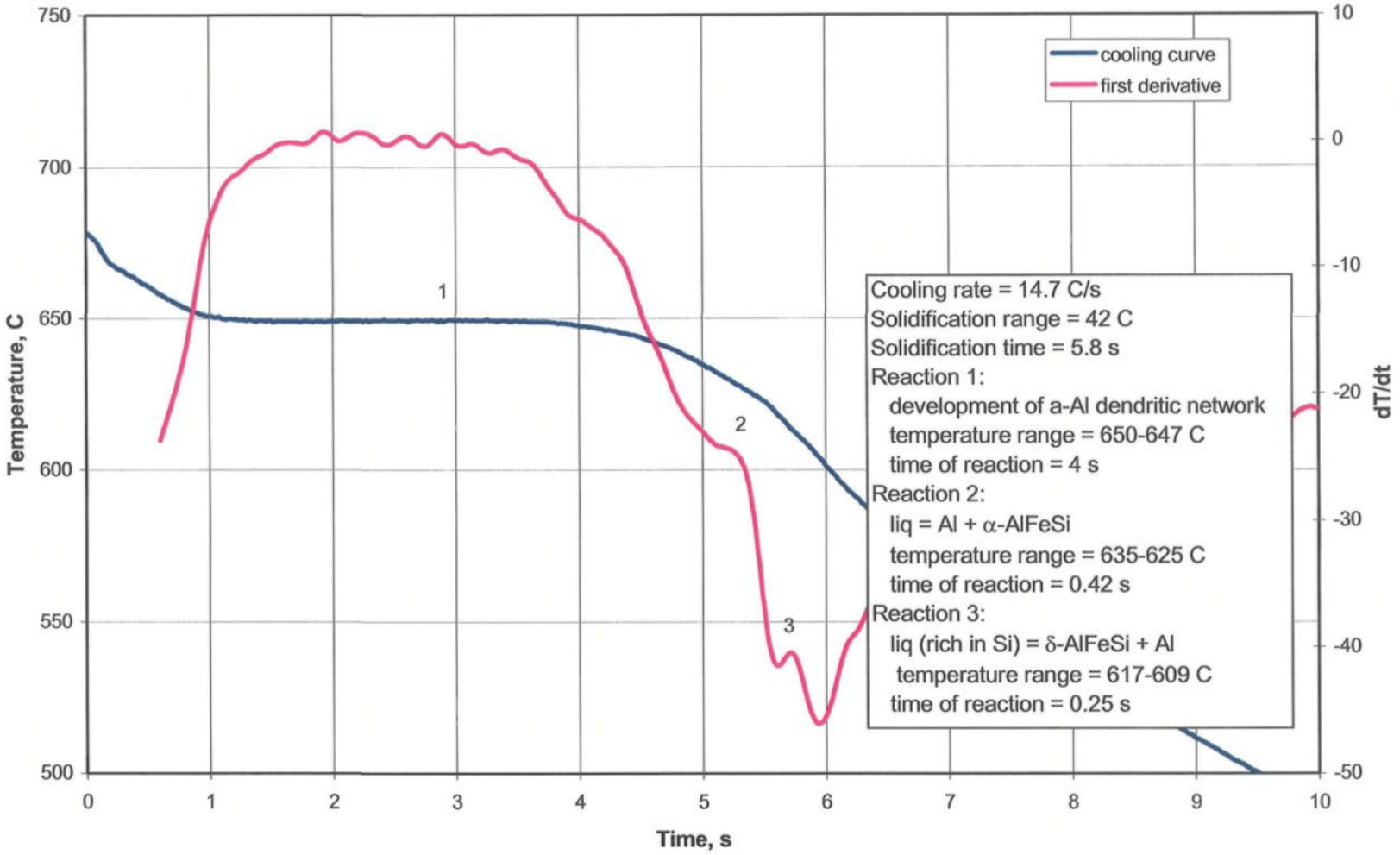

Figure 37 Plot of thermal analysis data obtained for alloy 3 (Al-0.62 % Si-0.55 % Fe) solidified in the metallic mold.

At the high cooling rate, only the δ-phase forms (Table 11). The δ-Al_4FeSi phase is the highest silicon-bearing phase in the Al-Si-Fe system. As can be seen from Figure 28, its morphology is needle-like. This phase was reported to have nearly equal weight percentages of iron and silicon.[24,124] Its melting temperature is 870°C (a peritectic decomposition).[24,124] Therefore, it is stable below this temperature.

The thermal analysis data for alloy 4 is presented in Figure 38. The α-phase, formed through a eutectic reaction simultaneously with aluminum, has a dendritic-like morphology. The reaction took place in the temperature range 634-625 °C for a period of 38 s, with a maximum derivative peak at 631.5 °C. At lower temperatures, 614-600 °C, the β-phase formed through peritectic decomposition of α-AlFeSi. This reaction has its maximum at 610 °C. The formation of δ-phase takes place at 621-611 °C. No other phase was observed in the microstructure except the δ-phase, and it showed some variation in the Fe/Si atomic ratio. This variation is the result of the partial transformation of the δ-phase to the β-phase through the peritectic decomposition:[124]

$$\text{liq.} + \delta\text{-}Al_4FeSi_2 \rightarrow \beta\text{-}Al_5FeSi + Si \qquad (29)$$

According to this reaction, the δ-phase particles start to transform into the β-phase. Under conditions of high cooling rates and short solidification times, only very fine δ-phase particles can succeed in undergoing complete peritectic decomposition,

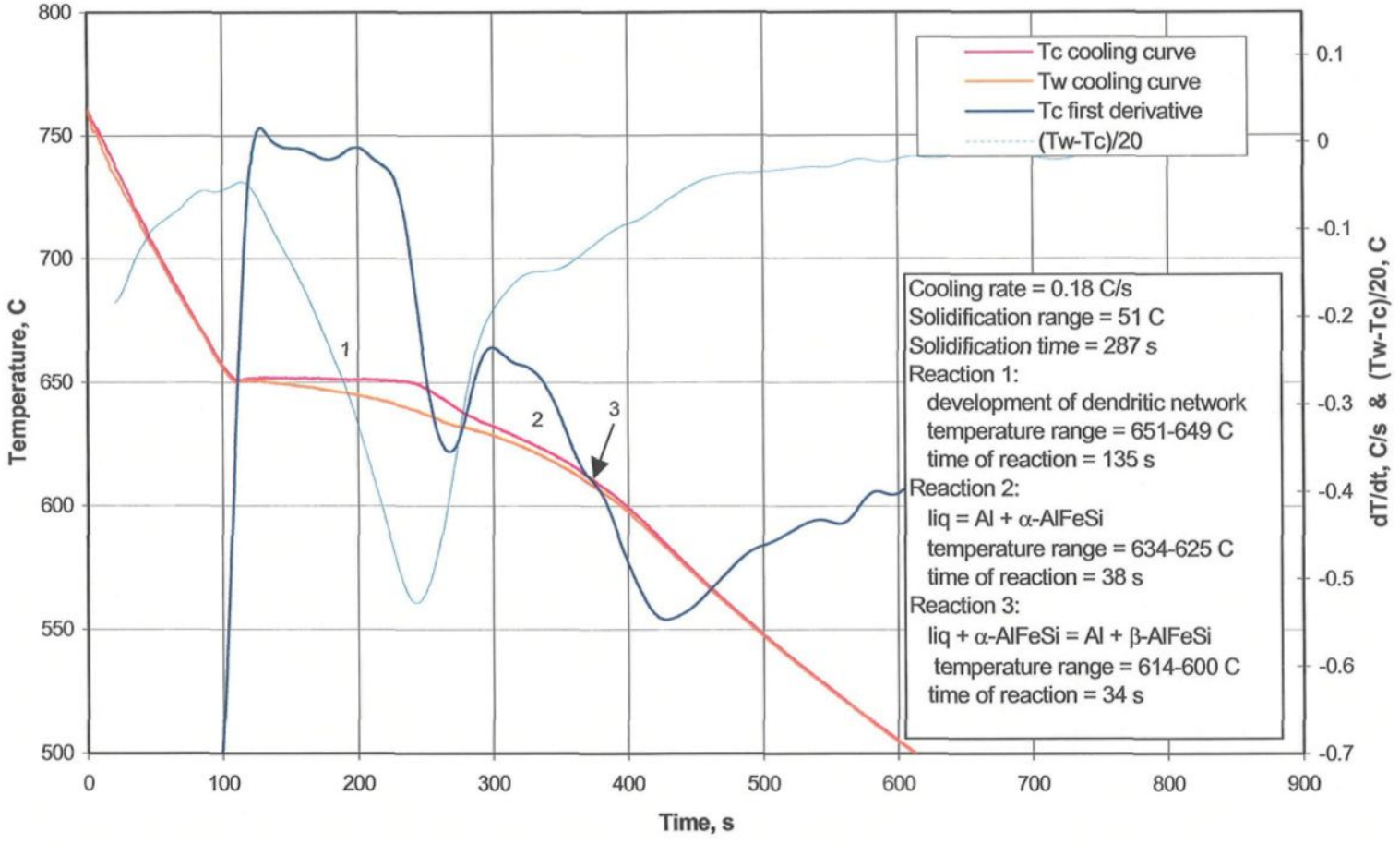

Figure 38 Plot of thermal analysis data obtained for alloy 4 (Al-0.9 % Si-0.56 % Fe) solidified in the graphite mold.

since the reaction is totally controlled by the diffusion of silicon out of the δ-phase, (which is generally slow.) In the case of large δ-phase particles, the reaction dies before completion, resulting in the formation of semi-decomposed/semi-precipitated δ-β, composite particles. These particles should contain a higher silicon content than the β-phase, corresponding to their δ-phase roots. In addition, the microanalysis of these composite particles should rarely reveal a silicon level as low as that observed in the β-phase (the condition of complete peritectic decomposition). Such particles composed of the δ-phase in the core and β-phase on the outside, constituted the majority of particles that were selected for WDS microanalysis due to their relatively large sizes. This is evident from the chemical analysis of the δ-phase (or δ-β composite particles) in alloys 1, 2, 3 and 4 listed in Table 11.

4.2.2.1.5. Alloy 5 (1.03 % Fe + 0.62 % Si)

Various iron intermetallic phases, both binary Al-Fe and ternary Al-Fe-Si, were observed to have formed in alloy 5 under the two conditions of solidification. It is to be mentioned that alloy 5 contains the highest iron content among the six alloys studied. At the slow cooling rate (0.19 °C/s), the binary Al_mFe, Al_3Fe and Al_6Fe phases are observed to precipitate. Their chemical compositions are listed in Table 11. The chemical composition of the Al_mFe phase (32.2 wt% Fe and 1.7 wt% Si) corresponded to an m

value of 4.25, which is higher than the m value obtained in alloy 1. The equilibrium phase, Al_3Fe, forms a eutectic with aluminum at about 652 °C. Its composition is 37.2 wt% Fe and 1.5 wt% Si, which gives a stoichiometry of $Al_{3.43}FeSi_{0.08}$. This formula lies in a composition range of $Al_{3.3\text{-}3.5}FeSi_{0.05}$, which was reported earlier by Dons.[45] On the other hand, the metastable Al_6Fe phase also forms a eutectic with aluminum,[23] the eutectic temperature being a few degrees lower than that of the Al-Al_3Fe eutectic.[46,125] The relation between the stable Al-Al_3Fe and the metastable Al-Al_6Fe systems resembles the well-known one between the stable Fe-C and metastable Fe-Fe_3C systems involved in the solidification of cast irons.[125] The iron content measured in Al_6Fe is similar to that found in alloy 1, *viz.*, ~26 wt%, but its silicon content is higher, 1.8 wt%. From these observations, we may conclude that the binary Al-Fe phases form only at slow cooling rates (0.16-0.19 °C/s) in low-Si alloys (*e.g.*, alloy 1 containing 0.35 wt% Si) and/or high-Fe alloys (*e.g.*, alloy 5 with 1.03 wt% Fe).

The α-phase also precipitated under the same conditions, and was observed more frequently in the microstructure. This leads to the conclusion that the composition of alloy 5 lies in the field of the Al + α +Al-Fe binary phases, and close to the boundary line of the α-phase. The α-phase has a composition of 29.2 wt% Fe and 8.1 wt% Si, with a stoichiometric formula of $Al_{9.2}Fe_2Si_{1.1}$ The Fe/Si atomic ratio measured in these particles

was roughly the same as that found in the α-phase particles after rapid cooling (Table 11).

The q_1-AlFeSi phase was composed of small, more or less rounded, particles that were arranged in feather-like or dendritic-like patterns (see Figure 34). These particles contained 13 wt% Fe and 4.3 wt% Si, a composition similar to that of the q_1-phase particles observed in alloy 2, both conforming to the composition range reported recently by Liu and Dunlop.[17,126] For commercial purity alloy with a Fe/Si weight ratio of 2, these authors noted that the α-AlFeSi and q_1-AlFeSi phases dominated at high cooling rates, which corresponds exactly to our observations in the case of alloy 5 (Fe : Si = 1.03 : 0.62) cooled in the metallic mold.

The Al_6Fe phase forms in the temperature range of 643-638 °C (for 18 seconds), as indicated by reaction 2 in the thermal analysis curve of the alloy shown in Figure 39. The α-AlFeSi phase precipitates subsequently, between 630° and 618 °C for 34 seconds, followed by the Al_mFe phase, which occurs between 618° and 604 °C, for duration of 43 seconds. Rapid cooling widened the range of α-phase formation to 629°-611 °C (*cf.*, 630°-618 °C in the slowly cooled sample), but still maintaining the reaction peak at 625 °C. In addition, the q_1-phase formed between 590° and 570 °C, the reaction showing a

weak heat effect and taking place over a long period of time (~ 3 s) when compared with the total solidification time, 6.8 s.

4.2.2.1.6. Alloy 6 (0.52 % Fe + 6.32 % Si)

The only iron intermetallic phase found in the microstructure of the graphite mold-cast alloy 6 sample was β-AlFeSi, with a composition of 56 wt% Al, 26.8 wt% Fe and 14.8 wt% Si, and containing some trace elements such as Cu, Mn and Cr (Table 11). This corresponded to a formula of $Al_{4.38}FeSi_{1.1}$, which is in good agreement with previous findings.[27,124] The lengths of the β-phase platelets observed in this case (an overall average of 15 μm, with certain platelets reaching up to 150 μm, Figure 40) are longer than those found in other cases (see Figure 31). This may be accounted for in part by the slow cooling rate, and in part by the high Si content of the alloy. It is believed that the exceptional high stability of the β-phase (equilibrium phase) within this region in the system also played a role.

The δ-phase was the only iron intermetallic phase that was found in this alloy at high cooling rates (Table 11). The phase was less distinguishable from the silicon particles (than, for example, the β-phase) when viewed in the optical microscope/image analyzer system, due to their similar gray levels.

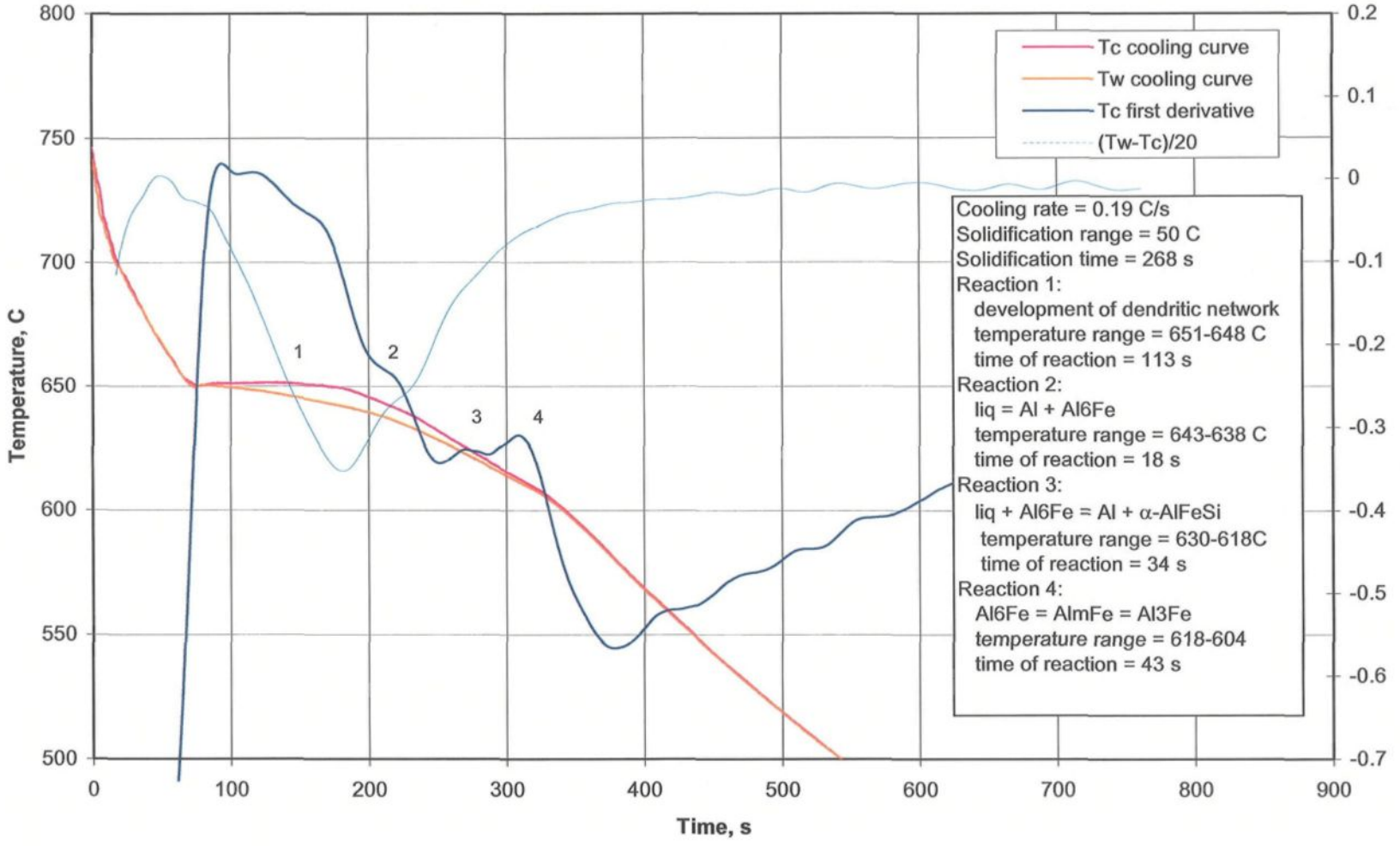

Figure 39 Plot of thermal analysis data obtained for alloy 5 (Al-0.62 % Si-1.03 % Fe) solidified in the graphite mold.

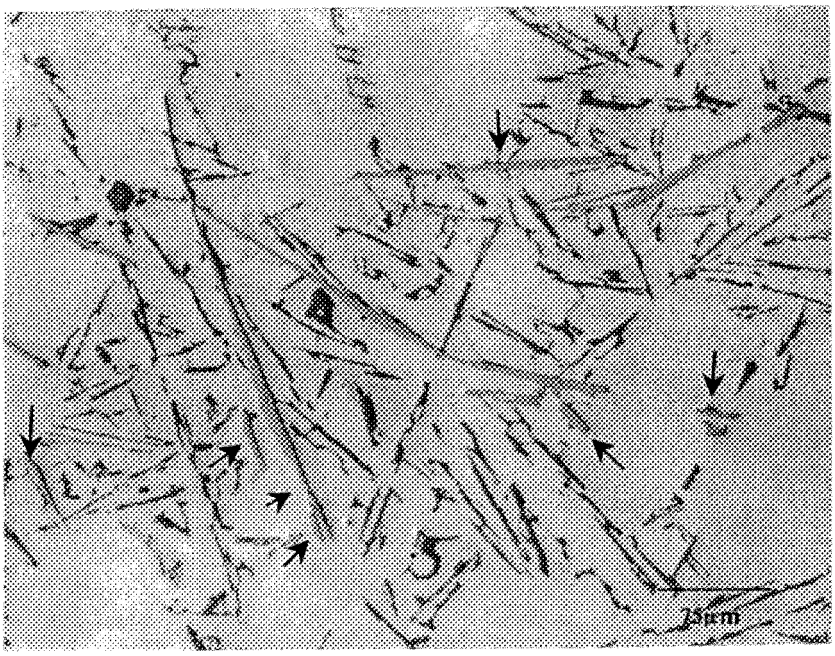

Figure 40 Microstructure of alloy 6 obtained from graphite mold (cooling rate 0.18 °C/s). Arrows show the β-AlFeSi phase in the ternary eutectic Al-Si-β (short fine particles), and the primary β-AlFeSi phase (long platelets).

Due to its high silicon content (6.3 wt%), the solidification range of alloy 6 is wide (82 °C). The solidification of the alloy at slow cooling rate, 0.18 °C/s, started with the development of the aluminum dendritic network (in the range 617°-610 °C for 76 s). After that, the silicon eutectic reaction took place around 575°-571 °C, lasting for a longer time (138 s) than the preceding or the succeeding reactions. Solidification ended with the final reaction corresponding to the formation of the β-phase, which precipitated between 565° and 536 °C for about 102 s (see Figure 41). The reaction of formation is a ternary eutectic reaction:

$$\text{liq (rich in Fe and Si)} \quad (\text{Al} + \text{Si}) + \beta\text{-AlFeSi} \tag{30}$$

The temperature range of this ternary eutectic reaction is relatively wide (565 to 536 °C, see the plot of thermal analysis data in Figure 41). This may be attributed to the smoothing

schedule that was followed in order to make the chart more readable, which flattens the peaks of the first derivative. This effect may be very great, especially when the projection target-curve (the cooling curve in this case) has a large slope. In addition, some trace elements such as Cu, Mn and Cr were analyzed in the β needles. These elements might lower the eutectic temperature through the concurrent formation of their complex compounds very late at the end of solidification.

The interesting aspect of β-phase reaction is that unlike the silicon eutectic temperature, which is only slightly affected (less than 7 °C) by variations in cooling rate, the β-phase start temperature decreases with decreasing iron content, increasing cooling rate and increasing melt superheat temperature until it eventually starts with the silicon eutectic temperature.[10,11,51] In the case of alloy 6, the silicon eutectic precipitates first then the β-AlFeSi phase as is clear from the thermal analysis data (Figure 41) and the short fine β-AlFeSi particles dispersed within the eutectic Si areas (Figure 40). However, for kinetic reasons, *i.e.*, difficulties to nucleate the silicon crystals (as a result of the purity and cleanliness of the alloy), some primary β-AlFeSi phase forms before the start of the main eutectic reaction. This would explain the appearance of some evidently large β-AlFeSi platelets in the structure (Figure 40). A similar situation took place during the solidification of the high purity alloy A356.2 as reported by Bäckreud *et al.*[46]

The formation of β-AlFeSi phase before the main eutectic is not highlighted in the sequence of solidification (Figure 41) since it is an exception that might occur or not, depending on the purity of the alloy. In addition, no evidence was encountered for this reaction in the thermal analysis data.

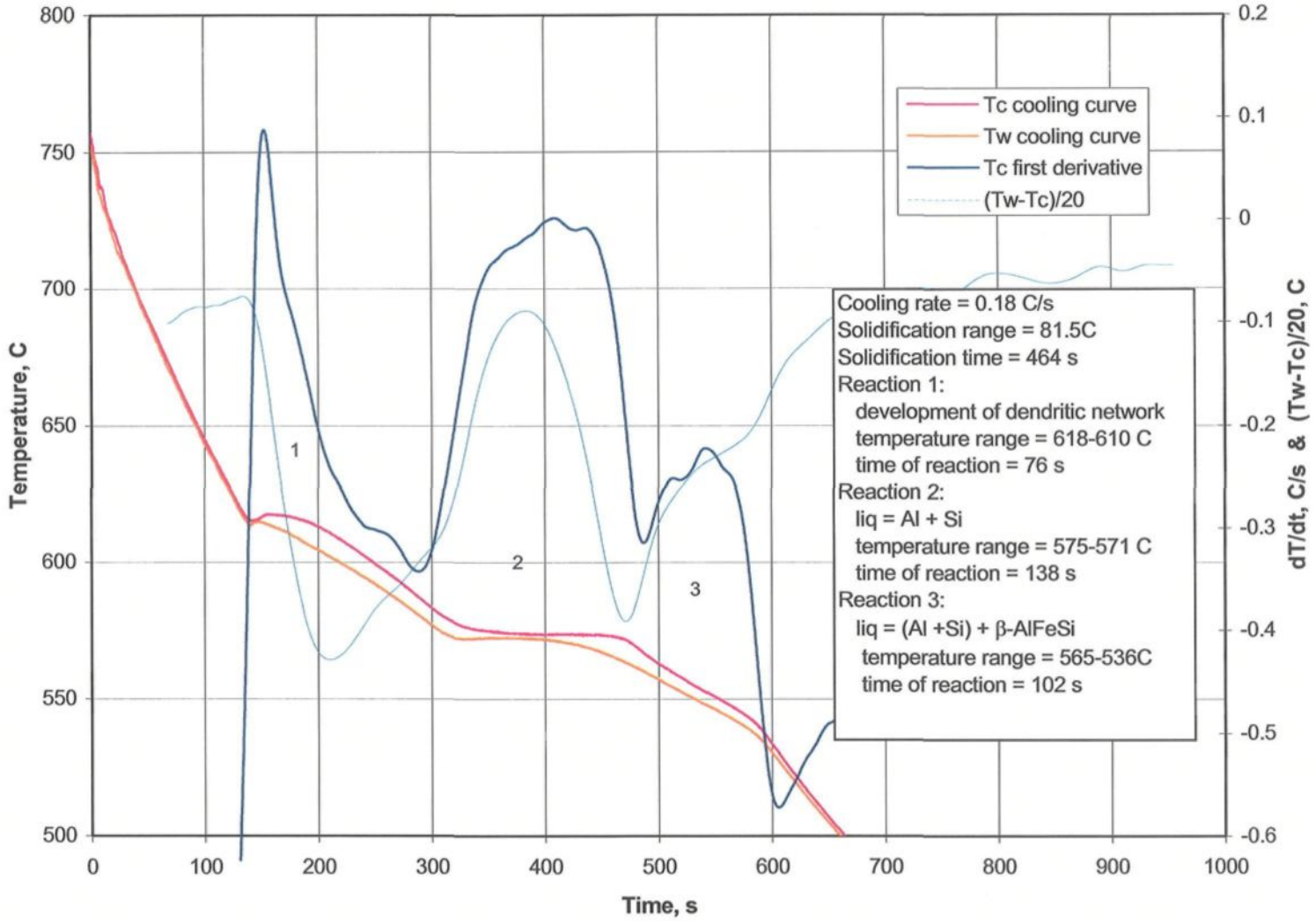

Figure 41 Plot of thermal analysis data obtained for alloy 6 (Al-6.32 % Si-0.52 % Fe) solidified in graphite mold.

The solidification range was observed to decrease from 82 °C at 0.18 °C/s to 61 °C at 12.8 °C/s cooling rate, owing to the fact that the δ-phase has precipitated as a pro-eutectic phase (610°-603 °C), whereas it increased at the slow cooling rate, due to the precipitation the β-AlFeSi as a post-eutectic phase after the completion of Si precipitation. The difference in solidification range between the two cases was about 20 °C, which corresponds to the range of β-phase formation. Consequently, this would explain the formation of a high-Si phase such as δ-AlFeSi in the alloy at high cooling rates, since it precipitated from a Si-rich liquid. It would also explain the precipitation of the β-AlFeSi phase (with a relatively lower silicon content compared to the δ-phase) during slow cooling, from the silicon-depleted liquid that remained after precipitation of silicon.

4.2.3. Effect of Cooling Rate

Cooling rate plays a basic role in stabilizing the different iron intermetallic phases in aluminum alloys, so that some phases are stabilized only at slow cooling rates, such as the binary Al-Fe phases, others are stabilized at intermediate cooing rates, and still others, such as the δ-AlFeSi and q_1-AlFeSi phases, at only high cooling rates. There are also some phases, *e.g.*, α-AlFeSi, which have high stability over a wide range of cooling rates.

Slow cooling rates result in the formation of stable phases, whilst high cooling rates lead to the precipitation of metastable phases. The intermetallic phases that appear in a microstructure are controlled not only in terms of whether the cooling rate is high or low, but, more accurately, also by the fact that each of these phases is associated with certain cooling rate ranges. This fact is indispensable for a proper understanding of the

alloy system. In view of this, some studies have specified the occurrence of Al-Fe binary phases in certain cooling rate ranges.[22,50] More recently, Young[23] has constructed cooling rate regimes for the formation of different intermetallic precipitates in hypoeutectic Al-Fe alloys. This problem was approached in part here by a thermal analysis study of the alloys investigated at different cooling rates.

4.2.4. Range of Homogeneity

Some of the phases which were investigated in this study displayed a range of homogeneity. Their chemical compositions are summarized in Figure 42. Among all of the identified phases, α-AlFeSi has the widest range of homogeneity, a fact that was mentioned by Rilvin and Raynor in their review.[24] However, they did not distinguish between the different types of α-AlFeSi which have close chemical compositions but different crystal structures. Figure 42 shows that there are two phase chemistries that are classified generally as the α-AlFeSi phase, and both have the dendritic-like (Chinese script) morphology. At the same time, their chemical compositions lie close to each other within the range of occurrence of the α-phase. The first type is designated α′ - the phase referred to repeatedly in the literature as Al_8Fe_2Si, after the formula was accepted by Mondolfo.[124] The α′-phase has a hexagonal symmetry and was reported earlier with slight variations in stoichiometry such as $Al_{11.8}Fe_3Si_{1.7}$[127] (or $Al_{7.86}Fe_2Si_{1.13}$) and $Al_{8-8.4}Fe_2Si_{1.06-1.33}$.[45] In the present work, the chemical composition of this phase was 29.48-30.75 wt% Fe and 6.71-9.34 wt% Si, exhibiting a larger range of homogeneity in silicon than in iron. The corresponding formula is expressed as $Al_{8.1-9.1}Fe_2Si_{0.87-1.25}$, covering a wider range of homogeneity than mentioned previously in the literature.[45,127]

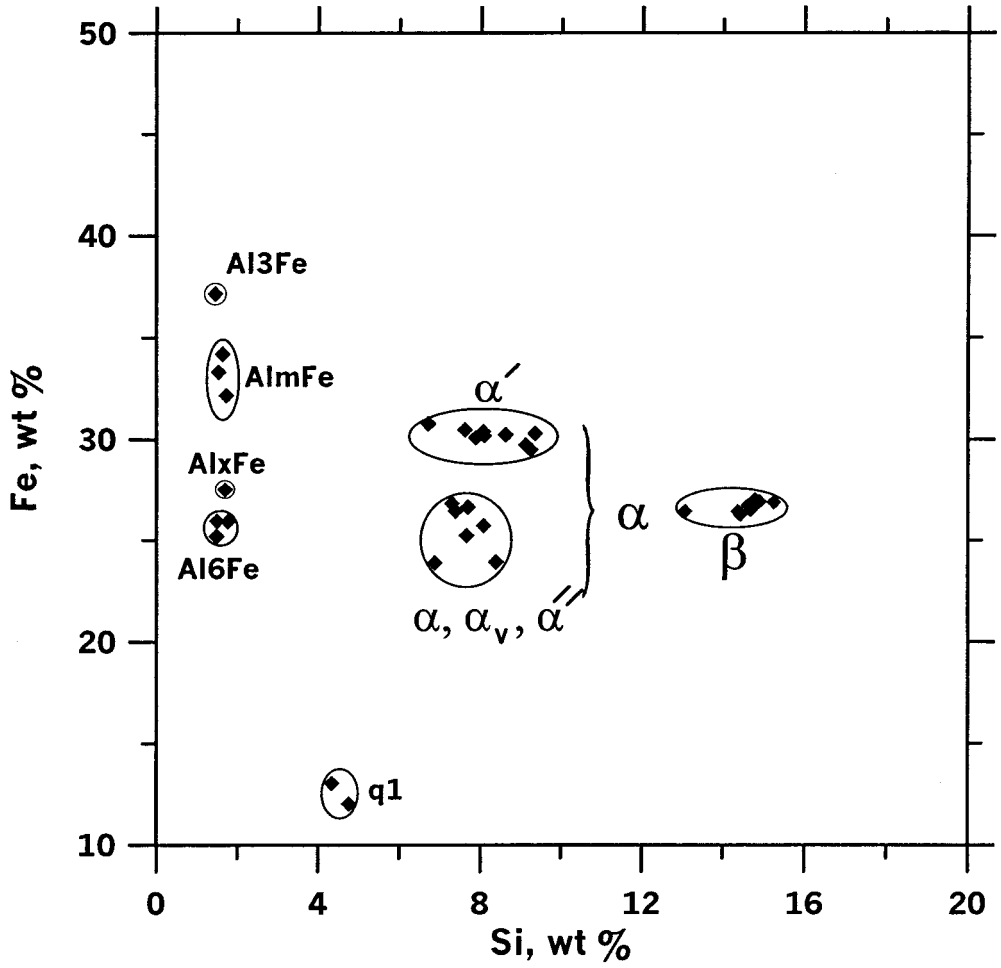

Figure 42 Chemical composition diagram of the observed phases showing their ranges of homogeneity.

The second type of the script-like α-phase has a lower iron content, between 23.88 and 26.79 wt%, a silicon content lying between 6.87 and 8.38 wt%, and a chemical formula of $Al_{10.42\text{-}11.67}Fe_2Si_{1.08\text{-}1.25}$, which may be accepted as corresponding to the α-phase (cubic crystal structure), the α_v-phase with a monoclinic symmetry,[128] or the α″-phase with a tetragonal symmetry, since all three phases have a very close composition

range. Regardless of the crystal symmetry of the phase, it displays a range of homogeneity in both its iron and silicon contents.

The β-AlFeSi phase has a range of homogeneity, as well (Figure 42), expressed by the formula $Al_{4.25\text{-}4.98}FeSi_{0.98\text{-}1.14}$. Almost all of the β-phase particles investigated in our study had iron contents ranging between 26 and 27 wt%, and silicon between 13 and 15 wt%. This was the case for the ternary phases. Among the binary Al-Fe phases, it appeared that Al_mFe had a small range of homogeneity, as seen from the formulae $Al_{4.25}Fe$ (in alloy 5) and Al_4Fe (in alloy 1). The Al_6Fe is most likely a "point phase" as defined by Ferro and Saccone,[129] *i.e.*, a stoichiometric phase.

It should be mentioned here that the number of particles corresponding to other phases that were observed in the present work was insufficient to calculate their ranges of homogeneity.

4.2.5. Silicon in Binary Phases

All the binary Al-Fe phases observed in this study contained silicon levels between 1.48 and 1.76 wt%. The silicon is most probably dissolved in the solid solution of these phases. Figure 43 shows maps of the iron and silicon distributions taken from the polished surfaces of the graphite mold cast samples corresponding to alloys 1 and 5. Alloy 1 contained only Al_mFe, Al_6Fe and Al_xFe phases. These phases are seen to contain the highest iron levels in the field. In addition, it is obvious that all phase particles contain higher silicon levels than the matrix. This observation supports the WDS analysis shown in Table 11. Although the binary Al-Fe particles in alloy 5 are similar to those seen in

alloy 1, the microstructure of alloy 5 also displayed α-AlFeSi phase particles that possessed a higher silicon content than the binary phases and the matrix (see arrows).

4.2.6. Microsegregation of Iron and Silicon During Solidification

Microsegregation is an inevitable result of solidification. As long as the partition coefficient of the solute atoms in the alloy is equal to a value other than unity, microsegregation will result. The equilibrium partition coefficients of Si and Fe in aluminum are 0.14 and 0.022, respectively. In addition, these were confirmed to be almost constant in the temperature range of 570°-620 °C in alloy 356.[130] Thus, successive enrichment of the liquid phase in these elements is expected to occur during crystal growth.

The iron and silicon contents measured in the matrix are listed in Table 12. The iron concentration in the matrices of alloys 3 and 4 obtained at high cooling rate reached its solubility limit in aluminum, which is 0.05%. In alloy 5, however, this value doubled to 0.103 wt% Fe in the matrix (at high cooling rate). At the same time, the Si content increased sharply to 0.6 wt%, a value much higher than those determined in alloys 3 and 4. In contrast, the iron level in the matrix of alloy 5 decreased to 0.043 wt% (lower than the solubility limit) at slow cooling rate. It can also be seen from Table 12 that, in alloy 6, silicon builds up to 1.43 wt% in the matrix, a value that is close to its solubility limit in aluminum (1.6 wt% at 577 °C).[131]

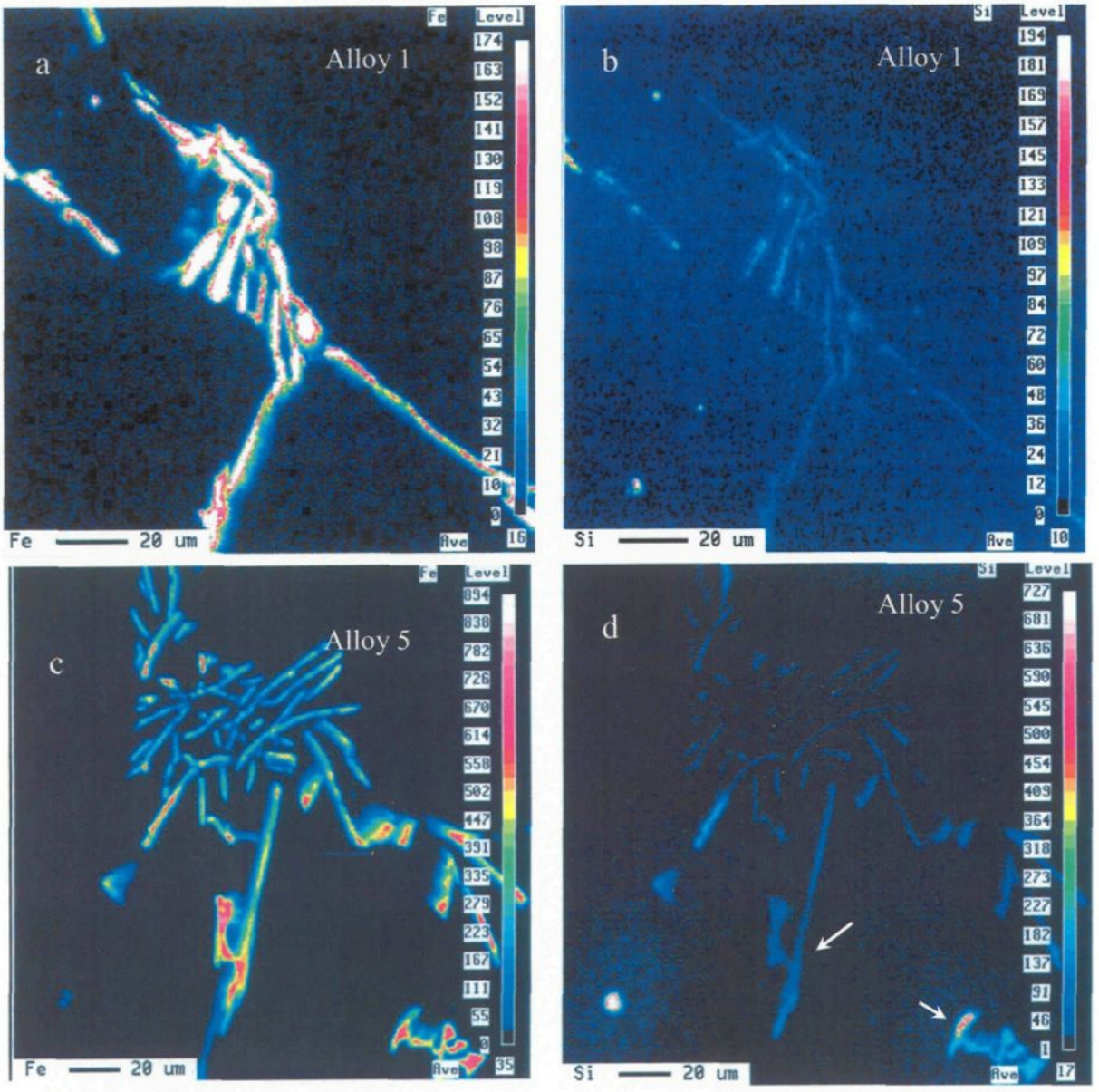

Figure 43 Maps of Fe and Si element distributions observed in the microstructures of (a,b) alloy 1 and (c,d) alloy 5 samples obtained from graphite mold castings (~0.2 °C/s). Arrows in (d) delineate the presence of α-AlFeSi ternary phase.

The behavior of iron and silicon in the aluminum matrix and the formation of Fe- and Si-rich phases can be explained using the theory of solidification and the available diffusion data. The diffusion coefficients of silicon and iron in aluminum were

determined by extrapolation of the diffusion coefficient-temperature diagram compiled by Hatch.[39] It can be observed from this diagram that the diffusion coefficient of silicon in aluminum is much higher than that of iron in aluminum (about 10^4 times higher, in the temperature range 500 – 650 °C). At 650 °C, the diffusion coefficients are 10^{-7} cm^2/s and 10^{-11} cm^2/s for silicon and iron, respectively. In addition, the diffusion coefficient of silicon in aluminum is also higher than that of aluminum (the self-diffusion coefficient). In other words, the diffusion of silicon in aluminum takes place much more easily than that of iron.

Table 12 Iron and silicon contents in the aluminum matrix of different alloys.

Alloy	Cooling rate, °C/s	Si, wt%	Fe, wt%
3	14.7	0.24	0.051
4	12.8	0.18	0.049
5	14.3	0.60	0.103
5	0.19	0.28	0.043
6	12.8	1.43	0.034

Diffusion during the process of crystal growth plays an important role. It affects, in part, the solute redistribution between solid and liquid, causing the production of a microsegregated structure. The well-known nonequilibrium lever rule or Scheil equation is usually used to describe solute redistribution in crystal growth processes. The Scheil concept supposes no solid diffusion and complete liquid diffusion. Applying the Scheil equation, calculations tracing the liquid composition as a function of solid fraction (solidification paths) were made. In these calculations, it was assumed that (i) there is no chemical interference between iron and silicon before they start to form intermetallic particles, and (ii) there is no physical interaction that can affect the solubility of either

species (Fe or Si) in aluminum. The results were plotted on the liquidus projection of the system, Figure 44.

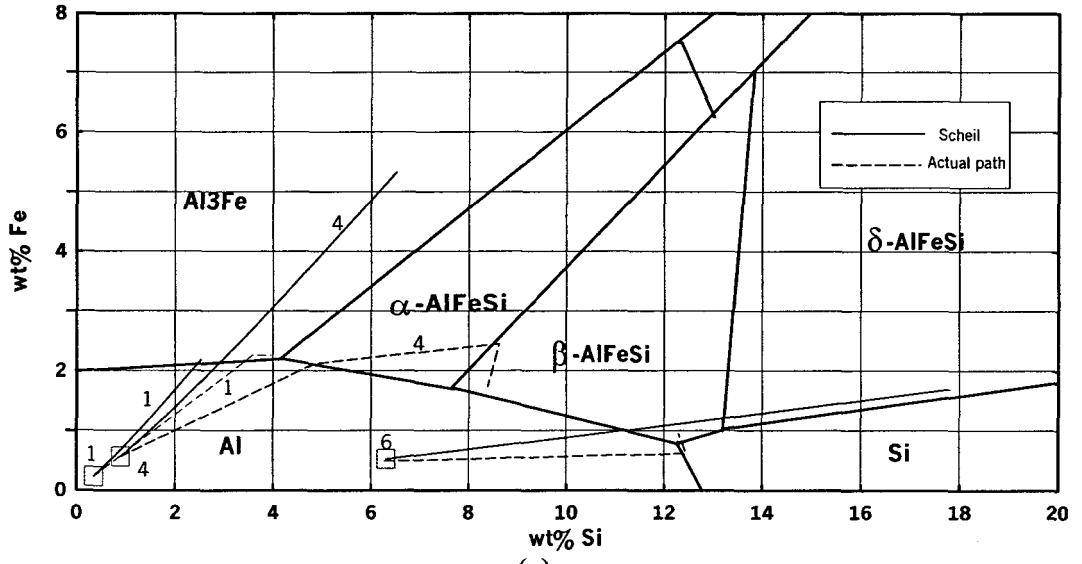

(a)

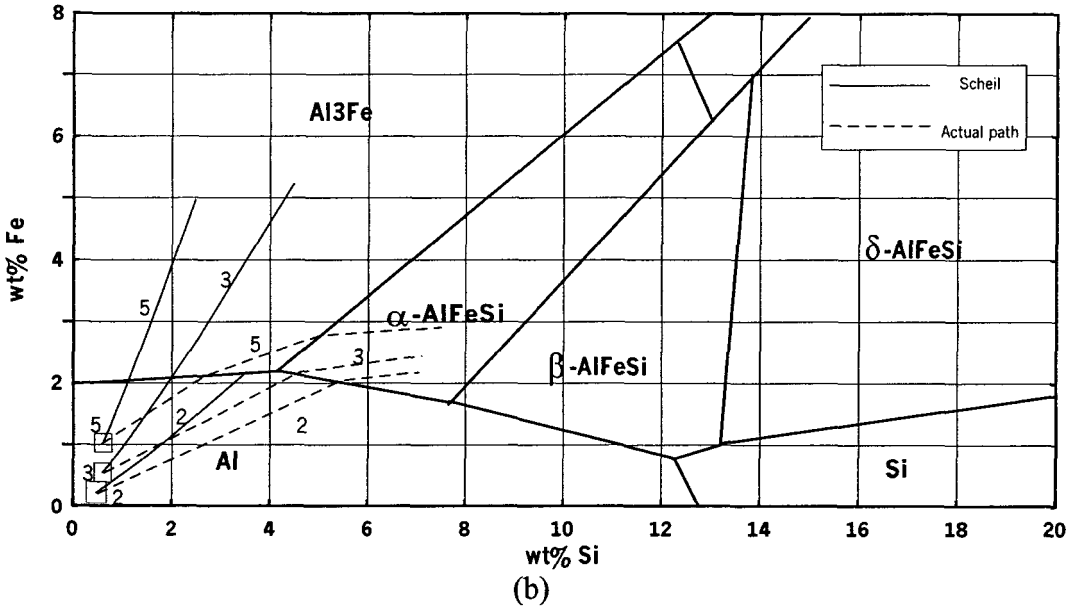

(b)

Figure 44 (a) Solidification paths for alloys 1, 4 and 6 according to the Scheil equation compared with the actual paths. (b) Solidification paths for alloys 2, 3 and 5 according to the Scheil equation compared with the actual paths. The squares marked 1, 2, 3, 4, 5 and 6 denote the respective alloy compositions.

As can be seen from the figure, the Scheil equation gives a poor estimation with regard to iron segregation. It overestimates the iron segregation to the liquid phase, leading to wrong estimations of the solidification sequence. Consequently, the segregation paths for five out of the six alloys are seen to intersect with the boundary line of the binary Al_3Fe phase, suggesting the formation of binary Al-Fe phases. Actually, only alloys 1 and 5 were observed to contain binary phases in their microstructures, as confirmed by the thermal analysis and element distribution mappings that were carried out for these alloys.

The precipitation behavior in the case of the other alloys (2, 3 and 4) was also quite different from that expected from Scheil approximation. In the case of alloy 6, the Scheil segregation path intersected with the boundary line of β-AlFeSi, thus estimating the formation of the β phase first. To the contrary, and according to the actual sequence, the formation of the binary Al-Si eutectic took place before the precipitation of the β-phase.

The assumption made by the Scheil equation that no solid diffusion takes place essentially implies that the calculations are made without taking into consideration any diffusion parameters. Considering the point that no use of the fact that silicon diffuses much more easily in aluminum than iron is made, would explain in general why the actual solidification paths deviate from the Scheil approximations for almost all of the alloys in this study.

In view of these results, trials to calculate solidification paths to account for the departures from the Scheil behavior were made according to the models of Brody and

Flemings[132] and Clyne and Kurz[133]. The first model assumes that the concentration gradient in the solid is constant, while the second one assumes that the concentration gradient in the solid at the end of solidification is very high and, therefore, the driving force for diffusion is also considerably high.

According to Brody and Flemings,[132] the extent of back diffusion taking place in the solid phase during solidification depends on a dimensionless parameter α (given by $\alpha = D_s/RL$),[21,132] where D_s is the solid-diffusion coefficient at the melting point, R (given by L/t_f) is the local interface velocity, L is half of the dendrite arm spacing and t_f is the local solidification time in the unit volume. The value of t_f is not known, so we assume the velocity of the interface R by dividing the radius of the sample by the solidification time, which gives R= 3 cm/ 300 seconds = 10^{-2} cm/s. The average dendrite arm spacing is about 100 microns in our alloys (L = 100/2 = 50 microns).

This parameter, α, can be regarded as describing the ratio of the diffusion boundary layer in the solid to the size of the unit volume, L. The larger the value of α, the more significant the role of solid diffusion in solute redistribution according to the equation:

$$C_L = C_O\left(1-\frac{f_S}{1+\alpha k}\right)^{k-1} \tag{31}$$

where, k is the partition coefficient, f_s is the solid fraction, C_L is the liquid composition, C_o is the initial composition of the alloy. Substituting the corresponding values of D_s and k, taking R = 10^{-2}cm/s and L = 50 microns, results in α values of 2×10^{-7} and 2×10^{-3} for iron and silicon, respectively. The very small values of the parameter α indicate that solid

diffusion (back diffusion) of silicon and iron are negligible according to this model, since the value of (1 + αK) in equation (1) is still equal to unity for both Fe and Si.

Clyne and Kurz[133] approached back diffusion through a spline-smoothing function α′, given by:[68,133]

$$\alpha' = \alpha\left(1 - \exp\left(-\frac{1}{\alpha}\right)\right) - \frac{1}{2}\exp\left(-\frac{1}{2\alpha}\right) \tag{32}$$

This function introduces the effect of back diffusion when α′ replaces α in the segregation equation:

$$C_L = C_O\left(1 - (1 - 2\alpha k) f_S\right)^{(k-1)/(1-2\alpha k)} \tag{33}$$

Substituting our values for the parameters in this relation leads to the Scheil behavior, as the α′ values are reduced to α values for both of iron and silicon. Thus, both of these models essentially revert to the Scheil behavior, as they give much less weight to the effect of solid diffusion. In addition, the low solid-state diffusivities of iron and silicon also play a role. These diffusivities are low because of the substitutional nature of the diffusion of iron and silicon in aluminum (atomic radii of iron and silicon are close to that of aluminum, 1.72, 1.46, and 1.82 Å, respectively.)

Although the theoretical models of Brody and Flemings[132] and Clyne and Kurz[133] cannot account for the deviation from Scheil behavior observed in our study, the experimental results of Potard *et al.*[134] support our proposal that these theoretical models give less weight to the effect of solid state back-diffusion than they should. Potard *et al.*[134] based on their work, reported that impurity distribution in aluminum (including iron) is influenced by its speed of diffusion in the solid phase. They also reported that

iron diffusion is very difficult and that the diffusion coefficient is independent of the Fe concentration.

The departure from the Scheil equation also arises from the assumption that there is no interaction or interference between the diffusing species, so considered for simplifying calculation of the solidification paths. Mondolfo[124] stated that iron does not appreciably affect the diffusion of other metals in aluminum. In contrast to the effect of iron, the activation energy for the diffusion of iron dissolved in aluminum is lowered by silicon: from a value of 1.65 eV for a pure Al-Fe alloy to a value of 1.35 eV with an addition of 0.12% Si. Miki and Warlimont[135] reported that silicon increases the Al_3Fe precipitation rate by lowering the activation energy for iron diffusion in solid aluminum.

These data[124,135] show that the diffusion of silicon is not affected by the presence of iron, whereas the diffusion of iron requires less energy and, therefore, becomes easier, in the presence of silicon. Consequently, the easier diffusion of iron in the solid phase in the presence of silicon would result in a more even distribution of the iron by lowering the concentration gradient in the solid close to the solid/liquid (S/L) interface. This, in turn, would lead to a lower iron concentration on the solid side of the S/L interface. According to the theory of solidification which postulates equilibrium at the S/L interface, this would necessitate a lower iron concentration on the liquid side of the interface, leading to less iron build-up in the liquid phase. If local equilibrium at the S/L interface does not persist, constitutional supercooling of the liquid in front of the interface will result, as is the case in dendritic growth.

In dendritic growth, the prediction of the Scheil equation concerning microsegregation will not be exactly correct,[136] since the assumption of complete mixing in the liquid phase is not valid, as complete homogeneity in the liquid cannot be attained. The diffusion analysis carried out by Allen and Hunt,[136] however, suggests that the deviations from Scheil behavior may often be negligible except at high growth rates. Thus, the formation of a solute-rich layer in the liquid would not be noticeable, since either Scheil (complete mixing in the liquid) or near-Scheil conditions (negligible effect of incomplete mixing in the liquid as encountered in dendritic growth)[136] would persist throughout solidification. The condition of equilibrium (planar or cellular interface) or near-equilibrium (dendritic growth) at the S/L interface coupled with the enhanced diffusion of iron in the solid phase would result in lower iron segregation to the liquid, which would explain the departure of the actual solidification paths from the Scheil approximation shown in Figure 44. A schematic representation of these arguments is depicted in Figure 45.

So far, we have discussed the situation when low cooling rates (which lead to slow growth rates) are dominant and have explained the departure from Scheil behavior that is observed in such cases. Now we shall consider what happens when high cooling rates are dominant, which are found to lead to the formation of Si-rich phases.

At fast growth rates, substantial departures from equilibrium at the S/L interface exist, so that solute concentrations far in excess of the equilibrium solid solubility limit are attained. This phenomenon rules out local equilibrium and the idea that major and minor components act independently at the interface during rapid solidification.[137]

Furthermore, Aziz[137] has demonstrated that the transition from equilibrium solidification to complete solute trapping occurs as the velocity of the S/L interface surpasses the diffusion speed of solute in the liquid. Alloys 3 and 4 have the same iron content (0.55 wt%), and on account of their short solidification times (5.8 s and 3.9 s, respectively), when solidified in the 1-inch diameter metallic mold, both of them achieve the same high iron level in the matrix (~0.05 wt%) which corresponds to the limit of solid solubility. The amount of the entrapped element depends on the alloy content, as is clear from Table 12, which indicates that more iron was entrapped in alloy 5 than in alloys 3 or 4. The entrapped silicon content in the matrix is relatively lower than that of iron, when considering their solid solubilities and the alloy compositions. In alloy 6, which contains 6.3 % Si, the matrix contains 1.43 % Si after rapid cooling. This can also be attributed to the higher diffusion coefficient of silicon in aluminum than that of iron.

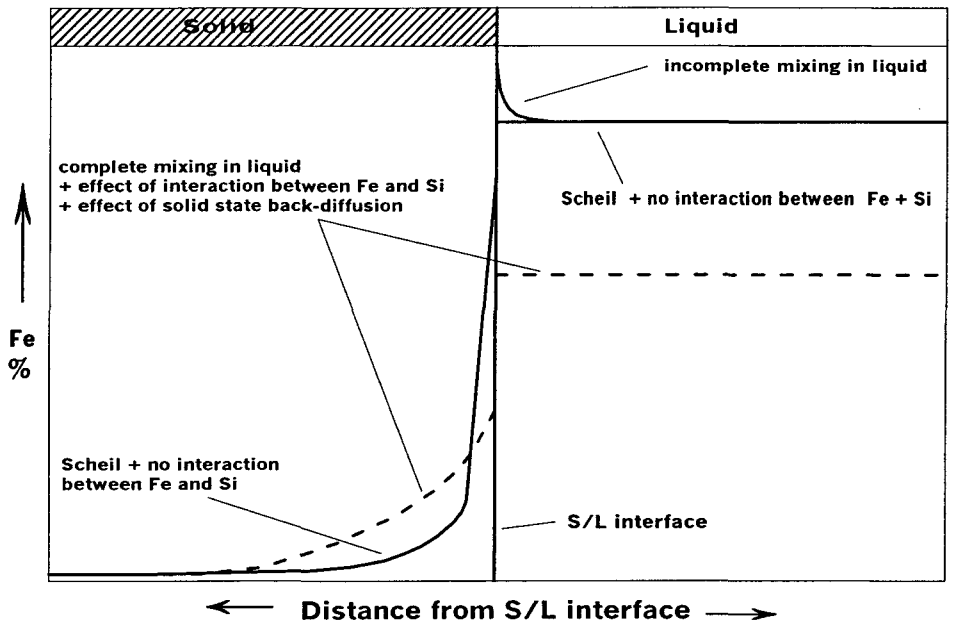

Figure 45 Schematic diagram showing the effect of Fe-Si interaction on the iron distribution between solid and liquid alloy regions.

Silicon solubility in aluminum is reduced with the increase in cooling rate.[124] As a result, the stability of phases changes. Thus, the reduced silicon solubility, coupled with the relatively small Si content entrapped in the solid phase at high cooling rates, can explain the formation of Si-rich phases such as the δ-phase in alloys that lie far outside the boundary of the δ phase region in the equilibrium phase diagram. In addition to the δ-phase, the alloy microstructures observed at high cooling rates were also characterized by the disappearance of the Al-Fe binary phases and the presence of ternary phases. Also, the high level of silicon content entrapped in alloy 5 matrix and, thereby, the depletion of Si in the liquid explains why the δ-phase was not observed in this alloy. On the other hand, at slow cooling rates, apart from the iron and silicon retained in the matrix (0.28 wt% and 0.043 wt%, respectively), the relatively high-Fe and low-Si contents of this alloy available in the interdendritic regions resulted in the formation of Fe-rich phases like binary Al-Fe phases or high-Fe ternary Al-Fe-Si phases such as the α-AlFeSi phase. In contrast to the supersaturation of iron in aluminum (alloy 5), due to the high diffusion coefficient of silicon in aluminum, silicon supersaturation of the matrix did not occur, even at high cooling rates and in the high-Si containing alloys (*viz.*, 6.3 wt% in alloy 6).

4.2.7. Phase Diagram Adjustment

The isothermal section of the ternary phase diagram of Al-Si-Fe at 500°C according to Philips[47] is shown in Figure 46. The 500 °C section is revised here since all the reactions that take place during the solidification of our alloys end at temperatures higher than 500 °C. The positions of the six experimental alloys of our study are marked on the diagram. Comparing these positions with the diagram predictions, it is evident that

the Philips diagram cannot be used to predict the phases observed in alloys 1, 2, 3, 4, and 5 after solidification at slow cooling rates (~0.2 °C/s, graphite mold). Similar observations were previously reported by Dons.[45]

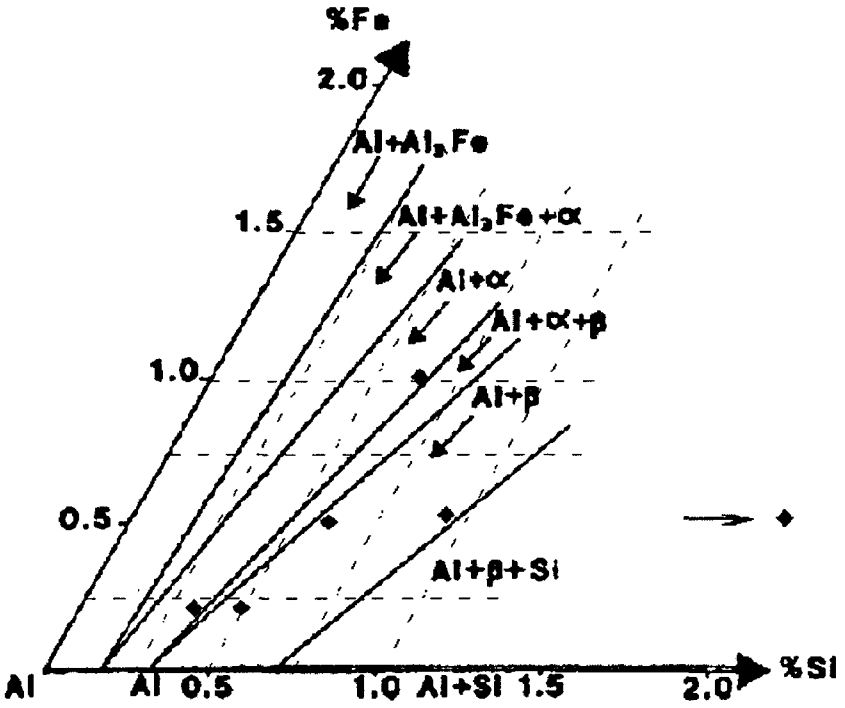

Figure 46 Positions of the experimental alloys (1 to 6) on the 500 °C isothermal section for the Al-corner of the Al-Si-Fe system.

An adjustment to the Philips isothermal section is proposed in Figure 47, where the phase boundaries have been shifted to the higher silicon side so as to conform to our experimental observations. The phase relations that appear in Figure 47 must be considered an approximation for the structure of the alloys after non-equilibrium cooling conditions. Thus, the diagram is termed "metastable section at the solidus temperature".

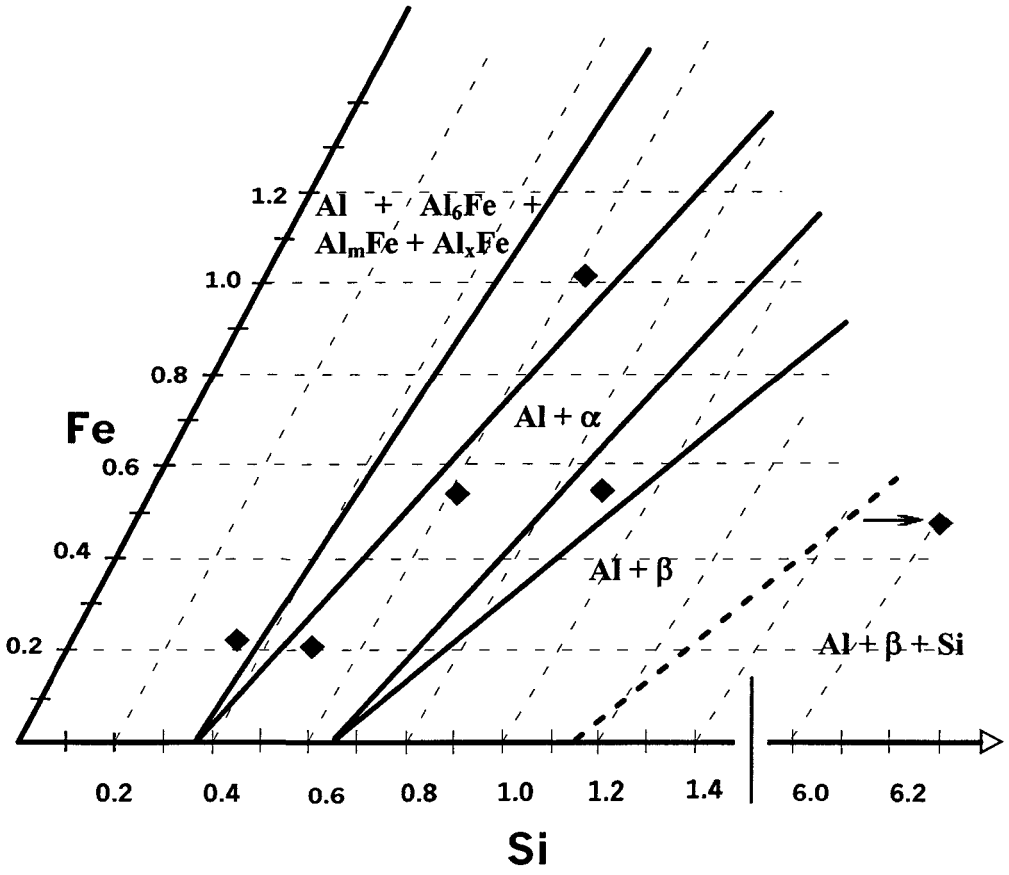

Figure 47 Metastable section at the solidus temperature for the Al-corner of the Al-Si-Fe system. The black squares denote the alloy compositions.

The phase boundary for silicon formation (see the dashed line between Al+β and Al+β+Si fields), however, has been plotted according to the isothermal phase projections published in the ASM Specialty Handbook.[131] These adjustments allow correct phase predictions for all the alloys without exception. In comparison, while the new adjustments respect the sequence of phase fields given in the Philips diagram, each field now exists in a higher silicon range.

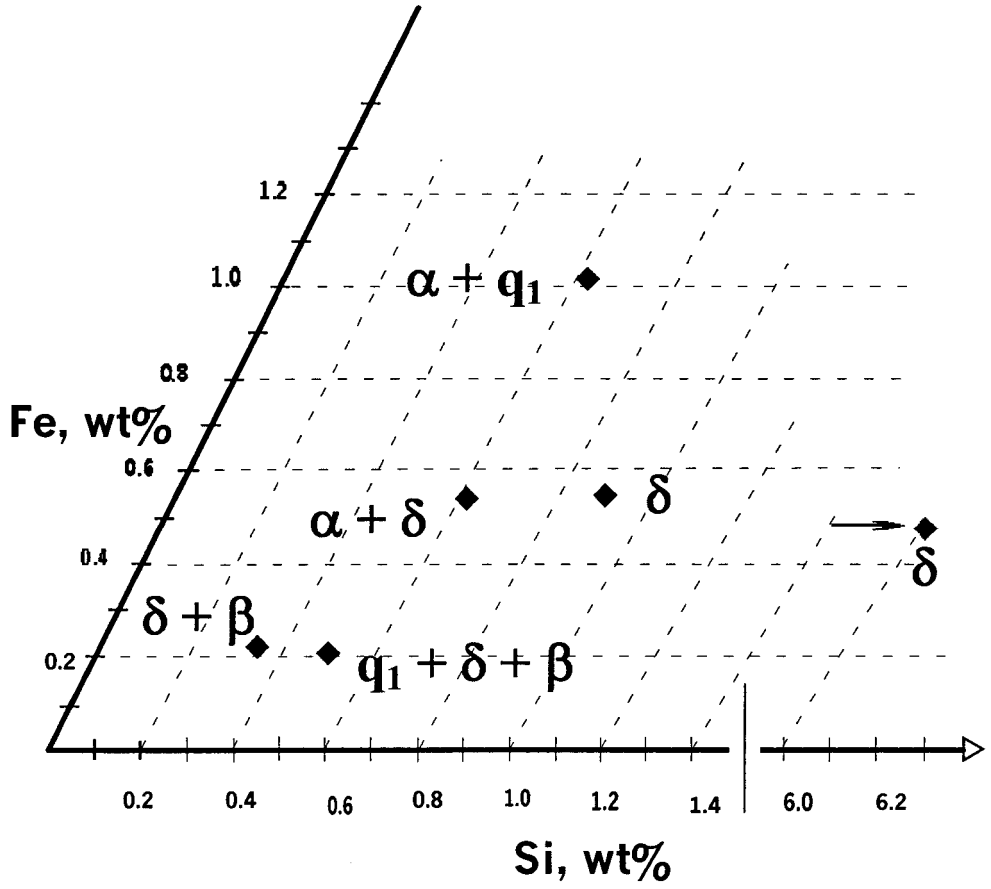

Figure 48 Schematic diagram showing the intermetallic phases observed in the alloys studied, obtained at high cooling rate (10-15 °C/s, metallic mold).

Figure 48 summarizes the intermetallic phases that were observed after solidification in the metallic mold (*i.e.*, at high cooling rate). It is clear that the δ-AlFeSi phase was the phase most frequently identified in the microstructures of these alloys, and became the dominant phase at high silicon contents. The α-AlFeSi phase was encountered in alloys containing relatively high iron and medium silicon levels (*viz.*, alloys with a relatively higher iron content compared to silicon), whereas the β-AlFeSi phase precipitated in the lowest iron content alloys (*i.e.*, in alloys whose Si levels were relatively higher than their Fe levels).

4.3. Summary

Optical microscopy, quantitative metallography, scanning electron microscopy, thermal analysis, micro-probe analysis and wave length dispersive x-ray spectroscopy were used to the study the iron intermetallic phases observed in six experimental dilute aluminum alloys at slow (0.16-0.21 °C/s, graphite mold) and high (10-15 °C/s, metallic mold) cooling rates. The volume fraction of iron intermetallic phases is higher in the former (slowly cooled samples) than the latter case. In both cases the volume fraction increases as the alloying content of iron and silicon increases. However, the iron content is more effective in producing intermetallics than the Si or Fe + Si contents. The density of iron intermetallics is also higher at high cooling rates. In contrast, large-sized intermetallics are obtained at slow cooling rates.

Phase stability changes with cooling rate and alloy composition. Thus, binary Al-Fe phases form only at slow cooling rates at Fe contents that are higher relative to the Si content of the alloy. The β-AlFeSi phase dominates at high silicon levels and slow cooling rate. The α-AlFeSi phase field exists between the binary Al-Fe phases and the β-phase. Rapid cooling stabilizes silicon-rich ternary phases such as the δ-phase and diminishes the binary ones since rapid cooling decreases the solubility of silicon in liquid aluminum and causes entrapment of iron in solid. The δ-AlFeSi phase is the dominating phase at 0.9wt % silicon levels and higher.

Solidification paths representing the segregation of iron and silicon to the liquid were calculated using the Scheil equation. The actual solidification paths did not conform to Scheil behavior, as less iron was observed to have actually segregated to the liquid

than that estimated by the Scheil equation. The reason for this overestimation (of iron content in the liquid) is that the Scheil equation postulates that there is no solid diffusion. Similarly, the theoretical models of Brody and Flemings[132] and Clyne and Kurz[133] cannot explain the departure from Scheil behavior as they give much less weight to solid state back-diffusion. It has been shown qualitatively that the interaction between iron and silicon (which facilitates the diffusion of iron in solid aluminum), together with the suggested role of more effective solid diffusion could account for the departure from Scheil behavior.

An adjusted 500 °C metastable isothermal section of the Al-Si-Fe phase diagram has been proposed. The adjustments were made to the published equilibrium section in order to correctly predict the phases that are observed in this part of the system at slow cooling rates (0.2 °C/s).

CHAPTER 5

ANALYSIS OF THE GAS INJECTION TECHNIQUE USED FOR INCLUSION ADDITIONS TO MOLTEN ALUMINUM ALLOYS

CHAPTER 5

ANALYSIS OF THE GAS INJECTION TECHNIQUE USED FOR INCLUSION ADDITIONS TO MOLTEN ALUMINUM ALLOYS

5.1. Introduction

It is well established that a large variety of inclusions are present in small quantities in commercial aluminum and aluminum alloys. The common types of inclusions in aluminum are: oxides, carbides, borides, nitrides, chlorides, and fluorides.[76,77,78,79] In addition, in aluminum matrix composites, reinforcing phases (particulates or fibers) such as Al_2O_3, graphite, mica, SiO_2, zircon, MgO, sand, TiC, ZrO_2, TiO_2 and lead are commonly used, to provide different characteristics to the composite properties.[80,81,82]

These inclusions and dispersed particles play an important and indispensable role in facilitating the crystal nucleation process of the matrix phase and other primary phases,[83] since the high-energy crystal-liquid interface is partly replaced by an area of low-energy crystal-inclusion interface.[68] Several observations have confirmed the nucleation of different phases on the surface of inclusions. For example, carbon, alumina and silicon carbide particles were shown to be preferential nucleation sites for the primary silicon particles in Al-Si alloys.[84] It was also observed that certain inclusions act as potential nucleation sites for some iron-bearing phases.[10] Other authors[19] reported that the addition of

grain refiner to dilute Al-Fe-Si alloys increased the presence of the θ-$Al_{13}Fe_4$ phase with respect to the Al_6Fe phase in the solidified microstructure. More recently, it was found that in casting practice, if pushed to solute rich interdendritic regions, boride particles could nucleate intermetallics with a well-defined orientation relationship.[85] Porosity was also observed to nucleate heterogeneously on the surface of solid particles.[20,138,139,140,141] Considering how inclusions (or dispersed particles) can affect the structure of engineering alloys, systematic studies of their role during solidification have to be carried out, in order to rule out the possibility of generalization. Such generalizations usually result from single observations and may lead to incorrect conclusions.

To conduct these systematic studies, the solid particles must be introduced into the molten alloys. A suitable technique that allows the introduction of different particles irrespective of their wettability and chemical reactivity must be used. In addition, the incorporation of undesirable surface oxides or gas bubbles has to be minimized, or even avoided, if possible. Among the different techniques of introducing particles in a melt,[142,143,144,145,146,147,148,149,150] the gas injection technique[151,152,153,154,155] is the only one that can avoid cluster formation and surface oxidation of the particles and still satisfy the aforementioned objectives.[87]

The purpose of the work described in this chapter is to develop an analysis of such a gas injection system which promotes the incorporation of relatively small solid particles (2 – 100-μm sized particles) into alloy melts having a high interfacial tension, even at low wettabilities, with particular emphasis on the influence of system parameters on the injection velocity. Such work is believed to be of practical and fundamental importance.

From the practical point of view, the general understanding of the injection process should aid in the design of these systems which have clear benefits in studies directed to understanding how inclusions affect the microstructure. From the fundamental standpoint, the current work extends previous works by addressing the role played by the kinetic energy supplied to particles and the drag energy the liquid exerts on particles during their entry to the liquid.

5.2. Analysis of the Gas Injection Process

5.2.1. Physical Properties of Aluminum Alloys

The aim of this chapter is to analyze and discuss some of the features characterizing the introduction of the inclusion powders into liquid aluminum alloys via an inert gas (argon). The physical properties of liquid aluminum alloys such as density, surface tension and viscosity are of considerable importance in this discussion. For this reason, these properties were determined as accurately as possible from the available literature.

5.2.1.1. Density of Aluminum Alloys

The density of liquid aluminum decreases with an increase in melt temperature. According to the data given by Mondolfo,[124] the density of liquid aluminum is 2.37 g/cm^3 at 750°C (*i.e.*, the processing temperature for injection). However, the value of 2.36 g/cm^3 was calculated from the following relation:[156]

$$\rho_L = 2.385 - 0.00028 \times (t - 660) \tag{34}$$

where ρ_L= the density of aluminum in g/cm^3 at the temperature t, °C.

The effect of alloying elements (only Fe and Si in the present case) is found to be +0.07% and –0.01% for additions of 0.1 wt% Fe and 0.1 wt% Si, respectively.[124] Accordingly, the densities of the six experimental alloys studied lie between 2.36 and 2.38 g/cm^3 at 750 °C. The arithmetic mean value of the six densities is 2.37 g/cm^3, which is the value used in the following analysis.

5.2.1.2. Viscosity of Aluminum Alloys

Two different empirical relations can be used to calculate the viscosity of liquid aluminum according to the temperature of the melt. The first is:[156]

$$\mu_L = 0.1492 \exp(1984.5/T) \tag{35}$$

The second is:[39]

$$\log \mu_L = \frac{720}{T} - 2.68 \tag{36}$$

where μ_L is the viscosity in mNs/m^2 in equation 35 and in poise in equation 36, and T is the melt temperature in degrees Kelvin. Values of 1.04×10^{-2} poise and 2.10×10^{-3} poise were obtained at 750 °C from equation 35 and equation 36, respectively. Equation 36 predicts much lower viscosities since it was developed for the viscosity of a very pure alloy specimen (zone refined specimen). The value of 1.04×10^{-2} poise was considered in the following analysis. Although iron increases the viscosity of aluminum whereas silicon decreases it, their effects were not introduced in the viscosity value because no accurate quantitative data was available from the literature.

5.2.1.3. Surface Tension of Aluminum Alloys

The surface tension of liquid aluminum was interpolated from a diagram in Ref (131) showing the effect of various elements on the surface tension of 99.99% Al in argon at 740 °C. A value of 850 dynes/cm was found as the mean value for the surface tension of our alloy compositions. However, the empirical relation:[156]

$$\gamma_{LG} = 914 - 0.35 \times (t°C - 660) \tag{37}$$

gives a value of 882.5 dynes/cm, since the effects of alloying additions of Fe and Si were not introduced. Surface tension is very sensitive to impurities and atmospheres, and this explains the widely contrasting experimental values reported. Generally, additions that have a lower surface tension reduce the surface tension of aluminum, but ones that have a higher surface tension do not affect the latter appreciably. This is consistent with the Gibbs rule that additions which reduce surface tension segregate to the surface.[124]

5.2.2. The Gas Injection Process

A complete analysis of the gas injection technique is provided in the following sections. The following points are thoroughly analyzed:

(1) The fluidization of solid particles;

(2) The argon bubbles: their sizes, terminal velocities and residence times in the aluminum bath;

(3) The energetics of inclusion transfer from gas to liquid;

(4) The effect of external kinetic energy; and

(5) The addition levels and the system efficiency.

5.2.2.1. Fluidization of Solid Particles

Proper preparation of the inclusion powders in the fluidizer tube before injection is vital for high recovery in the aluminum melt. The fluidization of a bed of solid particles is carried out to achieve certain goals. During the preheating period, fluidization without carryover of particles is used for the purpose of:

(1) drying the bed of particles,

(2) dividing solid particle lumps into finely separated particles, and

(3) heating and maintaining a uniform temperature within the bed.

Low gas velocities are usually used at this stage. The lifting effect of the gas is slight and the system behaves like a well-stirred boiling liquid. The minimum fluidization velocity, u_{mf}, is calculated by means of the simplified equation:[117]

$$u_{mf} = \frac{d_P^2 g(\rho_P - \rho_G)}{1650\mu_G} \tag{38}$$

where, u_{mf} is the minimum fluidization velocity, d_P is the average particle size, g is the gravitational acceleration, ρ_P is the particle density, ρ_G is the gas density and μ_G is the gas viscosity.

Fluidization will be initiated when the pressure drop across the bed is equal to the pressure exerted by the weight of particles on the cross-sectional area of the fluidizer tube.[157] The particles then become rearranged so as to offer less resistance to gas flow and the bed expands. At even higher velocities, the particles become freely suspended in the gas stream. For steady state fluidization, less than one-third of the fluidizer tube should be filled with powder.[87] Otherwise, in deeper beds, when the upper surface of the expanding

bed reaches the joint between the fluidizer and the carrier tubes (see Figure 24), the path of the gas can be blocked before uniform fluidization is initiated.

At the injection stage, fluidization with carryover of particles comes into play (*i.e.*, pneumatic transport of particles). Higher flow rates are used to increase the lifting power of the gas. The mass transfer depends on the depth of the bed and the gas flow pattern. Deep beds can result in low transfer rates since equilibrium can be attained before the gas reaches the upper surface of the bed.[157]

The lower limit of gas velocities in the fluidized bed is determined by the elutriation velocities of various particle sizes (assumed as spheres here for simplicity) contained in the bed. The elutriation velocity is assumed to be the terminal free-fall velocity, u_t, of the particles, and is calculated using a dimensionless particle size, d_P^*, a dimensionless terminal velocity of particles, u_t^*, and the terminal velocity of particles, u_t. These useful terms are defined as follows:[157]

$$d_P^* = d_P\left[\frac{\rho_G(\rho_P - \rho_G)g}{\mu_G^2}\right]^{1/3} \tag{39}$$

$$u_t^* = \left[\frac{18}{(d_P^*)^2} + \frac{0.591}{(d_P^*)^{0.5}}\right]^{-1} \tag{40}$$

$$u_t = u_t^*\left[\frac{\mu_G(\rho_P - \rho_G)g}{\rho_G^2}\right]^{1/3} \tag{41}$$

The set of equations from 38 to 41 can be used as a guide to carry out controllable fluidization processes. For example, the fluidization parameters (gas velocities, flow rates)

for different solids/beds according to these equations are calculated and listed in Table 13. It can be seen that the minimum fluidization velocity is generally very low and the ratio of u_t/u_{mf} is high enough (73 to 91) to allow the use of moderately high operating velocities during the preheating stage. The general rule to avoid or reduce the carryover of particles from the fluidized bed is to keep the gas velocity between u_{mf} and u_t. In calculating u_{mf}, it is advised to use the mean diameter d_P for the size distribution actually present in the bed, whereas for u_t the smallest size of solids present in appreciable quantities in the bed is used.[157]

Table 13 The fluidization parameters for different solid beds.*

Particle Type	d_P, μm	u_{mf}, cm/s	R_{eP} (at u_{mf})	Q_G,** cm^3/s (at u_{mf})	u_t, cm/s	Q_G,** cm^3/s (at u_t)	u_t/u_{mf}
α-Al_2O_3	25	0.014	2.4×10^{-5}	0.22	1.23	19.58	87
α-Al_2O_3	200	1.4	0.024	22.26	102.3	1627	73
SiC	15	0.0061	8.3×10^{-6}	0.096	0.558	8.87	91
TiC	2	0.0002	3×10^{-8}	0.003	0.015	0.244	75
TiB_2	8	0.0025	2×10^{-6}	0.04	0.225	3.57	90

* Fluidization is assumed to be carried out at uniform temperature (500°C), and therefore, argon properties are $\rho_G = 0.00063$ g/cm^3 and $\mu_G = 0.0007$ g/cm·s.
** Q_G is the gas flow rate.

The elutriation velocity, u_t, for hypothetical large particles such as 200 μm-sized α-Al_2O_3 particles is very high, 102.3 cm/s (see Table 13). To reach this velocity using the current fluidizer tube (diameter of 4.5 cm), the gas flow rate should be 1627 cm^3/s, which is extremely high and would severely destabilize the liquid metal during injection. Consequently, such large particles cannot be introduced into the liquid metal using the current injection system. Other techniques such as the vortex technique[147,149,150] may be

more suitable for large particles. Therefore, it should be understood that the dimensions of the injection system put certain limits on its usability.

To facilitate the calculation of the minimum gas flow rate required for the transport of particles from the fluidizer tube, a chart based on a fluidizer tube of cross-sectional area of 1 cm^2 as shown in Figure 49 is employed. The chart is created using the method of Haider and Levenspiel[158] developed for the calculation of u_t. To calculate the flow rate required for the elutriation of a certain powder, one must first calculate the dimensionless particle size, d_P^*, from equation 39, then use the chart in Figure 49 to determine the elutriation flow rate, Q_G, by matching or interpolating the particle density with the plotted curves. Multiplying the gas flow rate by the cross-sectional area of the fluidizer tube will give the required quantity.

As mentioned earlier, during the injection stage the operating velocity should be higher than u_t. However, a suitable design for the fluidizer tube should be considered, that will be capable of providing high enough gas velocity for the pneumatic transport of particles, and at the same time large enough to exceed the minimum injection velocity without the use of excessive flow rates, which can result in lowering the percentage of particles being retained in the melt (to be discussed elsewhere in this chapter).

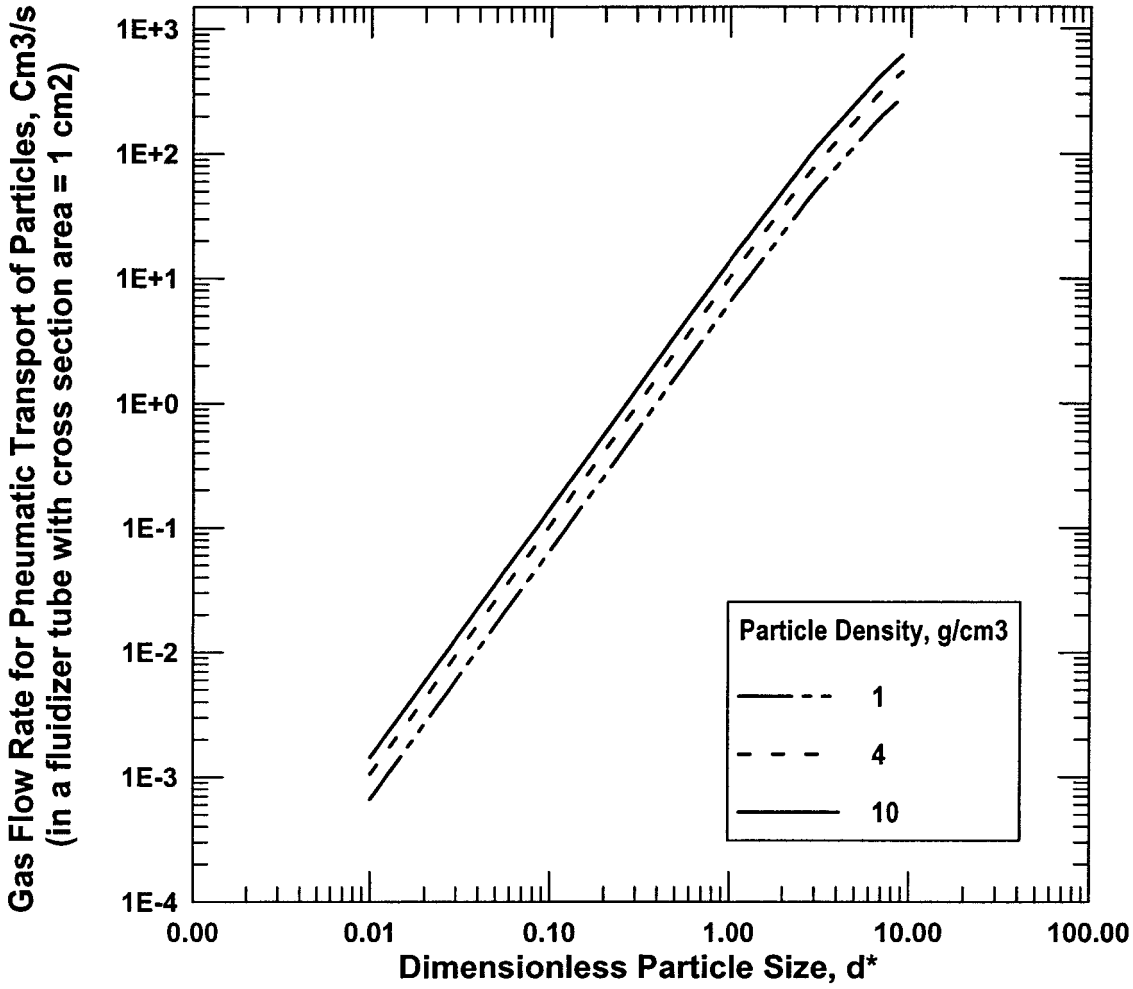

Figure 49 Chart for determining the min. gas flow rate required for pneumatic transport of particles from the fluidizer tube (for the particle sizes and densities of interest in the present study). The chart is drawn for high temperature fluidization (500 °C) using the argon as a carrier gas, (after Haider and Levenspiel[158]).

5.2.2.2. Argon Bubble Size

Since the argon is injected via a quartz nozzle, the argon bubble size can be estimated based on two simple equations. The first is:[94,117]

$$\frac{\pi}{6} d_b^3 g(\rho_L - \rho_G) = \pi d_o \gamma_{LG} , \qquad \text{for } R_{eG} < 500 \tag{42}$$

and the second is:[159]

$$d_b = 0.54(Q_G d_o^{0.5})^{0.289} \tag{43}$$

where d_b is the diameter of the bubble, g in the gravitational acceleration, d_o is the internal diameter of the orifice (tip of the nozzle), ρ_L is the density of the liquid, ρ_G is the density of the gas in the bubble, γ_{LG} is the surface tension of the liquid, R_{eG} is the Reynolds number of the gas at the orifice, and Q_G is the gas flow rate. Both of these equations were developed empirically for bubble sizes during gas injection in stationary liquids. Therefore, the use of these equations is expected to result in calculated bubble sizes which are larger than the actual size, if applied to non-stationary liquids.

At 750 °C, the mean density of the aluminum melts used in this study is 2.370 g/cm^3 and the surface tension is 850 dynes/cm. The total gas flow rate was usually kept between 10 and 25 ft^3/hr (80 and 200 cm^3/s). However, the value of 10 ft^3/hr is adopted for the calculations (it is equivalent to 4.8 l/min. or 80 cm^3/s). The orifice diameter is 0.2 cm. Equation 42 gives the bubble diameter as 3.53 cm, whereas equation 43 gives a bubble diameter of 1.52 cm. We took the bubble size to be 1.52 cm and neglected the value of 3.53 cm since no accurate physical properties for argon are available at 750 °C and hence R_{eG} cannot be calculated. The volume of one bubble is, then, 1.84 cm^3 at the standard

conditions of temperature and pressure (the effect of metallostatic pressure on the bubble was not introduced here for the sake of simplicity, as it varies depending on the depth of the bubble at different points of its path through the metal bath). If we assume that the bubble is completely heated to the melt temperature (750 °C) on emerging from the orifice, its volume would be 6.31 cm^3 and its diameter would be 2.29 cm. Thus, the flow rate of 80 cm^3/s under standard conditions should become 274.3 cm^3/s inside the melt, as a result of gas expansion. Then, the number of bubbles liberated in the melt per second is 43, with a total surface area of 177 cm^2.

Assuming 1 cm^3 of 10-μm particle size powder with a true density of 3 g/cm^3, the powder particles can cover a projected area of 0.15 m^2 or 1500 cm^2. About 90 g (or ~30 cm^3) of powder are used for injection in every experiment. Knowing that the total time of injection is 90 min, inclusions with a total projected area of 8.5 cm^2 are encapsulated every second in the argon bubbles. If we assume that the powder particles do not stick together and they evenly cover the internal surface of the bubble, approximately 5% of the bubble surface area is covered with inclusions. This value gives an estimation of the amount of particles injected relative to the gas flow rate, and thus, is a good measure of the efficiency of the injection process. As only half of the charged powders were usually injected during experiments, the percentage of the particle-covered bubble surface is actually much lower than 5%. The very low percentage of bubble-surface-occupation by inclusions shows the low efficiency of the current inclusion addition system, and is the reason for use of a prolonged injection time (~ 90 min).

5.2.2.3. Terminal Velocity and Residence Time of Argon Bubbles

The terminal velocity (steady state velocity) of a bubble in a liquid is a classical problem of fluid dynamics. Using Stokes' law, the terminal velocity of the bubble (V_t) is calculated according to the equation:[160]

$$V_t = \frac{d_b^2 g(\rho_L - \rho_G)}{18\mu_L} \tag{44}$$

Knowing that the argon density is 0.000511 g/cm^3 at 750 °C (calculated using the ideal gases law), and applying the parameter values of aluminum, a parametric curve (dependent on the bubble diameter) was drawn for the terminal velocity of argon bubbles. The head of liquid metal is about 11 cm above the orifice (see Figure 25). If we assume that the bubble travels directly in a straight line from the orifice to the surface, the minimum residence time of the bubble can then be calculated. Figure 50 shows these parametric curves. It can be seen that an argon bubble of 2.3 cm diameter (corresponding to the size of bubbles at 750 °C, as calculated previously) has a terminal velocity of about 660 cm/s and accordingly will rest 0.017 s in the melt before escaping to the atmosphere, whereas a bubble of 0.23 cm diameter should travel at a speed of 6.6 cm/s and thus stay about 1.7 s in the melt. The longer the residence time of the bubble in the melt, the greater the probability that the molten aluminum will wet the suspended inclusions, since the time factor enhances the wettability between solid particles and molten metal.[161,162] Conditions of vigorous stirring provide longer residence times, and consequently, play a role in the process of particle transfer from gas to liquid.

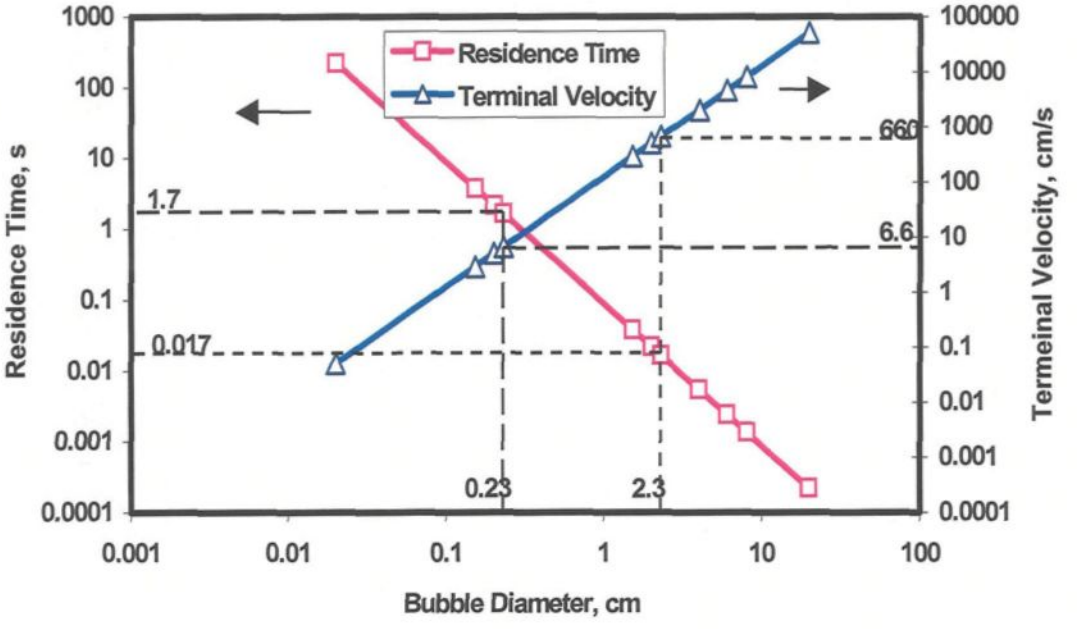

Figure 50 Residence time and terminal velocity of argon bubbles in aluminum bath of 11 cm depth kept at 750 °C.

5.2.2.4. Energetics of Inclusion Transfer from Gas to Liquid

The introduction of inclusion particles into metals and alloys includes three major stages: (1) the transfer of the solid particles from gas to liquid, (2) interaction of particles with the liquid and particle-particle interactions, and (3) the transfer of particles from liquid to solid. The magnitude of forces involved in the first and third stages is related to the wetting characteristics of the solid particles by the liquid metal. During the second stage, particles may develop a bonding with the liquid phase and/or agglomerate. The agglomeration kinetics for particles in a liquid are mainly affected by the nature of inclusions (*i.e.*, sticking coefficients) and the nature of the liquid flow during alloy processing (*i.e.*, the presence of flow separation regions).[175]

5.2.2.4.1. Theoretical Models

In order to predict particle transfer behavior during gas-to-liquid transfer, approximate thermodynamic and kinetic models have been proposed. The engulfment of particles by an electromagnetic stirred melt was studied by Ilegbusi and Szekely.[88] The balance among surface forces, the force of gravity, and the drag force exerted on the particles was established; hence, the melt velocity was estimated based on the system variables. The Neumann's[89] thermodynamic approach ignores the effect of buoyancy forces acting on the particle. According to this model, the total free energy change involved in the transfer of a particle from gas to liquid must be negative for spontaneous transfer. In comparison, the work of Rohatgi and coworkers[90,91] is more exact as it takes into account the buoyancy forces. The spontaneity of particle transfer can be predicted from an analysis of the energy path involved.

According to Rohatgi *et al.*,[91] the total thermodynamic force for isothermal introduction of particles in the melt is given by the change in free energy (ΔE_T), which comprises the surface energy (ΔE_S), buoyancy energy (ΔE_B), and potential energy (ΔE_P):

$$\Delta E_T = \Delta E_S + \Delta E_B + \Delta E_P \tag{45}$$

The following theoretical analysis of particle transfer across the gas–liquid interface is carried out based on this model,[91] taking into consideration the assumptions that all inclusions are spherical particles, the surface of particle is smooth and homogeneous and the contact angle is constant. The first assumption leads to a minimization of the surface energy factor since the sphere has the minimum surface area to volume ratio amongst all regular and irregular solid bodies. In addition, the melt is assumed stationary, *i.e.*, the drag

force resulting from the liquid motion was not introduced into the total balance of forces acting on the particle, since the calculation of the liquid velocity (magnitude and direction) in the current mechanical stirring system may be quite difficult.[88]

For a spherical particle, the energy components (in equation 45) can be written as:

$$\Delta E_S(\omega) = \pi r^2 \gamma_{LG}\left[-\sin^2\omega + 2\cos\theta(\cos\omega - 1)\right] \quad (46)$$

$$\Delta E_B(\omega) = \frac{\rho_L g \pi r^4}{48}\left[108\ln\left(\frac{2+\cos\omega}{3}\right) + 39 - 40\cos\omega + \cos^4\omega\right] \quad (47)$$

$$\Delta E_p(\omega) = -\frac{4}{3}\pi r^4 \rho_P g(1-\cos\omega) \quad (48)$$

where, ω is the immersion angle which represents the path of immersion ($\omega = 180^\circ$ for complete immersion), r is the particle radius, γ_{LG} is the liquid surface tension, θ is the wetting (contact) angle, ρ_L is the liquid density, and ρ_P is the particle density. Some of these terms are defined in Figure 51.

The wetting angle,[161] particle size and inclusion density for different inclusion/aluminum systems are listed in Table 14. The total energy required for particle transfer from gas to liquid aluminum alloy is calculated for several particles, namely, α-Al_2O_3, SiC, TiC, and TiB_2 following the above model.[91] In addition to the actual particle sizes, calculations were carried out for a hypothetical 200-μm α-Al_2O_3 particle in order to evaluate the effect of particle size since the particle size has a significant effect on both the buoyancy and potential energies due to the "r^4" term that appears in equations 47 and 48. The total energy changes obtained for the different systems as a function of the immersion angle ω are shown in Figure 52.

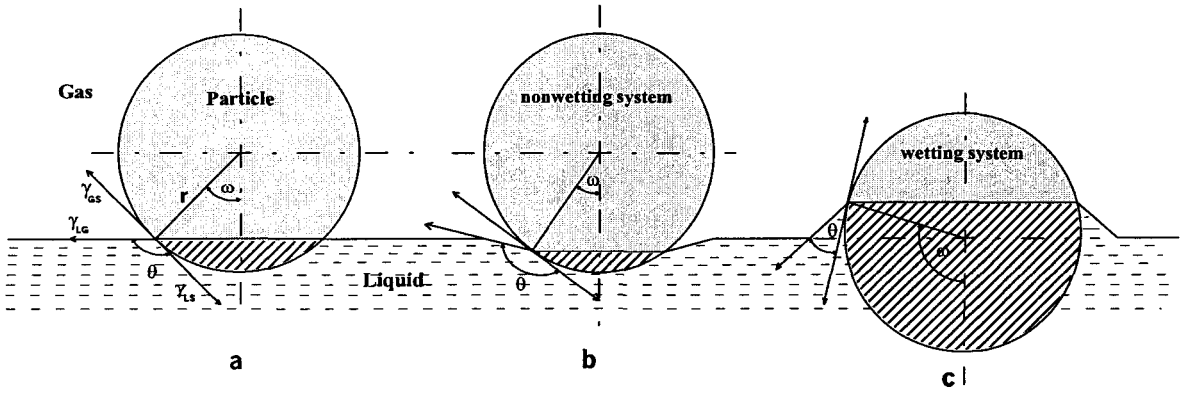

Figure 51 Immersional wetting of spherical particles. The definition of the wetting angle (θ) and the immersion angle (ω) are shown in (a), the effect of wetting angle on the immersion angle are shown in (b) for high wetting angle ($\theta > 90^{o}$) and (c) for low wetting angle ($\theta < 90^{o}$), for a light particle in equilibrium condition (in the absence of external kinetic energy).

Table 14 Wetting parameters of different particles with aluminum melt.[161]

Inclusion	Particle Radius, μm	Density, g/cm^3	Wetting Angle with Al, deg.	Temperature, °C	Vacuum, torr*
α-Al_2O_3	10	3.98	120°	750	10^{-5}
α-Al_2O_3	100	3.98	120°	750	10^{-5}
α-Al_2O_3	10	3.98	90°	900	2-6 x10^{-5}
SiC	7.5	3.2	154°	900	2.7 x 10^{-4}
SiC	7.5	3.2	40°	1100	2.7 x 10^{-4}
TiC	1	4.93	148°	900	---
TiB_2	3	4.52	37°	900	2.7 x 10^{-7}
TiB_2	3	4.52	98°	900	---

* 1 torr equals 1/760 atmospheric pressure.

As can be seen, all ΔE_T *vs.* ω plots showed minima in ΔE_T for almost all the systems. The immersion angles corresponding to the minima in ΔE_T characterize the state of particles on the surface of the liquid and indicate that, at equilibrium conditions, the particle is partly immersed (valid for both wetting and nonwetting systems). For spherical

particles, the characterizing immersion angle is inversely proportional to the wetting angle as shown in Figure 51.

It is well established that successful entry of solid particles into molten metal requires that the melt should wet the solid phase, *i.e.*, $\theta < 90^{o}$. When the particle/melt system experiences poor wetting ($\theta > 90^{o}$), external forces must by applied to facilitate particle incorporation. The role of an external force (or energy) is to overcome the energy barrier opposing particle penetration at the gas-liquid interface. For example, the behavior of TiB_2 particles shows a spontaneous entry into aluminum melts when θ is 37^{o} ($< 90^{o}$). On the other hand, a slight increase in ΔE_T has to be overcome for complete immersion (at ω = $150 - 180^{o}$) when θ is 98^{o} ($> 90^{o}$), Figure 52. A better example of the effect of wetting angle is observed in the case of the SiC particles which have the same size but different wetting angles due to different melt temperatures. The total energy change sharply increases when poor wettability conditions prevail, *i.e.*, for a wetting angle of 154^{o} with the aluminum melt at 900 °C. As a result, an external energy of $\sim 0.005 \times 10^{-7}$ J must be supplied to overcome the energy barrier for immersion. Spontaneous entry of SiC takes place when the particles possess good wettability ($\theta = 40^{o}$) with the melt at 1100 °C.

For the nonwetting α-Al_2O_3/Al system ($\theta = 120^{o}$) and particle sizes of 20-μm and 200-μm, the total energy change is negative for half of the immersion path, ω between 0 and 90^{o}, indicating that there is no energy barrier for the immersion of half of the particle. To complete the immersion of such particles, an external energy should be applied to enable the entire particle to penetrate the gas–liquid interface. The order of this energy is a

function of particle size: it is ~0.005 × 10^{-7} J for the 20-μm sized particle and ~0.5 × 10^{-7} J for the 200-μm sized particle. The ratio of the two energies is 1/100 which is equal to the square of the ratio of their particle sizes. It is obvious that the controlling factor here is the surface energy since it depends on "r^2" (equation 46). For very small particles (TiC particles of 2 μm size, wetting angle of 148°) a very small energy barrier, 0.0001 × 10^{-7} J, has to be overcome for complete immersion (Figure 52 (b)).

From the above analysis using the Rohatgi model,[90,91] it can be concluded that finer particles of nonwetted inclusions can be introduced into the liquid metal much more easily than large particles.

When the α-Al_2O_3 particles undergo some wetting (*i.e.*, θ = 90°) as a result of melt superheating, particle incorporation becomes easier, *i.e.*, ΔE_T is negative at almost all values of ω, owing to the improved melt-particle wetting (Figure 52 (b)). Russell *et al.*[161] have reported that the wetting angle is a function of liquid temperature. This fact can be utilized to improve the efficiency of the injection process.

For wetting systems like SiC/Al at 1000°C and TiB_2/Al at 900°C with nearly the same wetting angles (40° and 37°, respectively), the particle size has a considerable effect. The larger the particle, the easier it transfers to the liquid. The total energy change (algebraic value) for the immersion of TiB_2 (10 μm size) is seen to be higher than that of SiC (10-20 μm), at all values of ω. Therefore, the entry of SiC particles into the aluminum melt is more favorable than that of TiB_2 particles at their respective melt temperature conditions.

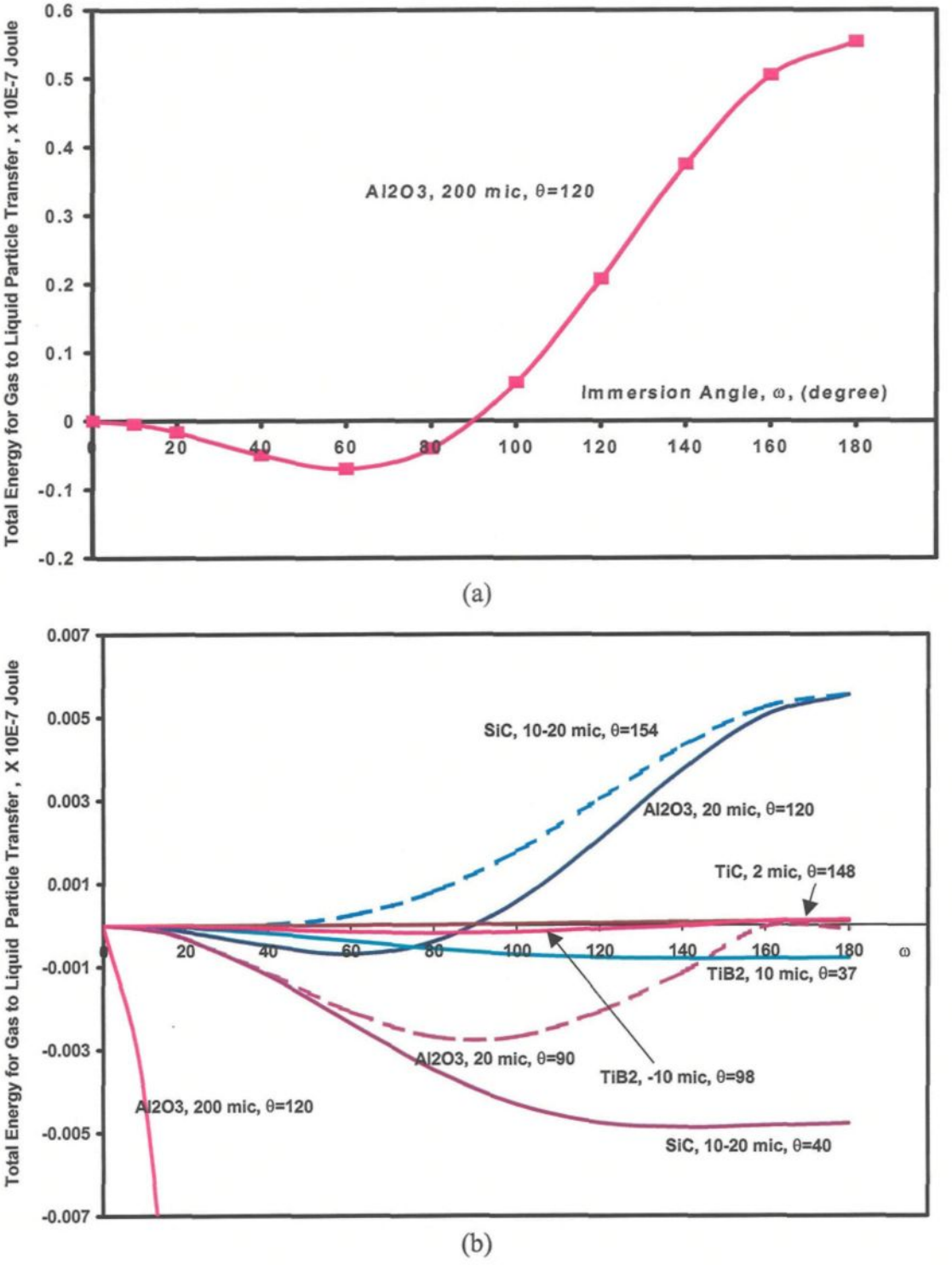

Figure 52 The total energy change for immersion of spherical inclusion particles in molten aluminum.

The ratios of the magnitudes of different energy components applying on solid particles during their transfer from argon to liquid aluminum are plotted in Figure 53 for two different particles. The magnitudes of $\Delta E_B/\Delta E_S$, $\Delta E_P/\Delta E_S$, and $(\Delta E_B + \Delta E_p)/\Delta E_S$ are shown as functions of the immersion angle, ω, for (a) an α-Al_2O_3 particle (200 μm, θ = 120°), and (b) a SiC particle (15 μm, θ = 40°). The first conclusion that can be drawn from these plots is that, from the energetics point of view, the interfacial energy is the decisive factor in the particle immersion process for the range of particle sizes explored in this work, since $\Delta E_S >> \Delta E_B$ and ΔE_p. In other words, almost all of the total energy barrier for particle immersion is due to the surface energy factor ($\Delta E_T \approx \Delta E_S$). The second conclusion is that the particle size has a significant effect on the energy component ratios. Larger particles experience higher magnitudes of ΔE_B and ΔE_P relative to ΔE_S than do smaller ones. Thus, the ratio of $(\Delta E_B + \Delta E_p)/\Delta E_S$ for a 200-μm sized particle of α-Al_2O_3 is in the order of 10^{-3}, whereas it is 10^{-6} for the 15-μm SiC particle. Consequently, excessively large particles should have an appreciable magnitude of $\Delta E_B + \Delta E_p$ that can override the ΔE_S effect.[91]

So far, the theoretical model of Rohatgi has been used to study the energetics of solid particle transfer across the argon/aluminum interface. The model evaluates the process depending on the inherent properties of gas, solid particle and liquid. No external variables, such as the kinetic energy of particles or the effect of external forces, have been taken into consideration in the analysis. Consideration of the external forces will enrich the treatment of the problem and shift the analysis from being purely theoretical to a more practical one.

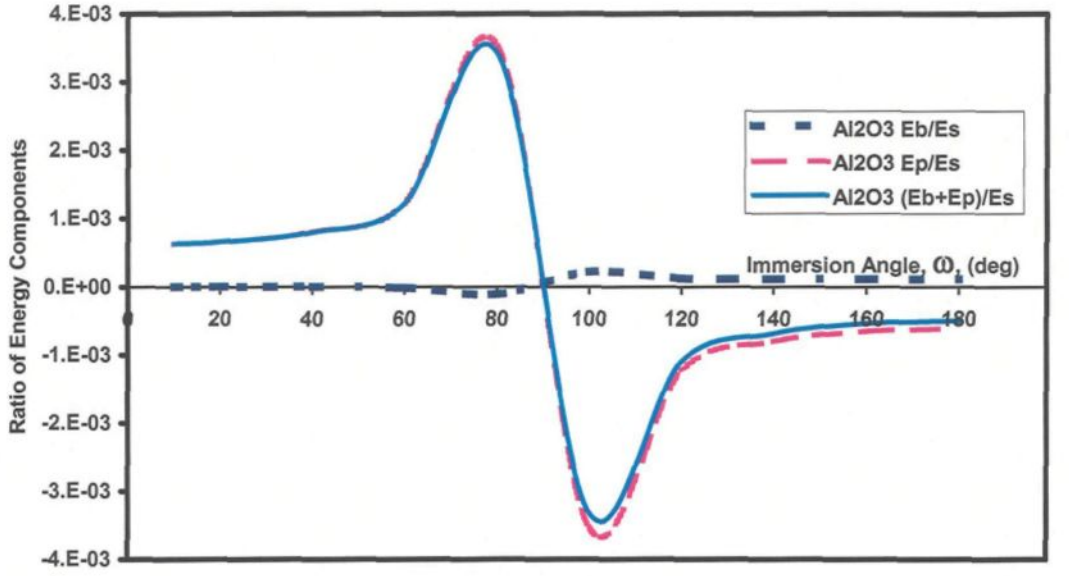

(a)

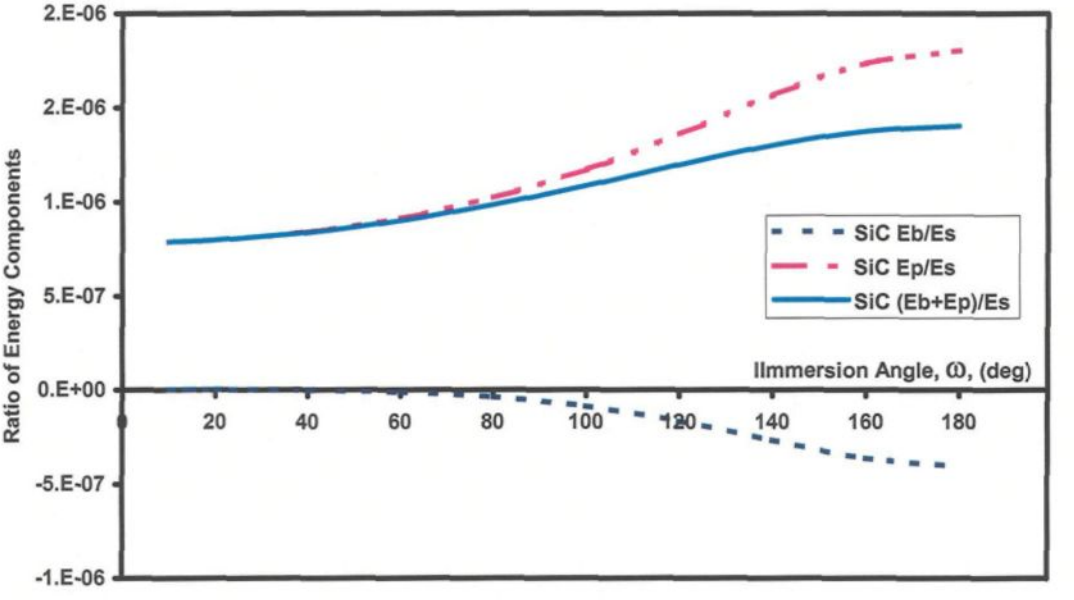

(b)

Figure 53 Ratios of the magnitude of different energy components that apply on (a) a 200 μm α-Al_2O_3 particle, $\theta = 120^{\circ}$, and (b) a 15 μm SiC particle, $\theta = 40^{\circ}$, during their transfer from argon to liquid aluminum.

5.2.2.4.2. Effect of External Kinetic Energy

During the injection experiments, particles carried in the argon flow are supplied with kinetic energy to facilitate their successful penetration of the gas-liquid interface. The magnitude of this energy should be high enough to overcome the energy barrier of incorporation for nonwetting particles. The kinetic energy of a body of mass m moving at velocity u is defined as:

$$E_K = \frac{1}{2}mu^2 \tag{49}$$

Heavier particles, either because of their density or their size, can gain more kinetic energy than light particles. For instance, if a spherical particle with a true density of 3 g/cm^3 and a diameter of 10 μm is used in our injection experiments (nozzle orifice diameter of 0.2 cm and average argon flow rate of 80 cm^3/s), it should gain a kinetic energy of 0.041 $\times 10^{-7}$ J. This energy (one order of magnitude higher than the energy required for particles of the same size (see Figure 52)) is high enough to enable the particle to overcome the energy barrier for entry into the liquid. On the other hand, for the hypothetical 200-μm sized α-Al_2O_3 particle, the kinetic energy is 54×10^{-7} J, whereas the energy barrier is only 0.5×10^{-7} J. In fact, suspended solid particles in a high-speed flowing gas can gain kinetic energy high enough to overcome even the yield strength of engineering alloys. For example, in the sand blasting technique, the sand grains cause permanent indents on the surface of metals. In our experiments, the difference between the kinetic energy supplied and the total energy barrier for these particles is surprisingly high, implying that even

nonwetted solid particles can be incorporated easily into the aluminum melt, which is in contrast to the classical observations.

A proper treatment of the problem must also include the effect of the kinetic force that the liquid exerts on the particle during its entry (*i.e.*, the drag force). This force is defined as:[160]

$$D = \frac{1}{2} A \rho_L u^2 f \tag{50}$$

where, A is the area of the solid as seen in projection along the direction of motion, u is the particle velocity, and f is the friction factor -a dimensionless constant that represents the effect of friction between the solid particle and the liquid. The constant f is usually referred to as the drag coefficient rather than friction factor in most texts on fluid mechanics. The value of f is 0.5 for rounded objects like spheres.

The energy that must be supplied to overcome the exerted fluid drag for complete immersion of a spherical particle (for an immersion distance of 2r from the liquid surface) is then given by:

$$E_D = 2rD = \frac{1}{2} \pi \rho_L r^3 u^2 \tag{51}$$

The drag energy, E_D, is a second component to be added to the energy barrier (ΔE_T) and should be balanced, as well, to allow for the incorporation of a solid particle. As previously demonstrated, for the range of particle sizes of interest in this study, the interfacial energy (ΔE_S) not only forms the major part of the energy barrier (ΔE_T) but often

comprises it entirely, *i.e.*, ($\Delta E_S \approx \Delta E_T$). Thus, a particle can penetrate the gas-liquid interface if an energy balance of the following form prevails during injection:

$$E_K = \Delta E_S + E_D \tag{52}$$

Substituting E_K, ΔE_S and E_D from equations 46, 49, and 51 in equation 52, setting $\omega = 180$ (for complete immersion) and solving for "u" gives the minimum injection velocity, u_{mi}, to enable complete incorporation of solid particles into the liquid:

$$u_{mi} = \left[\frac{-12\gamma_{LG}\cos\theta}{r(2\rho_P - 1.5\rho_L)}\right]^{1/2} \tag{53}$$

This equation is valid for nonwetting systems ($90^\circ < \theta \leq 180^\circ$) when $\rho_P > 0.75\rho_L$. It also draws attention to a point that has been previously addressed in the literature[163]. That is, even in wetting systems ($\theta < 90^\circ$) when the density of the solid particle is smaller than that of the liquid (*i.e.*, $\rho_P < 0.75\rho_L$ for spherical particles), the use of an external kinetic energy is indispensable for complete particle incorporation.

The effects of particle size and density on the minimum injection velocity are shown in Figure 54. It clear that the larger the particle and/or the heavier the particle type, the smaller the required injection velocity. Therefore, it is difficult to introduce small particles into the melt, especially when the particle density is low. Based on these results, the injection process can be explained as follows: during the journey through the bath, the buoyant forces slow down the gas bubble with little effect on the velocity of the suspended particles. This is because according to equation 50 the magnitude of the drag force, the slowed argon bubble applies on the particles is very small, given the very low density of

argon at the process temperature. The particles attached to the liquid surface of the bubble hit the liquid at the gas velocity. Subsequently, a larger particle, having sufficient kinetic energy, is able to penetrate the gas-liquid interface and enter the bath, a smaller particle cannot penetrate the barrier and is carried to the surface of the bath.

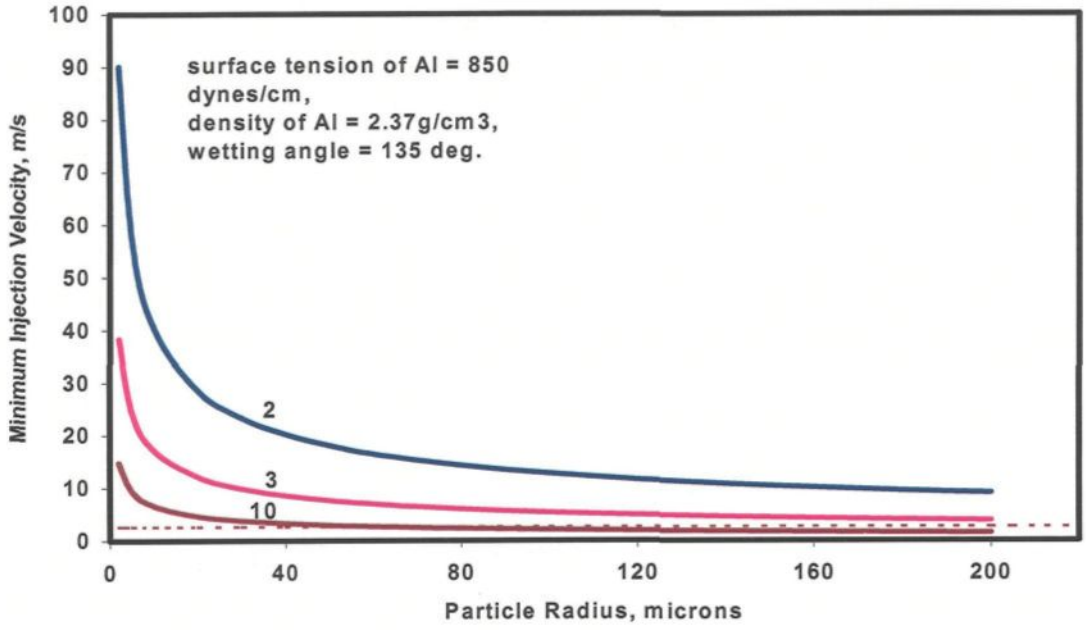

Figure 54 Effect of particle radius (r) and particle density (ρ_P) on the minimum injection velocity (Eq. 53). The horizontal dashed line represents the maximum tangential speed in the aluminum melt. The 2, 3, and 10 symbols denote the particle density, ρ_P, of 2, 3, and 10 g/cm^3, respectively.

It is worth noting here that, although the energy barrier according to the Rohatgi model (see Figure 52) for large particles is much higher than those for finer particles, due to the effect of the external kinetic energy, large particles are easier to incorporate into the liquid phase. The conclusion is that the kinetic energy supplied to the inclusion particles is the dominating factor for the determination of the ease of particle transfer from gas to liquid, and therefore the injection process which is more able to provide a higher kinetic

energy to the solid particles can be used to incorporate smaller particles than the vortex method can. However, very small particles, *i.e.,* submicron-sized particles, would require very high kinetic energy for incorporation and, therefore, extremely high injection velocities are needed. Very small particles cannot be added to liquid metals using the injection system.

Figure 55 illustrates the effects of liquid density and wetting angle on the minimum injection velocity. A high wetting angle (*viz.,* poor wettability) between the solid particle and the liquid necessitates a higher injection velocity. The density of the liquid has a similar effect, *i.e.*, solid particle incorporation in heavier liquids requires higher injection velocities.

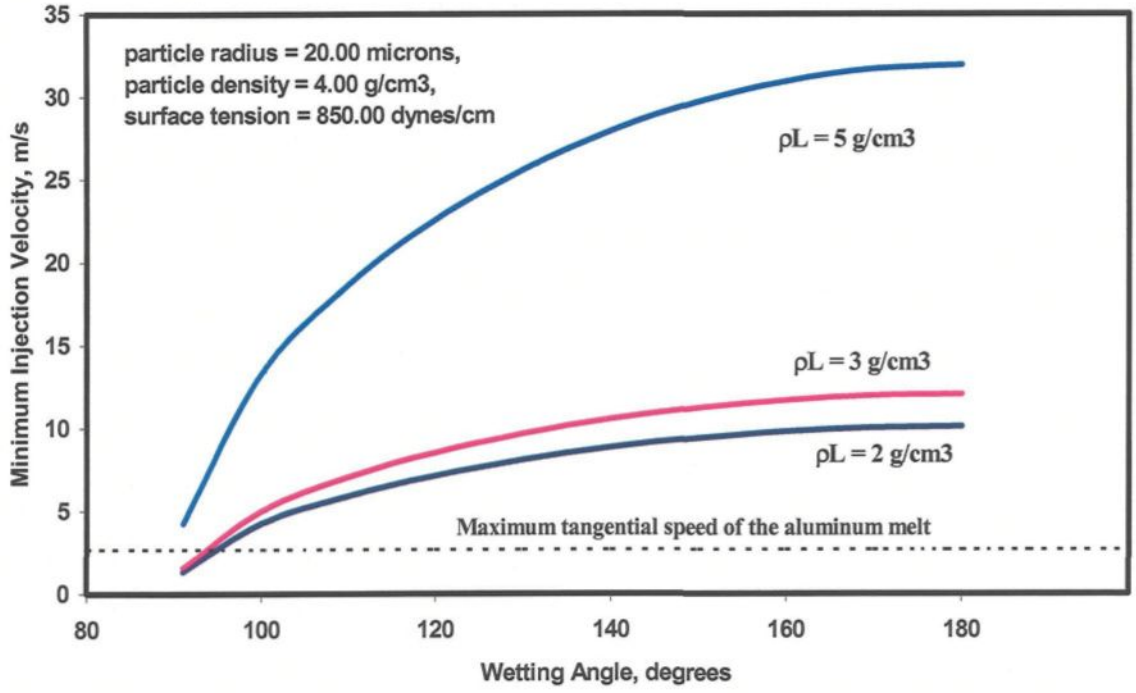

Figure 55 Effect of liquid density (ρ_L) and wetting angle (θ) on the minimum injection velocity (Eq. 53).

Under certain conditions of particle and liquid properties (*i.e.*, large and heavy particles and/or light liquid), the tangential speed of the liquid metal (see the horizontal dashed lines in Figure 54 and Figure 55) near the crucible walls is sufficient for the incorporation of solid particles. The incorporation of solids under these conditions is similar to particle addition using the vortex technique.

The concept of minimum injection velocity has been used previously in the literature. The minimum injection velocity to overcome the energy barrier (ΔE_T) according to Rohatgi[91] is:

$$u_{mi} = \left[1.92gr\left(\frac{\rho_L}{\rho_P} - 2.09\right) - \frac{6\gamma_{LG}}{r\rho_P}\cos\theta \right]^{1/2} \tag{54}$$

The minimum injection velocity required to overcome the dominant energy barrier (surface tension) can be easily derived from the analysis of O'Malley *et al.*[153] as:

$$u_{mi} = \left[\frac{4\gamma_{LG}}{r\rho_P}\cos\theta \right]^{1/2} \tag{55}$$

The injection velocities calculated from equation 55 (O'Malley *et al.*[153]) are lower than the velocities obtained from equation 54, since a factor of 6 appears in the surface energy component in equation 54, while it appears as 4 in equation 55.

Calculations of the minimum injection velocity, according to equations 53 and 54, for different particles that form nonwetting systems with aluminum (see Table 14) are given in Table 15. Equation 54 gives lower injection velocities than those given by equation 53. In fact, the omission of the important effect of fluid drag forces and the

inclusion of the negligible effects of buoyancy and potential energies in the derivation of equation 54 render it more complex and less accurate for the purpose of predicting the injection velocity.

The importance of equation 53 comes also from its simplicity and the fact that it can be used to calculate the minimum injection velocity required for particle incorporation using the physical properties of the system, since "$\gamma_{LG}\cos\theta$" can be calculated from sessile drop experiments or other techniques.[164,165] However, in performing the injection experiments, the particle incorporations were observed at higher injection velocities than those predicted by the model. Most of the successful injection experiments were carried out at 1.2 to 2 times of the minimum injection velocities calculated using equation 53. The most difficult to incorporate were the small poorly wettable TiC particles (~ 2-μm sized), while the easiest was the TiB_2 particles having the best wettability (37° at 900 °C) with liquid aluminum among the other particle types. Thus, inspection of the injection velocities given in Figure 54, Figure 55 and Table 15 should be only instructive in terms of studying the effect of physical properties of the particle and liquid on injection velocities, rather than using these velocities in practice.

Table 15 Minimum injection velocities for nonwetted particles with aluminum according to equations 53 and 54.

Inclusion	r, μm	$u_{mi.}$, m/s (Eq. 54)	$u_{mi.}$, m/s (Eq. 53)
α-Al_2O_3	100	2.53	3.40
α-Al_2O_3	10	8.00	10.76
SiC	7.5	13.82	20.72
TiC	1	29.62	37.04
TiB_2	3	7.23	9.29

The accuracy of calculating the injection velocity using equation 53 is highly influenced by the lack of, and the uncertainty in, wetting angles and the interfacial energies, $\gamma_{LG}\cos\theta$, reported in the literature, and also by the simplifications and assumptions of the model. It must be emphasized that sessile drop experiments and the other wettability data are usually measured under high vacuum environments. In injection experiments, the use of high purity argon (*viz.*, min. of 99.998% Ar) can produce an oxygen partial pressure as low as 1.6-5 torr depending on whether the impurity content is water vapor or oxygen, respectively. Also, at this level of argon purity, the oxidation of aluminum cannot be avoided at the melt temperature used (~750 °C),[166] and thus, the wettability should be poorer than that used in our calculations (*i.e.*, the wetting angles are higher).

It is assumed that the particles are spheres. This can affect the surface energy component and the assumption of a stationary liquid that ignores the effect of the drag force resulting from the liquid motion, leading to an increase or decrease in the required injection velocity, depending on the direction of the flow field surrounding the injection nozzle. If we recall these assumptions and simplifications, it should be obvious that equation 53 sets an approximate value for the minimum injection velocity required.

5.2.2.5. Addition Levels and System Efficiency

The volume fraction of retained particles that can be achieved by the gas injection technique is relatively low. According to a previous study,[87] up to 2 vol pct of particles could be added easily using the current apparatus, however, it was commented that the addition levels were limited by the size of the unit and process dynamics. About 1 vol pct

of different particles were added in the current work. In fact, the addition (or recovery) levels in the injection process should be simply viewed as the resultant of two factors acting in opposition to each other: the injection factor and cleaning factor. The injection factor introduces the solid particles into the melt, whereas the cleaning factor has the same effect that argon plays in the degassing process, where oxides and inclusion particles can be floated up to the melt surface as they come in contact with the argon bubbles.[167,168] Consequently, the addition levels of 1 or 2 vol pct must be regarded as being the balance levels between the injected and the floated quantities of particles.

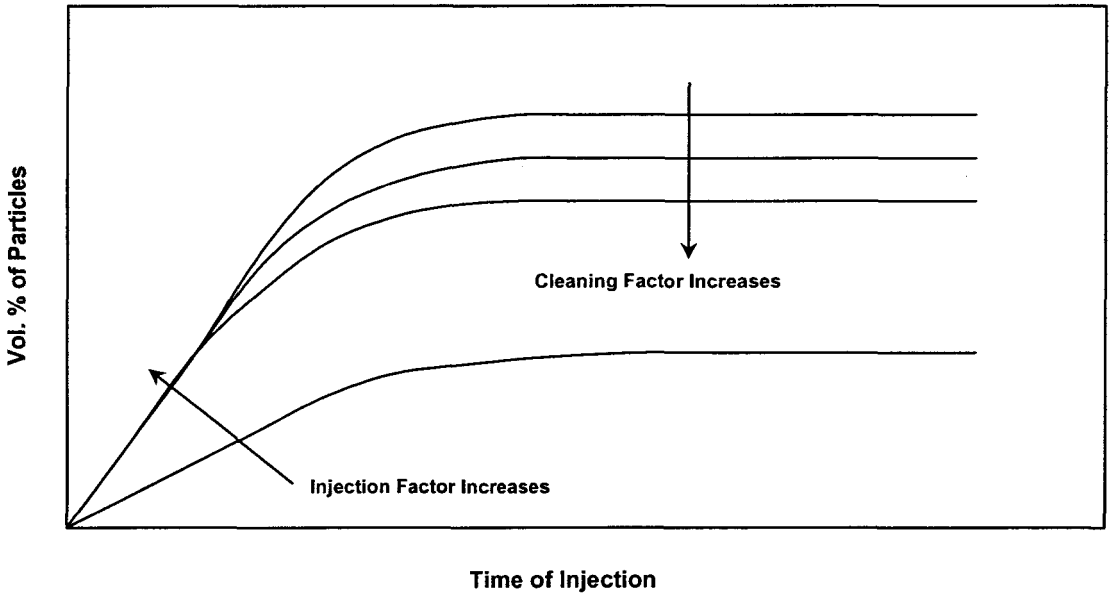

Figure 56 Schematic diagram showing the effect of cleaning and injection factors on the final addition level attained (expressed as volume fraction of inclusions retained in the liquid).

The efficiency of the gas injection system can be assessed by the addition level that can be achieved in a certain period of time. The system efficiency can be discussed based on the relative contribution of the injection and the cleaning factors to the percentage of

particles finally retained in the alloy. To increase the efficiency of the system, the injection factor must be maximized and the cleaning factor must be minimized. We conjecture that the population of solid particles in the melt continuously increases with the time of injection until equilibrium between the particles injected and the particles removed is attained, as depicted in the schematic diagram of Figure 56 .

Reducing the argon flow rate can reduce the cleaning effect. On the other hand, the relative weight of the injection factor can be increased if a considerable amount of particles is injected with a high enough velocity. The amount of particles that can escape from the fluidizer tube and pass into the melt depends directly on the argon velocity in the fluidizer tube and hence (from the direct application of the continuity equation) on the argon flow rate and the fluidizer tube dimensions. A low argon flow rate can lift a large amount of particles if a short narrow fluidizer tube is used. However, the fluidization of the particle bed must also be taken into consideration in the design of the fluidizer tube.

The injection velocity increases if a smaller diameter injection nozzle is used. For a flow rate of 10 ft^3/hr (80 cm^3/s), injection velocities of 6.36 and 25.46 m/s can be obtained if 0.4 and 0.2-cm diameter nozzles are used, respectively. The minimum required injection velocity depends on the physical properties of the system as governed by equation 53 (see also Figure 54 and Figure 55).

The capability of the injection technique is very much restricted by the size of the particles. Very small (< 1-μm) or very large (> 100-μm) particles cannot be introduced into the liquid metal using the present injection technique for several reasons related to the

capability of providing the appropriate flow rates for injection and fluidization without destabilizing the metal bath.

The argon flow rate, the dimensions of the fluidizer tube, and the diameter of the injection nozzle are the main parameters that influence the efficiency of the gas injection system. Adjustments for a low gas flow rate, a small diameter of the fluidizer tube, and a small diameter of the injection nozzle to obtain gas velocities higher than the minimum injection velocity can assure successful experiments.

5.3. Examples of Injected Inclusions

Different solid particles - irrespective of their wettability or chemical stability - were successfully incorporated into the melts of the aluminum alloys studied, using the gas injection technique. Figure 57 shows examples of the α-Al_2O_3 particles introduced into alloys 1 and 6. It is clear that the α-Al_2O_3 particles are driven to the interdendritic regions and they act as active nucleation sites for the iron intermetallic phases and the silicon. In contrast to α-Al_2O_3, γ-Al_2O_3 particles serve as potential nucleants for the α-Al phase as shown in Figure 58.

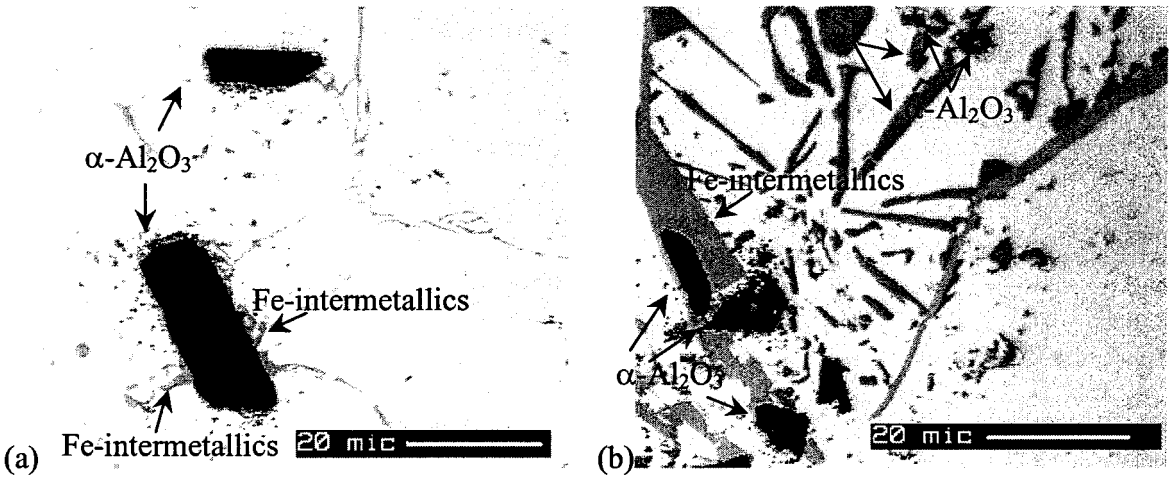

Figure 57 Microstructures of α-Al_2O_3 injected alloys showing (a) nucleation of intermetallics on the surface of α-Al_2O_3 particles in alloy 1, (b) nucleation of intermetallics and silicon on the surface of α-Al_2O_3 particles in alloy 6.

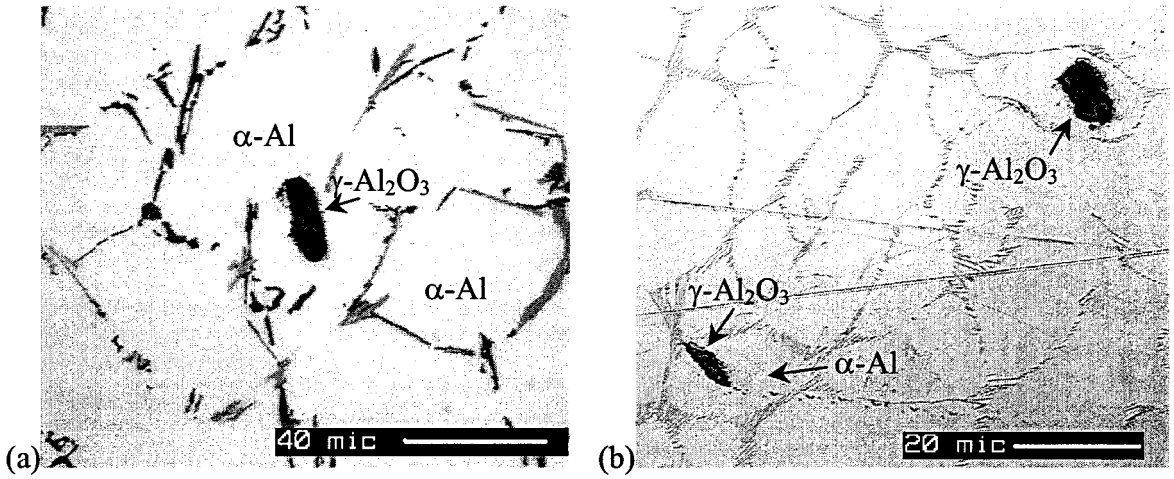

Figure 58 The high potency of γ-Al_2O_3 to nucleate α-Al at high cooling rates, 12 °C/s: (a) alloy 6, and (b) alloy 5.

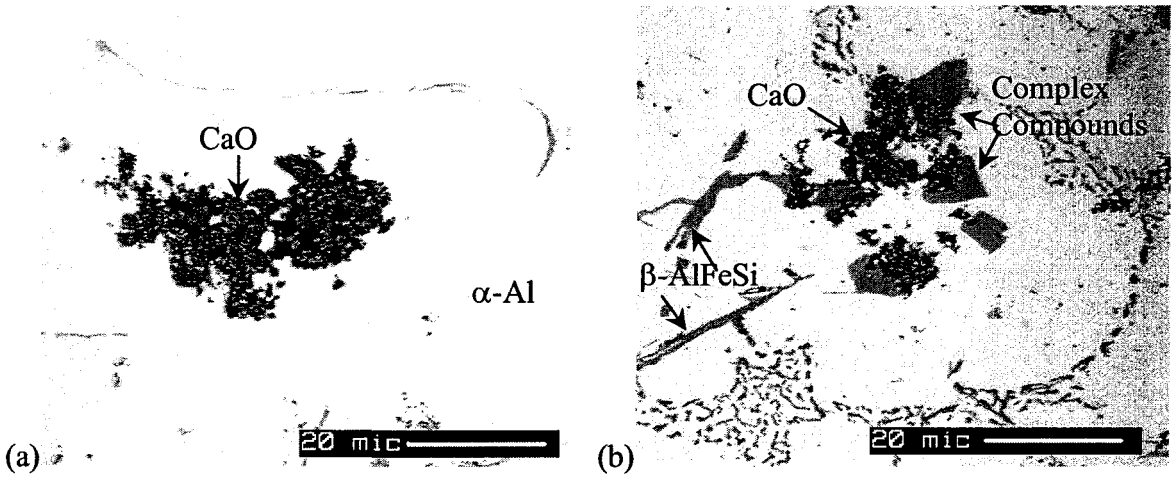

Figure 59 Effect of CaO particles on the microstructure of Al alloys (a) nucleation of α-Al on surface of CaO particles in alloy 1, (b) CaO react with Al-Si melt of alloy 6 and form complex compounds.

Figure 59 (a, b) shows CaO particles inside the α-Al phase, suggesting a favorable nucleation of Al on the surface of CaO. It is evident that CaO has a high sticking coefficient and, thus, a tendency to form clusters in the liquid aluminum alloy. As a result, CaO inclusions should be easily removed from Al-melts. The CaO particles react with aluminum oxide to form a compound ($CaAl_2O_4$) that resembles the spinel phase ($MgAl_2O_4$). Only in the high Si-containing alloys, did the CaO particles react with the Al and Si forming a polygonal block-like phase (Figure 59(b)). The formation of the plate-like β-AlFeSi phase is also observed in areas away from the CaO particles. The stoichiometry of the polygonal phase is roughly $Al_{2.7}Si_{1.7}CaO_{0.7}$. A comparison of the composition of this phase with that of several complex intermetallic compounds of calcium[169] observed in Al-Si alloys revealed no matches, implying that it is a new phase.

The role of titanium diboride in the grain refining process is the subject of different interpretations.[103,170,171,172,173,71,174] Very valuable and important information on this role are

obtained using the current injection technique. As Figure 60 shows, most of the TiB_2 particles are located within grain centers rather than the grain boundaries. This observation strongly confirms the role of TiB_2 as a grain refiner for the α-Al phase in the alloy compositions studied.

It is also very clear from Figure 60 that the TiB_2 particles have a high sticking coefficient and, thus, tend to form clusters in the molten metal during the liquid stage. The fading phenomenon related to grain refiners in alloy melts can therefore be attributed to the agglomeration and settling of the TiB_2 particles as was previously interpreted by some authors.[170,174] In contrast to this interpretation, Lee and Basaran[173] observed a time-related fade phenomenon when the melt was subjected to convection during solidification, and concluded that the distribution of TiB_2 particles in the melt has little or no effect on grain refinement. The micrographs in Figure 60, show that there is no contradiction between these two interpretations.[170,173,174] When they come in contact with each other, the TiB_2 particles form clusters. Melt convection helps the TiB_2 particles to come in contact and, consequently, agglomerate. The formation of TiB_2 clusters during the injection experiments, where vigorous convection took place, is evidence of the effect of melt convection in TiB_2 agglomeration (Figure 60).

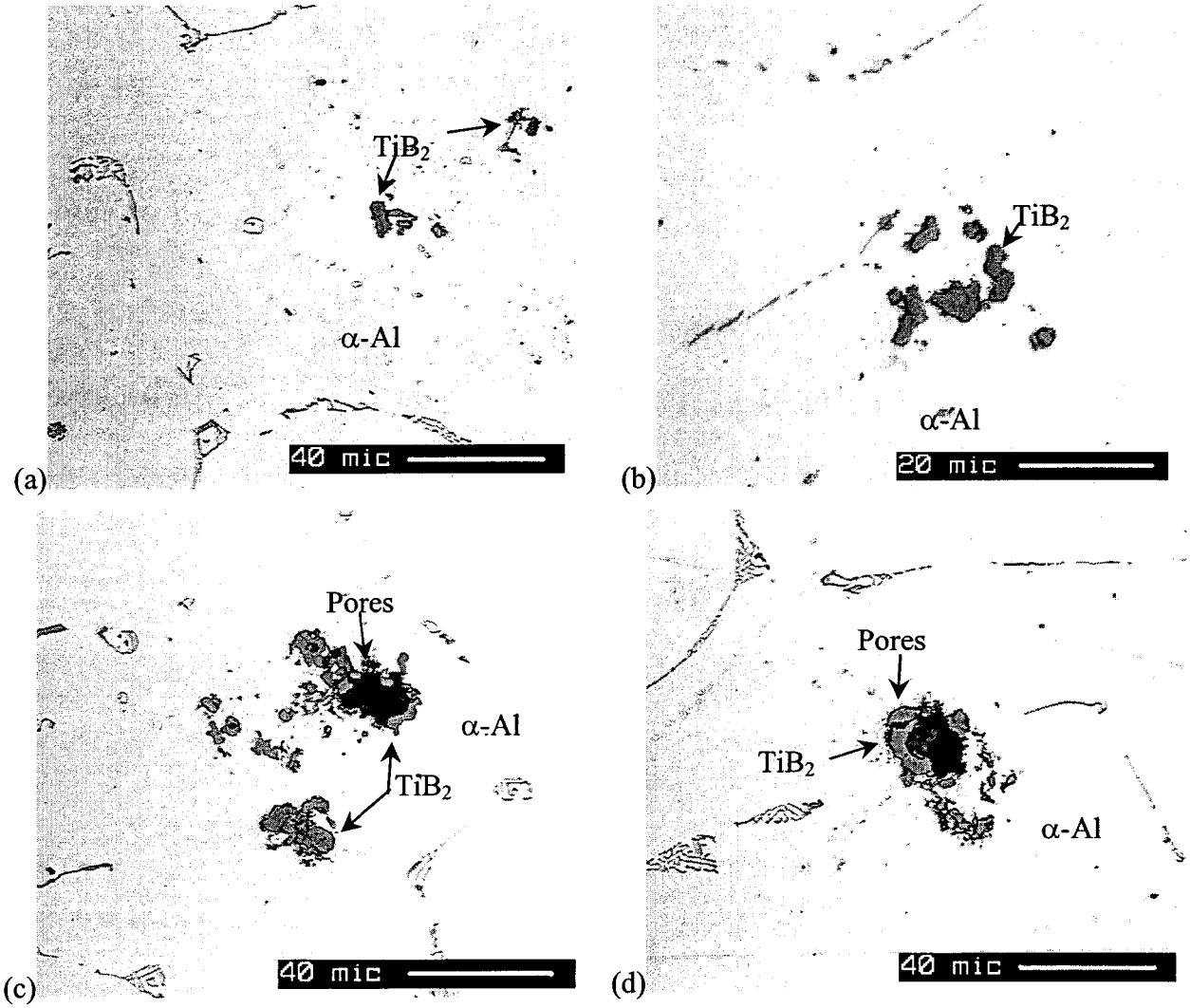

Figure 60 Optical micrographs showing; (a, b) nucleation of α-Al on the surface of TiB_2; (c, d) morphology of pores that form on the surface of the TiB_2 particles.

Another important factor in the agglomeration process is the nature of the particles. According to Marechal *et al.*,[175] the nature of the solid particles (*viz.*, their sticking coefficient) plays an important role in their agglomeration process in recirculating flows. This implies that for sticky particles (with high sticking coefficient), the longer the recirculation (stirring) period of the liquid phase, the greater the opportunity for the solid particles to coalesce and form clusters.

It can be noticed also from Figure 60 (c, d) that the shape of pores in contact with the TiB_2 particles is nearly round. This observation is in good agreement with the conclusions of Boudreault *et al.*,[176] who reported that pores in grain-refined aluminum alloy samples can be distinguished from those in the Sr-modified samples by their almost spherical shape, while, in non-grain-refined alloys, the pores are able to expand along the grain boundaries, and are thus more irregular in morphology.

5.4. Summary

The gas injection technique was used successfully to introduce different types of oxides, carbides and borides into liquid aluminum alloys. Several examples for the effect of these particles on the microstructure in aluminum alloys were given to show the significance of using the technique in conducting systematic studies of this type. The fluidization process of the solid particles has been described and discussed in detail. Equations and diagrams that put certain limits on the gas velocity and flow rates are given as guides for controllable fluidization. In addition, theoretical analysis of the gas injection process, including the energetics of particle transfer from gas to liquid and the effect of kinetic forces, was used to derive a theoretical relation for the minimum injection velocity required for successful particle transfer from gas to liquid.

The capability of the injection technique was found to be very much restricted by the size of the particles. Very small (< 1-μm) or large (> 100-μm) particles cannot be introduced into the liquid metal using the present injection technique for several reasons

related to the capability of providing the appropriate gas flow rates for injection and fluidization without destabilizing the metal bath.

While the discussion given in this work is closely related to the present gas injection system, the considerations, particularly those related to the effect of physical properties of the liquid and the solid particles on the process of particle transfer from gas to liquid are quite general and should be applicable to any injection process. The general practical considerations are: (i) the wettability has a great influence on the incorporation of particles, poor wettability necessitating higher injection velocities, (ii) the density of the liquid has an important effect on particle incorporation into metal baths, with solid particle incorporation in heavier liquids being more difficult and requiring higher injection velocities, and (iii) the larger and/or heavier the particle type, the smaller the injection velocity required.

CHAPTER 6

INFLUENCE OF INCLUSIONS ON THE NUCLEATION OF THE α-Al PHASE IN Al-Si-Fe ALLOYS

CHAPTER 6

INFLUENCE OF INCLUSIONS ON THE NUCLEATION OF THE α-Al PHASE IN Al-Si-Fe ALLOYS

6.1. Introduction

It is well established that a large variety of inclusions are present in small quantities in commercial aluminum and aluminum alloys. The common types of inclusions in aluminum are: oxides, carbides, borides, nitrides, chlorides, and fluorides.[76,77,78,79] In addition, reinforcements (particulates or fibers) such as Al_2O_3, graphite, mica, SiO_2, zircon, MgO, sand, TiC, ZrO_2, TiO_2 and lead are commonly used in aluminum matrix composites to provide different characteristics to the composite properties.[80,81,82]

These inclusions and dispersed particles play an important and indispensable role in facilitating the crystal nucleation process of the matrix phase and other primary phases,[83] since the high-energy crystal/liquid interface is partly replaced by an area of low-energy crystal/inclusion interface.[68] However, the inclusions differ in their nucleation catalytic activity.

According to Maxwell and Hellawell,[69] the ranking of the various particles in terms of their catalytic activity for nucleation is not an absolute measure that can be reflected in the degree of grain refining unless the cooling rate and alloy constitution are also

considered. In addition, it has been reported that not all the particles in a given nucleant addition are of equal effectiveness in promoting grain refining.[95] Therefore, a certain proportion of the added grain refiner particles is responsible for nucleation and for the final grain size attained.

However, a major part of the examination of nucleation in aluminum-base alloys has been spent in the study of the mechanisms of grain refinement, specifically, those associated with the presence of Al_3Ti, TiB_2, AlB_2, TiC, *etc*, where the focus was on rationalizing the usefulness of such grain refiners.[71] The actual evidence that any one nucleant may be associated with the initiation of solidification is not extensive. It does not seem to have been clearly established that these proposed nucleants operate singly or in association with each other or other nucleants already existing in the melt. Furthermore, the role and the catalytic activity of the inclusions in the solid nucleation process have not been systematically studied.

The inoculation experiments discussed in this chapter are part of the overall investigation that aims to evaluate the effect of different inclusions on the solidification microstructure of Al-Si-Fe alloys, especially on the nucleation of the Fe-intermetallic phases and the α-Al phase. Preliminary results on the formation of iron-bearing phases in Al-Si-Fe alloys and the analysis of the gas injection technique used for inclusion additions have been dealt with in chapters 4 and 5. This chapter discusses the influence of different inclusions on the nucleation of the α-Al phase in several Al-Si-Fe experimental alloys and at different cooling rates.

6.2. Results

Before discussing the results of the current inoculation experiments, it would be appropriate to highlight some principles related to the interaction of solid particles with the solid/liquid interface during solidification.

According to several investigators (see Ref 177, for example), there are two cases for the interaction between insoluble particles and the solid/liquid interface during the crystal growth process. The first one pertains to particle-matrix combinations in which the particles are captured by the solid/liquid interface at all growth conditions or growth rates so far tested. In these systems it is believed that the net free energy change in the particle transfer from liquid to solid is negative, otherwise pushing takes place. The condition for such particle pushing can either be given by:[178,179]

$$\gamma_{PS} > \gamma_{PL} + \gamma_{SL} \tag{56}$$

or by:[89,180]

$$\gamma_{PS} > \gamma_{PL} \tag{57}$$

where, γ_{PS}, γ_{PL} and γ_{SL} are the free energies at the particle/solid, particle/liquid and solid/liquid interfaces, respectively. It should be mentioned here that the term "particle" is used interchangeably with "inclusion" in this chapter.

These simple thermodynamic models are closely related to the heterogeneous nucleation theory and give an insight into the fundamental aspects of the interaction between the particles and the solidification front, but they are of limited predictive value

due to the lack of, and the uncertainty in, the interfacial energies reported in the literature.[177,181]

The second case of interaction between insoluble particles and the solid/liquid interface relates to the case where a critical solid/liquid interface velocity exists, above which the particles are captured by the solid/liquid interface, and below which they are pushed by the solidifying interface. This critical interface velocity is dependent on the interface chemistry, particle size, liquid viscosity, temperature gradient, thermal conductivities of particle and matrix, and solute content.[177]

In studies carried out by Wu *et al.*,[182] the critical interface velocities measured experimentally in rapidly solidified wedge-shaped castings were 13100, 14800, and 15600 m/s for Al-12.5Si/SiC, Al-7Si/SiC, and Al-4Si/SiC alloys, respectively. As this order of magnitude is difficult to achieve under normal casting conditions, particles which are inert in nucleating the solid phase will most likely be pushed to the interdendritic regions. Consequently, in microstructures produced at solidification rates lower than those reported by Wu *et al.*[182], the particles which are located within the α-solid phase should have some catalytic potency to nucleate the solid phase. The main object of the current chapter is to evaluate the relative nucleating potencies of inclusions in aluminum alloys.

In addition, one must also consider the case when two or more particles lie in close vicinity to each other in the α-aluminum grain as demonstrated in Figure 61. This issue can be discussed in view of several works[69,178,179,183,184,185,186] related to the nucleation process and the interaction between solid particles and the solid/liquid interface.

In their analysis, Maxwell and Hellawell[69] considered that only one grain should be nucleated per particle and, thus, nucleant particles beyond the optimum number necessary for nucleation would be pushed to grain boundaries by the growing solid. Cissé *et al.*[183] concluded that the ideal ratio between the number of nucleated crystals and the number of nucleant particles is either less than or equal to unity (ideally equal to unity) for complete epitaxy, and that the ratio will generally be greater than unity for partial epitaxy. Both Maxwell and Hellawell[69] and Cissé *et al.*[183] proposed that not more than one nucleant particle should be responsible for nucleation of one grain of solid. Observations of the presence of more than one solid particle within the same grain of the solid phase were not reported in their works.

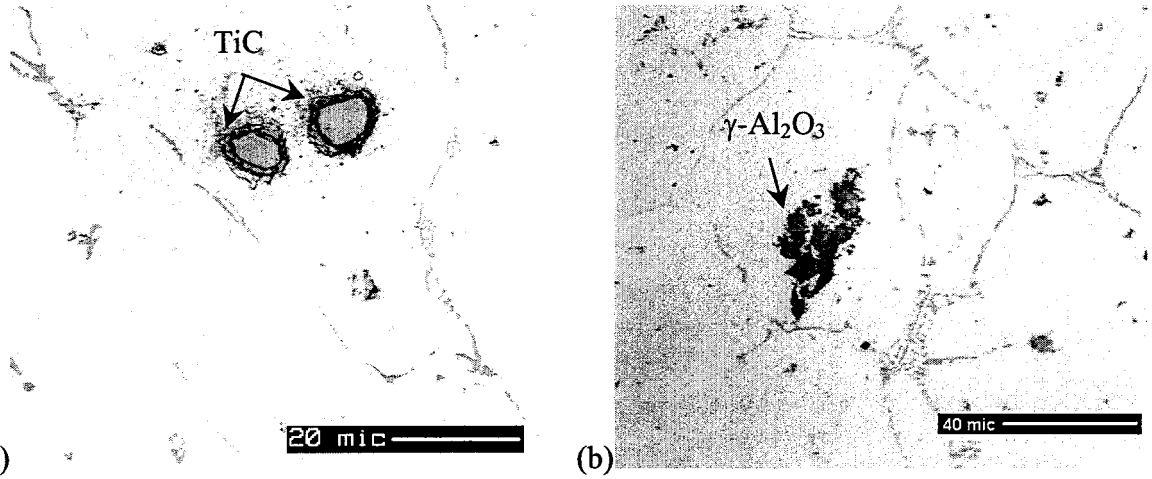

Figure 61 Microstructures showing the presence of two or more solid particle in close vicinity to each other within an α-Al grain.

However, observations similar to those presented in Figure 61 were also reported by Mohanty and Gruzleski[184] in their inoculation experiments. The work of Jin and Lloyd[185] demonstrated that there is no contradiction between the different works on

nucleation.[69,183,184] Jin and Lloyd[185] attributed the presence of several particles within the same grain to the similarity between the particle capture and the heterogeneous nucleation processes. In other words, particles that act as heterogeneous nucleation catalysts are not rejected by the solid/liquid interface. Consequently, the multiple presence of certain solid particles within the same solid grain does not indicate that these particles co-work in nucleating such grains, but rather that only one of them is responsible for the nucleation, while the rest are eventually incorporated into the growing solid phase.

However, it should be noted here that the greater the number of a certain type of particles captured by the solid phase, the higher their potency for nucleating the solid. Thus, in the quantitative results given here, the total number of certain particles within the solid phase has been considered a measure of the nucleating potency of these particles, regardless of whether they are heterogeneous nucleants or captured particles. In this respect, therefore, the results reported here should be considered to have only *qualitative significance.*

In developing the argument for the interfacial energy balance necessary for particle capture or rejection by the solid/liquid interface, Jin and Lloyd[185] confirmed the consistency of their results with those of Uhlmann *et al.*,[178] and Pötschke and Rogge.[179] Uhlmann *et al.*[178] assumed that solid/liquid interface is smooth when the interaction with the particle takes place -a condition that was not satisfied in the case of dendritic solidification of the Al-Si alloys in the work of Jin and Lloyd,[185] who, however, used the results of Uhlmann *et al.*[178] in discussing their results. More recently, based on their experimental results, Wilde and Perepezko[186] confirmed that the predictions of some models (*e.g.*, which assume a smooth solidification front) related to particle capturing also hold in the case of a dendritic

solidification front. The quantitative results presented in this chapter and their qualitative interpretations will be based on the theoretical and experimental evidences reported by these various workers and others in the literature.

6.2.1. Effect of Inclusions on the Crystallization of the α-Al Phase in Al-Si-Fe Alloys

6.2.1.1. Effect of CaO

Calcium as an impurity or alloying element has two main effects in Al-Si alloys: it is recognized as (i) a modifier of the Al-Si eutectic structure, and as (ii) a neutralizer for the iron intermetallic phases.[39,187,188] The chemical affinity of calcium for oxygen is very high relative to the other oxide inclusions used in this work (see Figure 62 (a)).[189] Thus, part of any elemental calcium added to Al-Si alloys as a modifier or neutralizer is expected to undergo oxidation. Evidence of calcium oxidation was confirmed by the presence of several calcium oxide particles in the microstructure of calcium-containing 319 alloy.[190] The role of calcium oxide inclusions in the nucleation of the α-Al will be elaborated upon.

The histogram of Figure 63 compares quantitatively the occurrence of CaO particles within the α-Al phase at different conditions of alloy composition and cooling rate. The occurrence of CaO is expressed as a percentage of the number of particles located within the aluminum phase to the total number of particles observed in the respective alloy and cooling rate condition. It is clear from the diagram that the CaO particles are mainly located within the α-Al phase. The occurrence level is minimum in alloy 5, the highest Fe-containing alloy in the present study, and is maximum in alloy 6, the highest Si-containing alloy (see Table 6).

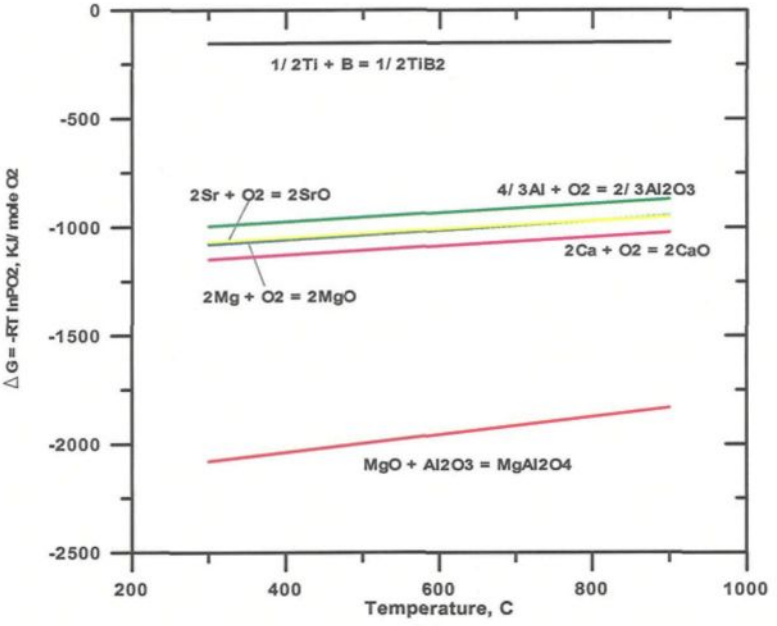

(a)

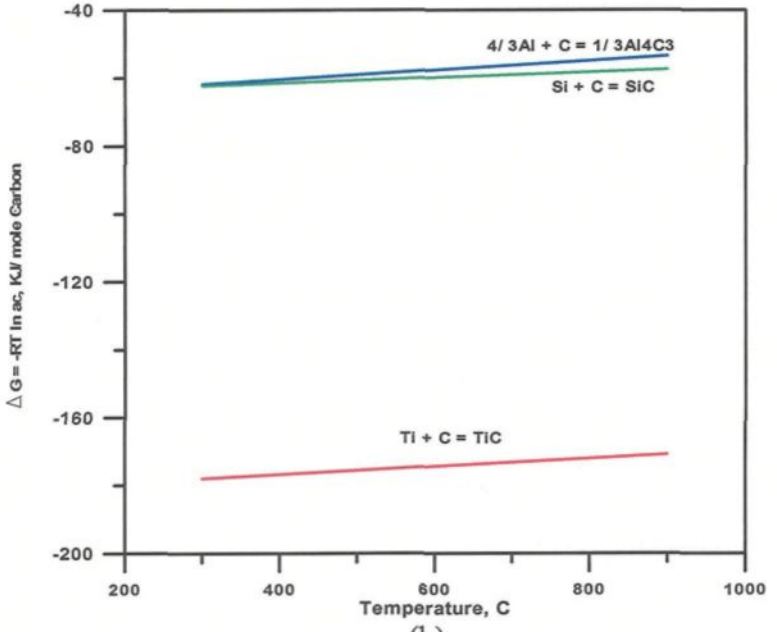

(b)

Figure 62 Standard free energy of formation of oxides, carbides and borides.[189]

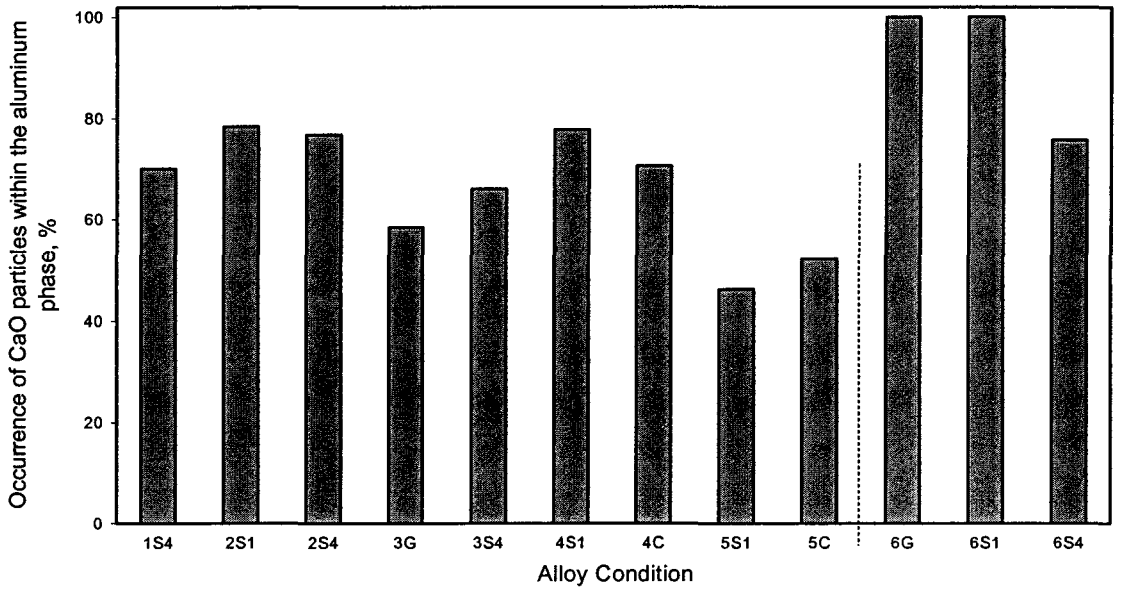

Figure 63 Quantitative evaluation of the percentage occurrence of CaO in the α-Al phase. Condition 1S4 corresponds to alloy 1, sample S4 in Figure 23, etc.

The highest occurrence levels that were observed in the high-Si alloy (alloy 6) may be attributed to the high chemical affinity of CaO for the formation of intermetallic compounds with the Al-Si melt (to be discussed elsewhere in this section). Thus, the high chemical affinity of CaO to react with Al-Si melts provides an advantage to the surface characteristics of CaO by keeping it active, which in turn promotes higher nucleation levels of the aluminum phase. In contrast to this, the minimum occurrence levels of CaO particles in the α-Al phase that were observed in alloy 5 (high-Fe alloy) could be attributed in part to the passivity between CaO and the Fe in the liquid solution, and in part to the lack of Si in alloy 5 that leads to the formation of binary Al-Fe phases in this alloy (Chapter 4).[1,2] The

passivity between CaO and the solute atoms of Fe impeded any kind of reaction between the two constituents, as will be demonstrated later.

Figure 64 shows some examples of the CaO particles injected into different alloys. The presence of a majority of CaO particles inside the α-Al phase suggests a favorable nucleation of α-Al on the surface of CaO. This phenomenon is observed whether there is evidence of interfacial reactions on the surface of CaO or not, Figure 64 (a-d). Inside the α-Al phase, some of the CaO particles are seen to nucleate Fe-bearing phases, as shown in Figure 64 (e). In the high-Fe alloy, *i.e.*, alloy 5, the larger part of CaO particles are pushed to the interdendritic regions, Figure 64 (f), and no evidence of reactions can be seen.

It is evident from Figure 64 that CaO has a high sticking coefficient and, thus, a tendency to form clusters in the liquid aluminum alloy. As a result, CaO inclusions should be easily removed from Al-melts.

In low-Si alloys, the calcium oxide reacts with the aluminum and/or aluminum oxide[a] to form two kinds of mixed oxides (see Figure 65). The first oxide is $CaAl_{1.9}O_{4.4}$ or ($CaAl_2O_4$) which is a mixed oxide that resembles the spinel phase ($MgAl_2O_4$). Traces of silicon, ~1 wt%, were also analyzed in this phase; as the Si map in Figure 65 reveals. In addition to this oxide, an oxide phase with the formula $CaAl_{6.4}O_{7.7}$ was also detected. The question arises as to what is the source for the excess oxygen that appears in these oxide phases.

---

[a] The oxidation of molten aluminum is thermodynamically unavoidable even under the highest vacuum levels attained by today's technology. In addition, it should be expected that aluminum oxidation will result according to the principles of mass action, since there is much more aluminum than the other elements present in the alloy regardless the affinity of these elements to the oxygen.

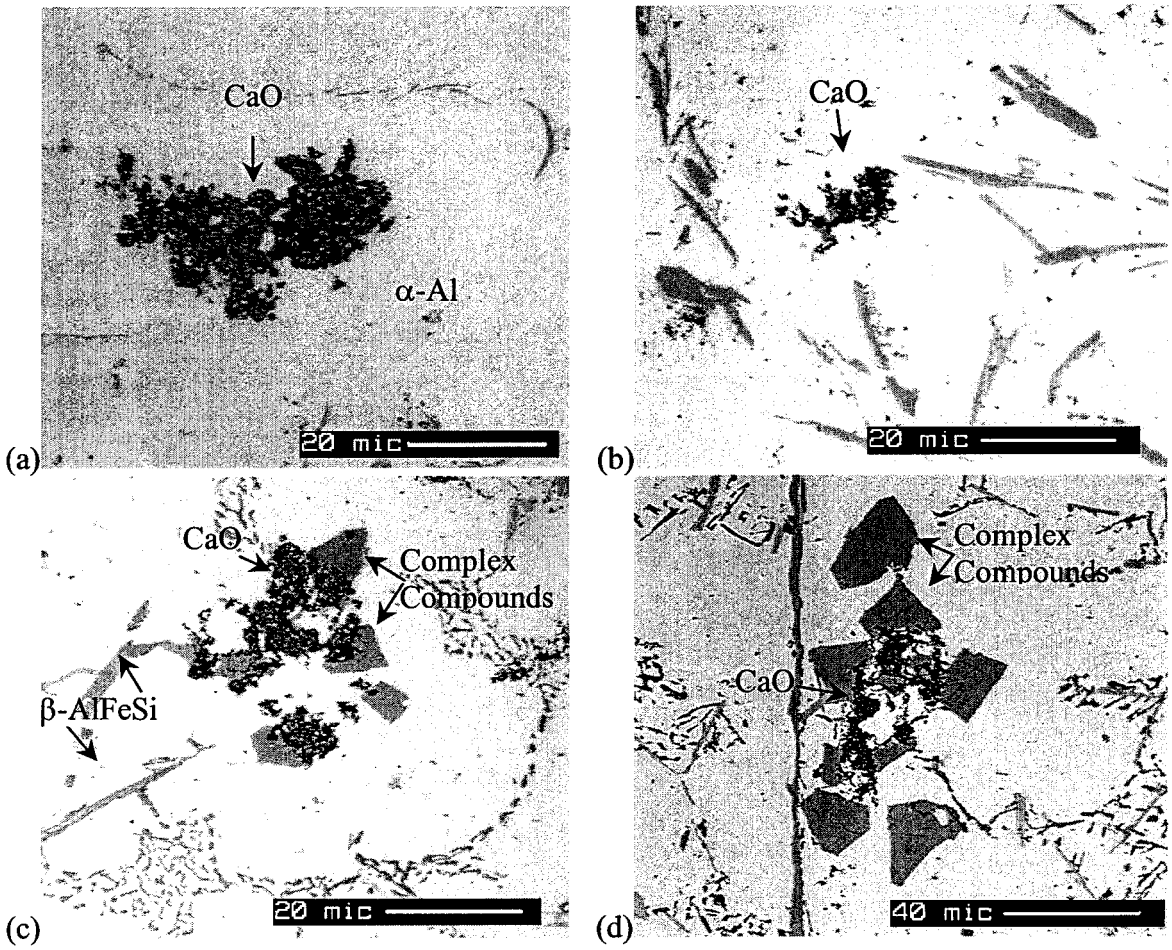

Figure 64 Effect of CaO particles on the microstructure of Al alloys. (a, b) nucleation of α-Al on surface of CaO particles in alloys 1 and 5 solidified at cooling rates of 8 and 0.19 °C/s, respectively; (c, d) the formation of calcium compounds (high-Si compounds) in alloy 6 solidified at cooling rates of 12.8 and 0.76 °C/s, respectively; (e) the nucleation of an AlFeSi phase on the surface of CaO particles within the α-Al phase of alloy 3, solidified at cooling rate of 0.21 °C/s; and (f) CaO particles pushed to the interdendritic regions in alloy 5, cooling rate of 1.2 °C/s, where no visible reaction at CaO interfaces can be seen.

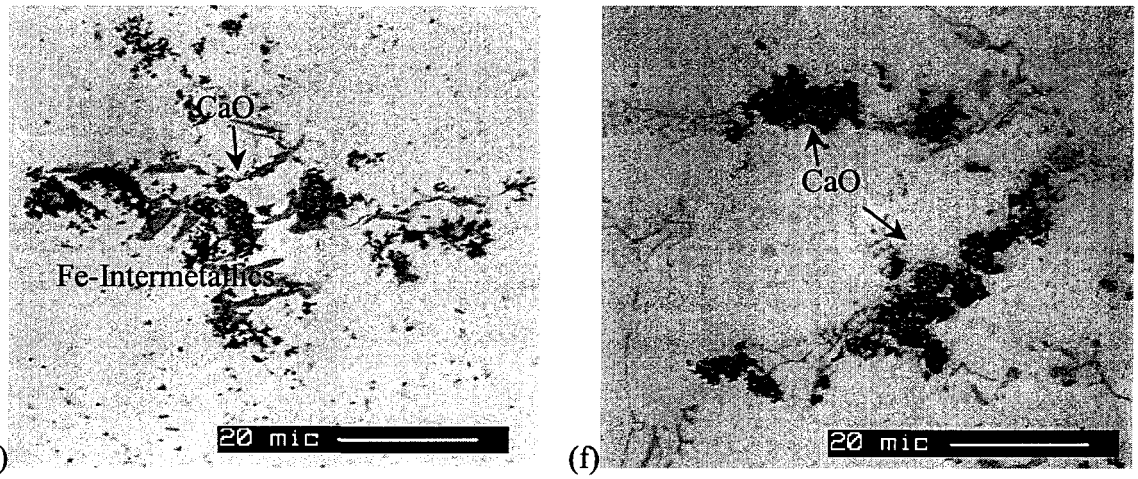

Figure 64 Effect of CaO particles on the microstructure of Al alloys. (a, b) nucleation of α-Al on surface of CaO particles in alloys 1 and 5 solidified at cooling rates of 8 and 0.19 °C/s, respectively; (c, d) the formation of calcium compounds (high-Si compounds) in alloy 6 solidified at cooling rates of 12.8 and 0.76 °C/s, respectively; (e) the nucleation of an AlFeSi phase on the surface of CaO particles within the α-Al phase of alloy 3, solidified at cooling rate of 0.21 °C/s; and (f) CaO particles pushed to the interdendritic regions in alloy 5, cooling rate of 1.2 °C/s, where no visible reaction at CaO interfaces can be seen.

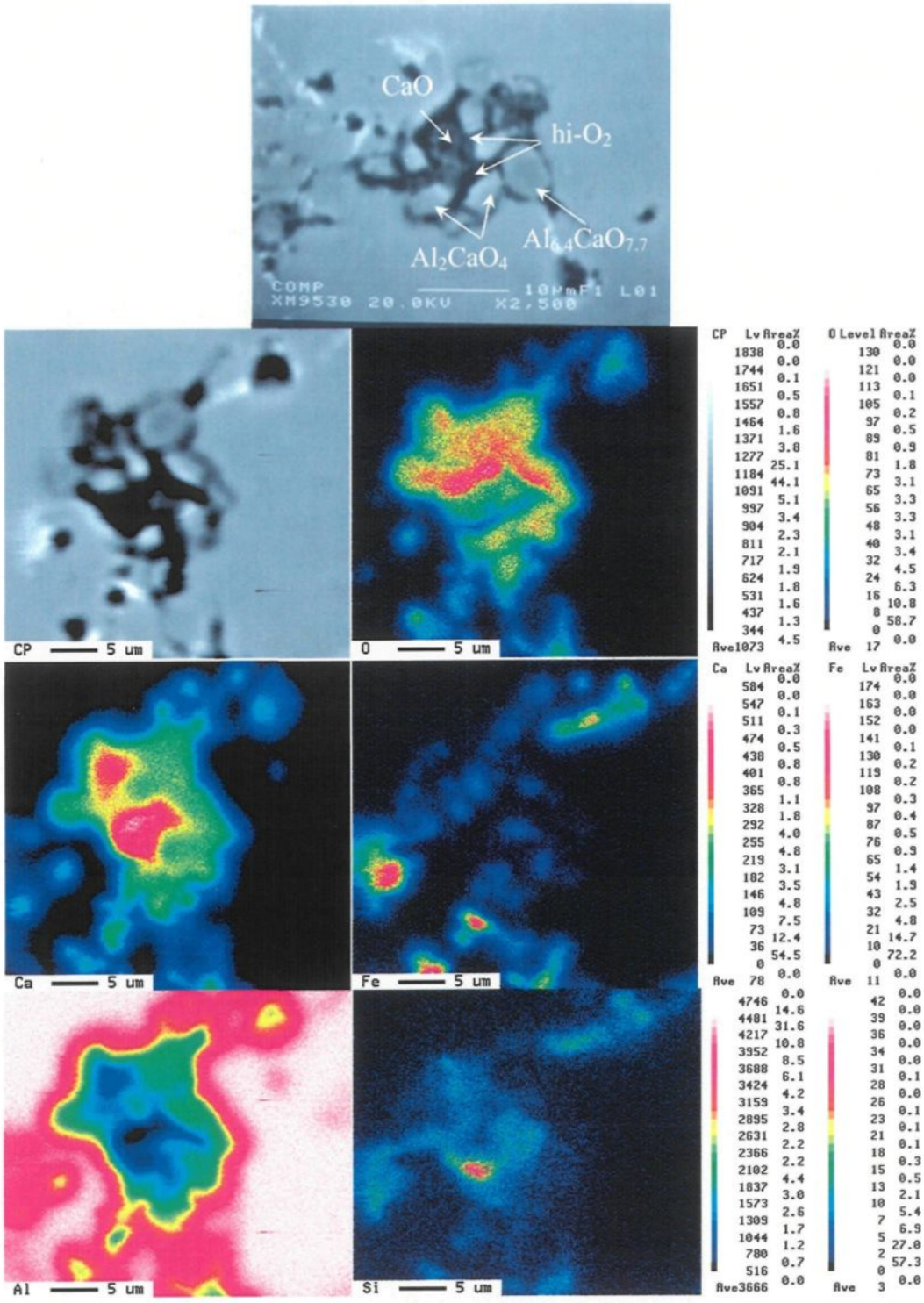

Figure 65 Maps of element distributions corresponding to the backscattered image (top) of alloy 2, showing the formation of different oxides at the interfaces between aluminum and the CaO particles (cooling rate 13.8 °C/s).

It has been reported that gases, other than hydrogen, are present in molten aluminum when nonmetallic inclusions react with the environment.[39] Oxygen is one of the components of the atmosphere that surrounds the liquid metal. In addition, according to the structural model of Weyl,[191] which is relatively well accepted,[177] the surface of an oxide, and most likely that of many oxidized metals in air, consists predominantly of highly polarized oxygen atoms. Freshly created oxide surfaces have high chemical reactivity compared to when they remain exposed to the air. Therefore, there is a tendency for such surfaces to adjust their structure to a low energy state through atom migration or adsorption of additional components. The very reactive high-energy oxide surface adsorbs oxygen from the air in order to lower its surface energy. Similarly, adsorption of an oxygen layer also occurs on carbide surfaces.[192]

Recent works provide more concrete observations for the adsorption of oxygen on the metal/oxide interfaces. For example, Levi and Kaplan[193] discussed the formation of an oxygen-rich interphase at the liquid aluminum/α-Al_2O_3 interface. Evidence of oxygen segregation at the Ag/MgO interfaces have been provided by Pippel *et. al.*[194] In addition, a model for the adsorption of oxygen at metal/oxide interfaces has been constructed, as well.[195]

Another possibility for the excess oxygen may be the dissolution of CaO in the liquid aluminum. The driving force for such a dissolution reaction is the liquid solubility of Ca in aluminum, which is 7.7 wt% at the eutectic temperature, 616°C.[169] This high solubility, if the reaction is thermodynamically favorable, suggests that the CaO dissolves in the liquid aluminum liberating free oxygen to the surrounding.

Thus, the source of oxygen observed in the interphase regions around the CaO particles is either due to its adsorption on the surface of CaO particles before they are injected into the melt, or from the dissolution of the CaO in the liquid aluminum. This explains the presence of excess oxygen in the interphase regions surrounding the CaO particles in Figure 65, and the formation of the mixed oxides.

In the high-Si alloy, *i.e.*, alloy 6, the CaO particles react with the Al and Si forming two distinct phases. The first one is an oxide phase similar to that observed in the low-Si alloy, and is identified as $CaAl_{6.3}O_{7.5}Si_{0.57}$, (arrowed in Figure 66). The difference between the two phases is that the latter phase contains much more silicon than that observed in the low-Si alloy.

The second phase that results from the reaction between the CaO and the Al-Si melt has a polygonal block-like morphology (Figure 64 (c, d)). This phase has a higher silicon content than the well-referenced phases in the Al-Si-Fe system,[24,124] and a chemical composition which can be expressed as $CaAl_{2.5}Si_{1.8}O_{0.37}$, with a range of composition given by $CaAl_{2.3\text{-}2.68}Si_{1.75\text{-}1.9}O_{0.16\text{-}0.7}$. It has a white contrast in the back-scattered images of Figure 66. A comparison of the composition of this phase with that of several complex intermetallic compounds of calcium observed in Al-Si alloys[169] revealed no matches, implying that it is a new phase.

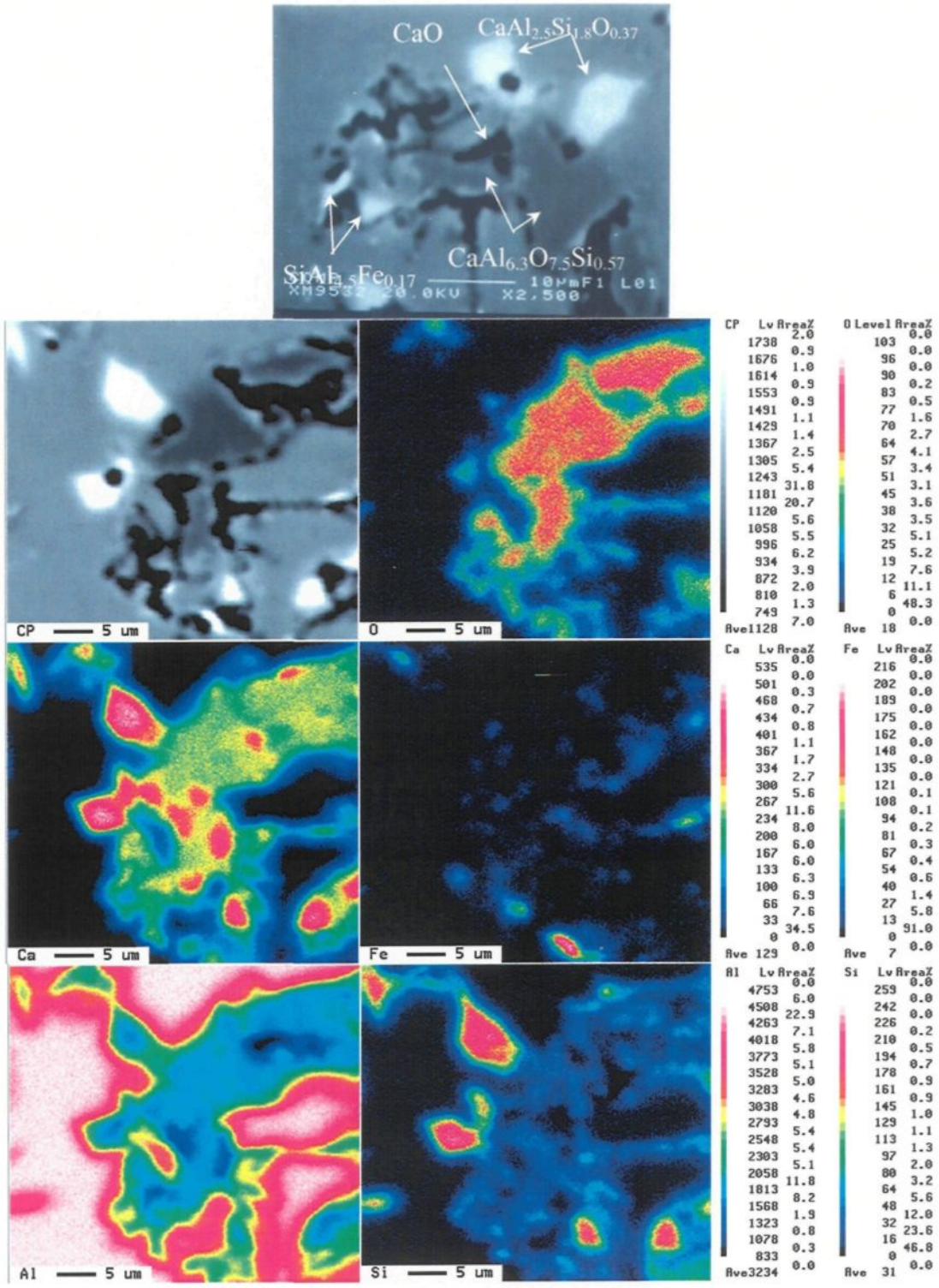

Figure 66 Maps of element distributions corresponding to the backscattered image (top) of alloy 6, showing the formation of calcium compounds as a result of the reaction between CaO and the Al-Si melt (cooling rate 12.8 °C/s).

A high-Si phase was also observed to form at the interphase region around the CaO particles, corresponding to $SiAl_{4.5}Fe_{0.17}$, with some traces of oxygen. The atomic ratio of Si/Al in the phase is much higher than that in the Al-Si eutectic. At the same time, it is not identical to the δ-Al_4FeSi_2 phase: the highest Si-containing phase among the ternary Al-Fe-Si phases. Consequently, it can be reasonably concluded that Si segregates to the CaO surface, and this segregation is likely the reason for the disappearance of eutectic silicon particles from regions near the CaO particles and the formation of high-Si phases in physical contact with CaO particles.

6.2.1.2. Effect of MgO

In alloys 1 to 5, the majority of MgO particles, determined from optical microscopy and image analysis, were observed to lie within the aluminum phase. In alloy 6, the percentages of MgO particles that were located within the aluminum phase decreased greatly, as shown in Figure 67. The optical micrographs of Figure 68 show examples of MgO particles in the microstructure of Al-alloys.

6.2.1.3. Effect of TiB_2

The role of titanium diboride, TiB_2, (conventionally called titanium boride) in the grain refining process is a matter of different interpretations.[71,170,173,174] Very valuable and important information on this role were obtained from the inoculation experiments carried out in the present chapter. The introduction of titanium boride particles into the molten aluminum alloys was greatly facilitated due to their good wettability with aluminum (Chapter 5). As can be seen from Figure 69, a huge number of particles can be readily

introduced into the molten metal. The uniform distribution of these particles in the alloy is the key for a successful evaluation of their role in the development of the solidification microstructure. To achieve or maximize this kind of distribution, casting should be done as soon as the injection stage is completed. In addition, stirring should be maintained up until the time of casting, to reduce the "density effect", which can result in the settling of heavy particles such as TiB_2 to the bottom of the crucible.

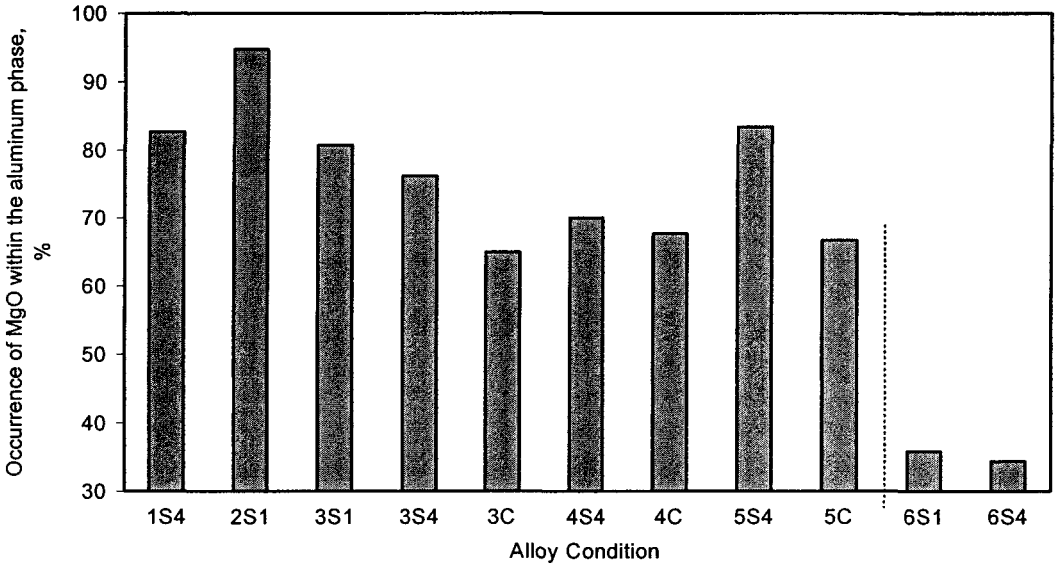

Figure 67 Quantitative evaluation of the percentage occurrence of MgO in the α-Al phase.

The diagram of Figure 70 provides a quantitative evaluation for the occurrence of TiB_2 particles in the α-Al phase. It is clear from the diagram that the TiB_2 particles have a high potency to nucleate the solid phase in almost all the alloys, *i.e.,* alloys 1 to 5, with the exception of alloy 6. As Figure 71 (a-f) shows, in alloys 1 to 5, and at different cooling rates, most of the TiB_2 particles are located within the Al-grains rather than the grain

boundaries or the interdendritic regions. This observation strongly confirms the role of TiB_2 as a grain refiner for the α-Al phase in the alloy compositions studied. In contrast to this, a high percentages of the TiB_2 particles studied in alloy 6 were found to be located in the interdendritic regions, as seen in Figure 71 (g, h) and also concluded from Figure 70. This finding confirms that the TiB_2 particles are inactive nucleants in high-Si alloys.

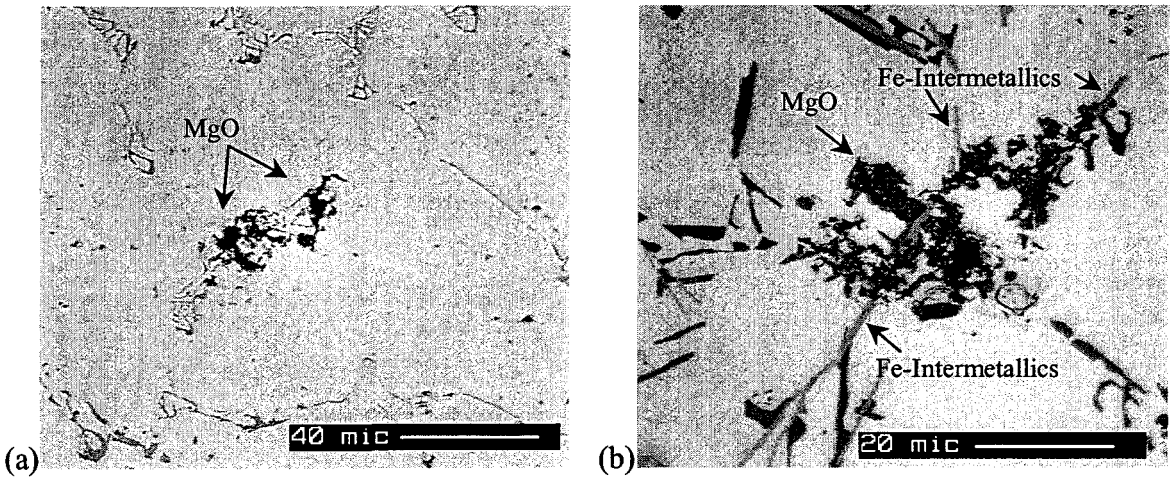

Figure 68 Examples of (a) the occurrence of MgO particles within the α-Al phase in alloy 4 cooled at 1.4 °C/s, and (b) the nucleation of iron intermetallics on the surface of MgO particles in alloy 6 cooled at 0.76 °C/s.

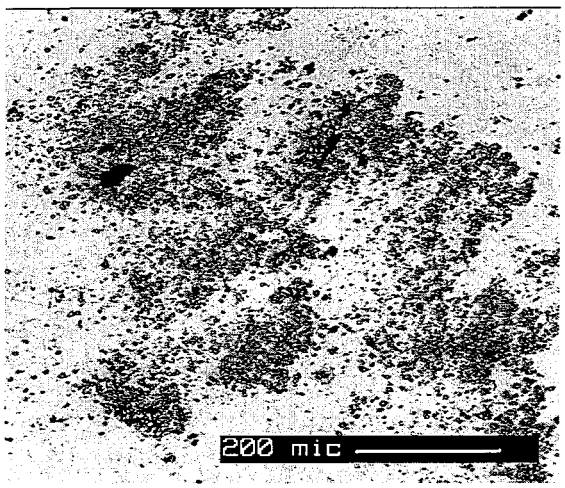

Figure 69 Optical micrograph taken from alloy 1, showing a huge number of TiB_2 particles in the microstructure.

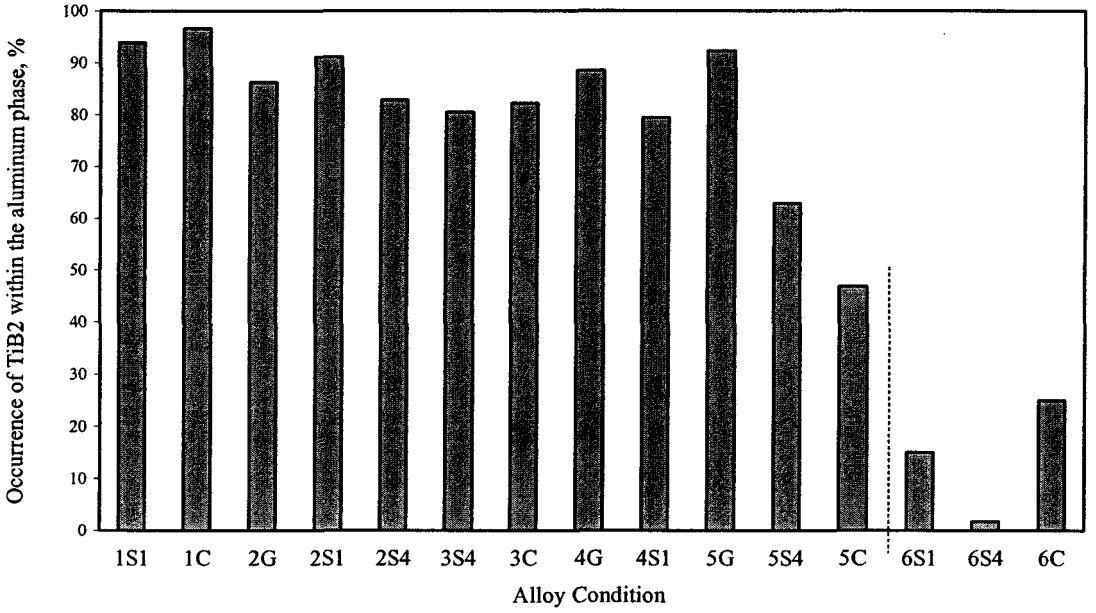

Figure 70 Quantitative evaluation of the percentage occurrence of TiB_2 in the α-Al phase.

It is also very clear from Figure 71 that the TiB_2 particles have a high sticking coefficient. TiB_2 particles tend to form clusters in the molten metal during the liquid stage. The fading phenomenon related to grain refiners in alloy melts can therefore be attributed to the agglomeration and settling of the TiB_2 particles as was previously interpreted by some authors.[170,174] In contrast to this interpretation, Lee and Basaran[173] observed a time-related fade phenomenon when the Al-melt was subjected to convection during solidification, and concluded that the distribution of TiB_2 particles in the melt has little or no effect on grain refinement. The micrographs of Figure 71, reveal that there is actually no contradiction between these two interpretations.[170,173,174] When they come in contact with

each other, the TiB_2 particles form clusters. Melt convection helps the TiB_2 particles to come into contact and agglomerate.

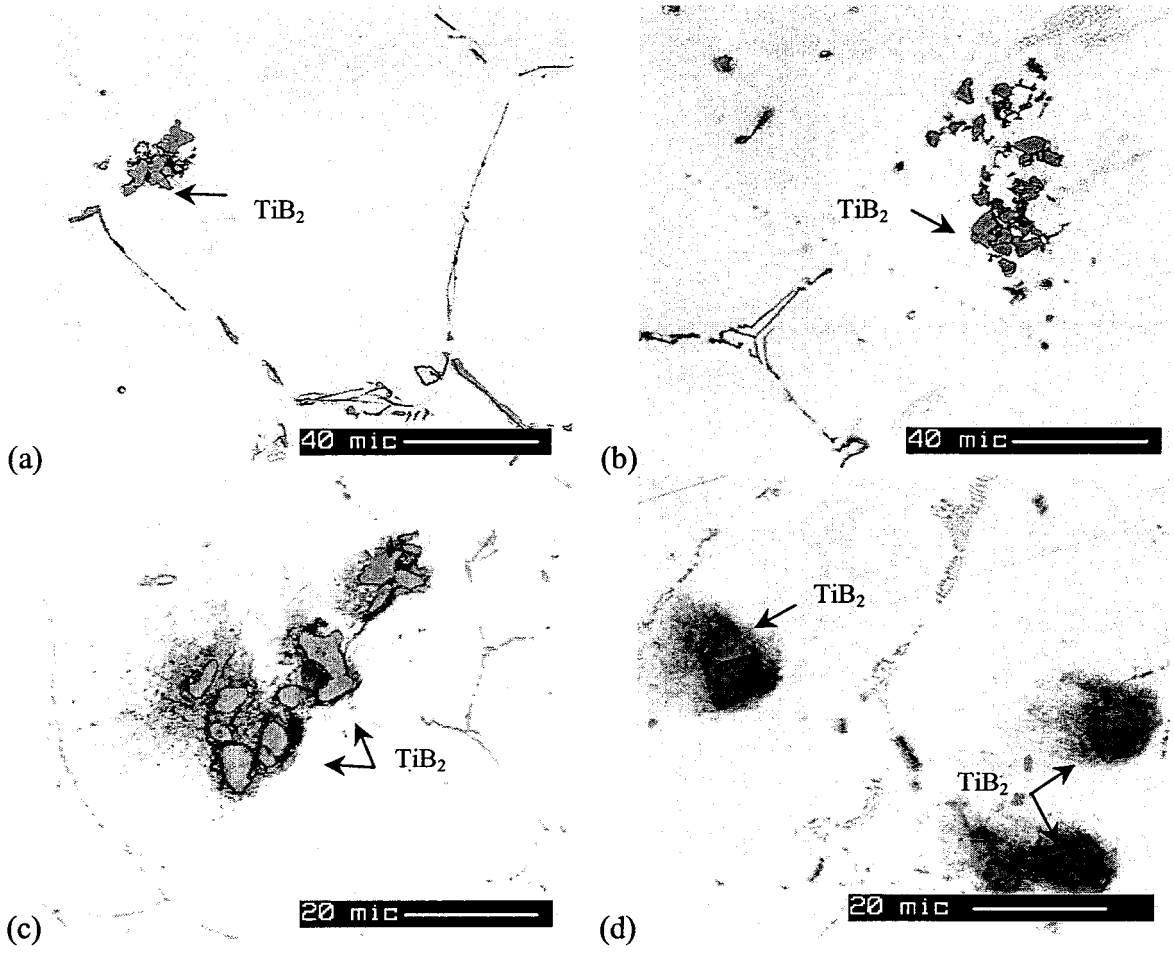

Figure 71 Optical micrographs showing: (a-f) TiB_2 particles within the α-Al phase of low-Si alloys: (a, b) alloy 1, cooling rate 0.16 °C/s, (c) alloy 2, 13.8 °C/s, (d) alloy 3, 14.3 °C/s, (e, f) alloy 4, 10.3 °C/s; (g, h) TiB_2 particles pushed to the interdendritic regions of alloy 6, 12.8 and 0.76 °C/s, respectively; (i, j) the morphology of pores that form on the surface of the TiB_2 particles.

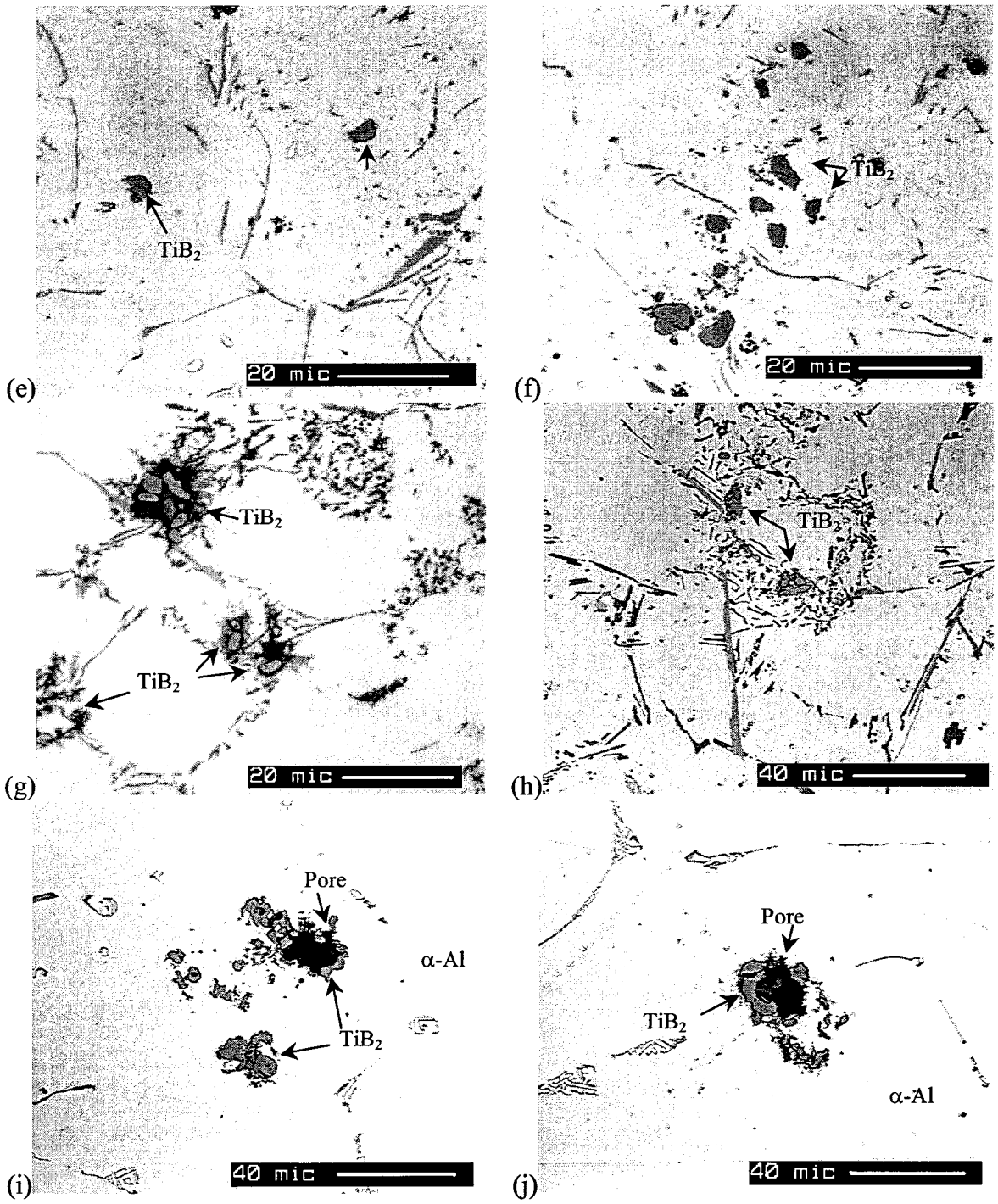

Figure 71 Optical micrographs showing: (a-f) TiB2 particles within the α-Al phase of low-Si alloys: (a, b) alloy 1, cooling rate 0.16 $^{oC/s,}$ (c) alloy 2, 13.8 $^{oC/s,}$ (d) alloy 3, 14.3 $^{oC/s,}$ (e, f) alloy 4, 10.3 $^{oC/s;}$ (g, h) TiB2 particles pushed to the interdendritic regions of alloy 6, 12.8 and 0.76 $^{oC/s,}$ respectively; (i, j) the morphology of pores that form on the surface of the TiB2 particles.

The formation of TiB_2 clusters during the injection experiments, where vigorous convection took place, is evidence of the effect of melt convection on TiB_2 agglomeration (Figure 71 (b, c, g, i, j). This behavior may be attributed to the fact that the surface energy of the fine particles is lowered in agglomeration since the exposed area of the particles is largely reduced. This implies that for sticky particles (with high sticking coefficient), the longer the recirculation (stirring) period of the liquid phase, the greater the opportunity for these particles to coalesce and form clusters.

It can be also noted from Figure 71 (i, j) that the shape of pores in contact with the TiB_2 particles is nearly round. This observation is in good agreement with the conclusions of Boudreault *et al.*,[176] who reported that pores in grain-refined aluminum alloy samples can be distinguished from those in the Sr-modified samples by their almost spherical shape, while, in non-grain-refined alloys, the pores are able to expand along the grain boundaries, and thus have a more irregular morphology.

The porosity in relation to the TiB_2 particles was studied in the current work as well. Figure 72 shows that the number of TiB_2 particles and/or clusters that act as potent substrates for the formation of porosity increases with the total alloying element content of the alloy. It is minimum in alloy 1 and maximum in alloy 6.

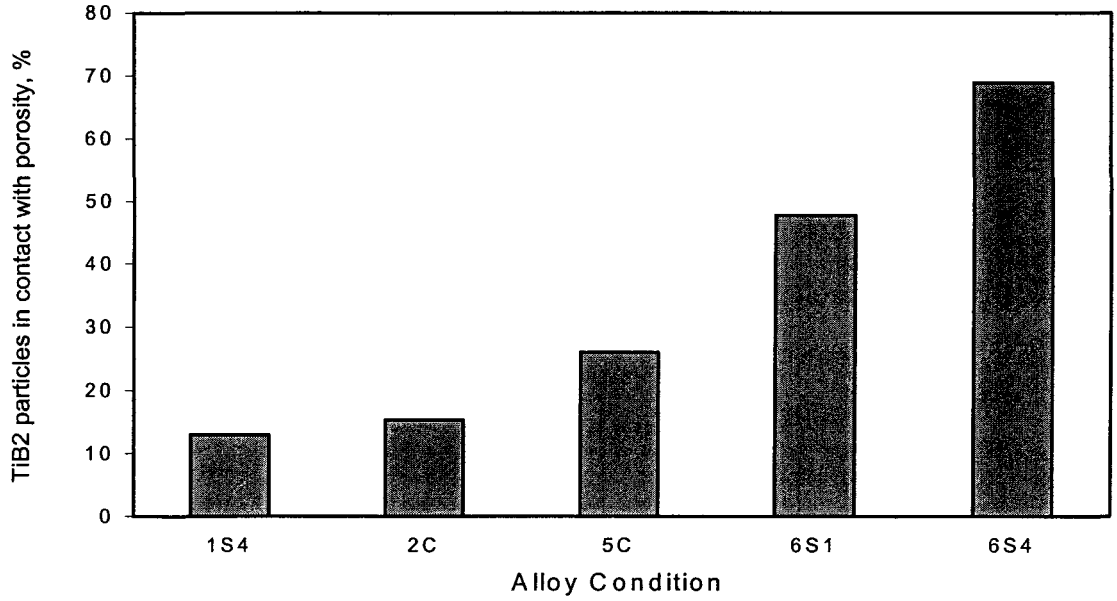

Figure 72 The percentage of TiB_2 particles (or clusters) in contact with pores.

6.2.1.4. Effect of TiC

The role of TiC in the grain refinement of aluminum alloys is a matter of contradiction between different authors.[196] The quantitative results for the occurrence of the TiC particles within the α-Al phase are shown in Figure 73. Similar to TiB_2 and MgO, a high percentage of the TiC particles are located within the α-Al phase in alloys 1 to 5, while in alloy 6, most of them are pushed to the interdendritic regions.

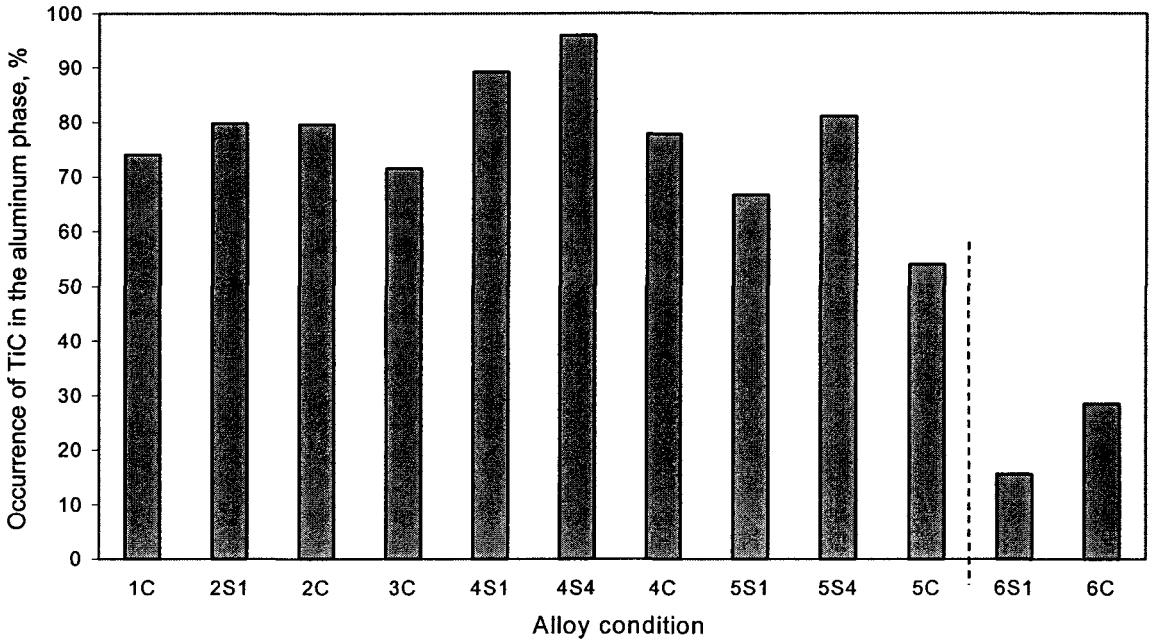

Figure 73 Quantitative evaluation of the percentage occurrence of TiC in the α-Al phase.

6.2.1.5. Effect of Al_4C_3

Aluminum carbide is a common inclusion found in the aluminums coming from the electrolysis process. The formation of Al_4C_3 phase in aluminum is due to the reduced solubility of carbon in aluminum from, 30-35 ppm Al_4C_3 at 1000°C to about 2-3 ppm Al_4C_3 at 700°C.[197]

In the present study, Al_4C_3 particles were mainly found within the α-phase in all the alloys studied including alloy 6, with an overall average of 70.5%. Figure 74 shows the distribution of the Al_4C_3 particles in the aluminum phase for the different alloy conditions. Some examples of the presence of Al_4C_3 particles inside the α-Al phase are displayed in the optical micrographs of Figure 75.

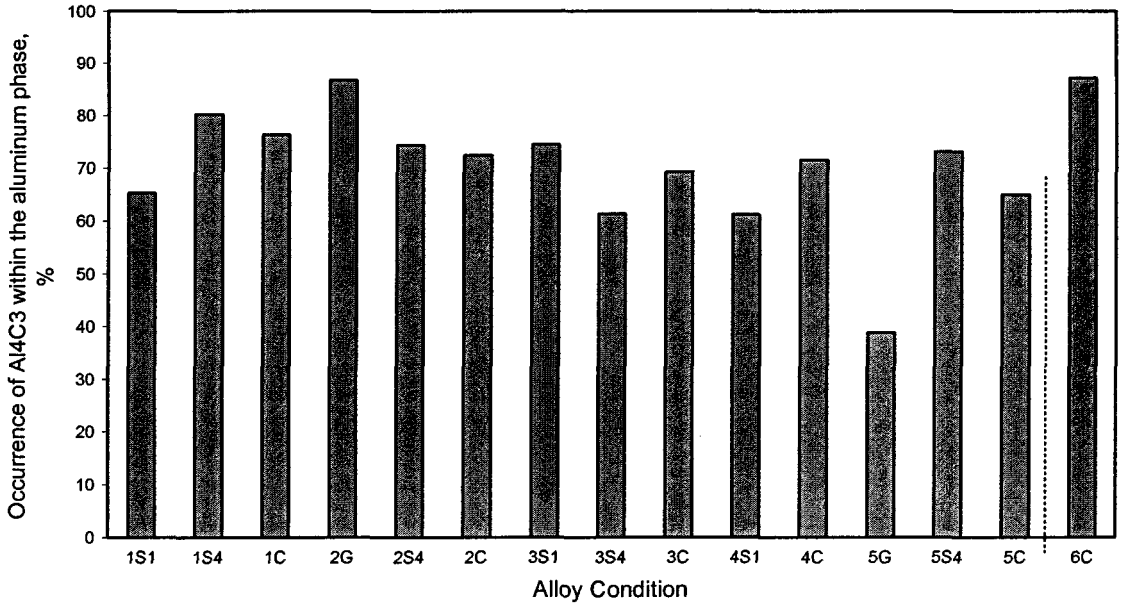

Figure 74 Quantitative evaluation of the percentage occurrence of Al_4C_3 in the α-Al phase.

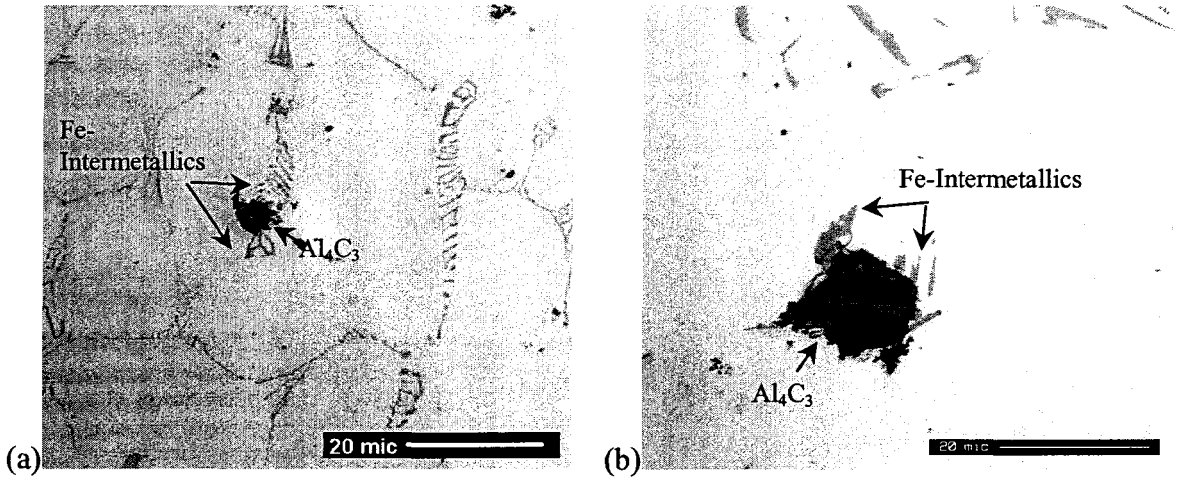

Figure 75 (a, b) optical micrographs showing evidence of the nucleation of Fe-intermetallics on the surface of Al_4C_3 particles within the α-Al phase of alloy 5 (cooling rate 1.2 °C/s).

The thermodynamic stability of carbides was shown previously in Figure 62 (b). According to the diagram, silicon carbide is more stable than aluminum carbide in the temperature range of our experiments. Consequently, transformation of aluminum carbide to silicon carbide is expected to take place in the Si-containing alloys, according to the reaction:

$$Al_4C_3 + (Al\text{-}Si)_{liq} = SiC + Al_{liq} \quad (58)$$

Evidence for this transformation is shown in Figure 76. In high-Fe containing alloys (*i.e.*, alloy 5 with 1 wt% Fe), the transformation of Al_4C_3 to SiC was observed as well (maps not shown).

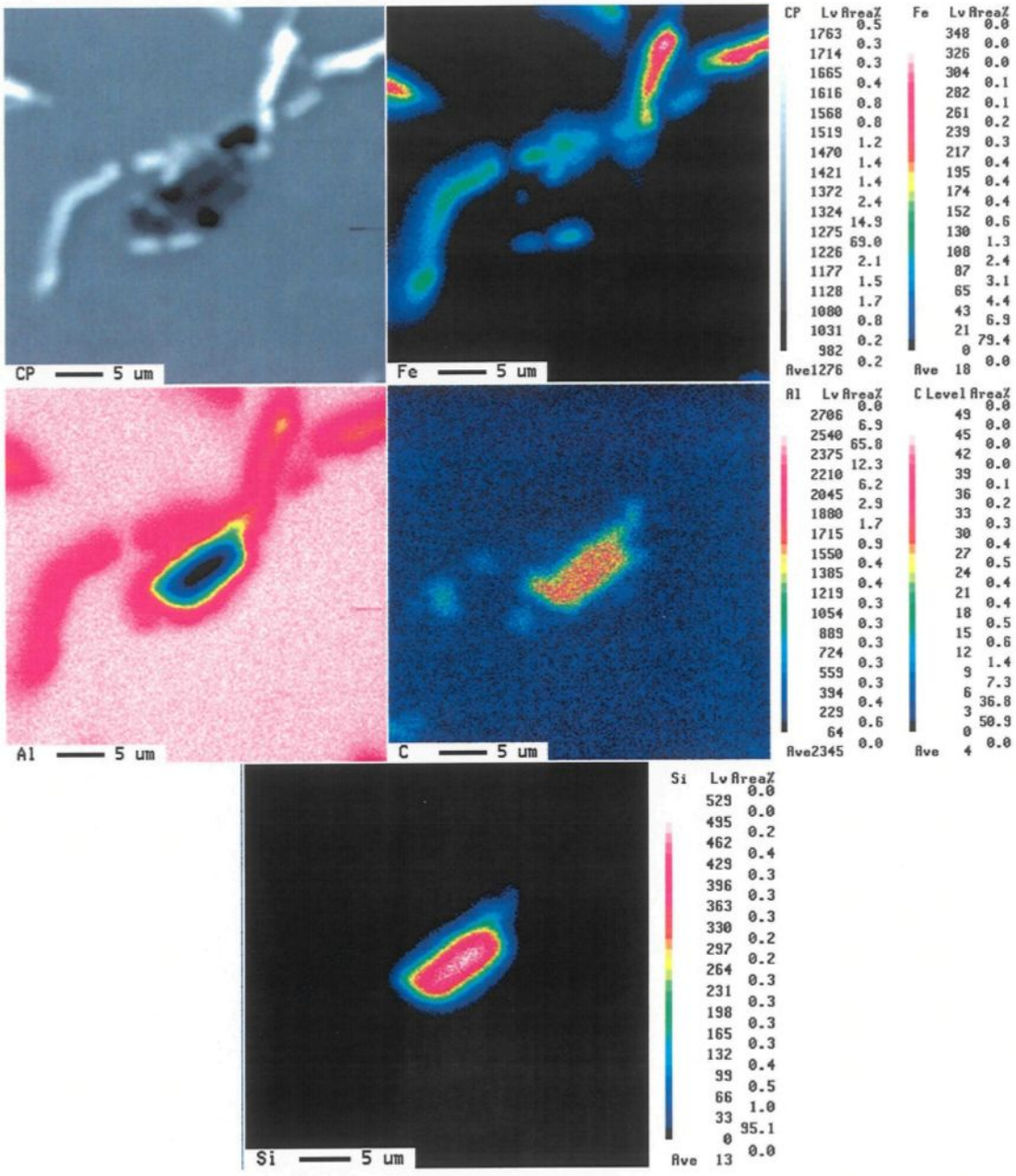

Figure 76 Maps for element distributions corresponding to the backscattered image (top left) of alloy 3 (cooling rate 1.3 °C/s), showing evidence of Al_4C_3 = SiC transformation.

6.2.1.6. Effect of α-Al_2O_3

The role of α-Al_2O_3 in the development of the solidification microstructure in aluminum alloys is of considerable importance, since α-Al_2O_3 is one of the most common oxides found in aluminum alloys. The occurrence levels of the α-Al_2O_3 particles in the α-Al phase are shown in Figure 77 for the different alloy conditions. The occurrence level of the α-Al_2O_3 particles in the α-Al phase is generally high. However, as can be seen from the diagram, the occurrence level decreases in the alloys containing high alloying additions such as alloys 5 and 6.

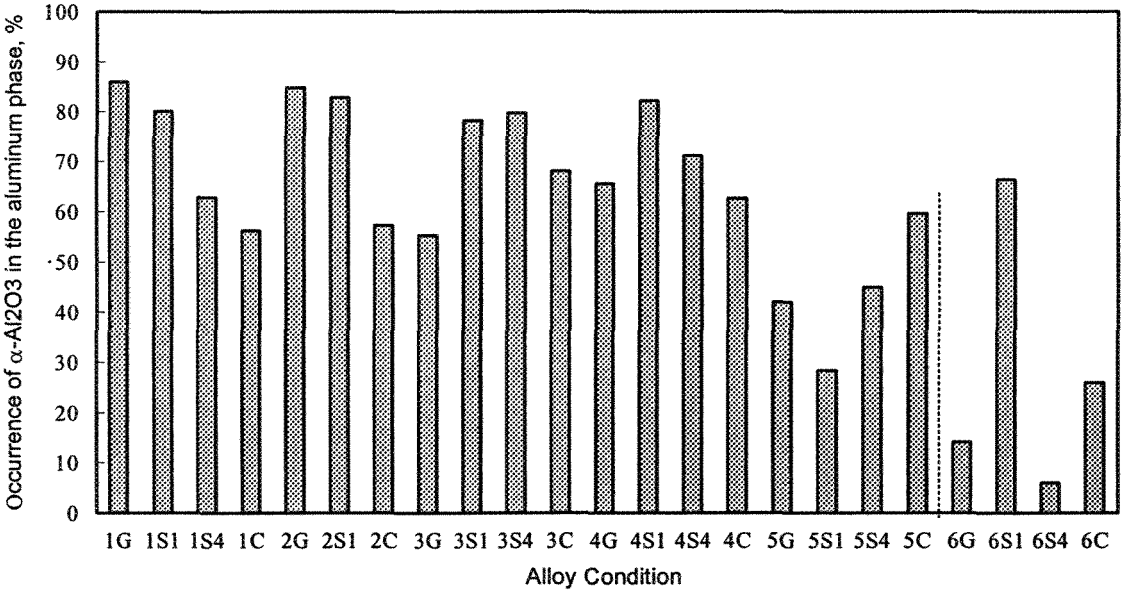

Figure 77 Quantitative evaluation of the percentage occurrence of α-Al_2O_3 in the α-Al phase.

6.2.1.7. Effect of γ-Al_2O_3

In addition to α-Al_2O_3, the γ-Al_2O_3 phase is also one of the most common oxides in aluminum alloys.[76] It is a stoichiometric oxide of aluminum with a defect spinel structure.

In the case of unalloyed aluminum, the oxide film is initially γ-Al_2O_3.[198] It is a thin film that inhibits further oxidation through prolonged heating at higher temperatures (~800°C)[124]. After an incubation period, this oxide transforms to α-Al_2O_3.[198] It is expected that stirring of the melt will result in the entrapment of the γ-Al_2O_3 into the liquid metal. Consequently, not all the γ-Al_2O_3 particles will inhibit further oxidation and transform into α-Al_2O_3. The role of γ-Al_2O_3 in the development of the solidification microstructure of aluminum alloys is discussed later on.

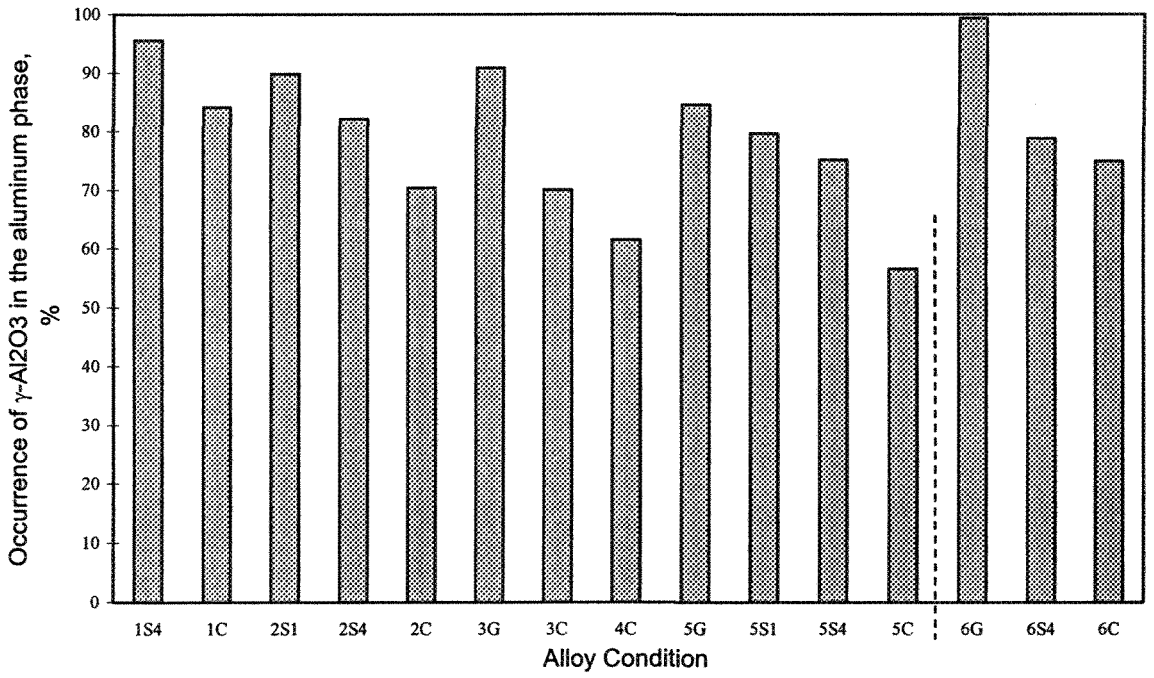

Figure 78 Quantitative evaluation of the percentage occurrence of γ-Al_2O_3 in the α-Al phase.

Among all the inclusions used in this work, the γ-Al_2O_3 particles were found to have the highest occurrence level in the α-Al phase (Figure 78). Several examples of micrographs depicting this observation are given in Figure 79. These particles are believed

to be very potential substrates for the crystallization of the matrix phase. Such inclusion particles are very important in the heterogeneous nucleation process in aluminum alloys.

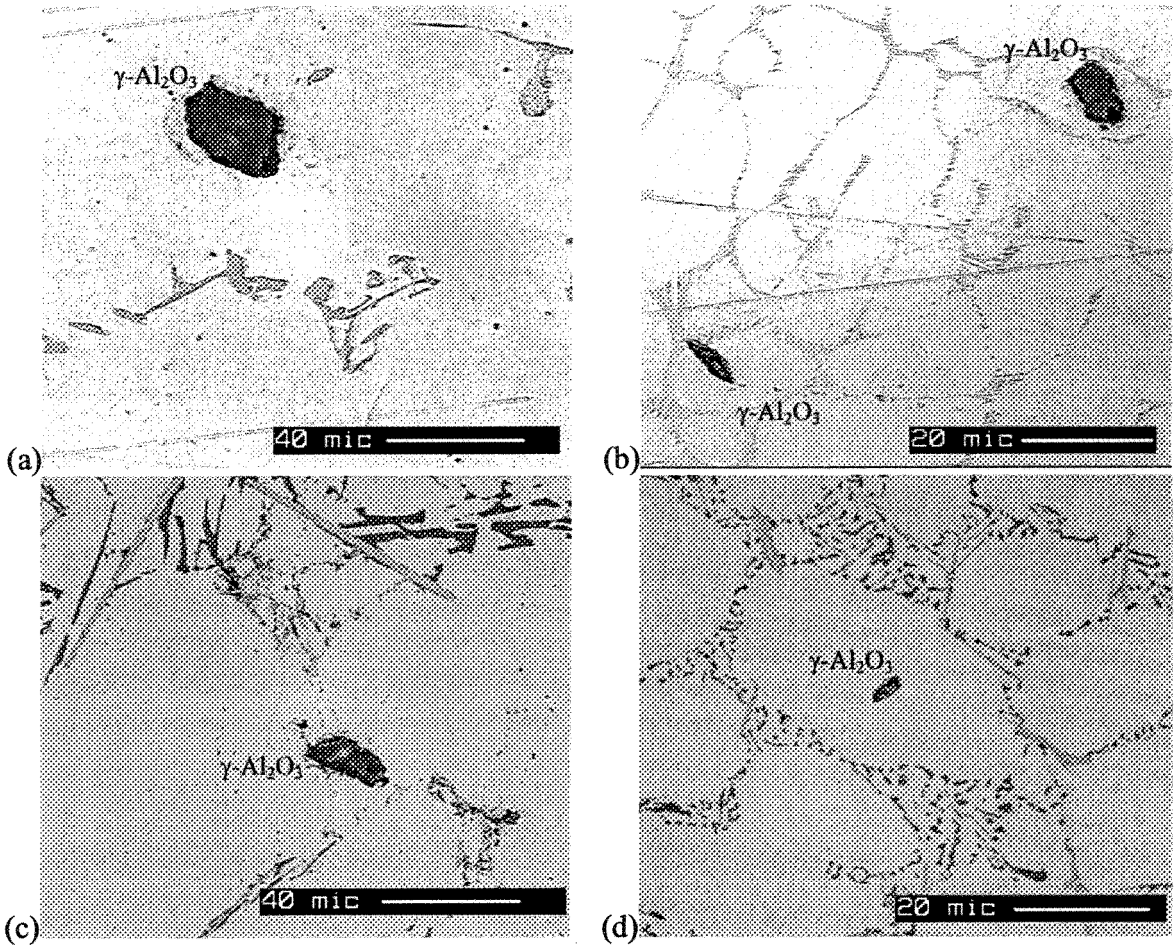

Figure 79 Optical micrographs showing how the majority of γ-Al_2O_3 particles injected into different alloys were observed to act as potential nucleants for the α-Al phase: (a) alloy 4, cooling rate 0.18 °C/s, (b) alloy 5, cooling rate 14.3 °C/s, and (c, d) alloy 6, cooling rates 0.18 and 5.1 °C/s, respectively.

6.2.1.8. Effect of SiC

The majority of the SiC particles were located within the aluminum phase of alloys 1 to 5 after solidification, as shown in Figure 80. In comparison, lower percentages were observed in alloy 6.

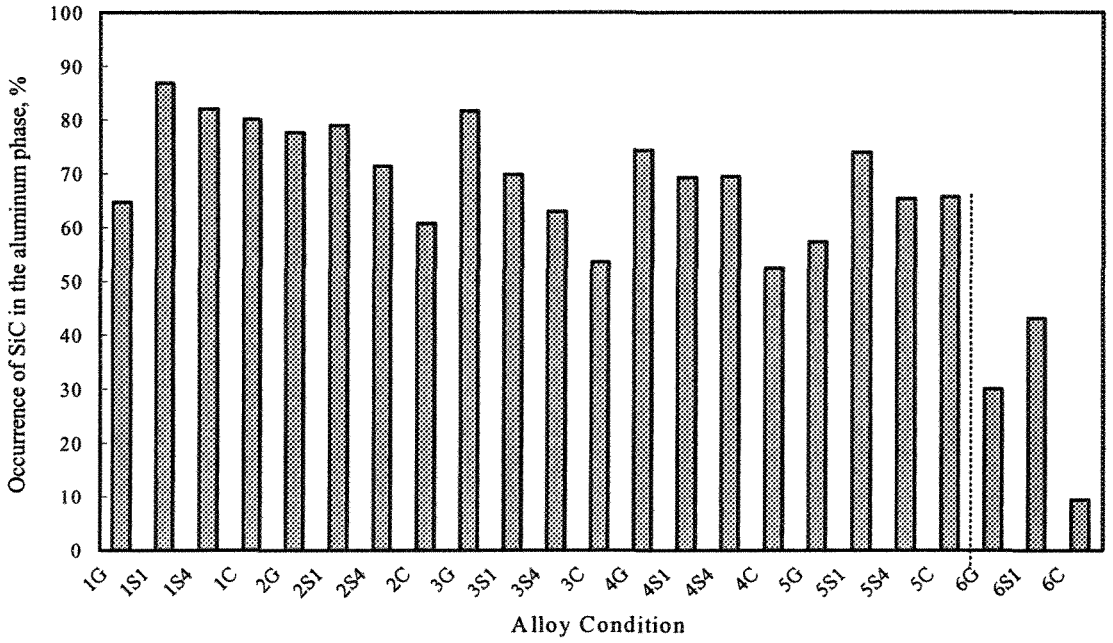

Figure 80 Quantitative results for the occurrence of SiC particles in the α-Al phase.

The stability of SiC is higher than that of Al_4C_3 in the temperature range of interest as shown in Figure 62 (b). Consequently, it is not expected that the SiC will transform to Al_4C_3 during the solidification of the Al-Si-Fe alloys. Actually, the reverse process is observed in the Al alloys injected with Al_4C_3 (see Figure 76):

However, some kind of reaction does take place on the surface of the SiC particles injected into the Al-Si-Fe melts, as seen in Figure 81 (a-d) in the interphase regions around the SiC particle edges, in the low-Si alloys, *i.e.*, alloys 1, 2 and 4. As Figure 81 (e, f) shows, such reactions were not observed in alloy 6. The maps of Figure 82 give an example of this phenomenon. The carbon distribution through lines taken from within the SiC phase (termed *core*) and passing along the interphase region (termed *rim*) are given in the diagram

of Figure 83. The diagrams show that Si diffuses out of the SiC particle leading to the formation of a C-rich interphase region outlining the original SiC particle.

In fact, these layers are not formed because of the higher stability of Al_4C_3 phase since the transformation of SiC to Al_4C_3 is not a favorable reaction according to the thermodynamic data given in Figure 62 (b). The reason for the formation of such shells, richer in carbon and aluminum and poorer in Si when compared with the matrix, is the high liquid and solid solubility of Si in Al. This can be explained as follows. The presence of SiC particles in the low-Si[a] liquid Al alloy leads to the dissolution of the SiC phase, starting from the surface in contact with the liquid. The longer the residence time of the SiC particles in the liquid aluminum, the more severe the dissolution reaction. In a stationary melt -assumed stationary if no appreciable convection or stirring occurs- the rate of dissolution diminishes with time as a result of the formation of a Si-rich layer of liquid in immediate contact with the C-rich interphase region. Stirring of the liquid increases the dissolution process.

The formation of Al_4C_3 is a result of the very small solubility of carbon in solid aluminum. During solidification, aluminum combines with the carbon liberated in the alloy to form Al_4C_3 phase. If the aluminum alloy has a high Si content, the rate of the dissolution reaction decreases until the reaction is eventually stopped, as shown in Figure 81 (f).

---

[a] Low-Si means the concentration of silicon in the alloy is lower than the saturation limit of Si in the alloy. This indicates that in the liquid state, this kind of reaction should theoretically take place in all the alloys containing Si amounts lower than the liquid saturation limit, which is ~12 wt%.

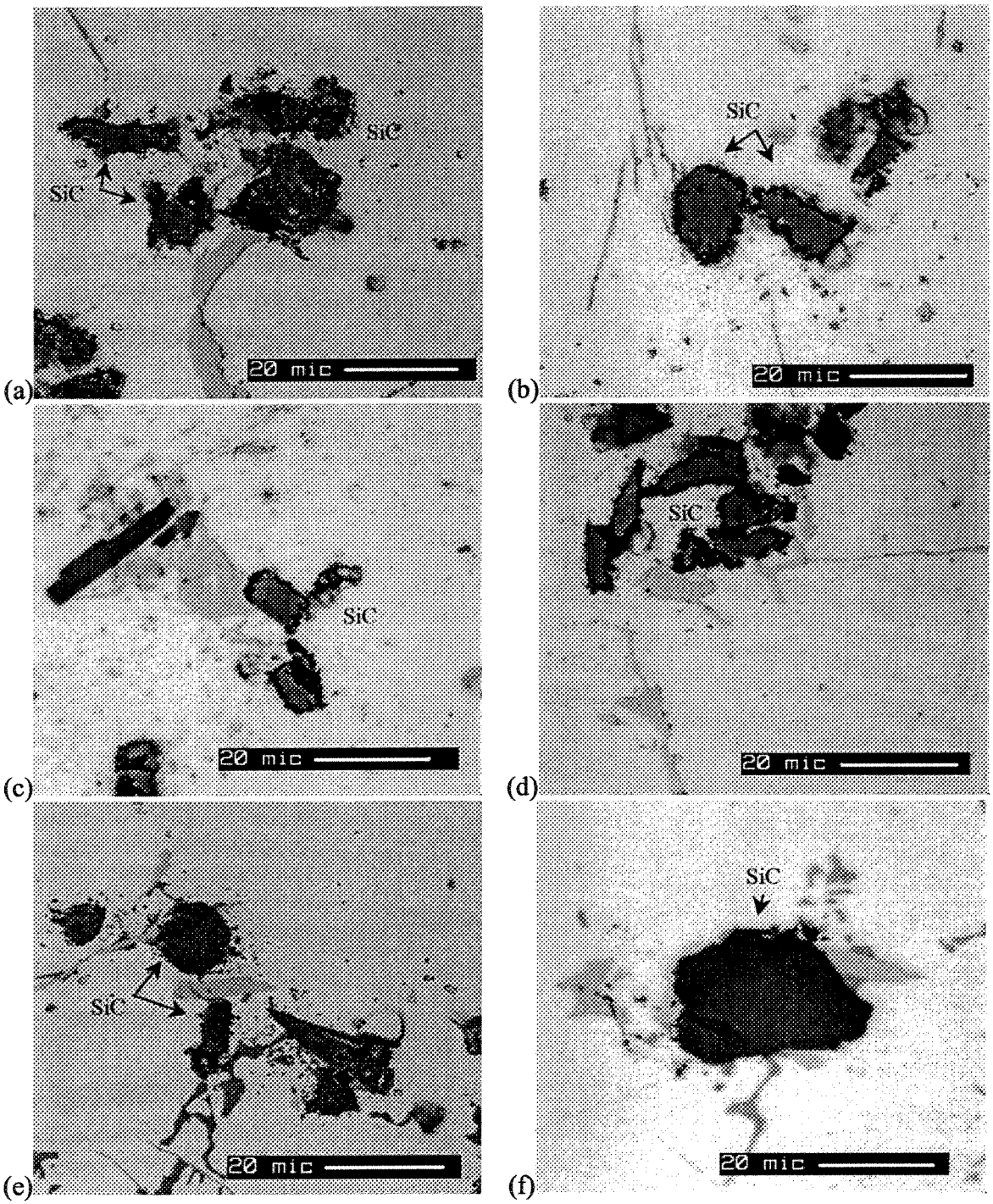

Figure 81 The reaction of SiC with Al alloys: (a-d) reactions around SiC particles in alloys 1, 2 and 4, (cooling rates 0.16, 1.53 and 0.18 °C/s, respectively, and (e, f) no reactions in alloy 6, cooling rate 0.18 °C/s.

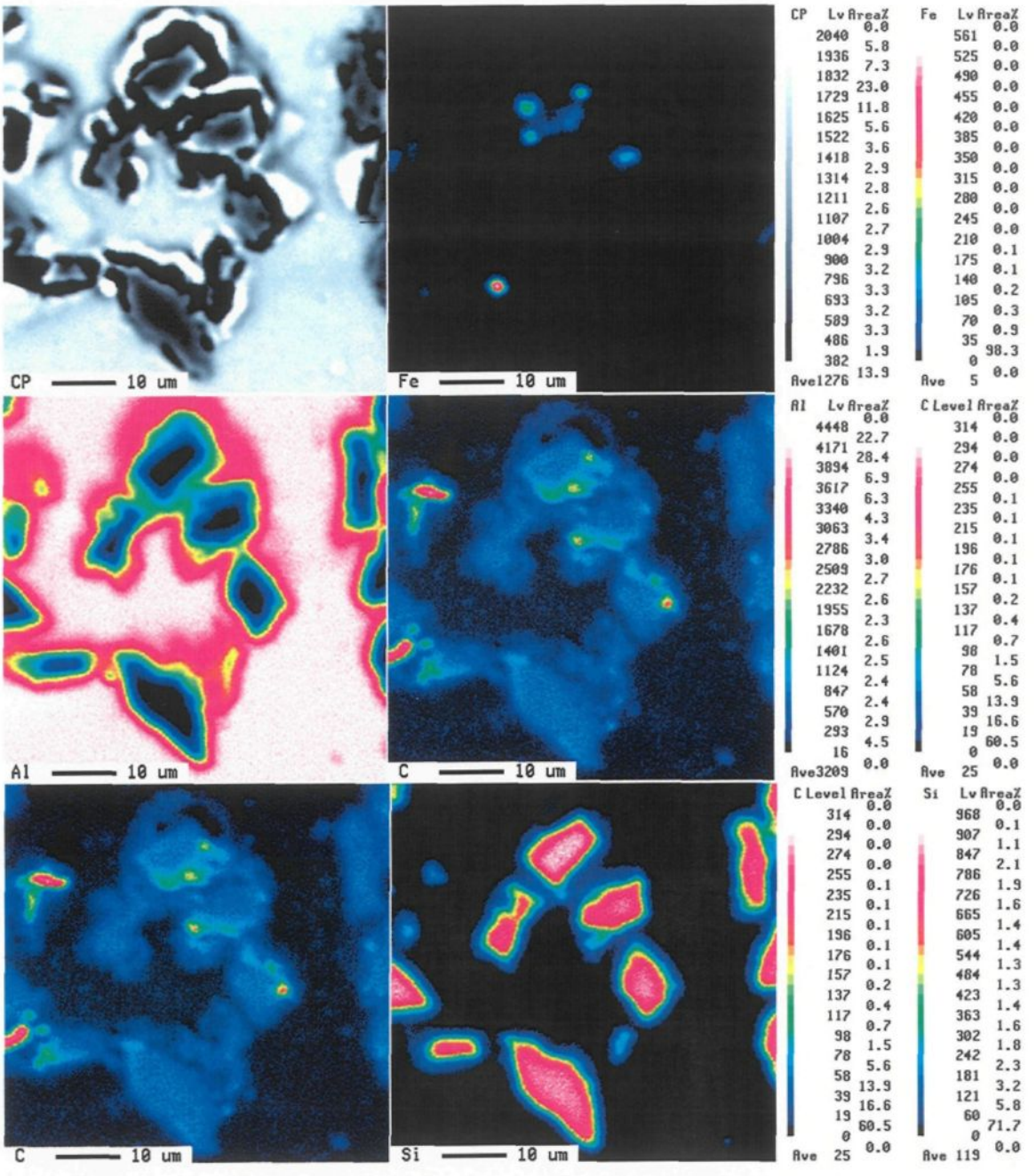

Figure 82 Maps of element distributions showing the formation of aluminum and carbon rich shells on the surface of silicon carbide particles injected in alloy 4, solidified at cooling rate of 0.18 °C/s.

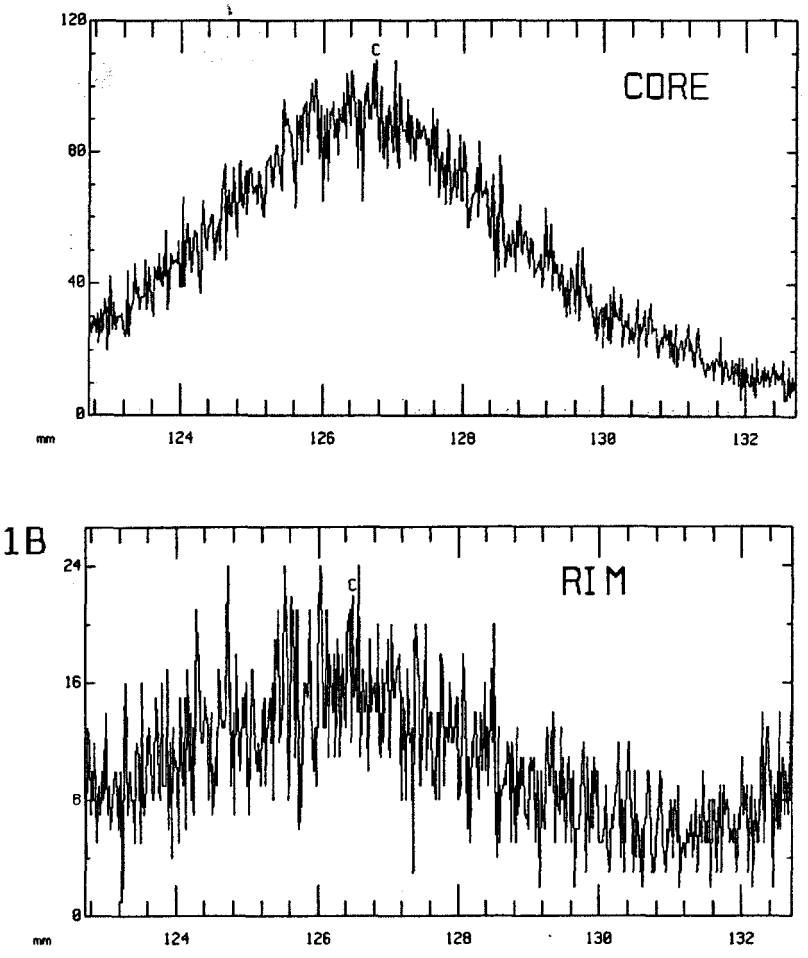

Figure 83 Line scans for carbon within the SiC particle (CORE) and along the interphase region sheathing the particle (RIM), for one of the particles shown in Figure 82.

6.3. Discussion

6.3.1. Nucleation of α-Al in the Diluted Alloys

The role of different inclusions in the nucleation of the matrix phase has been presented in the previous sections. Almost all the inclusions studied possess high occurrence levels in the α-Al phase for alloys 1 to 5. However, the highest levels were achieved by the particles of TiB_2, γ-Al_2O_3, and TiC, respectively. These results imply that such compounds are suitable nucleants for the α-Al solid phase in the alloy compositions and cooling rates examined here (*i.e.*, the composition range covered in alloys 1 to 5, and the cooling rates between 0.2 and 15 °C/s). In alloy 6, most of the inclusion particles that are apparently not reactive with the liquid alloy, *e.g.*, MgO, TiB_2, TiC, α-Al_2O_3, and SiC were pushed to the interdendritic regions.

The most efficient nucleant is the one that can initiate solidification at the smallest undercooling. It is worth noting here that the present results cannot provide an accurate determination of the kind of inclusion that is most efficient and responsible for the initiation of solidification. To do so, one should separate the inclusion content from the melt such that only one type of inclusion is present in the liquid phase. By this means, the potency of this type of inclusion could be reliably estimated from the accompanying nucleation undercooling. However, in the liquid dispersal experiments[95] that aimed to isolate nucleants from the melt, the results were found to be inconclusive. The only output of such experiments was the surprisingly high undercoolings achieved, but which, unfortunately, could not be attributed to specific nucleants.

The measured undercoolings for nucleation of the α-Al phase in three virgin alloys (*viz.*, alloys not injected with inclusion particles) are given in Table 16. Knowing that the alloying element content increases from alloy 1 to alloy 6, it is clear that the value of undercooling increased with the alloy content at both cooling rates (*i.e.*, graphite and metallic mold castings). It is low in diluted alloys, *e.g.*, alloys 1 and 3, and high in the alloy containing high silicon addition, *i.e.*, alloy 6. This provides an insight regarding the nucleation of the α-Al phase in these alloys. The increase in the undercooling in alloy 6 implies that some of the active nucleation sites that played a role in the diluted alloys have become inert or at least less active and require higher undercoolings to initiate nucleation events in the high-Si alloy. The quantitative results of Table 17 confirm this point of view, where the fraction of inclusion particles that are pushed to interdendritic regions is much higher in the case of the high-Si alloy than in the diluted alloys.

Table 16 Nucleation undercooling of the matrix phase for solidification in graphite and metallic molds.

	Nucleation Undercooling of α-Al, °C	
Alloy	Graphite Mold	Metallic Mold
1	0.9	0.6
3	1.2	0.8
6	2.7	1.0

6.3.2. Grain Refinement in Hypoeutectic Al-Si Alloys

A similar phenomenon for the loss of nucleant activity is well documented in grain refinement practice. Wrought or primary aluminum alloys can be readily grain-refined, while cast alloys, containing large amounts of Si, Cu or Zn, exhibit some difficulty in

attaining an acceptable level of grain refinement using conventional grain refiners designed for wrought alloys. The alloying additions hinder the effect of Al-Ti-B grain refinement. The master alloys used to refine the grains in wrought alloys are not equally efficient when used in cast alloys.[106] For example, the Al-5Ti-1B master alloy, which is a foolproof grain refiner in wrought alloys, cannot provide an acceptable level of refining in cast alloys. However, other master alloys such as Al-2.5Ti-2.5B and Al-4B have been developed in order to provide powerful grain refining in cast alloys. The latter alloys also operate using the grain refinement effect of Al-Ti-B or Al-B. Why they are more powerful than the Al-5Ti-1B master alloy will now be discussed in terms of the quantitative results obtained in the present study.

Table 17 Summary of the overall occurrence levels of inclusions in the aluminum phase.

Inclusion	Average of occurrence in the aluminum phase, %		
	Overall (Alloys 1 to 6)	Alloys 1 to 5	Alloy 6
α-Al_2O_3	59.1	65.7	28.1
SiC	64.9	67.0	27.5
TiC	67.8	77.0	22.5
TiB_2	68.3	81.9*	13.9*
MgO	68.8	76.4	35.1
Al_4C_3	70.4	69.3	87.2
CaO	72.7	66.3	91.9
γ-Al_2O_3	79.6	78.4	84.4

* The ratio of the active TiB_2 particles in alloy 6 to those in the dilute alloys is (13.9/81.9 =) 0.17.

The noticeable improved nucleation effects of Al-2.5Ti-2.5B and Al-4B master alloys over that of Al-5Ti-1B in the grain refinement of high-Si alloys can be explained in a rather simple way, originating from the results of the current inoculation experiments.

Before we do so, the efficient nucleants in each master alloy should be determined. In Al-5Ti-1B alloy, the efficient nucleant should be either Al_3Ti or TiB_2 (borides generally), or both. In Al-2.5Ti-2.5B, the excess B stabilizes TiB_2, AlB_2 and/or $(Ti,Al)B_2$, thus, only boride particles may be found in this alloy. This is different from the case in alloy Al-4B, where only AlB_2 particles can be found. Apparently, the Al_3Ti phase should be excluded from our analysis because it can only be found in the low-B master alloy (*i.e.*, alloy Al-5Ti-1B), which is a weak refiner for the cast alloys in question. In addition, it is not an effective refiner in casting alloys containing a few percentages of Si, Cu or Si combined with Cu.[199] It is assumed that TiB_2 is the most active nucleant as proposed by Cibula[200] and confirmed later by Sigworth *et al.*[199,201]. The disregistries of TiB_2 and AlB_2 with α-Al at certain orientations are 4.3 and 3.5 pct, respectively.[202] Both boride types have similar lattice parameters and are isomorphous, confirming the similar nucleation potency of borides. The mixed borides $(Al, Ti)B_2$ should also be good nucleants.[202] In addition, the potency of AlB_2 was also proposed to be equal to that of TiB_2 in the work of Perepezko.[71]

According to simple mass balance calculations, the number of boride moles that form in a master alloy is only proportional to the B content. Therefore, the ratios of boride mole numbers that form in the Al-5Ti-1B, Al-2.5Ti-2.5B and Al-4B master alloys are 1: 2.5: 4, respectively. Assuming that the boride particles have the same average size in the three master alloys, and knowing that the molar volumes of TiB_2 and AlB_2 are almost the same (*i.e.*, 15.4 and 15.2 cm^3, respectively), the number of boride particles will follow the approximate ratios of 1: 2.5: 4 for the master alloys Al-5Ti-1B, Al-2.5Ti-2.5B and Al-4B, respectively. Thus, the number of boride particles contained in samples of the same weight

will be proportional to the B content of each alloy. Consequently, for samples of the same weight, alloy Al-4B will contain four times more boride particles than alloy Al-5Ti-1B.

The result of such simple mass balance calculations in conjunction with our quantitative results can explain qualitatively why the Al-2.5Ti-2.5B and Al-4B master alloys offer more powerful grain refinement in the high-Si alloys than the Al-5Ti-1B alloy. Assume, for example, that Al-5Ti-1B alloy provides 100 active nucleation sites (supposedly borides) when added to a wrought alloy (similar to alloys 1 to 5). The number of active particles reduces to only 17 particles [100 x (13.9/81.9)] if this master alloy is added to a high-Si alloy, such as alloy 6 (multiplication factors taken from Table 17). To compensate for the nucleant efficiency loss, more nucleant particles should be added. The use of master alloys that provide more boride particles than the Al-5Ti-1B alloy can help to achieve a level of grain refinement in the high-Si alloys similar to that in wrought alloys. The commercial practice of grain refinement where Al-2.5Ti-2.5B and Al-4B grain refiners are used for cast alloys is proof of these simple calculations. If alloy Al-4B is used instead of alloy Al-5Ti-1B, the number of active TiB_2 particles may reach 68 (4×17); consequently, a better level of refining will be achieved.

According to our analysis, it follows that the Al-2.5Ti-2.5B master alloy will be a less powerful grain refiner than the Al-4B alloy in the high-Si alloys, since it provides a lesser number of boride particles (ratio of 2.5: 4). The diagrams given in Ref (106) confirm this assumption. Typical grain sizes are borrowed here to demonstrate the relative nucleation efficiencies of Al-2.5Ti-2.5B and Al-4B master alloys, after additions of 0.5 and 1.0 wt pct of each refiner to 356 alloy: the resulting average grain sizes are 370 and 280 μm

when using Al-2.5Ti-2.5B, and 220 and 200 μm when using alloy Al-4B, respectively. Therefore, the quantitative results of the percentage of inclusions (*i.e.*, TiB_2) located within the α-Al phase can be used successfully to rationalize the efficiency differences between different grain refiners in hypoeutectic Al-Si alloys.

6.3.3. Nucleation of α-Al in the High-Si Alloys

According to the distribution of the inclusion particles between the α-Al phase and the interdendritic regions of alloy 6, one can distinguish between two groups of inclusions. The first group includes CaO, Al_4C_3, and γ-Al_2O_3, which have high occurrence levels in the α-Al phase. The second group of inclusions includes MgO, TiB_2, TiC, α-Al_2O_3, and SiC, which are mainly pushed to the interdendritic regions.

The first group of inclusions has therefore uniform high occurrence levels within the α-Al phase in all the alloys studied (see Table 17). Consequently, their behavior with respect to the nucleation of the matrix phase can be generally characterized by constancy (or near constancy) over the range of alloys and cooling conditions studied, see Figure 63, Figure 74, and Figure 78. Two of these inclusions, CaO and Al_4C_3, were observed to react with the alloy components and form several chemical compounds.

The second group of inclusions exhibits a large drop in their occurrence levels in the α-Al phase of alloy 6 (Table 17). In other words, these inclusion particles become less potent in nucleating the α-Al phase with the increase in the alloying element content in the alloy (*i.e.*, Si). This may be attributed to the so-called poisoning of the nucleation sites,

which takes place due to the segregation of Si to the surface of nucleant particles, altering their surface characteristics, see Figure 67, Figure 70, Figure 73, Figure 77, and Figure 80.

Based on these data, one can conclude that in the dilute Al-Si-Fe alloys almost all inclusions are good nucleants for α-Al phase, in particular, the TiB_2, γ-Al_2O_3 and TiC particles. On the other hand, the γ-Al_2O_3, CaO and Al_4C_3 particles are efficient nucleants for α-Al in the high-Si alloy (a hypoeutectic Al-alloy).

6.3.4. Solute Segregation to the Liquid-Al/Inclusion Interfaces

The theory of solute or impurity segregation to surfaces and grain boundaries in metals is well developed and several models have been proposed to describe a variety of segregation and adsorption conditions.[203] In contrast, the segregation of solutes to the heterophase interfaces in metals is far from being well understood. The metal/inclusion or metal/ceramic interfaces represent the case of segregation to heterophase interfaces and are of interest in the present work. Solute segregation to heterophase interfaces is more complicated due to the nature of the metal/inclusion bond[204], and the poor accessibility of such interfaces.[205] The Gibbs adsorption concept, which is usually used to describe solute segregation to a metal surface, is adopted here in a qualitative sense since both phenomena result from identical processes. The basic prediction of the Gibbs adsorption isotherms is that if they lower the surface energy of the interface, the solute atoms will segregate preferentially to the interface.[206] This can be predicted from the equation:[203]

$$\left(\frac{d\gamma}{d\ln X_c}\right)_T = -RT\Gamma \qquad (59)$$

where γ is the surface or interfacial free energy, X_c is the bulk solute molar concentration and Γ is the interfacial excess of the solute species expressed in mol/m^2. Units of atomic fraction and number of atoms/m^2 can be alternatively used to express X_c and Γ to describe the interfacial solute segregations.[203,207]

The resultant interface is characterized by a lower energy and a higher solute concentration, which therefore give rise to zones of chemical heterogeneity at the interface. It follows that the equilibrium level of solute enrichment at the interface depends on system parameters such as the magnitude of the interfacial energy, bulk solute concentration, and the nature of the solute atoms. For instance, the effect of the latter on the surface tension of aluminum alloys can be estimated as follows. Generally, additions that have a lower surface tension reduce the surface tension of aluminum, but ones that have a higher surface tension do not affect the latter appreciably.[124] This is consistent with the Gibbs rule that additions that reduce surface tension segregate to the surface (Eq. 59). The equilibrium solute segregation to the interfaces results in the formation of only one or two solute-rich atomic layers, which in fact cannot explain the formation of segregation layers of up to several microns that are usually observed in metallurgical practice.

The segregation process is very sensitive to the rate of cooling from a high temperature.[203] A high cooling rate leads to nonequilibrium segregation, which results in the build-up of a large interface layer. In nonequilibrium segregation, the thickness of the solute-rich layer depends more probably on the kinetic parameters involved. For example, Si solubility in aluminum is reduced with the increase of cooling rate,[124] a condition that can lead to greater Si segregation at the interfaces. The diffusion coefficient of the solute

atoms is also an important factor in nonequilibrium segregation. The diffusion coefficient of Si in Al is much higher than that of Fe.[39] Thus, if both solute types have the same driving force for segregation, Si will be more concentrated at the interface than Fe within a given period of time, as long as equilibrium is not attained.

The solute segregations of Si and Fe in the current Al-alloys are discussed qualitatively here. The surface tensions of Al, Si and Fe at their respective melting points are 866, 730, and 1880 ergs/cm^2, respectively.[164] Consequently, Si is expected to segregate preferentially to external and internal surfaces and by analogy to the heterophase interfaces of aluminum alloys, while Fe is not. However, the driving force for Si segregation, as visualized by its surface tension relative to that of aluminum is not very high, implying that the enrichment of Si at the aluminum surface will be only slightly pronounced even in alloys containing high Si contents. The experimental observations confirm this point where Si is seen to lower the surface energy of the liquid aluminum only slightly, even at high concentrations such as 12 wt pct.[39]

In the situation where the free energy at the metal/inclusion interface is substantially high, pronounced Si segregation is expected to take place. This deduction is supported by the observation of a high-Si interphase region around the CaO particles and the formation of high-Si containing phases (*i.e.*, $CaAl_{2.5}Si_{1.8}O_{0.37}$ and $SiAl_{4.5}Fe_{0.17}$), in alloy 6. It can also be noted that the Fe/Si atomic ratio in the second compound is far below that observed in the Fe-intermetallic phases, namely Al_5FeSi and Al_4FeSi_2, that form in the alloy at the two extreme cooling rates explored (Chapter 4). This supports the deduction that Fe does not

segregate to interfaces in Al alloys. If this is the case then one must question the role that Si plays in the nucleation of α-Al in the high-Si alloys.

6.3.5. The Influence of Si on the Nucleation of the α-Al Phase

It is clear from the current quantitative results for the number of inclusion particles that lie within the α-Al phase in alloy 6 that, in most cases, the high silicon content hinders the nucleation of the solid α-Al phase. The nucleation process is affected by the interfacial attachment kinetics. Atomic attachment becomes favorable only when the segregated atoms are of similar size. The solvent/solute atomic size ratio will therefore dictate whether or not precipitation of a crystal layer is favorable.[184] When atomic misfit is significant, even though segregation is thermodynamically favorable, stabilization of the crystal layer will not be feasible.

Bäckerud *et al.*[208] presented a qualitative index for the performance of various solute elements as nucleants for aluminum when added as borides through their atomic size match/mismatch with aluminum. When the solvent/solute size ratio is close to unity, the probability of providing a well-ordered crystal is greatly enhanced, and efficient grain refinement is achieved, as was experimentally verified with Nb, Ti, and Ta.[208]

On the other hand, significant mismatch leads to poisoning by hindering the precipitation of a stable crystal layer.[184] Knowing that the atomic sizes of Ti, Al and Si are 2, 1.82 and 1.46 Å, respectively, it should be expected that the presence of segregated Si at the interface of TiB_2 particles would hinder the nucleation of the solid aluminum phase, since the segregated Si atoms would change the atomic size matching from 0.91 in Al/Ti to

0.73 in Si/Ti after segregation. This effect should be higher in alloy 6, containing 6.32 % Si, since the probability of a continuous Si monolayer formation on the surface of nucleants is expected. While the effect of Si in hindering the nucleation of the aluminum in the high-Si alloys is readily explained by its poisoning effect due the atomic mismatch with Ti in TiB_2, similar and likely other mechanisms may be operating in the case of the other inclusions (*i.e.*, MgO, TiC, α-Al_2O_3, and SiC), where low nucleation activity was observed.

The effect of Si in reducing the nucleation efficiency of the different inclusions can be justified alternatively, in terms of the general observations of solute effects as quantified by the growth restricting factor, GRF.[202,209] The growth restricting factor is given by:

$$GRF = mC_0(k-1) \tag{60}$$

where m is the liquidus gradient, C_0 is the bulk composition, and k is the solute partition coefficient between solid and liquid. The value of $m(k-1)$ is 5.9 and 2.9 for Si and Fe, respectively. The grain refining effect of the solute is attributed to the constitutional undercooling that slows down the growth of the dendrite due to the diffusion of the solute in front of the interface until the activation of the other nucleation sites takes place. This effect is usually observed at low solute concentrations. At high solute concentration, the growth mode changes from being diffusion-controlled to dendrite-tip-radius-controlled. In terms of GRF, grain refining is observed as long as the GRF is lower than 20. At values greater than 20, grain sizes begin to increase. Silicon promotes grain refining at about 3 wt pct concentration; above this level grain size begins to increase. This may be attributed to the increasing magnitude of the Si poisoning effect with the increase in Si content of the alloy as discussed previously. This indicates that at this level of Si, the segregation to the

surface of nucleant particles is large enough so that continuous monolayers of excess Si are stable at the surface of an increasing number of the active nucleants that are vital for achieving the required level of grain refining.

So far, we have discussed the effect of Si segregation to the surface of inclusions and have shown qualitatively how this phenomenon can affect the nucleation of the α-solid on the surface of substrates in the high-Si alloys (*viz.*, high enough to induce poisoning of nucleation sites). Since nucleation is an energetic process, the poisoning effect of Si should be discussed in view of its effect on the interfacial energy balance required for nucleation.

The catalytic efficiency, f(θ), of a substrate is given by:[68]

$$f(\theta)=\frac{(2+\cos\theta)(1-\cos\theta)^2}{4} \tag{61}$$

where θ is the contact angle between the nucleus and the substrate. The smaller the value of f(θ), the greater the catalytic efficiency of the substrate. The value of f(θ) can be adversely affected by the segregation of Si at the inclusion/liquid interfaces.

It is well demonstrated that Si segregates to the heterophase interfaces between the liquid metal and inclusions to lower the interfacial energy at such interfaces. This can be interpreted in another sense as follows. The segregation of Si to the metal/inclusion interfaces lowers the free energy of such interfaces. Consequently, the energy balance necessary for nucleation, that holds at the triple line in the case of a virgin liquid-metal/inclusion interface would not persist after Si segregation.

Figure 84 gives a schematic illustration of the effect of Si segregation on the energy balance at the triple line and, therefore, on the catalytic efficiency of inclusions. It is

assumed that the interfacial energies at the solid/liquid interface, γ_{SL}, and inclusion/solid interface, γ_{PS}, are constants and given by 1320 and 400 erg/cm^2, respectively. Only the interfacial energy component at the inclusion/liquid interface, γ_{PL}, is assumed to change with the excess Si concentration. It is assumed also in this example that with no Si segregation, the contact angle between the solid and the substrate is 5° and the catalytic efficiency, f(θ), of the given substrate is therefore 0.00001 (Figure 84 (a)). It can be seen that even a small decrease in the magnitude of γ_{PL} can drastically lower the catalytic efficiency of the substrate, from 0.00001 at γ_{PL} of 1715 erg/cm^2 to 0.00017 at γ_{PL} of 1700 erg/cm^2 (Figure 84 (b)). The decrease in the interfacial energy component is in the order of 0.99 [=1700/1715], while the decrease in the catalytic efficiency is 17 times [=0.00017/0.00001]. Further decrease in γ_{PL} to 1540 erg/cm^2 (corresponding to 0.90 of the original γ_{PL}) leads to an exponential decrease in the catalytic efficiency of about 1300 times [=0.013/0.00001], *i.e.*, three orders of magnitude lower, as seen in Figure 84 (c).

The diagram of Figure 85 shows the variation of catalytic efficiency, f(θ), as a function of the reduction in the liquid/inclusion interfacial energy, γ_{PL}. The reduction in the latter is given by the fraction $\gamma_{PL(Si)}/\gamma_{PL(virgin)}$, where $\gamma_{PL(Si)}$ is the expected reduced interfacial energy due to Si segregation, and $\gamma_{PL(virgin)}$ is the original liquid/inclusion interfacial energy. The diagram is drawn for a substrate that has an initial condition corresponding to that of Figure 84 (a). It is clear that the catalytic efficiency is very sensitive to the variation of the interfacial energy component, γ_{PL}: slight decreases in γ_{PL} cause considerable losses of the catalytic efficiency of the substrate surface.

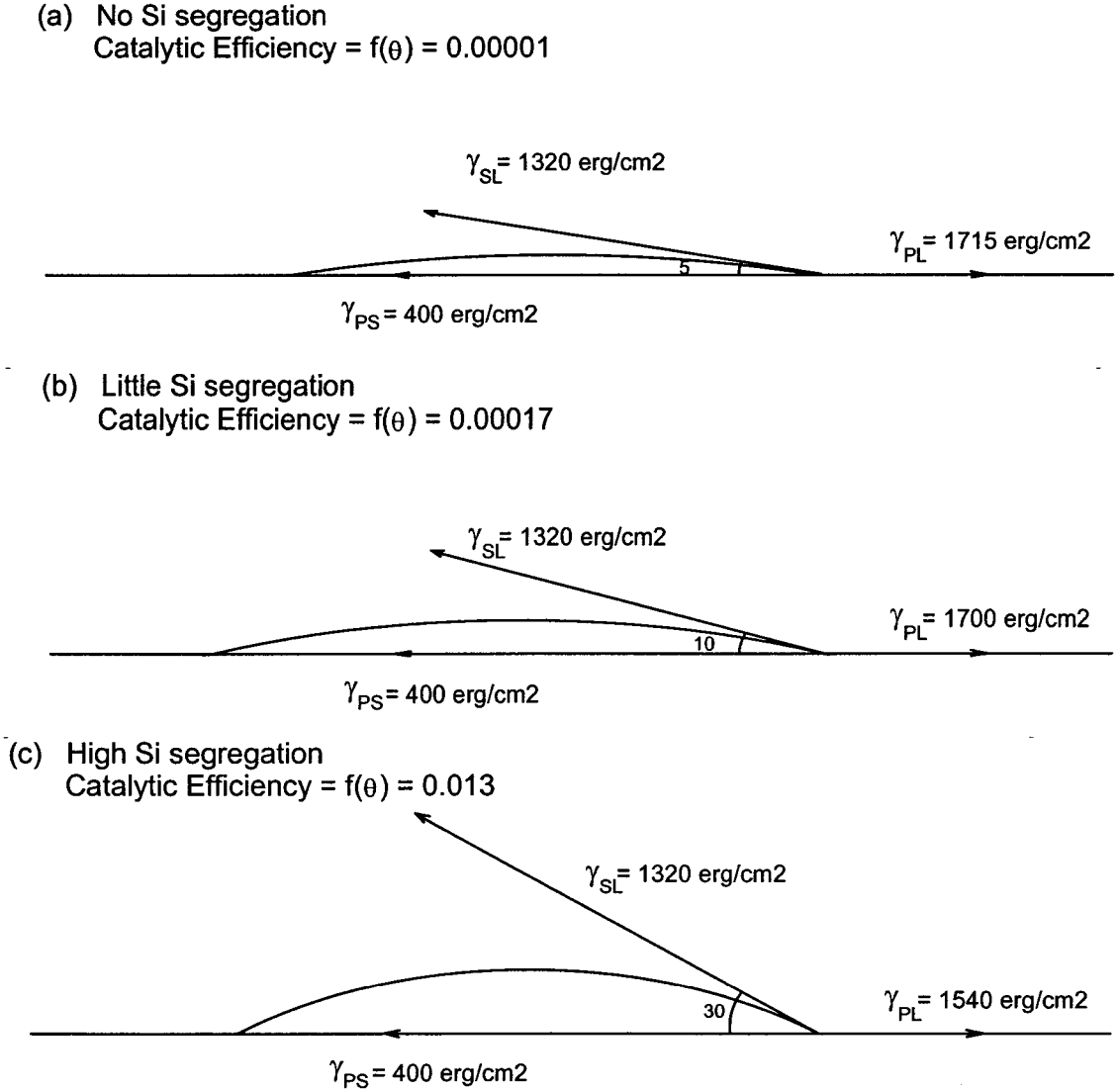

Figure 84 Schematic showing the influence of variation in the liquid/inclusion interfacial energy on the nucleation catalytic efficiency of substrates.

We proceed with our assumption that the solute segregation to heterophase interfaces in aluminum is analogous to solute segregation to the liquid metal surface, in order to discuss the significance of Figure 85. For liquid aluminum, the surface tension is lowered from 868 to 815 erg/cm^2, *i.e.*, 0.94, with minor (< 1 wt pct) additions of Si.[39] By

analogy, reductions of this order in γ_{PL} can cause a drastic decrease in the catalytic efficiency of nucleants in the liquid aluminum from 0.00001 to 0.0075, *i.e.*, 750 times lower (see Figure 85). As a result, a few wt pct of Si additions can cause poisoning of the active nucleants in the liquid aluminum through the change of the interfacial energy balance so that the characteristic contact angle increases and therefore the catalytic efficiency of nucleants decreases dramatically. This conclusion explains our experimental results that showed large reductions in the occurrence levels of different inclusions, such as TiB_2, MgO, TiC, α-Al_2O_3, and SiC in the α-Al phase of alloy 6 (containing 6.3 pct Si).

The question now arises as to why some inclusions, such as CaO, Al_4C_3 and γ-Al_2O_3 are exceptionally active nucleants for the matrix phase in the high-Si alloy (alloy 6). To answer this question, we should recall the features of the efficient nucleant and verify whether these inclusions possess specific merits or not.

6.3.6. Influence of Surface Characteristics on the Heterogeneous Nucleation Process

The requirements of an efficient nucleant (or grain refiner) can be listed in order of priority according to Perepezko[71] as follows:

(1) To promote the formation of crystals on a nucleant, the energy of the interface between the nucleant and the liquid should be higher than that between the nucleant and the crystal solid (the cap model of nucleation[99]).

(2) A theoretical means to achieve requirement (a) is to have a good crystallographic fit between the nucleant and the solid crystal.

(3) The melt should wet the surface of the nucleant.

(4) The solid nucleant should remain widely dispersed in the liquid for a uniform refining.

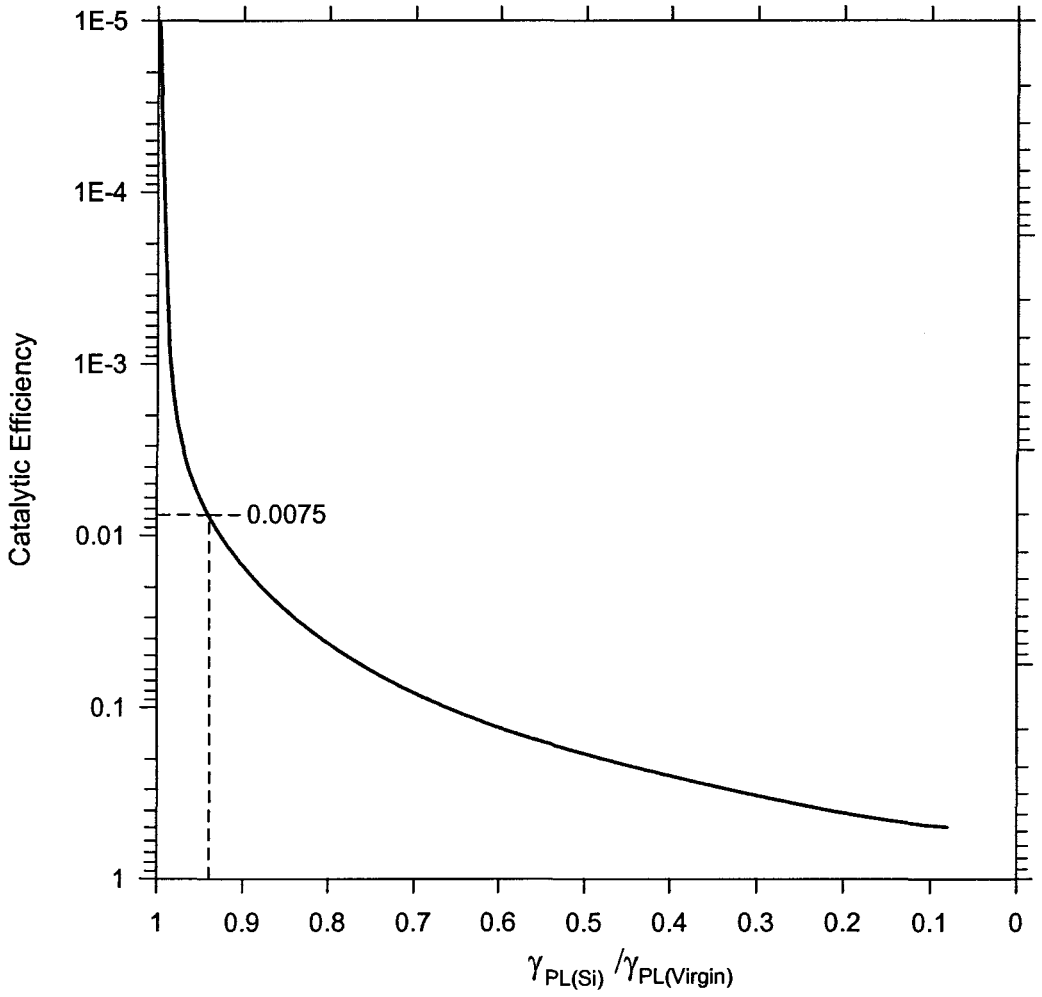

Figure 85 Variation of catalytic efficiency, f(θ), as a function of the reduction in the liquid/inclusion interfacial energy (given by $\gamma_{PL(Si)}/\gamma_{PL(virgin)}$).

It is clear from our results that the first requirement for the efficient nucleant - concerning the energetic requirements- is largely satisfied by most of the inclusions studied here, since high percentages of these inclusions were observed within the α-Al phase. However, this does not mean that all these inclusion types satisfy the lattice compatibility

requirement with the α-Al phase. It can be thought that the crystallographic fit (or lattice compatibility) between the nucleant and the solid crystal is not so important a requirement in the process of solid nucleation. As a consequence, one can deduce that there are other factors besides the lattice compatibility that can favor the solid heterogeneous nucleation process.

Glicksman and Childs[98] observed that *the chemical and physical characteristics of the surface are more important for the nucleation than lattice registry.* Their conclusion is very consistent with our results, and can explain the exceptional potency of CaO and Al_4C_3 and γ-Al_2O_3 to nucleate the α-Al phase in alloy 6.

The γ-Al_2O_3 phase, for which the highest occurrence levels in the α-Al phase were recorded, is an enormously important catalyst in several industrial applications.[210] The high catalytic potency of the γ-Al_2O_3 particles can therefore be attributed in part to their very high surface energy, and in part to the fact that the crystal structure of γ-Al_2O_3 is characterized by the occurrence of cation vacancies, which have a significant influence on surface morphology,[211] such that a larger specific area of active surface is exposed. On the surface, additional active sites were identified due to the cation vacancies.[211]

The very high surface energy implies that the γ-Al_2O_3 particle maintains a very high energy, γ_{PL}, at its interface with the liquid aluminum, comparable to γ_{SL} and γ_{PS}. Therefore, solute (Si) segregation to the surface of γ-Al_2O_3 should not lower the surface free energy to a level at which the poisoning effect dominates the catalytic effect. On the other hand, the cation vacancies (*viz.*, the sites of lost Al^{+3}) are expected to accommodate the segregated Si

atoms at the surface of γ-Al_2O_3 particles. The resultant partial saturation of the surface cation vacancies due to excess concentration of the segregated Si atoms should cause some relaxation of the surface energy. However, the difference between the surface and internal densities of cation vacancies constitutes a potential difference and therefore a driving force for Si migration from the surface to the interior of γ-Al_2O_3 particles (*i.e.*, the concept of diffusion in solids). Consequently, the surface relaxation exerts a driving force for the diffusion of Si from the surface to the interior of particles in order to reach a uniform density profile of either Si or cation vacancies in the γ-Al_2O_3 particles.

Such diffusion is energetically feasible since the process takes place at a high temperature, 750 °C. In addition, a Si atom is smaller than an Al atom, resulting in easier Si-diffusion than Al-diffusion. The whole image of such a process is the dynamic segregation of Si to the surface of γ-Al_2O_3 particles and a concurrent diffusion of Si from the surface to the interior of these particles. The resultant Si concentration at the surface depends on the time elapsed and the diffusion rate. The diffusion rate in solids is generally slow, and in the liquid, it is most likely disturbed by the convection. As a result, it is expected that Si segregation to the liquid-Al/γ-Al_2O_3 interfaces will not cause a noticeable poisoning effect for such particles under the present process conditions. Thus, it can be concluded that the high potency of γ-Al_2O_3 particles to nucleate the α-Al phase in the high-Si alloy, alloy 6, can be attributed to its crystal and surface physical characteristics, which relate to the necessary physical characteristics of the surface as proposed by Glicksman and Childs.[98]

The next two inclusions that possessed the highest occurrence levels in the α-Al phase of alloy 6 are CaO and Al_4C_3 (see Table 17). We confirmed in our study that both CaO and Al_4C_3 are reactive with the aluminum alloy, and form several compounds and oxides. In alloy 6, CaO forms the $CaAl_{2.5}Si_{1.8}O_{0.37}$ phase, which has a very high Si content. The Al_4C_3 particles transform to the SiC phase in the Al-Si alloys due to the higher thermodynamic stability of SiC compared to Al_4C_3. As a result, excess concentrations of the segregated Si at the surface of CaO and Al_4C_3 are continuously consumed in the formation of reaction products. Therefore, due to their chemical reactivity, the poisoning effect of Si on such nucleant particles would not be noticeable. In other words, the chemical reactivity of the substrate promotes heterogeneous nucleation on its surface. In conclusion, the high potencies of CaO and Al_4C_3 in nucleating the α-Al phase represent the chemical characteristics of the surface required for an efficient nucleant, as proposed by Glicksman and Childs.[98]

Therefore, the chemical and physical characteristics of the surface, if suitable, can provide efficient nucleation on the substrate. It is worth mentioning here that, it was not possible to verify the conclusions of Glicksman and Childs[98] before the utilization of the injection technique, since there were no means of introducing enough quantities of virgin solid particles into liquid metals to enable a reliable quantitative evaluation.

6.3.7. Role of Wettability in the Solid Nucleation and Grain Refinement Processes

The last two requirements for an efficient nucleant, namely the wettability of the inclusion by the liquid and its uniform distribution, are discussed in this section. Among all

the inclusions used in the present study,[161] TiB_2 has the smallest wetting angle, 37° (*i.e.*, best wettability) with the liquid aluminum in the temperature range of conventional melting processes. In fact, the wettability data of some inclusions such as γ-Al_2O_3, CaO, MgO and Al_4C_3 with aluminum alloys, are not available in the literature. However, a special sense for predicting qualitatively the wettability of inclusions was developed based on our observations when conducting the injection work. Based on these observations, almost all the inclusions used in this work have poor wettability with Al-alloys in comparison with TiB_2. Furthermore, only TiB_2 particles can be readily introduced into liquid aluminum in large quantities. The proof of our claim is the huge number of TiB_2 particles that can be added into the aluminum melts, as is clear from the micrograph of Figure 69. Consequently, although some inclusions have higher occurrence levels than TiB_2 in the α-Al, they cannot be retained inside the liquid aluminum in appreciable quantities to accomplish grain refining on account of their poor wettability.

If wettability is the barrier for introducing sufficient amounts of a given efficient nucleant for the purpose of grain refining, one may ask why conventional solid-to-liquid addition techniques[86] are not used for this purpose. This may be argued as follows.

The well-established processes of introducing solid particles into a melt, such as the vortex method that are used in the manufacturing of composite materials, are not capable of adding suitable quantities of very fine powders (micron- and sub-micron-sized particles) into the liquid metals. The addition of such fine particles, if possible, can lead to efficient refining. The reason for the deficiency of such techniques lies in the indispensable requirement of considerably high rotation speeds in the melt, which are important to

provide the kinetic energy necessary to overcome the energy barrier of incorporation (Chapter 5). On the other hand, if successful additions are made using the vortex technique, the surface properties of the added particles are most likely changed during their residence time in the vortex,[87] a fact that can drastically alter their potency to nucleate the solid phase.

Why cannot the injection technique be used for the introduction of such very fine particles? The capability of the injection technique is very much restricted by the size of the particles. Very small or very large particles cannot be introduced into the liquid metal using the injection technique for several reasons as described in Chapter 5. As a consequence, the inclusions (or inoculants) other than TiB_2, which have poor wettability with liquid aluminum alloys, cannot be used in industrial grain refining, for the aforementioned reasons.

However, if the wettability of these particles is improved due to their chemical reactivity with the alloy components, which may be the case for the CaO and Al_4C_3 inclusions in alloy 6, attention should be paid to avoid the effect of these reactions on the chemical composition of the alloy. For example, CaO and Al_4C_3 particles react with Al-Si melts and form high-Si compounds (details given in a previous section). If 1 or 2 wt pct of these nucleants are added to the Al-Si alloy, a drastic reduction in the silicon content of the alloy is expected, similar to the loss of Si reported by Loper and Cho[169] when elemental Ca was added to an Al-5% Si alloy. Therefore, the reactivity of CaO or Al_4C_3 with the Al-Si alloys constitutes the main obstacle for their role as nucleants even if the other requirements are fulfilled. It can be concluded, therefore, that an efficient grain refiner

should be chemically inert with the liquid phase and, if it is reactive, the reaction products should not tend to alter the chemistry balance of the alloy.

The last requirement of an efficient nucleant is the wide dispersion of the nucleant particles in the liquid phase before solidification. The results of the current work indicate that CaO, MgO, and TiB_2 particles are prone to clustering because of the convection due to the stirring of the liquid alloy. This fact was also noted in Chapter 5. The potency of the grain refiner, which also depends on its uniform distribution, is at risk when clustering of the nucleant particles takes place. This fade phenomenon causes a high deficiency in the role of TiB_2 if prolonged time elapses in the liquid state before solidification, as has been often reported in the literature.

6.4. Summary

The systematic inoculation experiments carried out to study the influence of various inclusions on the nucleation of the α-Al phase in Al-Si-Fe alloys at different cooling rates showed that in the dilute alloys (containing less than 1.5 pct Si+Fe), almost all the inclusion types have high percentages of occurrence within the α-Al phase, indicating that nucleation is promoted on the surface of such inclusions. In a hypoeutectic Al-Si alloy containing 6.3 wt pct Si, the inclusion particles of MgO, TiB_2, TiC, α-Al_2O_3, and SiC become mostly inactive nucleants and are pushed to the interdendritic regions because of the dominant poisoning effect of Si.

The present results were used successfully to explain the efficiency differences between commercial grain refiners in hypoeutectic Al-Si alloys. Silicon is observed to preferentially segregate to the liquid-Al/inclusion interfaces so as to lower their free energy. A theoretical analysis of the poisoning effect of Si showed that Si segregation to the liquid/nucleant interface alters the interfacial energy balance so that the catalytic efficiency of the nucleant particles is dramatically reduced. Careful analysis showed that the poisoning effect of Si in the hypoeutectic Al-Si alloy is overcome when the nucleant particles have active surface characteristics as represented by the high catalytic potencies of γ-Al_2O_3, CaO and Al_4C_3 particles in nucleating the α-Al phase in the alloy. Although some inclusions have comparable or higher occurrence levels than TiB_2 in the α-Al phase, they cannot be used as efficient nucleants either due to their poor wettability with liquid aluminum or their chemical reactivity.

CHAPTER 7

NUCLEATION OF Fe-INTERMETALLICS IN THE Al-Si-Fe ALLOYS: THE ROLE OF INCLUSIONS

CHAPTER 7

NUCLEATION OF Fe-INTERMETALLICS IN THE Al-Si-Fe ALLOYS: THE ROLE OF INCLUSIONS

7.1. Introduction

It has been established that even in a sample of high-purity liquid metal there is a nucleant (inclusion) particle concentration of the order of about $10^{12}m^{-3}$.[71] This value is much higher in commercial purity alloy melts. In commercial aluminum and aluminum alloys, a large variety of inclusions are present in small quantities. The common types of these inclusions are: oxides, carbides, borides, nitrides, chlorides, and fluorides.[76,77,78,79]

Inclusions were observed to be responsible for the heterogeneous nucleation of different phases.[83,84,10] The nucleation of certain Fe-intermetallic phases was reported to be enhanced by the addition of Al-Ti-B grain refiners.[19,85,25] Some of these works were based on the assumption that TiB_2 particles added with the grain refiner nucleate the second-phase particles in the same manner as they do for the matrix phase, while others suggested that the promotion of certain phases in the presence of Al-Ti-B grain refiner is due to its effect on altering the growth conditions that stabilize some intermetallics over others.[25] However, there is apparently no direct observation of the nucleation of Fe-intermetallics on the surface of TiB_2 particles in these works.[59] Other workers attributed the preferential

formation of certain Fe-intermetallic phases to the promotion of nucleation on certain inclusions[10] and unidentified potent catalysts in the melt (see for example the review of Allen *et al.*[25]).

Experiments of the present chapter were done to evaluate systematically the potency of different inclusions for the nucleation of the Fe-intermetallic phases formed in Al-Si-Fe alloys. The results of this work are based on direct observations, through the optical microscope, for the evident physical contact between the nucleated intermetallics and the inclusion particles. These particles were introduced into the molten alloys using the gas injection technique.[87]

The results on the formation of iron-bearing phases in dilute Al-Si-Fe alloys, the analysis of the gas injection technique used for the inclusion additions in the present study and the role of inclusions in the nucleation of the α-Al phase in Al-Si-Fe alloys have been presented in chapters 4, 5 and 6. This chapter places emphasis on of the influence of different inclusions on the nucleation of the Fe-intermetallic phases.

7.2. Results

It was generally noticed that the Fe-intermetallics observed in contact with inclusions have the same morphology as those found distant from the inclusion particles in the microstructure. Verification by microanalysis was carried out is several cases. The Fe-intermetallic phases found on the surface of inclusions were similar to those phases, which form in alloys under identical cooling conditions, indicating that nucleation of the inclusion

particles does not change the identity of the stable phases under a given alloy composition and cooling rate.

The formation of the Fe-intermetallic phases in the present experimental alloys was studied in detail, in particular, the effect of alloy composition, cooling rate and solute segregation on the type of Fe-intermetallic phase, their volume fraction and density characteristics (Chapter 4).[2] The chemical composition of the Fe-intermetallic phases formed in the present alloys are given in Figure 42. From this figure, it can be seen that the formation of these phases is mainly dependent on the alloy composition and, therefore, the solidification paths. In diluted Al-Si-Fe alloys, the liquid approaches the composition of these phases very late during solidification, resulting in formation of a majority of such phase particles in the interdendritic regions, a fact that complicates the interpretation in the current work regarding the nucleation of these phases in the interdendritic regions. Due to the small volume of the interdendritic regions and the high concentration of the solute atoms (Si and Fe), the nucleation of Fe-intermetallics can be easily promoted on the efficient nucleants in these regions. In this work, the physical contact between a substrate and the nucleated phase (as usually considered in the literature) is an indication of nucleation.

Before we present our results, a few points concerning the distribution of the inclusion particles between the microstructure regions and the nature of second-phase content in the present alloys should be clarified. In alloys 1 to 5, the major part of the injected inclusions was observed to lie within the α-Al phase with the rest rejected to the interdendritic regions. Thus, the overall ratio of inclusion particles observed in contact with

Fe-intermetallic phases is mainly affected by the percentage of physical contacts within the α-Al phase. As is well known, the majority of the Fe-intermetallics form in the interdendritic regions. Therefore, percentages above 20 and 40 within the α-Al phase are usually considered high and very high, respectively. Similar percentages in the interdendritic regions are considered to be low.

In alloy 6, high percentages of the injected inclusions were observed in the interdendritic regions, and little within the α-Al phase. The phenomenon of the Si-poisoning effect was also observed in the nucleation of Fe-intermetallics on the inclusion particles. Inclusion particles that have as high as 20 pct nucleation events in alloy 6, therefore, are classified as potent nucleants.

In microstructures containing two or more intermetallic phases, it is not possible to determine which one of these phases nucleates heterogeneously and efficiently on the inclusion particles when these phases exhibit similar morphology. In some cases it is possible to identify the relative potency of a nucleant for nucleation in a multi-phase microstructure. When there is a dominating phase in the microstructure, the potency of the inclusion relates to the dominating phase. This is applicable, for example, in alloys 4 and 5 cooled in the graphite mold (cooling rates of 0.18 °C/s and 0.19 °C/s, respectively). The phase content of alloy 4 is α-AlFeSi and β-AlFeSi, the former being the dominating phase. In alloy 5, α-AlFeSi and binary Al-Fe phases (*i.e.*, Al_6Fe, Al_mFe and Al_3Fe) exist; the α-AlFeSi is the dominating phase. Therefore, the potency of the inclusion particles is applicable for the α-AlFeSi in these alloy conditions.

Secondly, when the overall percentage of physical contact of inclusion particles with the Fe-intermetallics is very high, the high percentage should imply that one or both intermetallic phases nucleate heterogeneously on the surface of the injected inclusion. To identify the nucleating potency of the substrate for each of these intermetallic phases, it is necessary to compare these data with the other alloy conditions, where additional results for the same combination of inclusion and intermetallic phase can be found.

The quantitative data for the nucleation events of Fe-intermetallic phases on inclusion particles are presented in this thesis only when a sufficient number of inclusion particles was successfully added to the alloy with a well-identified second-phase content. In other cases, when a small number of inclusions was observed in the microstructure or the intermetallic phase content is unidentified, some micrographs are shown as examples. However, results in this latter case do not contribute to the assessment of the nucleant potency for specific intermetallic phases, but rather contribute to the overall nucleate/inclusion potency for the Fe-intermetallics as given in Table 18.

In microstructures obtained at high cooling rates containing (δ + β) phase, such as alloys 1 and 2 (Chapter 4),[2] heterogeneous nucleation of the β-AlFeSi phase was neglected in the present analysis since β-AlFeSi forms via a peritectic decomposition of the δ-AlFeSi phase (Chapter 4).[2] Thus, the β-AlFeSi phase nucleation on the surface of inclusions in these cases is most likely precluded.

7.2.1. Role of Inclusions in the Nucleation of Fe-Intermetallics in Al-Si-Fe Alloys

7.2.1.1. Effect of CaO

Image analysis for the microstructure of the experimental alloys solidified under different cooling conditions showed that CaO has the highest overall physical contact (*i.e.*, 44.6 pct) with Fe-intermetallics in comparison with the other inclusions studied in the current work as can be seen from Table 18. It is worth mentioning that CaO is very reactive with the aluminum alloy, and forms several compounds that have a very high Si content.[3] It can be noted from Table 18 that, for particles located within the α-Al phase, CaO has the highest percentage of physical contact with Fe-intermetallics, 27.1 pct. At the same time, it has a very high percentage in the interdendritic regions, *i.e.*, 73.9 pct.

Table 18 Summary of the percentages of inclusions in contact with the Fe-intermetallics in different microstructure regions.

Inclusion	Overall (%)	α-Al (%)	Interdendritic regions (%)	Interdendritic regions/total
CaO*	*44.6*	27.1	73.9	67.3
MgO	27.8	13.4	*75.5*	71.4
TiB_2	26.9	14.5	64.0	61.7
TiC	30.6	17.7	68.0	61.1
Al_4C_3	32.8	19.0	66.5	66.7
α-Al_2O_3	31.0	13.4	65.3	*79.7*
γ-Al_2O_3	*18.7*	*8.1*	65.0	70.3
SiC	30.7	16.9	65.8	67.7

*Data presented excluding alloy 6 due to the formation a chemical compound on the surface of CaO particles in the α-Al phase of the alloy with a similar gray level to the Fe-intermetallic phase.

More precise data on the role of CaO in the nucleation of different Fe-intermetallic phases can be seen in Table 19. It is clear that the CaO particles serve as potent nucleants

Table 19 Quantitative results of the nucleation of Fe-intermetallics on the CaO particles.

Phase	Condition		α-Al	Interdendritic Regions	Overall		Potency
	Alloy, dT/dt, C/s	Existing Phases in the microstructure.	%	%	%	level	
α-AlFeSi	3, 0.21	α	58.3	82.4	68.3	very high	✓
	3, 14.7	α, δ	24	78.0	51	very high	✓
	4, 1.4	α, β	34.9	88.9	46.9	very high	✓
	5, 1.2	α, binary Al-Fe	63.4	87.5	76.5	very high	✓
	5, 14.3	α, q_1	41.3	83.8	61.5	very high	✓
δ-AlFeSi	1, 10.7	δ	5.7	61.6	31.0	high	✓
	2, 13.8	δ, q_1	24.4	63.9	40.8	very high	✓
	3, 14.7	α, δ	24	78.0	51	very high	✓
	4, 12.8	δ	13.8	66.7	29.3	medium	medium
q_1-AlFeSi	2, 13.8	δ, q_1	24.4	63.9	40.8	very high	✓
	5, 14.3	α, q_1	41.3	83.8	61.5	very high	✓

for the α-AlFeSi phase formed under both slow and fast cooling conditions in alloys 3 and 5. In alloy 3 at slow cooling rate, the only stable intermetallic phase is the α-AlFeSi, whereas in alloys 3 and 5 at high cooling rates the stable intermetallic phases are (α, δ) and (α, q_1), respectively. Examples of the physical contact of CaO particles with the α-AlFeSi phase in alloys 3 and 5 are given in Figure 86 (a, b). It was noted that the CaO particles have very high physical contacts with α-AlFeSi within the α-Al phase and the interdendritic regions of these alloys. This suggests a high potency of CaO for nucleating the α-AlFeSi.

Hsu *et al.*[212] demonstrated that 0.4 wt% Ca in 6XXX series can promote the formation of the α-AlFeSi via the formation of the $CaAl_2Si_2$ phase during solidification. The addition of elemental Ca to such alloys can promote the formation of the α-AlFeSi by the possibility of a preferred nucleation on the surface of CaO, similar to the findings of the present work, or equally due to solute effects of Ca addition on the Si content of the alloy. The formation of α-AlFeSi in the alloys (6XXX series) may, therefore, be interpreted in view of the Ca effect on depletion of Si from the bulk alloy composition as a result of the formation of the high-Si phase, $CaAl_2Si_2$. The α-AlFeSi contains a low Si content relative to the other ternary Al-Fe-Si phases such as β-AlFeSi and δ-AlFeSi, and therefore it can be stabilized over these phases by reducing the Si and/or increasing the Fe content of the alloy. For example, the 6063 alloys may contain as high as 0.2-0.6 wt% Si, less than 0.35 wt% Fe and 0.45-0.9 wt% Mg. The typical structure of these alloys contains mainly β-AlFeSi and Mg_2Si phases.[46] The addition of 0.4 wt% Ca which has a very low solubility in solid

aluminum, ~ 0.08 wt% at the eutectic temperature,[169] can cause as high as 0.56 wt% loss of Si, impeding the formation of the β-AlFeSi and Mg_2Si phases and stabilizing the formation of poorer-Si phases such as α-AlFeSi. In alloy 6 of the present work, containing high silicon content (6.3 wt%) the stability of the β-AlFeSi phase located in a close vicinity to the injected CaO particles was not affected even when a high-Si phase, $CaAl_{2.5}Si_{1.8}O_{0.37}$, was observed to form on the CaO particles (see Figure 86 (c))

The δ-AlFeSi nucleates efficiently on the CaO particles as can be seen from Table 19. A high percentage of nucleation events was observed in microstructures of alloys 1 and 4, containing only δ-AlFeSi phase, and alloys 2 and 3 containing (δ, q_1) and (α, δ) phases, respectively. The micrographs in Figure 86 (d, e) show the nucleation of the δ-AlFeSi phase on the CaO injected particles.

The nucleation of the q_1-AlFeSi phase, as can be seen in Table 19, is more probably promoted on the CaO particles since very high nucleation events were observed. However, due to the presence of the q_1-AlFeSi phase coupled with other phases, such as δ and α in alloys 2 and 5 cooled at 13.8 °C/s and 14.3 °C/s, respectively, and due to the difficulty in differentiation between these phases through the optical microscope (see Figure 86 (f)) a firm proof for the nucleation of q_1 phase on inclusion particles is not possible.

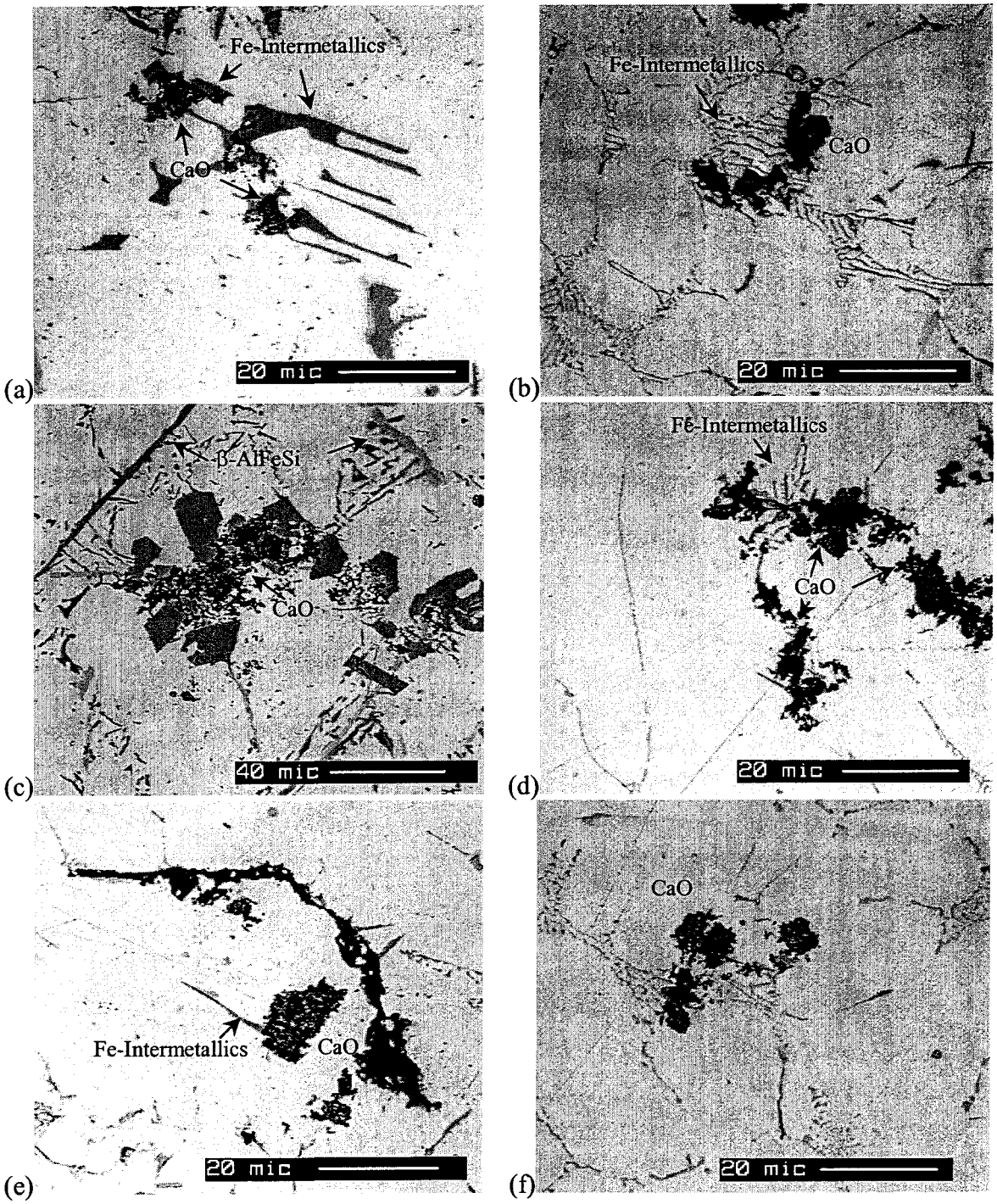

Figure 86 Nucleation of Fe-intermetallics on the CaO particles: (a, b) α-AlFeSi in alloys 3 and 5, cooling rates 0.21 and 14.3 °C/s, respectively, (c) stability of β-AlFeSi near CaO particles in alloys 6, cooling rate, 0.76 °C/s, (d, e) δ-AlFeSi in alloy 4, cooling rate, 12.8 °C/s, and (f) q_1- and α-AlFeSi phases in alloy 5, cooling rate 14.3 °C/s.

7.2.1.2. Effect of MgO

In the aluminum grain centers, it was found that 13.4 pct of the MgO particles have direct physical contact with Fe-intermetallic phases. This percentage increased to 75.5 in the interdendritic regions, and represents the highest order achieved for physical contact between inclusions and intermetallics in the present study, as shown in Table 18. Thus, when the MgO particles are pushed to the interdendritic regions in Al-Si-Fe alloys, they are believed to act as active substrates for the nucleation of iron bearing phases. More precisely, 75.5 pct of these particles are active substrates for the crystallization of Fe-intermetallics. Of all the MgO particles studied, 71.4 pct of those associated with Fe-bearing phases are located in the interdendritic regions, Table 18.

The MgO particles are active nucleants for the α-AlFeSi phase at high cooling rates in alloys 3 and 5 containing (α, δ) and (α, q_1) phases as shown in Table 20. On the other hand, a poor potency to nucleate the δ-AlFeSi was observed. Low percentage nucleation events of δ-AlFeSi phase on the MgO particles were observed in alloys 1 and 4, where a unique stability of δ-phase was identified (Chapter 4).[2] Quantitative results on the nucleation of other intermetallic phases on MgO particles are not presented since the number of particles required for such evaluation was not observed in all alloy conditions.

Optical micrographs, which show the MgO particles as preferential sites for the nucleation of some Fe-intermetallics, can be seen in Figure 87. Figure 87 (a, b) show the nucleation of α-AlFeSi on MgO particles within the α-Al phase, and the interdendritic regions of alloy 4. Binary Fe-intermetallic phases were seen to nucleate on MgO particle in

Table 20 Quantitative results of the nucleation of Fe-intermetallics on the MgO particles.

Phase	Condition		α-Al	Interdendritic Regions	Overall		Potency
	Alloy, dT/dt, C/s	Phases existing in the microstructure.	%	%	%	level	
α-AlFeSi	2, 1.53	α	0.8	71.4	4.5	low	
	3, 1.3	α	9.0	80.3	22.5	medium	
	3, 14.7	α, δ	20.4	67.9	37.1	high	✓
	4, 1.4	α, β	46.6	100	66.7	very high	✓
	5, 14.3	α, q_1	28.9	80.3	45.8	very high	✓
δ-AlFeSi	1, 10.7	δ	16.1	87.5	18.6	low	×
	3, 14.7	α, δ	20.4	67.9	37.1	high	?
	4, 12.8	δ	4.4	45.9	17.8	low	×
q_1-AlFeSi	5, 14.3	α, q_1	28.9	80.3	45.8	very high	?

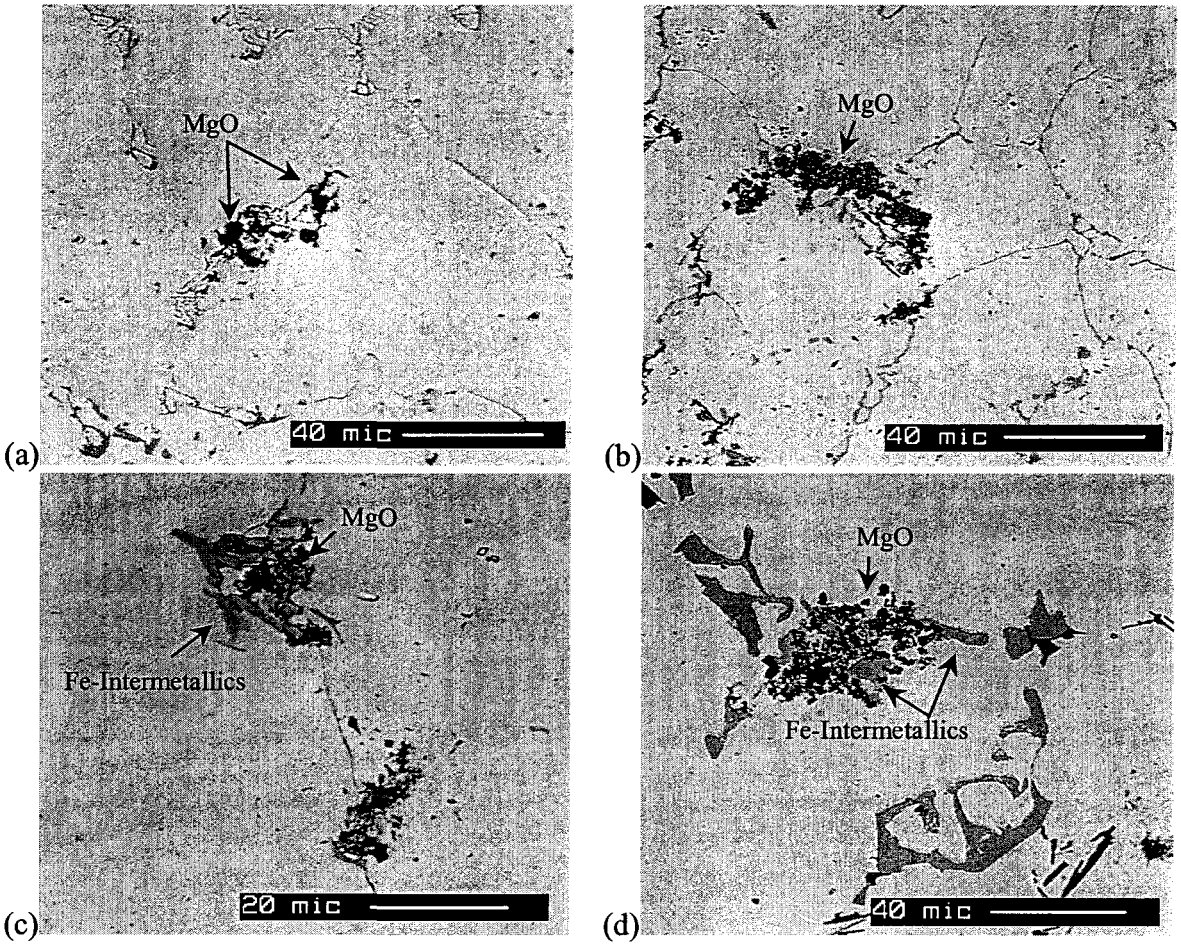

Figure 87 Optical micrographs showing the physical contact between MgO particles and Fe-intermetallics in the microstructure of Al alloys: (a) inside the α-Al phase in alloy 4, cooling rate 1.4 °C/s, and (b-d) in the interdendritic regions of alloys 4, 5 and 6, cooling rates of 1.4 °C/s, 0.19 °C/s, and 0.18 °C/s, respectively.

the interdendritic regions of alloy 5 (Figure 87 (c)). A good example of the nucleation control in the phase selection process is shown in Figure 87 (d), in the interdendritic regions of alloy 6 where an exceptional stability of the β-AlFeSi phase was observed (Chapter 4),[1,2] α-AlFeSi was seen to nucleate instead of β-AlFeSi on the MgO particles. This observation supported the quantitative results on the high potency of MgO particles to nucleate the α-

AlFeSi phase. The maps in Figure 88 show the formation of α-AlFeSi phase on the surface of MgO.

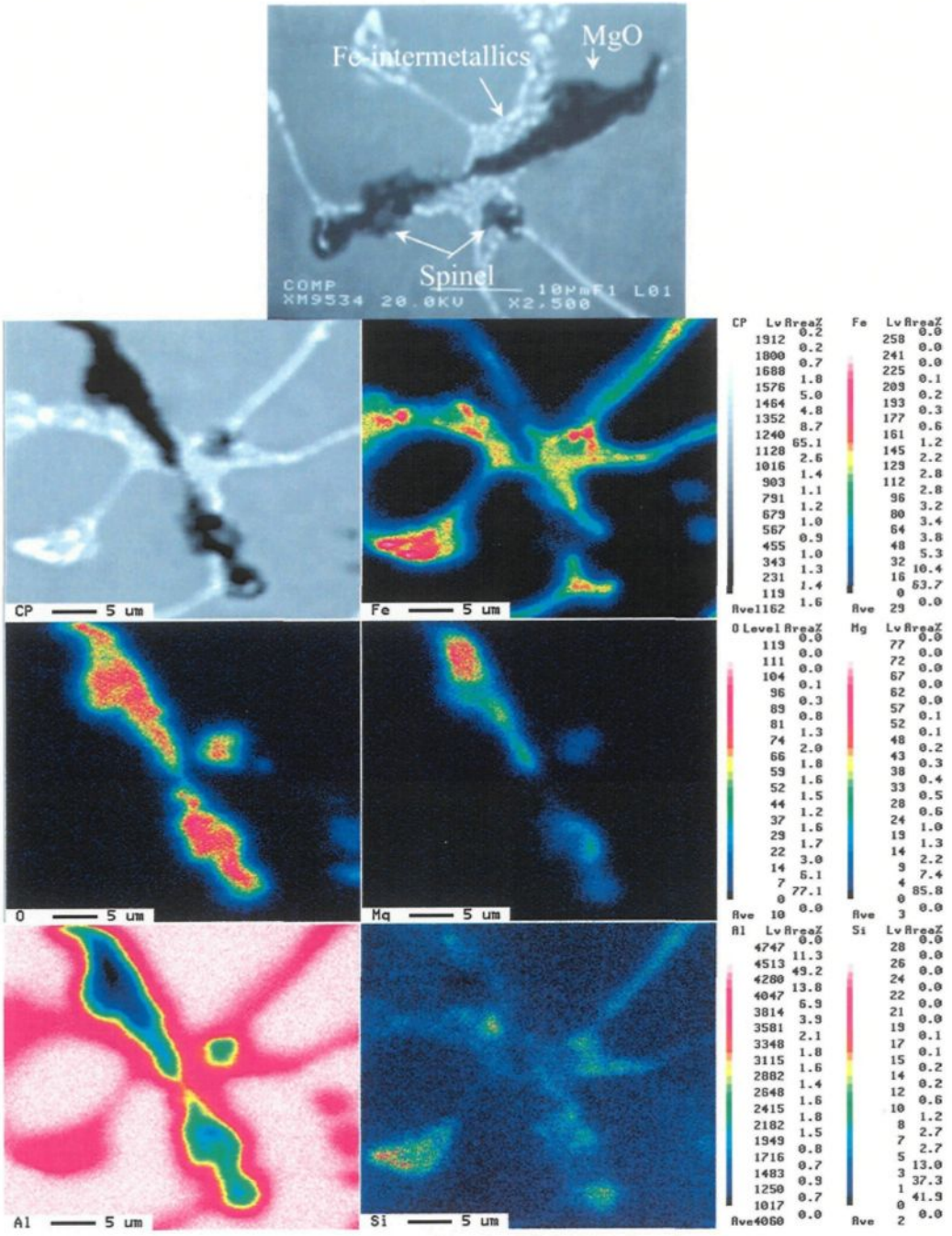

Figure 88 Maps of element distributions in the microstructure of alloy 5, cooling rate 14.3 °C/s, showing the nucleation of the α-AlFeSi phase on the surface of MgO particles, and the formation of the spinel phase.

7.2.1.3. Effect of TiB_2

The role of TiB_2 particles, which form an important constituent of commercial grain refiners, in the nucleation of Fe-intermetallics, was also evaluated in this work. It can be seen from Table 18 that a ratio of 26.9 % of the overall TiB_2 particles studied in this work were observed to have physical contact with Fe-intermetallics, among which 61.7% occur in the interdendritic regions. Very few nucleation events (*i.e.*, evident physical contacts) were observed on the surface of TiB_2 particles when particles are located within the gains of α-Al, *i.e.*, on only 14.5 % of the TiB_2 particles that lie inside the Al phase did nucleation take place. On the other hand, 64 % of the TiB_2 particles located in the interdendritic regions were seen to promote nucleation of Fe-intermetallics on their surface.

The details of these quantitative results are given in Figure 89. The general trend for the nucleation of Fe-bearing phases on the TiB_2 particles is that the percentage of TiB_2 particles that possess nucleation events, and hence their nucleation potency, decreases with the increase of the total alloying element content from alloy 1 to alloy 6, specifically in the interdendritic regions. This indicates that the poisoning effect of Si also influences the nucleation of the second-phase particles.

Table 21 shows that TiB_2 particles are potential nucleants for several Fe-intermetallic phases in several alloys at different cooling rates. High percentages of physical contacts in alloys containing binary Al-Fe phases, and δ-AlFeSi phases have been observed. The effect of TiB_2 on the nucleation of α-AlFeSi and β-AlFeSi was not observed, while that of q_1-AlFeSi phases was unclear. Figure 90 gives some examples of these observations. The nucleation of the binary Al-Fe phases on TiB_2 particles within the α-Al

phase can be seen in Figure 90 (a). The δ-AlFeSi phase nucleated efficiently on TiB_2 particles in alloys 4 and 6 as shown in Figure 90 (b – d). In contrast to this, less efficient nucleation was observed in alloys containing lower solute concentrations such as alloy 1 (see Table 21). This may highlight the effect of solute concentration on the nucleation of second-phase particles.

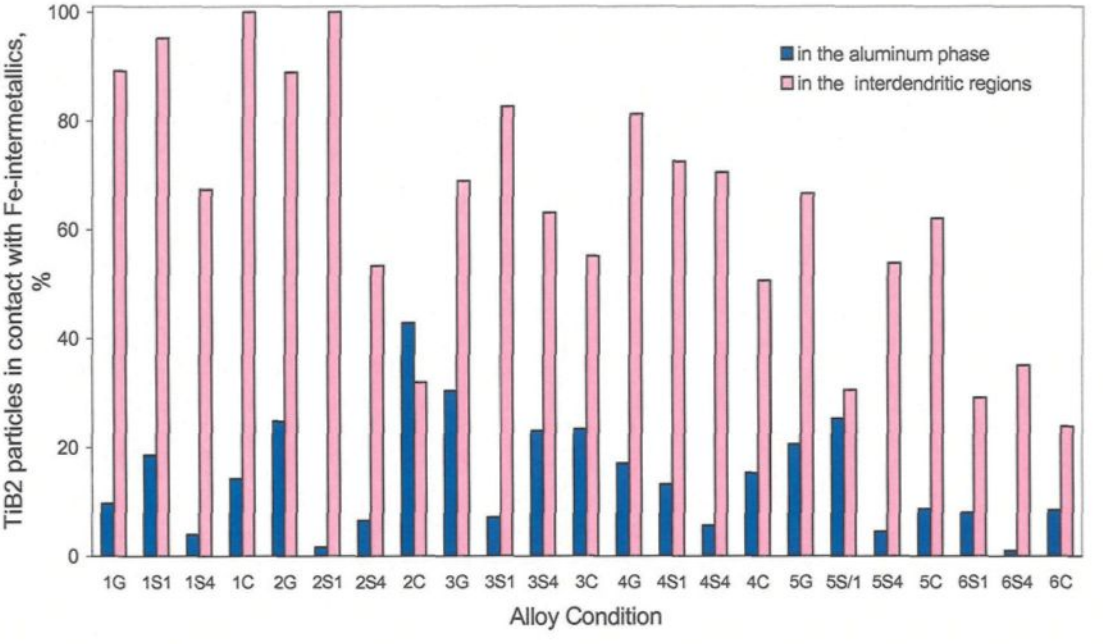

Figure 89 The number of nucleation events of Fe-intermetallics on the surface of TiB_2 in the α-Al phase and in the interdendritic regions, measured in percentages of the TiB_2 particles that exist in the respective alloy region.

Figure 91 shows that when TiB_2 particles are pushed to interdendritic regions they are active in the nucleation process of the Fe-intermetallic phases, whereas those particles that lie in the grain centers are inactive. The maps in Figure 92 show the physical contact of Fe-intermetallics with the TiB_2 particles in the interdendritic regions.

Table 21 Quantitative results of the nucleation of Fe-intermetallics on the TiB_2 particles.

Phase	Condition		α-Al	Interdendritic Regions	Overall		Potency
	Alloy, dT/dt, C/s	Phases existing in the microstructure.	%	%	%	level	
Al-Fe binary phases	1, 0.16	Al_6Fe, Al_mFe, Al_XFe.	9.7	89.2	36.7	high	✓
	5, 0.19	α, Al_6Fe, Al_mFe, Al_3Fe.	20.5	66.7	24.0	medium	?
α-AlFeSi	3, 14.7	α, δ	23.3	55.1	29.0	medium	?
	5, 0.19	α, Binary Al-Fe	20.5	66.7	24.0	medium	medium
	5, 14.3	α, q_1	8.7	62.1	37.0	high	?
β-AlFeSi	6, .76	β	8.0	29.0	25.9	high	✓
δ-AlFeSi	1, 10.7	δ	14.2	100	17.2	low	×
	2, 13.8	δ, q_1	42.9	31.9	39.1	high	?
	3, 14.7	α, δ	23.3	55.1	29.0	medium	?
	6, 12.8	δ	8.5	23.9	25.0	high	✓
q_1-AlFeSi	2, 13.8	δ, q_1	42.9	31.9	39.1	high	?
	5, 14.3	α, q_1	8.7	62.1	37.0	high	?

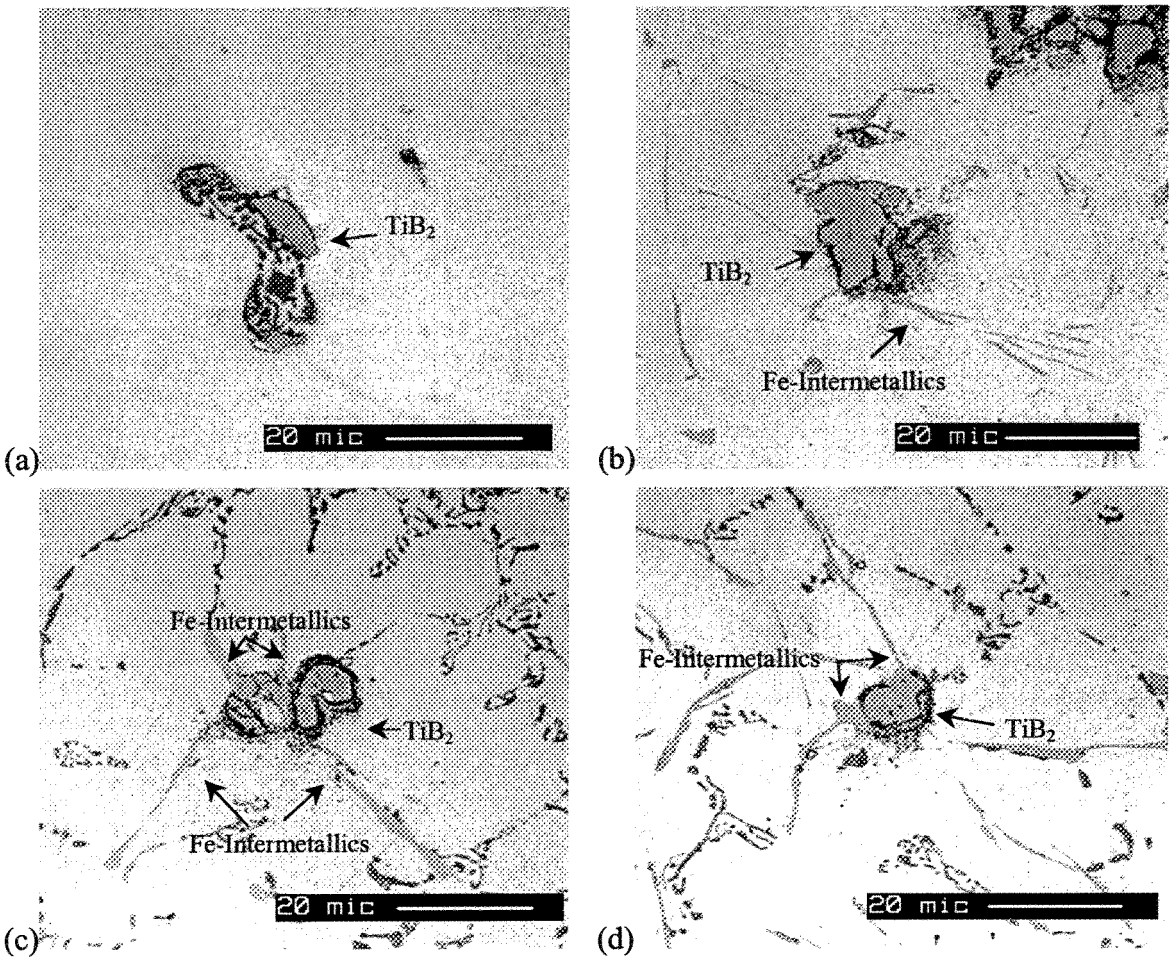

Figure 90 Optical micrographs showing the nucleation of Fe-intermetallics on TiB_2 particles: (a, b) in the interdendritic regions in alloys 2 and 4, cooling rates 1.53 and 12.8 °C/s, respectively, and (c, d) inside the α-Al phase in alloy 6, cooling rate 12.8 °C/s.

Evidence of the high nucleation potency of TiB_2 for different Fe-intermetallic phases has been reported in the literature. The addition of Al-Ti-B grain refiner (i.e. TiB_2) to different wrought Al alloys, containing Fe and Si, promoted the nucleation of Al_mFe,[59,60,108,109,111,112] $Al_{13}Fe_4$,[19] α-AlFeSi,[111,112] and other phases.[85] It was proposed that there may be a small lattice mismatch between the hexagonal lattice of TiB_2 and phases with orthogonal crystal axes such as cubic α-AlFeSi and Al_mFe[112] In some cases, phases

such as Al_mFe are promoted in the grain-refined alloys but only in the presence of certain elements such as V[59,60] and Si.[59,61]

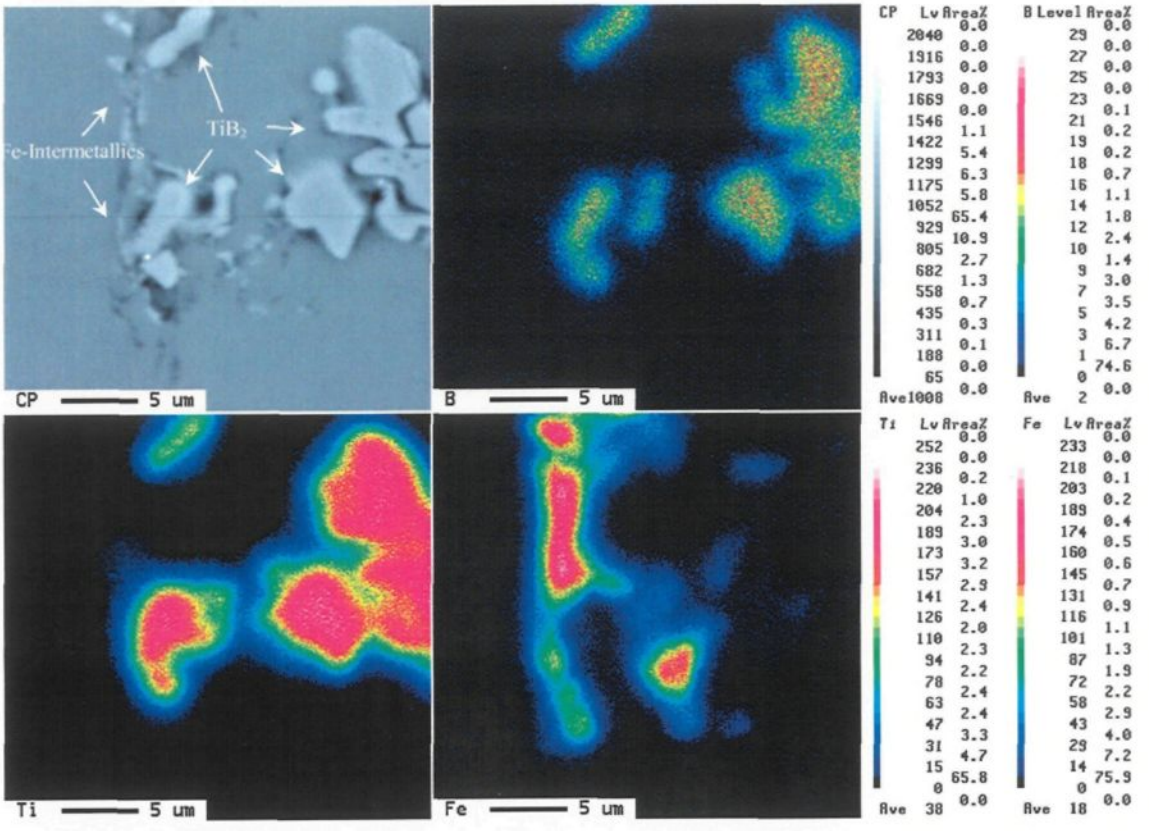

Figure 91 Maps of element distributions in the microstructure of alloy 2 (solidified at cooling rate of 1.53 °C/s) showing the selective formation of Fe-intermetallics on the TiB_2 substrates when present in the interdendritic regions rather than the α-Al phase.

In their review, Allen *et al.*[25] proposed that grain refiners may affect the second-phase selection in three ways. Firstly, TiB_2 and TiC particles that do not nucleate the α-Al may be partitioned into the interdendritic spaces, where they may affect the solidification of the second phase particles.[109,110] The local chemistry of these interdendritic spaces (*i.e.*, solute element and impurity levels) may be as important for second-phase selection as it is

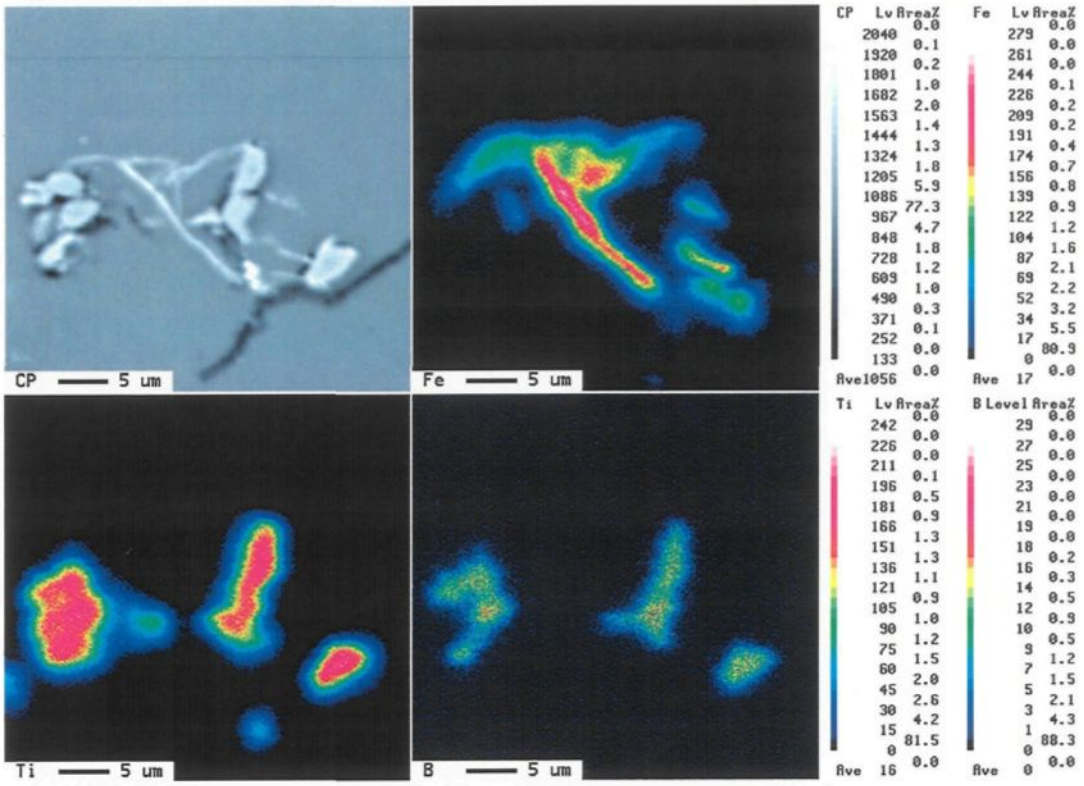

Figure 92 Maps of element distributions in the microstructure of alloy 2, solidified at cooling rate of 1.53 °C/s, showing the physical contact between the TiB_2 and the Fe-intermetallics, confirming the nucleation of the later on TiB_2.

7.2.1.4. Effect of TiC

The overall average of TiC particles that have direct physical contact with Fe intermetallics is 30.6 pct, among which 61.1 pct were located in the interdendritic regions (Table 18). A ratio of 17.7 pct of the TiC particles located within the α-Al phase was observed to have physical contact with Fe-intermetallic phases, whereas a higher percentage (68 pct) was identified in the interdendritic regions.

It was observed that TiC particles are potent nucleants for the α-AlFeSi and δ-AlFeSi phases (Table 22, Figure 93). Very high percentages of physical contact between the TiC particles and Fe intermetallics in alloys containing (α, δ) and (α, q_1) were

in determining the effect of grain refiner. Secondly, primary grain refinement may result in a greater number density of interdendritic liquid spaces towards the final stages of solidification. With increasing division of the liquid volume, nucleation and hence impurity levels play a more important role in influencing second-phase selection. Thirdly, primary grain refinement may change the shape of the interdendritic liquid channels (*e.g.*, from long channels between columnar dendrites to more convoluted shapes between equiaxed grains), forcing the second-phase particles that form in these spaces to change their growth morphology. This may influence which is the preferred second-phase under given solidification conditions.[61]

Apparently there is no direct observation of the nucleation of Fe-intermetallics on the surface of TiB_2 particles in the literature. Several reports were based on the assumption that TiB_2 particles added with the grain refiner nucleate the second-phase particles in the same manner as the primary matrix phase, while others suggested that the promotion of certain phases in the presence of Al-Ti-B grain refiner is due to its effect on the growth conditions that stabilize some intermetallics over the other possible phases, and still others attributed the effect of grain refiners on the promotion of certain second-phase particles to the impurity contents. Direct observation of these nucleated intermetallic phases on TiB_2 particles, similar to those given in the present work, were not reported. Thus, the present results constitute reliable experimental evidence for the absolute nucleation potency of the TiB_2 particles in the absence of impurity elements.

Table 22 Quantitative results of the nucleation of Fe-intermetallics on the TiC particles.

Phase	Condition		α-Al	Interdendritic Regions	Overall		Potency
	Alloy, dT/dt, C/s	Existing Phases in the microstructure.	%	%	%	level	
α-AlFeSi	2, 1.53	α	7.5	83.0	22.8	medium	
	3, 14.7	α, δ	40.8	76.9	51.0	very high	✓
	4, 1.4	α, β	23.6	50.0	26.4	medium	
	5, 1.2	α, binary Al-Fe	11.9	88.1	37.3	high	
	5, 14.3	α, q_1	49.1	80.4	63.5	very high	✓
β-AlFeSi	4, 1.4	α, β	23.6	50.0	26.4	medium	
	6, 0.76	β	4.5	34.5	29.8	high	✓
δ-AlFeSi	1, 10.7	δ	8.44	46.3	18.3	medium	?
	2, 13.8	δ, q_1	14.6	59.5	23.8	medium	?
	3, 14.7	α, δ	40.8	76.9	51.0	very high	?
	4, 12.8	δ	23.2	75.0	34.7	high	✓
	6, 12.8	δ	11.4	47.9	27.8	high	✓
q_1-AlFeSi	2, 13.8	δ, q_1	14.6	59.5	23.8	medium	?
	5, 14.3	α, q_1	49.1	80.4	63.5	very high	?

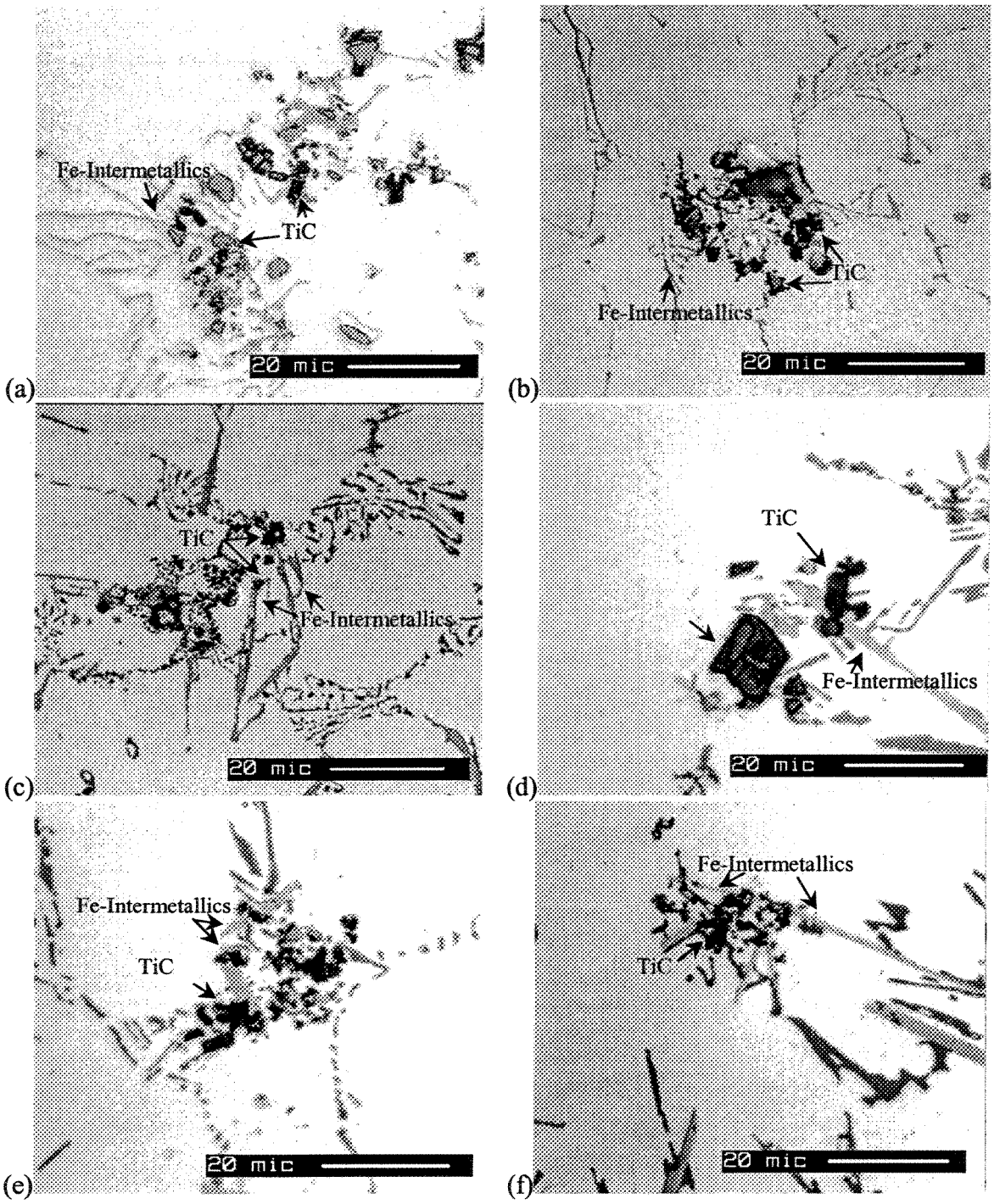

Figure 93 The TiC particles that are pushed to the interdendritic regions act as potential substrates for the formation of Fe-intermetallics in (a, b) alloy 3, cooling rate 1.3 °C/s and 14.7 °C/s, (c) alloy 6, cooling rate 12.8 °C/s, and (d-f) alloy 6, cooling rate 0.76 °C/s.

observed, which supposes the heterogeneous nucleation of the α-AlFeSi phase on TiC (see Figure 93 (a, b).) In alloys 4 and 6, containing only δ-AlFeSi, high percentages of physical contact were found, implying a preferred nucleation of δ on TiC particles (Figure 93 (c)). In alloy 6 at slow cooling rate, *i.e.*, stability conditions for β-AlFeSi, evident nucleation of Fe-intermetallics was observed on TiC as shown in Figure 93 (d, e).

The element distribution maps of Figure 94 and Figure 95 show examples of the nucleation of the Chinese script Fe-intermetallics (*i.e.*, α-AlFeSi) and the platelets of β-AlFeSi phases on TiC particles.

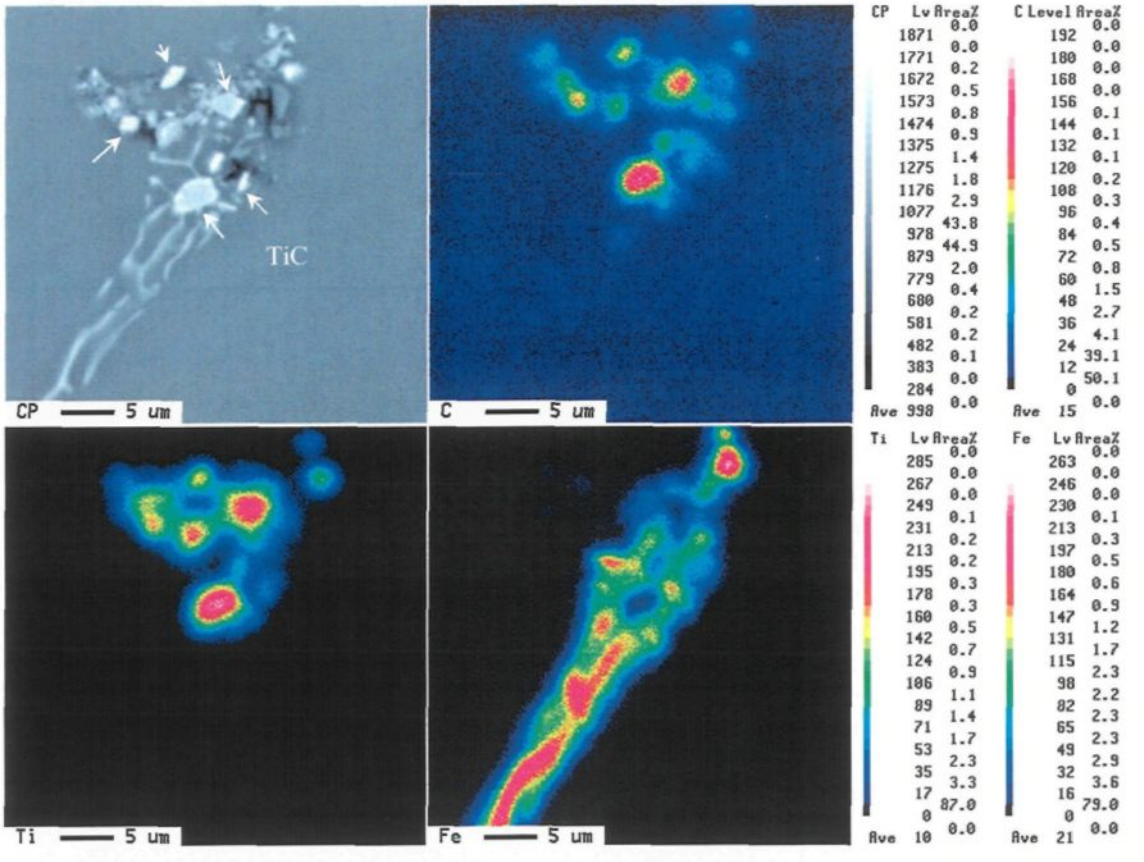

Figure 94 Maps of element distributions in the microstructure of alloy 3, cooling rate 14.7 °C/s, showing the formation of Chinese script Fe-intermetallics (α-AlFeSi) on the TiC particles (arrowed).

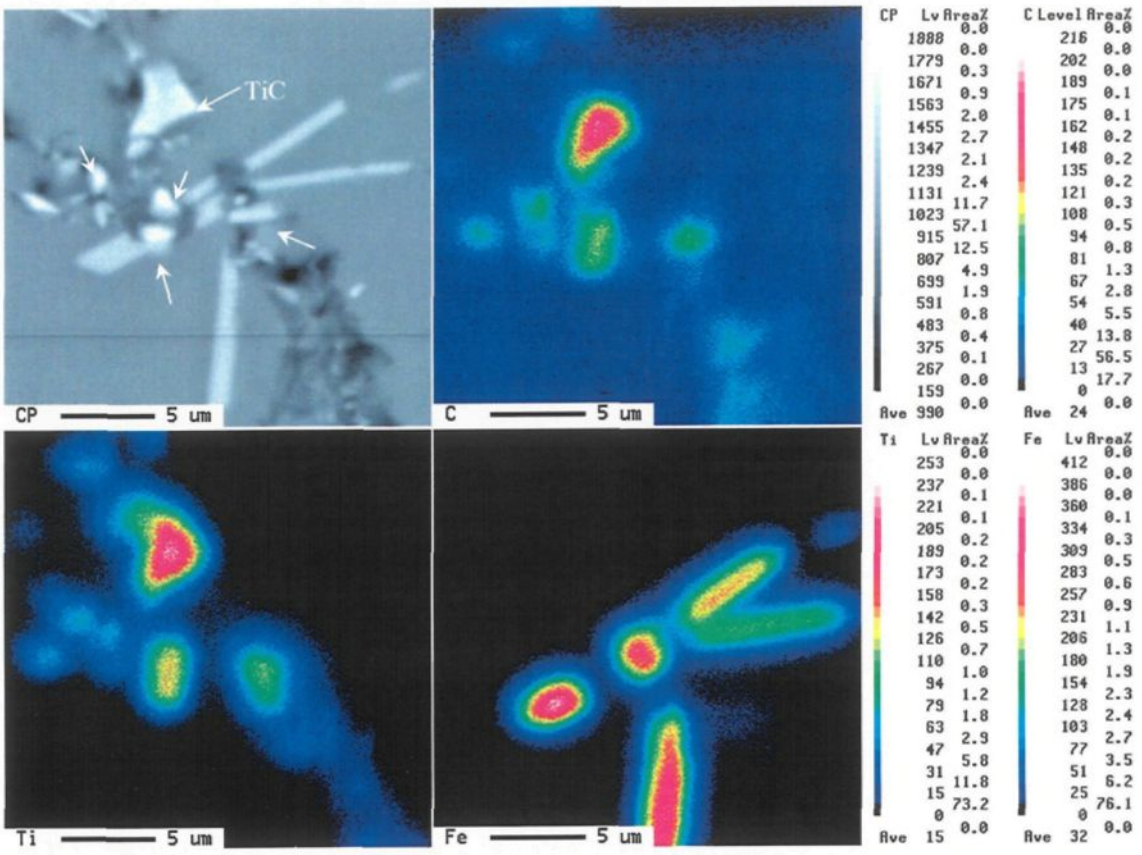

Figure 95 Maps of element distributions in the microstructure of alloy 6, cooling rate 0.76 °C/s, showing the formation of Fe-intermetallics (β-AlFeSi) on the TiC particles (arrowed).

7.2.1.5. Effect of Al_4C_3

A ratio of 32 pct of the aluminum carbide particles was found to be active substrates for the nucleation of Fe-intermetallic phases. Among the Al_4C_3 particles in the aluminum phase 19 pct have nucleation of Fe-intermetallics on their surface (see Table 18). This is the second highest ratio of nucleation within the α-Al phase. The general trend of nucleation on Al_4C_3 is that the overall average of nucleation events of Fe-intermetallics on Al_4C_3 particles

in the interdendritic regions is always much higher than that in the α-Al phase. In other words, 66.5 pct of the Al_4C_3 particles in the interdendritic regions are in contact with the Fe-intermetallics (compared with 19 pct in the aluminum phase).

It is clear from Table 23 that the percentages of Al_4C_3 particles in physical contact with Fe-intermetallics are generally high. The δ-AlFeSi and α-AlFeSi phases nucleate more frequently on the Al_4C_3 particles than other phases. High nucleation events were seen in microstructures containing two phases such as (δ, q_1) and (α, q_1), however, this does not imply a promotion of a q_1-AlFeSi relation since both δ-AlFeSi and α-AlFeSi phases showed separately numerous nucleation events on Al_4C_3 particles. The same applies to the binary Al-Fe phases since α-AlFeSi phase is the dominating one in alloy 5 cooled at 0.19 °C/s, therefore, the nucleation of the binary Al-Fe phases cannot be separately evaluated.

The micrographs of Figure 96 show the nucleation of different Fe-intermetallic phases on Al_4C_3 particles within the α-Al grains (Figure 96 (a, b)) and in the interdendritic regions (Figure 96 (c, d)). Chinese script and binary Al-Fe phases nucleate heterogeneously on Al_4C_3 particles as shown in Figure 96 (a, c) and Figure 96 (b, d), respectively. The formation of the δ-AlFeSi phase on the Al_4C_3 particles is shown in micrographs (e, f). Maps of Figure 97 show examples of this observation in alloy 3.

Table 23 Quantitative results of the nucleation of Fe-intermetallics on the Al_4C_3 particles.

Phase	Condition		α-Al	Interdendritic Regions	Overall		Potency
	Alloy, dT/dt, C/s	Existing Phases in the microstructure.	%	%	%	level	
Al-Fe binary phases	1, 0.76	Al_6Fe, Al_mFe, Al_xFe	17.0	60.0	32.0	high	✓
	5, 0.19	α, Al_6Fe, Al_mFe, Al_3Fe.	14.3	75.8	51.9	very high	?
α-AlFeSi	2, 0.16	α	5.1	66.7	13.3	low	×
	3, 1.3	α	13.3	61.4	25.6	high	✓
	4, 1.4	α, β	11.6	68.8	33.8	high	✓
	3, 14.7	α, δ	24.4	70.0	38.5	high	?
	5, 0.19	α, Binary Al-Fe	14.3	75.8	51.9	very high	
	5, 14.3	α, q_1	48.6	82.1	60.4	very high	?
δ-AlFeSi	2, 13.8	δ, q_1	17.2	66.7	30.1	high	?
	3, 14.7	α, δ	24.4	70.0	38.5	high	?
	6, 12.8	δ	41.2	23.1	25.0	high	✓
q_1-AlFeSi	2, 13.8	δ, q_1	17.2	66.7	30.1	high	?
	5, 14.3	α, q_1	48.6	82.1	60.4	very high	?

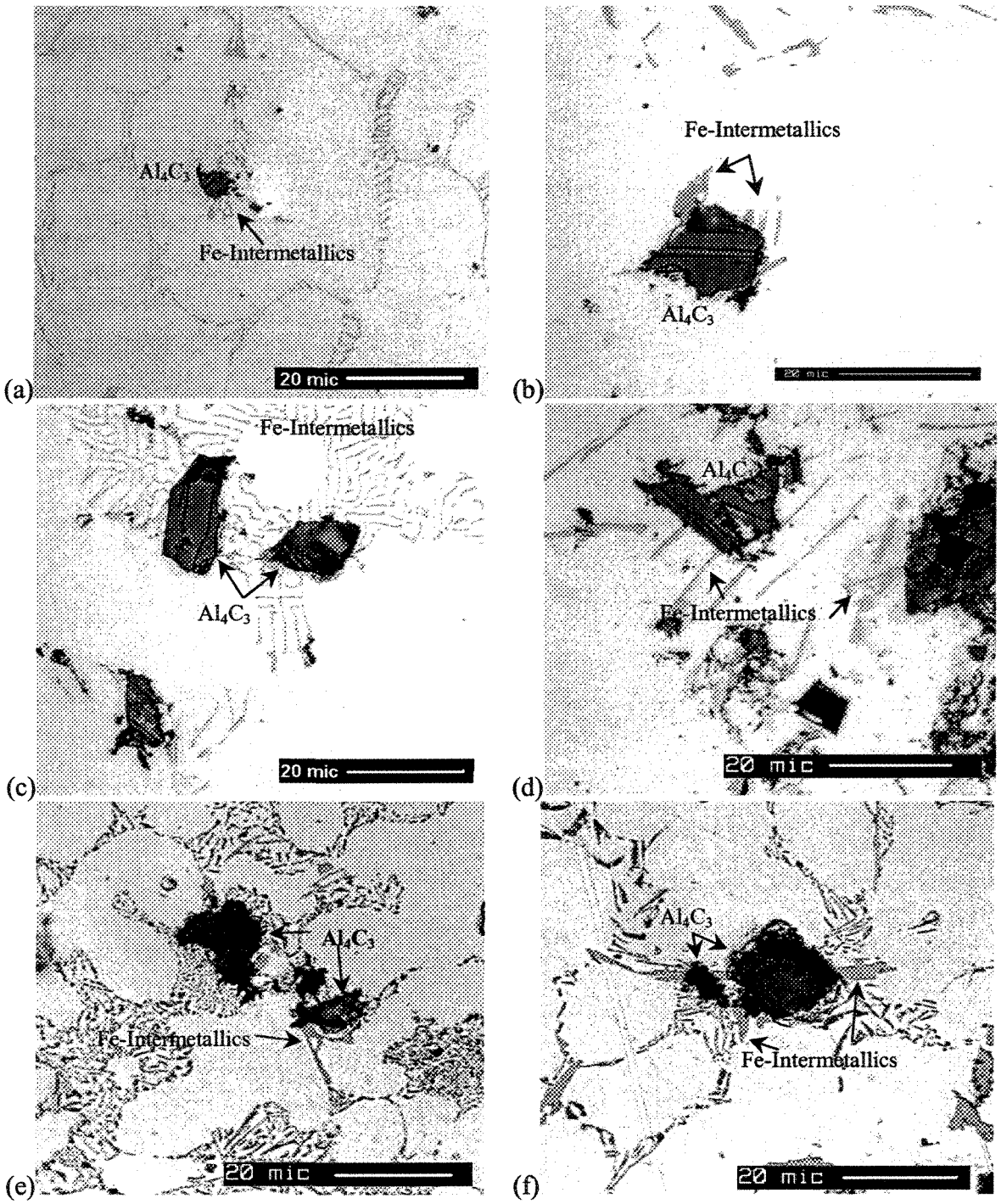

Figure 96 Optical micrographs showing evidences of the nucleation of Fe-intermetallics on the surface of Al_4C_3 particles. (a, b) within the α-Al phase of alloy 5, cooling rate 1.2 °C/s, (c, d) in the interdendritic regions of alloy 5, cooling rate is 1.2 °C/s and 0.19 °C/s, respectively, and (e, f) in the interdendritic regions of alloy 6, cooling rate 12.8 °C/s.

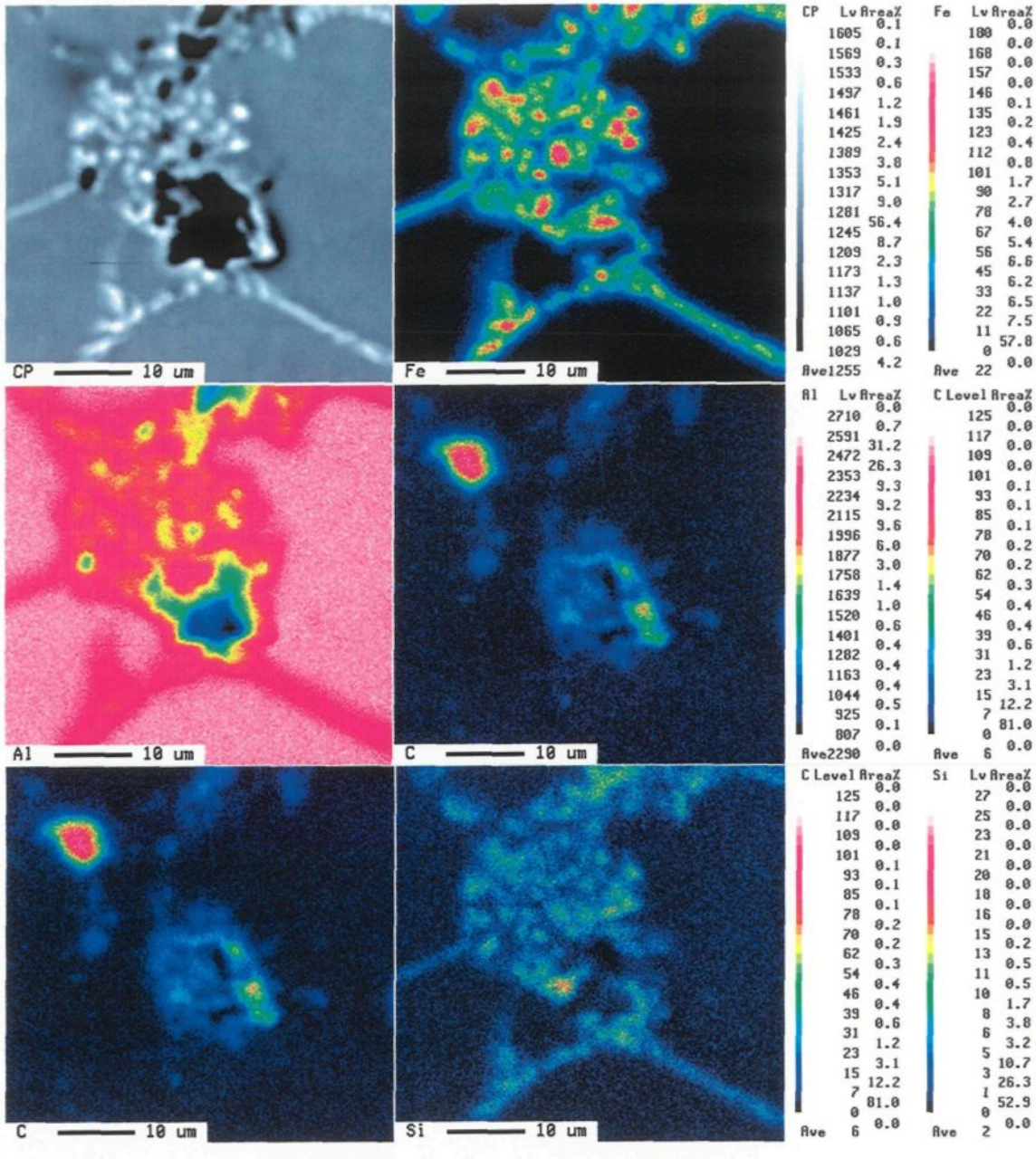

Figure 97 Maps of element distributions in the microstructure of alloy 3, cooling rate 1.3 °C/s, showing the nucleation of Fe-intermetallics on the surface of Al_4C_3 particles.

7.2.1.6. Effect of α-Al_2O_3

The role of α-Al_2O_3, which is one of the most common oxides in aluminum alloys,[76] in the development of the solidification microstructure in aluminum alloys is of considerable importance. The overall average of nucleation levels of Fe-intermetallics on the surface of α-Al_2O_3 particles is 31 pct of the studied particles, among which 79.7 pct were identified in the interdendritic regions (Table 18). Thus, the nucleation of iron intermetallics on the surface of the α-Al_2O_3 particles was extensively observed in the interdendritic regions, rather than in the aluminum phase. This represent the highest level seen in the present study.

More detailed quantification results for the nucleation events of Fe-intermetallics in the aluminum phase and the interdendritic regions are given in Figure 98. The potency of the α-Al_2O_3 particles for the nucleation of Fe-intermetallics in the interdendritic regions decreases with the increase in the content of the alloying elements, Si and Fe, in the alloy as can be seen in Figure 98. The opposite is observed in the aluminum phase. The overall average of Fe-intermetallics nucleation on the α-Al_2O_3 particles in the interdendritic regions is 65.3 %, and in the aluminum phase is 13.4 %.

Table 24 gives more specific data on the nucleation of certain phases on the α-Al_2O_3 particles. It is clear that the α-Al_2O_3 phase is a poor nucleant for the binary Al-Fe phases in alloy 1, and a potent nucleant for the α-AlFeSi, β-AlFeSi and δ-AlFeSi phases in different alloys. However, the low nucleation events of α-AlFeSi phase on α-Al_2O_3 particles that were observed in alloy 2 cooled at 0.16 ^{o}C/s are an exception. The nucleation

of the binary Al-Fe phases on the α-Al_2O_3 particles in alloy 5 seems to be favorable as can be seen from Figure 99.

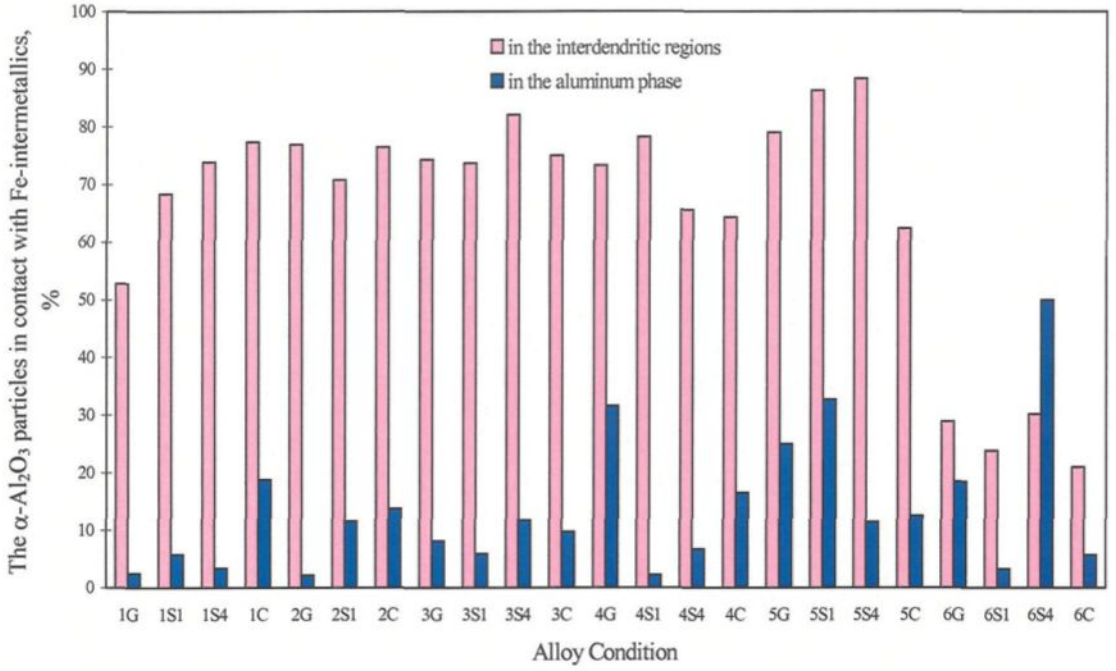

Figure 98 The nucleation events of Fe-intermetallics on substrates of α-Al_2O_3 in the aluminum phase and the interdendritic regions

Figure 100 shows examples of the α-Al_2O_3 particles introduced into alloys 1, 3, 5 and 6. It is clear that the α-Al_2O_3 particles are driven to the interdendritic regions and they serve as active nucleation sites for the iron intermetallic phases and the silicon.

Table 24 Quantitative results of the nucleation of Fe-intermetallics on the α-Al_2O_3 particles.

Phase	Condition		α-Al	Interdendritic Regions	Overall		Potency
	Alloy, dT/dt, C/s	Existing Phases in the microstructure.	%	%	%	level	
Al-Fe binary phases	1, 0.16	Al_6Fe, Al_mFe, Al_XFe.	2.5	52.8	9.5	low	×
	5, 0.19	α, Al_6Fe, Al_mFe, Al_3Fe.	25.0	79.0	32.7	high	?
α-AlFeSi	2, 0.16	α	2.2	76.9	13.5	low	×
	3, 0.21	α	8.1	74.3	37.7	high	✓
	3, 14.7	α, δ	9.7	75.0	30.5	high	?
	4, 0.18	α, β	31.6	73.3	46.0	very high	✓
	5, 0.19	α, Binary Al-Fe	25.0	79.0	56.4	very high	✓
	5, 14.3	α, q_1	12.5	62.4	32.7	high	?
β-AlFeSi	4, 0.18	α, β	31.6	73.3	46.0	very high	✓
	6, 0.18	β	18.4	28.9	27.4	high	✓
δ-AlFeSi	1, 10.7	δ	18.8	77.3	44.4	very high	✓
	2, 13.8	δ, q_1	13.7	76.5	40.5	very high	✓
	3, 17.4	α, δ	9.7	75.0	30.5	high	?
	4, 12.8	δ	16.4	64.3	34.4	high	✓
	6, 12.8	δ	5.7	21.0	17.0	medium	✓
q_1-AlFeSi	2, 13.8	δ, q_1	13.7	76.5	40.5	very high	✓
	5, 14.3	α, q_1	12.5	62.4	32.7	high	?

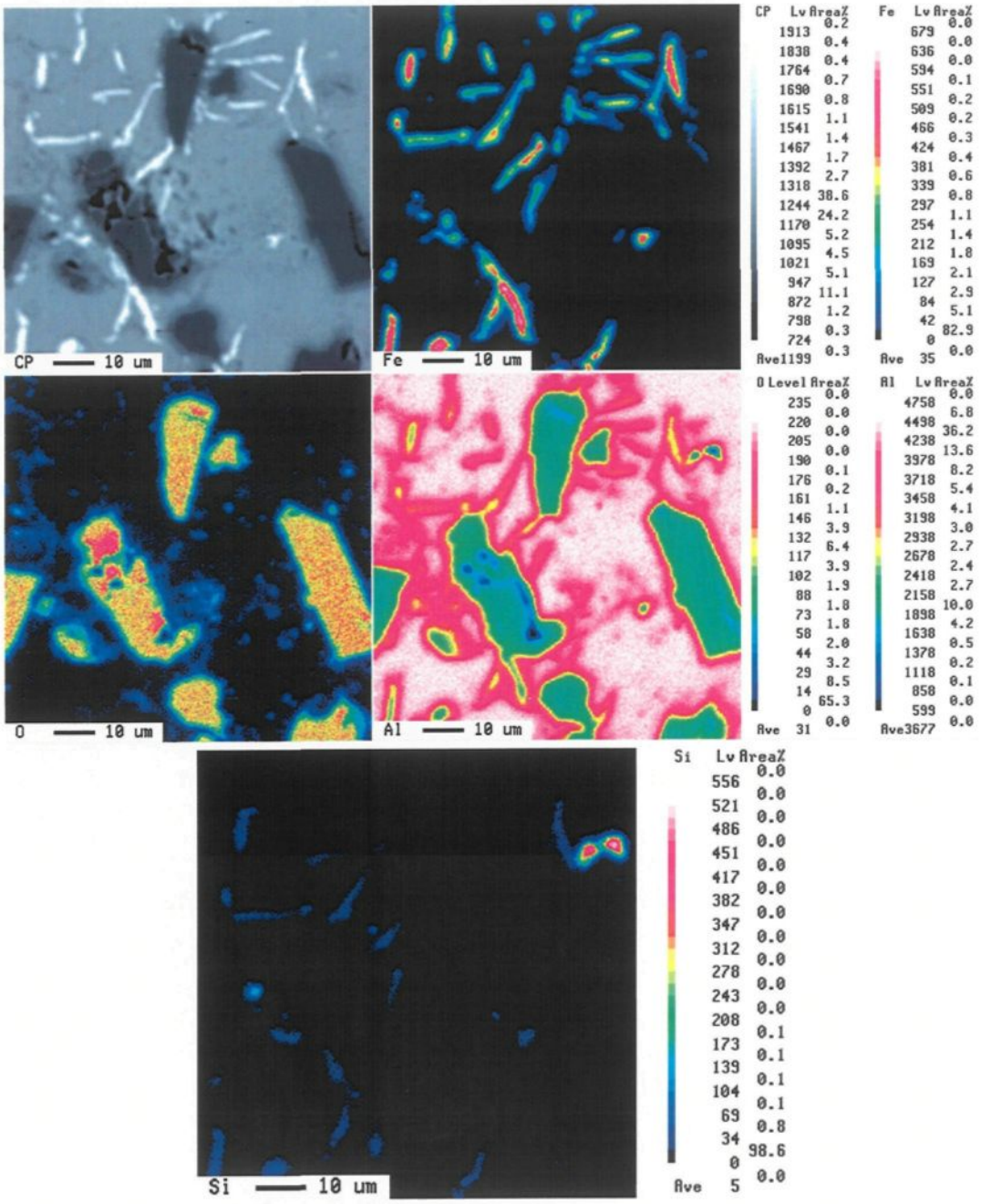

Figure 99 Element distribution maps showing the nucleation of the Fe-intermetallic phases on the surface of the injected particles of α-Al_2O_3, in alloy 5, cooling rate 0.19 °C/s.

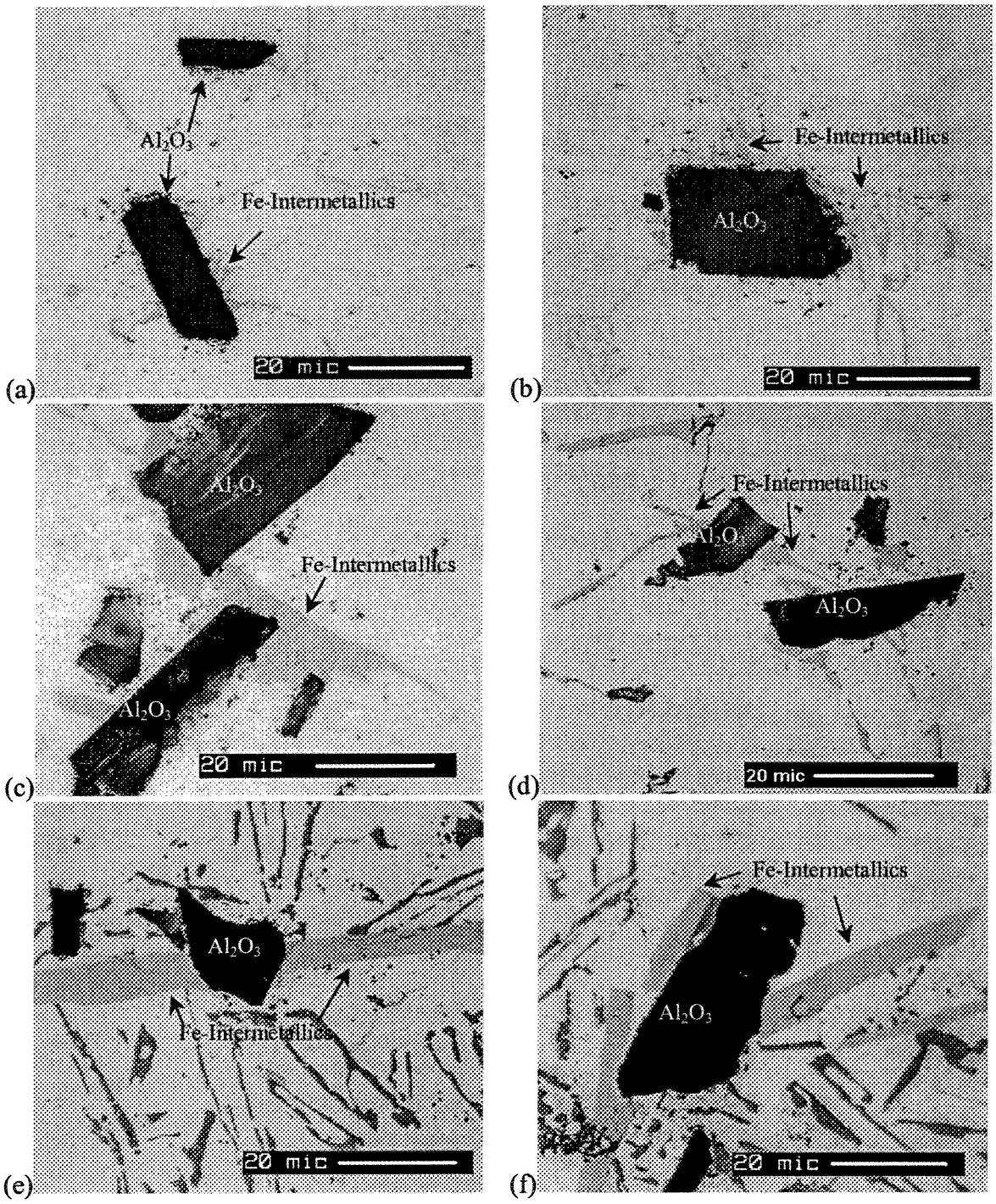

Figure 100 Examples for the nucleation of Fe-intermetallics on the surface of α-Al_2O_3 particles existed in the interdendritic regions: (a) alloy 1, cooling rate 10.7 °C/s, (b) alloy 3, cooling rate 1.3 °C/s, (c, d) alloy 5, cooling rate 0.19 °C/s, and (e, f) alloy 6, cooing rate 0.18 °C/s.

7.2.1.7. Effect of γ-Al_2O_3

The average of Fe-intermetallic nucleation events on the surface of the γ-Al_2O_3 particles is 18.7 % over all the alloy conditions studied here (Table 18). Similar to what was observed with other inclusions, more nucleation events (70.3 %) took place in the interdendritic regions; see for examples the micrographs of Figure 101 (a, c, d). Among the γ-Al_2O_3 particles in the interdendritic regions 65 % of particles were associated, *i.e.*, in contact, with Fe-intermetallics. The ratio is only 8 % in the α-Al phase, see for example the micrograph of Figure 101 (b). It can also be noticed that the number of nucleation events on the γ-Al_2O_3 particles in the α-Al phase is the minimum among the inclusions studied in this work (Table 18).

These results imply that the γ-Al_2O_3 particles, which are efficient nucleants for the matrix phase, are attracted early to the growing solid phase before the build up of solute rich regions during solidification. This explains the high potency of γ-Al_2O_3 particles as nucleants for the α-Al phase as reported in Chapter 6,[3] and shows that the nucleation of the second-phase particles are highly affected by the solute concentration rather than the potency of the substrate. Typical examples for γ-Al_2O_3 particles in physical contact with Fe-intermetallics at the interdendritic regions are given by the maps of Figure 102.

Many more nucleation events are observed in the interdendritic regions rather than the α-Al phase at all the alloy conditions. The general trend for the number of nucleation events observed in the interdendritic regions relative to the overall number of events in a given alloy condition shows that the percentage decreases with increasing alloying element

content, *i.e.*, from alloy 1 to alloy 6. It can be concluded here that the γ-Al_2O_3 particles, which are pushed to the interdendritic regions, are suitable sites for the nucleation of Fe-intermetallics. The potency of γ-Al_2O_3 to nucleate the Fe-intermetallics decreases with the content of alloying elements, Si and Fe.

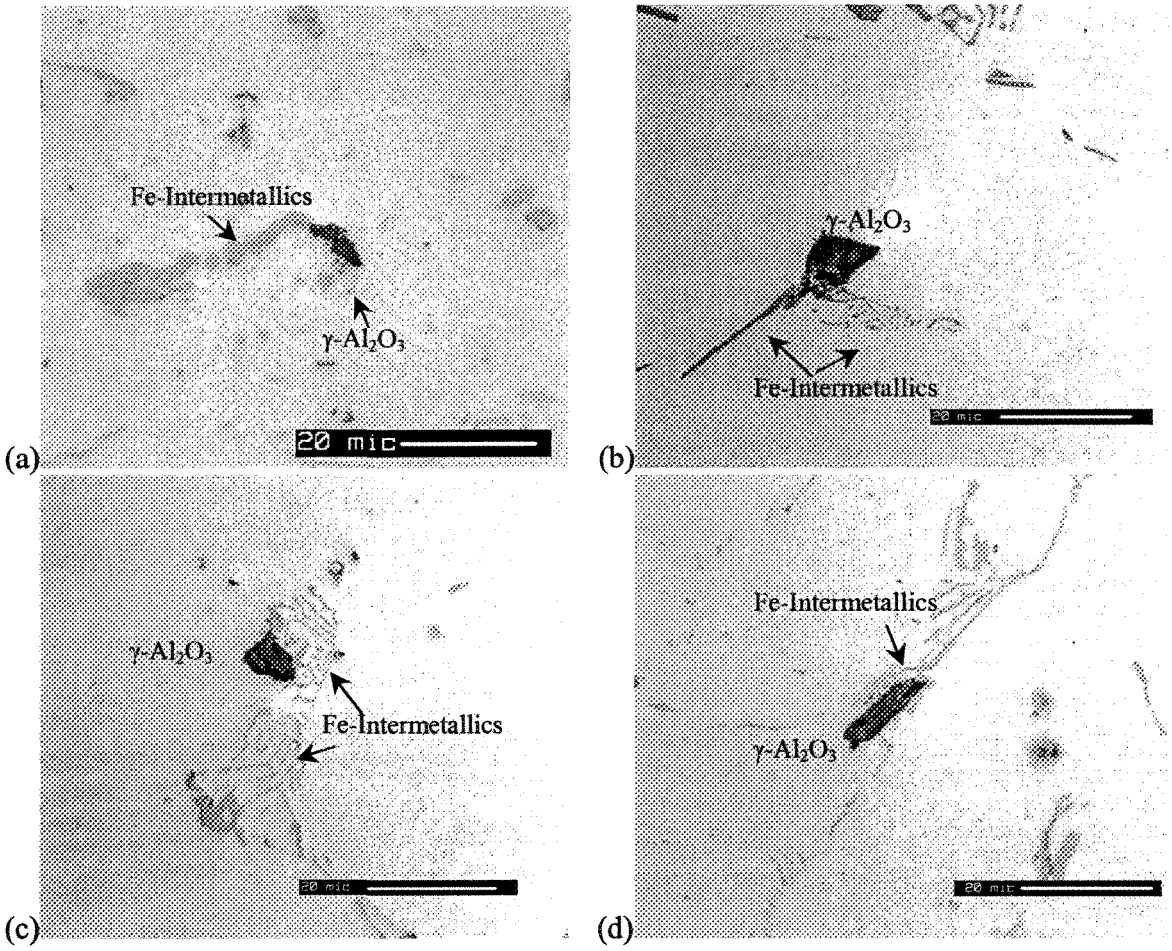

Figure 101 Optical micrographs showing the nucleation of Fe-intermetallics on the γ-Al_2O_3 particles in alloy 5, (a) binary Al-Fe phases, cooling rate 0.19 °C/s, (b-d) Chinese script, α-AlFeSi, and needle-like Al-Fe phases, (b) cooling rate 1.2 °C/s, (c, d) cooling rate 8 °C/s

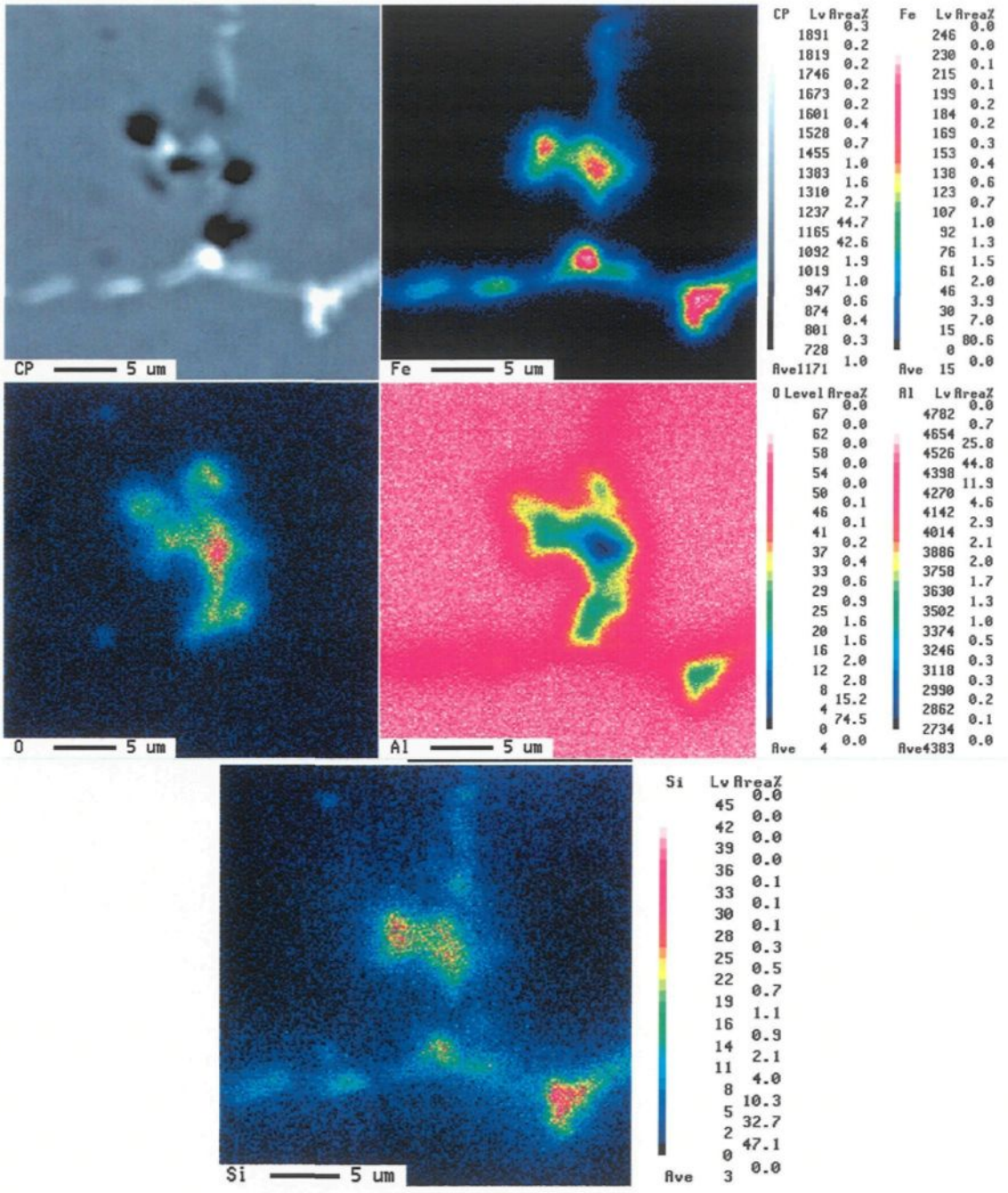

Figure 102 Maps of element distributions showing typical example of γ-Al_2O_3 particles in physical contact with Fe-intermetallics at the interdendritic regions of alloy 4, cooling rate 12.8 °C/s.

Table 25 confirms the above results. It can be seen that, generally, the γ-Al_2O_3 particles are not potent nucleants for the Fe-intermetallic phase in the alloys studied. In a few cases, there are high percentages of physical contact, such as the case of alloys 3 and 5 cooled at 14.7 and 14.3 °C/s, respectively. The microstructure of these alloys at their respective cooling conditions contains (α, δ) and (α, q_1) phases, respectively. The α-AlFeSi is the common phase between these microstructures. It can also be seen from Figure 101 (b, c) that α-AlFeSi phase can nucleate on the γ-Al_2O_3 particles. Therefore, this may suggest a high potency of γ-Al_2O_3 particles to nucleate the Chinese script -α-AlFeSi phase.

7.2.1.8. Effect of SiC

A high efficiency of SiC particles to heterogeneously nucleate the Fe-intermetallic phases is observed in this work. The ratio of 30.7 pct of the overall SiC particles studied were observed to have physical contact with Fe-intermetallic phases, 67.7 pct of which are located in the interdendritic regions (Table 18). It was found that 16.9 pct and 65.8 pct of the particles located in the α-Al phase and the interdendritic regions, respectively, are in evident physical contact with Fe-intermetallics.

The SiC particles showed a high potency to nucleate several Fe-intermetallic phases (see results in Table 26). Binary Al-Fe phases, α-AlFeSi, β-AlFeSi and δ-AlFeSi phases had high physical contact values with the SiC particles in microstructures containing either one or more phases.

Table 25 Quantitative results of the nucleation of Fe-intermetallics on the γ-Al_2O_3 particles.

Phase	Condition		α-Al	Interdendritic Regions	Overall		Potency
	Alloy, dT/dt, C/s	Existing Phases in the microstructure.	%	%	%	level	
Al-Fe binary phases	5, 0.19	α, Al_6Fe, Al_mFe, Al_3Fe.	1.5	77.8	13.2	low	?
α-AlFeSi	2, 1.53	α	3.8	50.0	8.5	low	?
	3, 0.21	α	0.5	75.0	7.3	low	×
	3, 14.7	α, δ	21.3	73.0	36.8	high	?
	5, 0.19	α, Binary Al-Fe	1.5	77.8	13.2	low	×
	5, 14.3	α, q_1	29.6	82.3	52.4	very high	?
β-AlFeSi	6, 0.18	β	0.7	100	1.4	very low	×
δ-AlFeSi	1, 10.7	δ	14.0	66.7	22.4	medium	Medium
	2, 13.8	δ, q_1	17.9	48.9	27.0	medium	?
	3, 14.7	α, δ	21.3	73.0	36.8	high	?
q_1-AlFeSi	2, 13.8	δ, q_1	17.9	48.9	27.0	medium	?
	5, 14.3	α, q_1	29.6	82.3	52.4	very high	?

Table 26 Quantitative results of the nucleation of Fe-intermetallics on the SiC particles.

Phase	Condition		α-Al	Interdendritic Regions	Overall		Potency
	Alloy, dT/dt, C/s	Existing Phases in the microstructure.	%	%	%	level	
Al-Fe binary phases	1, 0.16	Al_6Fe, Al_mFe, Al_XFe.	22.7	78.0	42.2	very high	✓
	5, 0.19	α, Al_6Fe, Al_mFe, Al_3Fe.	11.7	83.9	42.5	very high	✓
α-AlFeSi	2, 0.16	α	21.0	72.7	32.5	high	✓
	3, 0.21	α	5.0	66.2	16.2	low	×
	3, 14.7	α, δ	21.6	80.7	49.0	very high	✓
	4, 0.18	α, β	23.6	74.1	36.5	high	✓
	5, 0.19	α, Binary Al-Fe	11.7	83.9	42.5	very high	✓
	5, 14.3	α, q_1	25.7	40.2	30.7	high	?
β-AlFeSi	4, 0.18	α, β	23.6	74.1	36.5	high	?
	6, 0.18	β	49.3	18.9	28.1	high	✓
δ-AlFeSi	1, 10.7	δ	2.1	60.6	13.7	low	×
	2, 13.8	δ, q_1	16.5	81.3	41.9	very high	✓
	3, 14.7	α, δ	21.6	80.7	49.0	very high	✓
	4, 12.8	δ	15.6	90.0	50.9	very high	✓
	6, 12.8	δ	17.1	20.9	20.5	high	✓
q_1-AlFeSi	2, 13.8	δ, q_1	16.5	81.3	41.9	very high	?
	5, 14.3	α, q_1	25.7	40.2	30.7	high	?

Quantitative data for the nucleation events are given in Figure 103. According to these data the nucleation of Fe-intermetallics mostly takes place in the interdendritic regions (see also Figure 104). However, the number of nucleation events that were observed in the interdendritic regions decreased sharply in alloy 6. In contrast to this, the number of nucleation events in the interdendritic regions increased in alloy 6. This indicates that a poisoning effect similar to that of Si on the nucleation of the α-Al phase applies in the case of the heterogeneous nucleation of the second-phase particles within the α-Al phase.

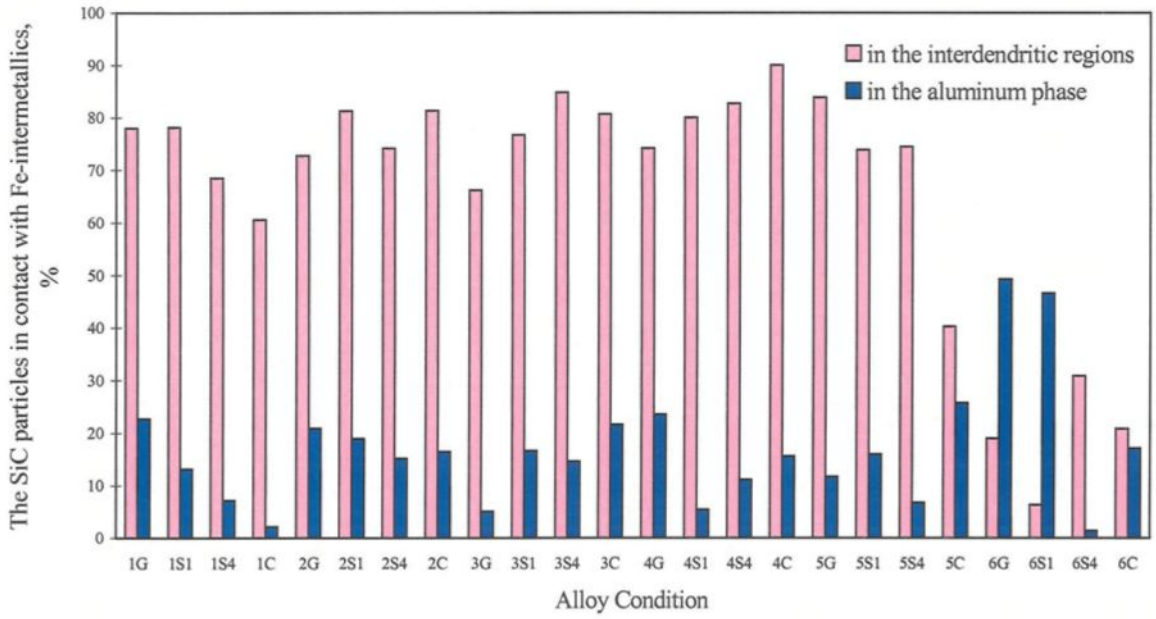

Figure 103 Quantitative results on the SiC particles in direct contact with Fe-intermetallics.

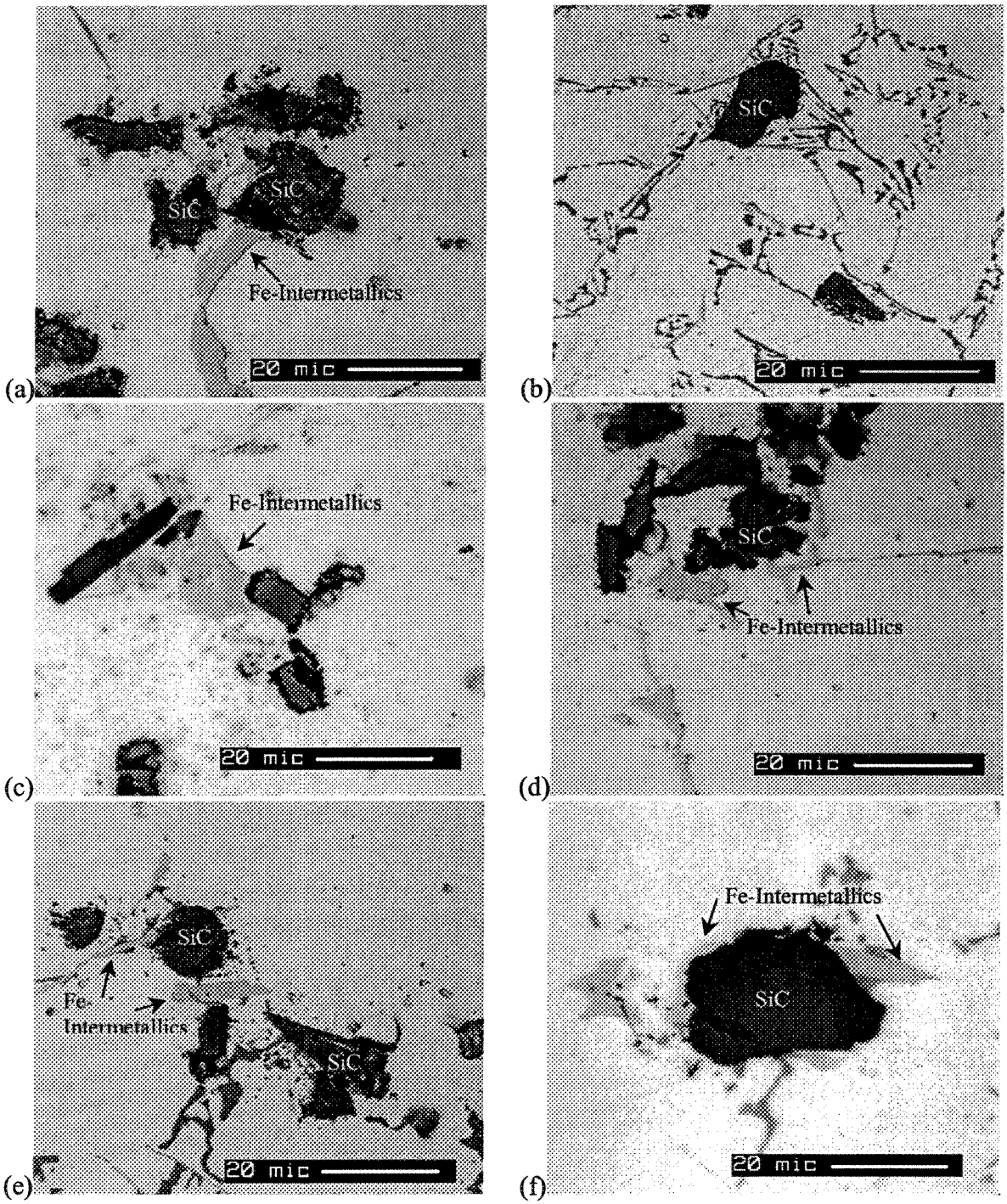

Figure 104 Optical micrographs showing the nucleation of Fe-intermetallics on surface of SiC particles, (a, b, d, e) in the interdendritic regions, and (c, f) in the aluminum phase (a) alloy 1, cooling rate 0.16 °C/s, (b) alloy 6, cooling rate 12.8 °C/s, (c, d) alloy 4, cooling rate 0.18 °C/s, and (e, f) alloy 6, cooling rate 0.18 °C/s.

7.3. Discussion

7.3.1. The Requirements for Intermetallic Phase Nucleation

The nucleation of intermediate phases containing higher solute concentrations is still not well understood since the nucleation of such phases is too system dependent. For example, to promote the nucleation of an Fe-intermetallic phase in an Al-Si-Fe alloy, it is necessary to reach certain solute concentrations, corresponding to the composition of the phase in the liquid, at the nucleation temperature of the phase. Both conditions must be met concurrently to promote the nucleation of the phase. Thus, nucleation of the second phase takes place at certain isotherms of the liquid phase where the solute concentration requirement is met, provided that an appropriate substrate is present in the liquid at that moment. Therefore, the role of substrates in the nucleation of the intermetallic phases is largely limited by the satisfaction of solute concentration and the nucleation temperature requirements.

According to the above description of intermetallic phase nucleation, it follows that the inclusion particles that serve as potent nucleants for the primary phase should exhibit poor nucleation potency for the second-phase particles. The poor potency of γ-Al_2O_3 for the nucleation of different Fe-intermetallics confirms this deduction. The γ-Al_2O_3 particles showed the highest potency for the nucleation of α-Al phase in the present experimental alloys (Chapter 6).[3] Within the α-Al phase, the γ-Al_2O_3 particles exhibited the poorest potency for the nucleation of the Fe-intermetallic phases in different alloys at different cooling rates (as shown in Table 25). Therefore, although a high number of nucleation

events on the surface of the γ-Al_2O_3 particles were observed in the interdendritic regions as shown in Table 18 and Table 25, the overall nucleation potency of these particles is still very low since the majority of these particles lie within the α-Al phase as observed in Chapter 6.[3]

The diagram of Figure 105 shows schematically the influence of solute concentration, nucleation temperature, supercooling and potency of the nucleant particles on the nucleation of second-phase particles. In this diagram, the round symbols denote the potent nucleants while the triangles represent the less potent inclusion particles. At the early stages of solidification, the solute concentration does not reach the required level, and hence does not allow the nucleation of the solute-rich phase even when the nucleation temperature is satisfied and potent nucleants are available (see particles 1 and 2 in Figure 105 (a, b)). Less potent particles such as particles 3 to 6, cannot promote the nucleation of the intermetallic phase even if these particles lie in the nucleation temperature isotherm of the liquid unit volume that contains the appropriate solute concentrations (see Figure 105 (c, d)). At the last stage of solidification, potent nucleants such as particles 7 and 8 can promote the nucleation of the intermetallic phase given that the requirements of nucleation temperature, solute concentration and supercooling condition are met at this stage (Figure 105 (d)). Other less potent particles can be activated if they lie in a supercooled liquid volume and hence can promote the nucleation of the intermetallic phase if the solute concentration requirement is satisfied as represented by particle 9 in Figure 105 (d).

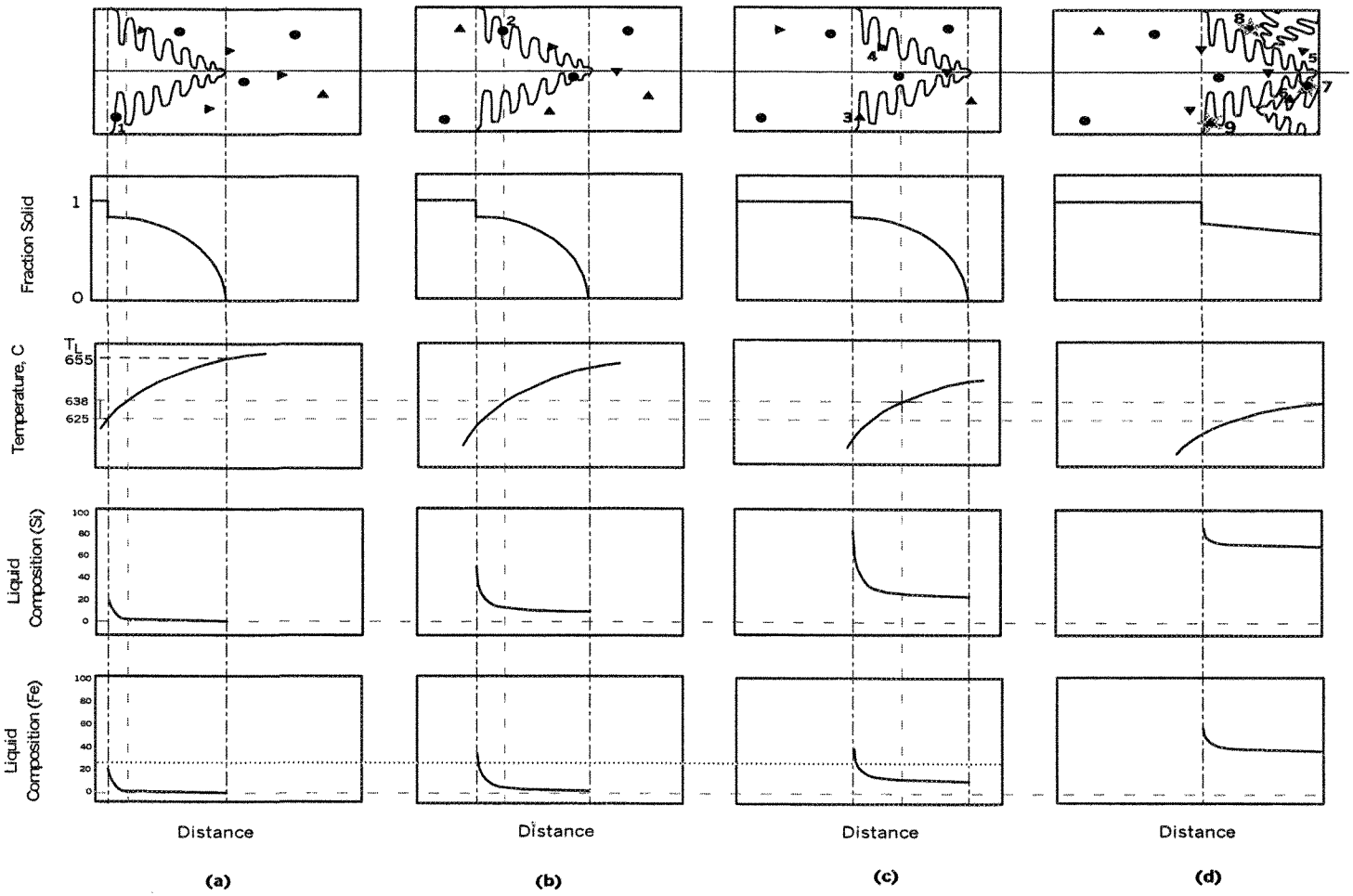

Figure 105 A schematic diagram showing the influence of solute concentration (segregation), nucleation temperature, supercooling and potency of nucleant particles on the nucleation of second-phase particles.

7.3.2. Effect of Cooling Rate on the Nucleation of Fe-Intermetallics

In general, the inclusion particles introduced served as active nucleation sites for the different Fe-intermetallic phases that form at the studied cooling conditions (see Table 18). However, there is evidence that cooling rate and alloy composition do influence the potency of the inclusions for nucleation of the second-phase particles.[78] These factors were observed to affect the number of the heterogeneous nucleation events associated with the inclusion particles.

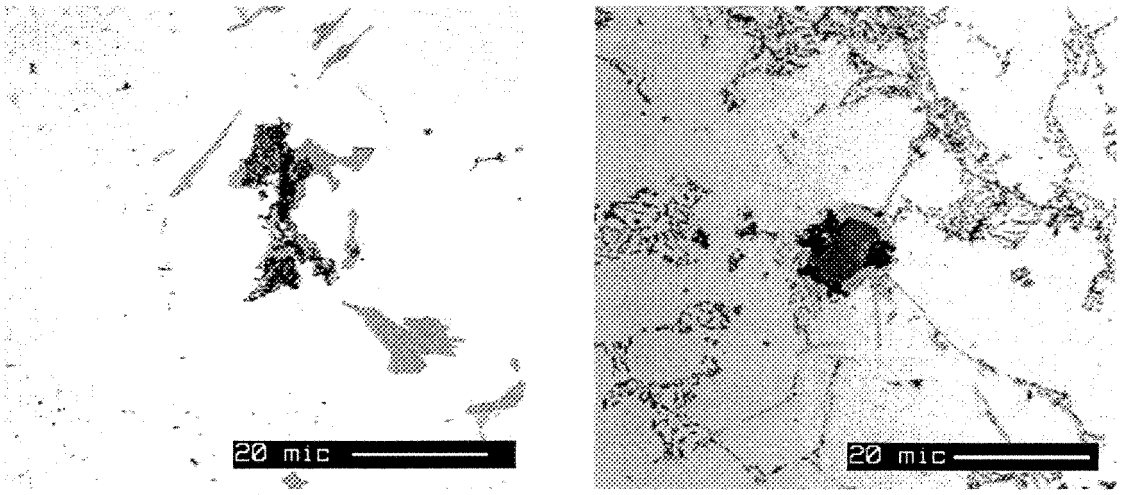

Figure 106 (a) alloy 3, CaO, cooling rate is 0.21 °C/s, (b) alloy 6, α-Al_2O_3, cooling rate is 12.8 °C/s.

According to the spherical cap model of nucleation,[99] the heterogeneous nucleation of a phase on a particle in the melt requires a certain amount of undercooling. The better the wettability between the nucleant and the solid phase, the more potent the nucleant which can lead to nucleation at small undercoolings. In some cases, complete wetting of the inclusion particles by the solid intermetallic phases was observed (see for example Figure

106). This condition is the optimum and indicates that the interfacial energy between the nucleus and that specific nucleant particle is minimal and the nucleus is able to envelope the nucleant. However, this takes place on only very few particles from a population of the same kind, a fact that confirms that not all the nucleant particles have the same potency. Therefore, such cases cannot be considered as a proof of the catalytic efficiency of any specific kind of inclusion.

Not all the inclusion particles that are added to the liquid Al-Si-Fe alloys possess very high potency similar to those presented in Figure 106. The inclusion particles have different nucleating potencies and, therefore, require different undercoolings to activate nucleation events on their surfaces. The undercooling has a noticeable effect on the potency of nucleants as it enhances the potency of the poor nucleants. In other words, high undercooling can render the poor nucleants more potent. This classical phenomenon, which was reported for the nucleation of the primary phases such as aluminum,[106] was observed in the nucleation of the Fe-intermetallic phases in the present study.

7.3.2.1. Nucleation of Fe-Intermetallics on SiC and α-Al_2O_3 in Alloy 1

The undercooling may change the number of nucleation events occurring on the surface of inclusions in two ways. It can change the Fe-intermetallic phase that dominates in the microstructure, or enhance the potency of the inclusion particles. Figure 107 shows the effect of cooling rate (and thus the applied undercooling) on the potency of α-Al_2O_3 and SiC particles for the nucleation of Fe-intermetallics in alloy 1 at four cooling rates. The as-cast microstructures of alloy 1 contains binary Al-Fe phases (*i.e.*, Al_6Fe, Al_mFe and Al_xFe)

and δ-AlFeSi phases after cooling at 0.16 and 10.7 °C/s, respectively. It is believed that the intermetallic phase content of the alloy changes continuously with the cooling rate from binary Al-Fe phases to the δ-AlFeSi phase.

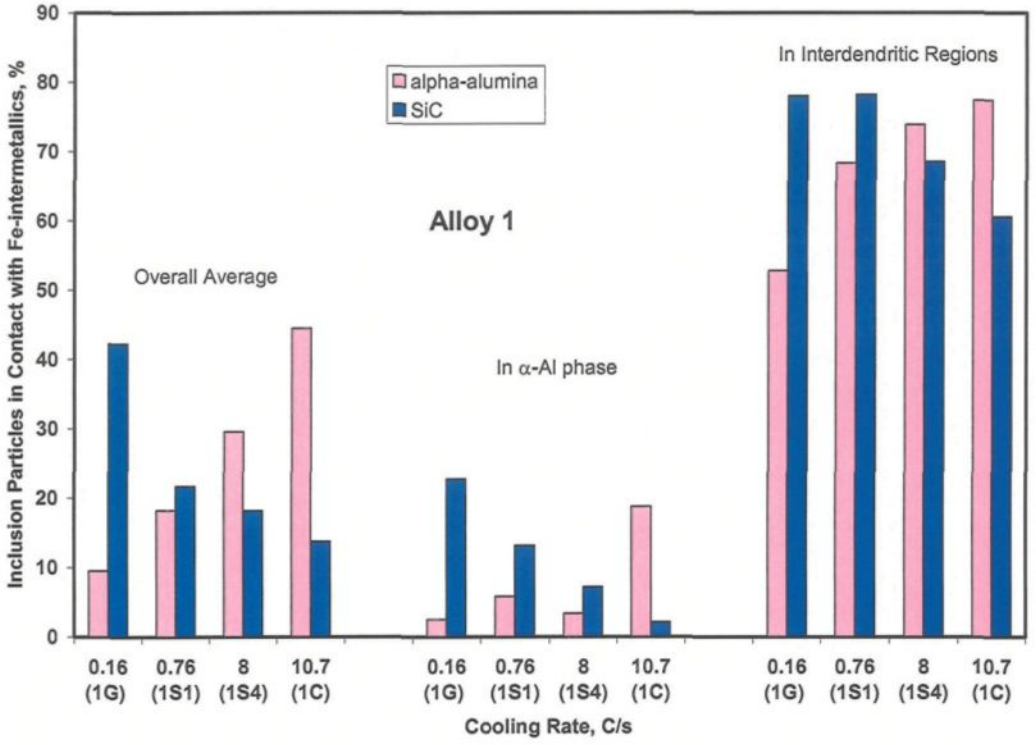

Figure 107 The effect of cooling rate on the potency of α-Al_2O_3 and SiC particles for the nucleation of Fe-intermetallics in alloy 1 at four cooling rates

The diagrams of Figure 107 show that nucleation of binary Al-Fe intermetallic phases is promoted on the surface of SiC particles while that of the δ-AlFeSi phase is not. The opposite was observed to take place on the α-Al_2O_3 particles: nucleation of the binary Al-Fe phases was not favored on α-Al_2O_3 particles while that of δ-AlFeSi phase took place. The transition from high potency to poor potency in both cases was gradual over the range of cooling rates inspected as shown in Figure 107. It can be summarized that even at high

cooling rates (and hence high undercoolings) nucleation of intermetallic phases can be promoted preferentially on certain types of nucleants. However, one can expect that the applied undercooling resulting from the cooling rate of 10.7 °C/s might not be enough to activate the nucleation of δ-AlFeSi phase on the surface of SiC particles in the case of alloy composition and solidification conditions studied here.

7.3.2.2. Effect of Cooling Rate on the Nucleation of α-AlFeSi

Another example for the effect of cooling rate (and undercooling) on the potency of nucleant particles is the nucleation of the α-AlFeSi phase. The latter was observed to nucleate more frequently at high cooling rates than at low ones on the surface different inclusions such as MgO, TiC, Al_4C_3 and γ-Al_2O_3 (Table 27). It clear that the number of nucleation events observed increases with cooling rate. A low or medium number of events were observed at a low cooling rate, while high and very high events were observed at high cooling rates. Thus, it can be summarized that increasing the cooling rate or the applied undercooling enhances the heterogeneous nucleation of intermetallic phases.

7.3.2.3. Nucleation of the Metastable δ-AlFeSi and q_1-AlFeSi Phases

It can be seen from Table 19 to Table 26 that the nucleation of Fe-intermetallics in alloy 2 containing (δ + q_1) and alloy 5 containing (α + q_1) phases are highly promoted on the surface of most inclusions inspected in the present work. The nucleation of the α-AlFeSi phase on inclusion particles is enhanced by increasing the cooling rate as discussed earlier. The microstructures containing these phase fields are obtained under high cooling rates in the order of 13.8 °C/s and 14.3 °C/s. The δ-AlFeSi and q_1-AlFeSi phases are

metastable phases in the present alloys and form only at high cooling rates, whereas the α-AlFeSi phase is stable over a wide range of cooling rates (Chapter 4).[2] However, we did not observe preferential nucleation of the δ-AlFeSi and q_1-AlFeSi phases on certain inclusions. This indicates that the heterogeneous nucleation of both δ-AlFeSi and q_1-AlFeSi phases is highly promoted by the high cooling rate (high undercooling). In conclusion, the nucleation of the Fe-intermetallic phases in Al-Si-Fe alloys obeys the general rules of the theory of heterogeneous nucleation in terms of the effect of undercooling on the potency of the nucleant particles.

7.3.3. Effect of Alloy Composition on Nucleant Potency and Nucleation of Fe-Intermetallics

The alloy composition also influences the catalyzing potency of nucleants. This topic is discussed in three cases; the nucleation of α-AlFeSi phase in alloys 2, 3, 4 and 5; the nucleation of δ-AlFeSi phase in alloys 1, 4 and 6; and the poisoning effect of Si.

7.3.3.1. Nucleation of α-AlFeSi in Alloys 2, 3, 4 and 5

The solute concentration can affect the heterogeneous nucleation of the intermetallic phases by affecting the activity of the nucleant particles in the liquid. It is evident from Table 27 that the observed nucleation events of the α-AlFeSi phase on MgO, TiC, Al_4C_3 and γ-Al_2O_3 particles increases with increasing the alloying addition from alloy 2 to alloy 5. It is important to note that the α-AlFeSi phase is the only stable intermetallic phase in alloys 2 and 3, and is the dominating one in alloys 4 and 5 at their respective cooing rates (see Table 27). Thus, up to the level of alloying additions in these alloys, the solute

concentration enhances the heterogeneous nucleation of the second-phase particles. The effect of solute concentration is in agreement with the Growth Restricting Factor concept (GRF),[213] in which the solid growth is slowed as a result of the constitutional undercooling produced by the solute enrichment at the solid/liquid interface. Consequently, more nucleant particles become active.

However, the effect of the GRF depends on the solute type and concentration. The solute effects of Si and Fe on the nucleation of the α-Al have been studied by Johnsson.[209] He found that these elements restrict the growth rate and are additive in effect which is quantified by the GRF. The gradual increase in the number of nucleation events with the solute content (Si + Fe) from alloy 2 to alloy 5 indicates that the same effect holds for the nucleation of Fe-intermetallics in the present alloys.

7.3.3.2. Nucleation of the δ-AlFeSi in Alloys 1, 4 and 6

Table 28 shows the observed nucleation events of δ-AlFeSi phase within the α-Al phase and the interdendritic regions of alloys 1, 4 and 6. It is clear from the number of nucleation events in alloys 1 and 4 that the nucleation of the δ-AlFeSi phase is enhanced by increasing the content of alloying elements in the alloy. However, the number of nucleation events observed on TiC, α-Al_2O_3 and SiC particles in alloy 6, containing 6.3 wt% Si, is much lower than that found in alloys 1 and 4. The phenomenon is best shown in Figure 89, Figure 98 and Figure 103.

Table 27 Effect of cooling rate on the potency of inclusions in the nucleation of Fe-intermetallics.

Alloy, dT/dt, C/s	Phases existing in the microstructure.	MgO	TiC	Al_4C_3	γ-Al_2O_3
2, 0.16	α			13.3	
2, 1.53	α	4.5	22.8		8.5
3, 0.21	α				7.3
3, 1.3	α	22.5		25.6	
4, 1.4	α, β		26.4	33.8	
5, 0.19	α, binary Al-Fe			51.9	13.2
5, 1.2	α, binary Al-Fe		37.3		
3, 14.7	α, δ	37.1	51.0	38.5	36.8
5, 14.3	α, q_1	45.8	63.5	60.4	52.4

Table 28 Effect of alloy composition on the nucleation of δ-AlFeSi phase on different inclusions.

Alloy, dT/dt, C/s	Phases existing	TiC			α-Al_2O_3			SiC		
		α-Al	Int. reg.	Overall	α-Al	Int. reg.	Overall	α-Al	Int. reg.	Overall
1, 10.7	δ	8.44	46.3	18.3	18.8	77.3	44.4	2.1	60.6	13.7
4, 12.8	δ	23.2	75.0	34.7	16.4	64.3	34.4	15.6	90.0	50.9
6, 12.8	δ	11.4	47.9	27.8	5.7	21.0	17.0	17.1	25.9	20.5

Thus, the potency of nucleant particles in both microstructure regions (the α-Al and the interdendritic regions) improves with increasing solute concentration up to a certain level of alloying additions. Above this level, the solute concentration negatively affects the potency of the nucleation sites. In other words, alloying addition at certain levels poisons the nucleation sites. Similar observations were reported in the literature concerned with the grain refining of aluminum alloys. However, the poisoning effect of the Si was expected to influence the heterogeneous nucleation of the second-phase particles in the same way that it affects the nucleation of the primary phase (α-Al), since the Si-poisoning degrades the potency of the nucleant itself.

It is evident that the nucleation of the Fe-intermetallic phases in the Al-Si-Fe alloys is influenced by solute concentration. The nucleation events of intermetallics increases with increasing solute concentration up to certain level, after which the poisoning effect of Si operates in just the same way it does with the primary phase (α-Al).

7.3.4. Effect of Nucleant Properties on the Nucleation of Fe-Intermetallics

According to Turnbull and Vonnegut,[96] the heterogeneous nucleation of crystals on a catalyst is enhanced by good lattice disregistry across the nucleation interface. This theoretical approach, which was adopted as a basis for the prediction of useful inoculants, failed in practice. Some workers reported experimental results in full disagreement with the Turnbull and Vonnegut[96] crystallographic theory of crystal nucleation (see for example the work of Zhang and Cantor[97]). Others proved that the physical and chemical characteristics of the nucleant surface are more important for nucleation than the lattice disregistry[98] while

Porter and Easterling[99] concluded that the lattice disregistry is unable to account for the effectiveness of nucleants. In their review, Cantor and O'Reilly[100] showed that catalysis is dominated by chemical rather than structural compatibility at the nucleating interface. As a result the nucleation theory, based on the theoretical model of lattice registry, has failed in the prediction of efficient nucleant and, therefore, it has been primarily used to rationalize the identification of useful nucleants.[71] The question now is that, based on the present results, is there any preferential nucleation of specific Fe-intermetallic phases on certain inclusions that can reflect good crystallographic fit? The answer can contribute to this open debate.

7.3.4.1. Chemical Characteristics of the Nucleant Surface

It is evident that the reactive inclusions such as CaO and Al_4C_3 that form several compounds containing high Si with the aluminum alloy (Chapter 6),[3] are potent for the nucleation of the intragranular Fe-intermetallic particles (within the α-Al phase), (see Table 18). This may be attributed to their capability of consuming the poisoning species (i.e. Si atoms) and, therefore, maintain high potency for nucleation.

In the interdendritic regions all the inclusion types were observed to effectively promote the nucleation of Fe-intermetallic phases (Table 18). This means that the potency of nucleants with chemically active surface such as CaO or Al_4C_3 in the nucleation of Fe-intermetallic phases is not evident in the interdendritic regions. The high concentration of solutes peculiar to these regions may be the reason for the activation of high percentages of

several inclusion particles regardless of the surface characteristics (effect of solute concentration is discussed in more details in section **7.3.3**).

7.3.4.2. Orientation Relationships at the Nucleation Interface

The crystallographic fit between the nucleant and the solid phase was used to rationalize the observed nucleation events. The nucleation of $Al_{13}Fe_4$ on the α-Al phase is given here as an example. The orientation relationships between these two phases according to two authors (from the review of Allen *et al.*[25]) are given below:

Donnelly and Rudee[214] observed the following orientation relationship:

$$(001)_{Al_{13}Fe_4} // (100)_{Al}$$

$$[100]_{Al_{13}Fe_4} // [001]_{Al} (\pm 10^{o})$$

While Ping *et al.*[215] observed another three different orientation relationships:

$$[001]_{Al_{13}Fe_4} // [001]_{Al} \qquad [100]_{Al_{13}Fe_4} // [100]_{Al} \qquad [100]_{Al_{13}Fe_4} // [10\bar{1}]_{Al}$$

$$(200)_{Al_{13}Fe_4} // (200)_{Al} \qquad (020)_{Al_{13}Fe_4} // (020)_{Al} \qquad (200)_{Al_{13}Fe_4} // (020)_{Al}$$

$$(020)_{Al_{13}Fe_4} // (020)_{Al} \qquad (001)_{Al_{13}Fe_4} // (002)_{Al} \qquad (001)_{Al_{13}Fe_4} // (202)_{Al}$$

On the other hand, Adam and Hogan[216] did not observe any orientation relationship between the $Al_{13}Fe_4$ and the α-Al phases. Recently, based on nucleation undercooling measurements, Allen *et al.*[58] proposed that there should be a potent catalyst for the nucleation of the $Al_{13}Fe_4$ phase and suggested this to be the primary Al matrix or an undetected impurity which is present even in the super pure alloys. In addition, they found that the metastable phase content is largely controlled by the concentration of the solute

atoms of V and P. Thus, the constitution of the alloys has a major effect on the intermetallic phase selection. In contrast, Allen *et al.*[59] concluded that α-Al is not an efficient nucleant for the Fe-rich eutectic liquid. More recently, Allen *et al.*[60] observed an undercooling of 2 °K associated with the nucleation of $Al_{13}Fe_4$ at a slow cooling rate of 2 °K/min and confirmed that there was a kinetic barrier to nucleation of the Al-$Al_{13}Fe_4$ eutectic, presumably by Al. The work of Allen *et al.*,[59,60] in turn, contradicts the well-defined orientation relation ships reported by Donnelly and Rudee[214] and Ping *et al.*[215]

Another example is the role of the TiB_2 particles in the nucleation of binary Al-Fe phases (specifically the Al_mFe,[60,108,109,110,111,112] and $Al_{13}Fe_4$[19] phases) and the α-AlFeSi[111,112] phase. It was proposed that the addition of the TiB_2 grain refiner promotes the nucleation of these phases via the increase the number density of potent nucleation sites, presumably TiB_2.[109,110] The crystallographic theory of nucleation was used to suggest that there might be a small lattice mismatch between the hexagonal lattice of TiB_2 and phases with orthogonal crystal axes such as the Al_mFe and the α-AlFeSi phases.[112] Some of these workers showed that the Al_mFe phase forms in the grain refined alloys provided that a certain level of V[59,60] or Si[59,61] is attained in the alloy composition.

Allen *et al.*[59] showed that the formation of Al_mFe is equally promoted in alloys grain-refined with Al-B, Al-Ti-B and Al-Ti-C additions, indicating that the chemical identity of the grain refiner in the promotion of Al_mFe is unimportant. They suggested, therefore, that Al_mFe is not directly nucleated either by the corresponding grain refiner particles (AlB_2, TiB_2 and TiC, respectively), or by some reaction product between V and the grain refiner particles. They found that in alloys of a sufficiently high Si content neither

V nor grain refiner is prerequisite for the Al_mFe formation.[59] Metastable binary Al-Fe phases were observed in the present alloys, containing high Si content relative to that of Fe in the alloy composition (Chapter 4).[2]

It is clear from these examples that the nucleation of Fe-intermetallics does not follow a specific orientation relationship and is not promoted on certain nucleation sites. This indicates that the epitaxial crystallization of Fe intermetallic phases on a substrate can take place on surfaces with different crystallographic orientations. The results of the present work support this conclusion. Table 29 shows the percentages of different inclusion particles in physical contact with the α-, β- and δ-AlFeSi phases. It is clear that the Fe-intermetallic phases (*e.g.*, α-, β- and δ-AlFeSi phases) can nucleate on the surface of several inclusions under identical conditions of alloy composition and cooling rate. In other words, nucleation of each Fe-intermetallic phase particle can take place on a variety of heterogeneous nucleation sites with different crystallographic structures. It follows that the absence or presence of certain inclusions in a molten alloy does not affect the solidified intermetallic phase content by stabilizing certain phases over others. Therefore, the competitive nucleation of two phases during solidification is more probably controlled by their nucleation temperatures as previously argued in the literature,[25,217] rather than the crystallographic orientation (or the lattice disregistry), which seems to have a minimum influence on the nucleation process. This conclusion rules out the idea that nucleation is basically promoted by crystallographic fit at the nucleation interface.

Table 29 Nucleation of Fe-intermetallics on different inclusions.

Phase	Alloy	Percentage of Inclusion Particles in Physical Contact with Intermetallic Phases							
		CaO	MgO	TiB_2	TiC	Al_4C_3	α-Al_2O_3	γ-Al_2O_3	SiC
α-AlFeSi	2		4.5		22.8	13.3	13.5	8.5	32.5
	3	68.3	22.5			25.6	37.7	7.3	16.2
β-AlFeSi	4				26.4		46.0		36.5
	6			25.9	29.8		27.4	1.4	28.1
δ-AlFeSi	1	31.0	18.6	17.2	18.3		44.4	22.4	13.7
	4	29.3	17.8		34.7		34.4		50.9
	6			25.0	27.8	25.0	17.0		25.5

Therefore, the selective formation of certain phases during solidification (usually referred to as phase selection) on the basis of nucleation does not seem to be largely affected by the types of nucleants present in the liquid phase. In other words, nucleation control of the second-phase particles such as the Fe-intermetallics in the present alloys is most likely influenced by chemical factors (*i.e.*, alloy composition and solute segregation characteristics), nucleation temperatures and cooling conditions rather than the crystallographic structure of the nucleating surface.

7.4. Summary

Nucleation of Fe-intermetallic phases (*i.e.* binary Al-Fe, α-AlFeSi, β- AlFeSi, δ-AlFeSi and q_1-AlFeSi phases) on the surface of different inclusions in the six experimental Al-Si-Fe alloys was studied through a quantitative evaluation of the number of inclusion particles that have a direct physical contact with the nucleated phase as seen through the optical microscope. It was found that nucleation of each of the Fe-intermetallic phases was

generally observed to be promoted on the surface of several inclusions under the same conditions of alloy composition and cooling rates. However, some inclusions exhibited high potency for the nucleation of particular Fe-intermetallic phases under certain conditions and poor potency under other conditions. The potent nucleants for the primary α-Al phase such as γ-Al_2O_3 exhibited poor potency for the nucleation of the Fe-intermetallic particles that lie within the primary phase (intragranular particles). Reactive inclusions such as CaO and SiC are very potent nucleants for the intragranular Fe-intermetallic phase particles.

The nucleation of the Fe-intermetallic phases in Al-Si-Fe alloys obeys the general features of nucleation, in particular, the effect of cooling rate and solute concentration on the potency of the nucleant particles: (i) it was observed that increasing the cooling rate enhances the heterogeneous nucleation of the Fe-intermetallic phases on the surface of different inclusions, and (ii) the nucleation potency of inclusion particles in both α-Al and interdendritic regions improves with increasing solute concentration up to a certain level. Above this level, the solute concentration poisons the nucleation sites. Nucleation of the Fe-intermetallics in the alloys studied does not seem to be largely affected by the type (crystallographic structure) of the nucleating surface.

CHAPTER 8

CONCLUSIONS

CHAPTER 8

CONCLUSIONS

The formation of Fe-intermetallics and the α-Al phase in dilute liquid Al-Si-Fe alloys, on nuclei of common inclusion particles found in commercial aluminum alloys was studied using six experimental alloys representative of the Al-rich corner of the Al-Si-Fe system and different cooling rates, where the inclusions (α- and γ-Al_2O_3, MgO, CaO, TiC, SiC, Al_4C_3 and TiB_2) were introduced into the alloy melts using a gas injection technique.

From an analysis of the results obtained, the following may be concluded:

I. Effect of cooling rate and alloy composition on the formation of Fe-intermetallics

1. The volume fraction of iron intermetallic phases is higher at slower cooling rates. Whether the cooling rate is high or low, the volume fraction increases as the alloying contents of iron and silicon increase. However, the iron content is more effective in producing intermetallics than are the Si or Fe+Si contents.
2. The density of iron intermetallics is higher at high cooling rates. At slow cooling rates, large-sized intermetallics are obtained.
3. Phase stability changes with cooling rate and alloy composition. Binary Al-Fe phases form only at slow cooling rates when Fe contents are higher relative to the Si content of the alloy. The β-AlFeSi phase dominates at high silicon levels and slow cooling rate. The α-AlFeSi phase field exists between the binary Al-Fe phases and the β-

AlFeSi phase. Rapid cooling stabilizes Si-rich ternary phases such as the δ-AlFeSi phase and diminishes the binary phases since rapid cooling decreases the solubility of silicon in liquid aluminum and causes entrapment of iron in solid. The δ-AlFeSi phase is the dominating phase at 0.9wt % silicon levels and higher.

4. Solidification paths representing the segregation of iron and silicon to the liquid were calculated using the Scheil equation. The actual solidification paths did not conform to Scheil behavior, as less iron was observed to have actually segregated to the liquid than estimated by the Scheil equation. The reason for this overestimation (of iron content in the liquid) is that the Scheil equation postulates that there is no solid diffusion. Similarly, the theoretical models of Brody and Flemings[132] and Clyne and Kurz[133] cannot explain the departure from Scheil behavior as they give much less weight to solid state back-diffusion. It has been shown qualitatively that the interaction between iron and silicon (which facilitates the diffusion of iron in solid aluminum), together with the suggested role of more effective solid diffusion could account for the departure from Scheil behavior.

5. An adjusted 500°C metastable isothermal section of the Al-Si-Fe phase diagram has been proposed. The adjustments were made to the published equilibrium section in order to correctly predict the phases that are observed in this part of the system at slow cooling rates (0.2°C/s).

II. Analysis of the gas injection technique

6. Theoretical analysis of the gas injection process, including the energetics of particle transfer from gas to liquid and the effect of kinetic forces, were used to derive a theoretical relation for the minimum injection velocity required for successful particle transfer from gas to liquid.
7. The capability of the injection technique is found to be very much restricted by the size of the particles. Very small (< 1-μm) or very large (> 100-μm) particles cannot be introduced into the liquid metal using the present injection technique for several reasons related to the capability of providing the appropriate flow rates for injection and fluidization without destabilizing the metal bath.
8. The wettability has a great influence on the incorporation of particles, poor wettability necessitating higher injection velocities.
9. The density of the liquid has an important effect on particle incorporation into the metal baths: solid particle incorporation in heavier liquids is more difficult and requires higher injection velocities.
10. The larger the particle and/or the heavier the particle type, the smaller the injection velocity required.

III. Influence of inclusions on the nucleation of the α-Al phase

11. Nucleation of the α-Al phase in dilute Al-alloys, containing less than 1.5 pct (Si + Fe), was observed to take place on the surface of a number of inclusions, and at different cooling rates, indicating nucleation is promoted on the surface of such inclusions.

12. In the hypoeutectic Al-Si alloy containing 6.3 wt pct Si, MgO, TiB_2, TiC, α-Al_2O_3, and SiC inclusion particles become mostly inactive nucleants and are pushed to the interdendritic regions due to the dominating poisoning effect of Si.
13. Si is observed to preferentially segregate to the liquid-Al/inclusion interfaces so as to lower the free energy of such interfaces.
14. A theoretical analysis of the poisoning effect of Si shows that Si segregation to the liquid/nucleant interface alters the interfacial energy balance so that the catalytic efficiency of the nucleant particles is dramatically reduced.
15. The quantitative results on the number of TiB_2 particles found located within the α-Al phase successfully explain the efficiency differences between commercial grain refiners used in hypoeutectic Al-Si alloys.
16. The poisoning effect of Si is overcome when the nucleant particles have active surface characteristics as represented by the high catalytic potencies of γ-Al_2O_3, CaO and Al_4C_3 particles in nucleating the α-Al phase in the hypoeutectic Al-Si alloy.
17. Although some inclusions have comparable or higher occurrence levels in the α-Al phase than TiB_2, they cannot be used as efficient nucleants on account of either their poor wettability with liquid aluminum or their chemical reactivity which can alter the alloy chemistry.

IV. The role of inclusions in the heterogeneous nucleation of the Fe-intermetallics

18. Nucleation of each of the Fe-intermetallic phases is generally observed be promoted on the surface of several inclusions under the same conditions of alloy composition

and cooling rate. However, some inclusions exhibit higher potency for the nucleation of particular Fe-intermetallic phases under certain conditions and poor potency under other conditions.

19. Potent nucleants for the primary phase (α-Al) such as γ-Al_2O_3 exhibit poor potency for the nucleation of the Fe-intermetallic particles that lie within the primary phase (*i.e.*, intragranular Fe-intermetallic particles).
20. Reactive inclusions such as CaO and SiC are highly potent nucleants for the intragranular Fe-intermetallic phase particles.
21. The nucleation of the Fe-intermetallic phases in Al-Si-Fe alloys exhibits the general features of nucleation, in particular, with respect to the effect of cooling rate and solute concentration on the potency of the nucleant particles.
    (a) Increasing the cooling rate enhances the heterogeneous nucleation of the Fe-intermetallic phases on the surface of different inclusions.
    (b) The nucleation potency of inclusion particles in both microstructural regions (*i.e.*, α-Al and interdendritic regions) improves with increasing solute concentration up to a certain level. Above this level, the solute concentration poisons the nucleation sites.
22. Nucleation of Fe-intermetallics in the alloys studied does not seem to be largely affected by the type (crystallographic structure) of the nucleating surface.

SUGGESTIONS FOR FURTHER WORK

To deepen our understanding of the formation and nucleation of phases from liquid Al-Si-Fe alloys, work in the following points can be suggested:

1. Construction or modification of the available solute segregation models in order to appropriately predict the solidification paths of multicomponent alloys. To achieve this, the effect of diffusion behavior of solute atoms, and the physical and chemical interaction between them should be properly introduced into the model.
2. Evaluation of whether the poisoning effect of Si and Fe on the heterogeneous nucleation of phases in Al alloys is additive in nature of not. This can be carried out using a group of inclusion-injected alloys with gradual increase in each of the alloying additions.
3. Determination of the level of Si and Fe or both, at which a transition in their effect, from enhancing heterogeneous nucleation to poisoning the nucleation sites, occurs.
4. Extensive examination of the orientation relationships at the nucleation interface between inclusion and nucleated phase. Determination of whether these relationships are consistent and repetitive at different nucleation interfaces in a close vicinity to each other in the microstructure or not (*i.e.*, on surface of several inclusion particles of the same type in a small unit volume of the solidified alloy) can be used to rule out the effect of cooling rate (undercooling effects) and, thus, systematically examine the crystallographic theory of nucleation.

References

References

1. W. Khalifa, F. Samuel and J. Gruzleski, "Iron Intermetallic Phases in the Al Corner of the Al-Si-Fe System", *Proc. Int. symp. on Light Metals 2002*, Metallurgical Society of the Canadian Institute of Mining and Metallurgy, Montreal, 2002, pp. 285-303.
2. W. Khalifa, F. Samuel and J. Gruzleski, "Iron Intermetallic Phases in the Al Corner of the Al-Si-Fe System", *Metallurgical and Materials Transactions A*, 2003, vol. 34A, pp. 807-25.
3. W. Khalifa, F. H. Samuel, and J. E. Gruzleski, "Influence of inclusions on the nucleation of the α-Al Phase in the Al-Si-Fe Alloys", paper submitted to the *Metallurgical and Materials Transactions*, 2003.
4. W. Khalifa, F. H. Samuel, and J. E. Gruzleski, "Analysis of the Gas Injection Technique Used for Inclusion Additions to Molten Aluminum Alloys", prepared for submission to the *International Journal of Cast Metals Research*, 2004.
5. W. Khalifa, F. H. Samuel, and J. E. Gruzleski, "Heterogeneous Nucleation of the Fe-Intermetallics in the Al-Si-Fe Alloys: the Role of Inclusions", prepared for submission to the *Metallurgical and Materials Transactions*, 2004.
6. A. Griger and V. Stefaniay, E. Csetenyi and T. Turmezey, "Formation and Transformation of Binary Intermetallic Phases in High Purity Al-Fe Alloys", *Key Engineering Materials*, 1990, vol. 44 & 45, pp.17-30.
7. D. Liang, P. Gilgien and H. Jones, "Effect of Silicon Alloying Additions on Growth Temperature and Primary Spacing of Al_3Fe in Al-8wt%Fe Alloy", *Scripta Metallurgica*, 1995, vol. 32, pp. 1513-18.
8. H. Tanihata, K. Matsuda and S. Ikeno, "Effect of Iron Content on the Occurrence of Al-Fe-Si Intermetallic Phases in 6063 Aluminum Alloy Ingots", *Journal of Japan Institute of Light Metals*, 1997, vol. 47, pp. 515-20.
9. L. Narayanan, F. H. Samuel and J. E. Gruzleski, "Thermal Analysis Studies on the Effect of Cooling Rate on the Microstructure of 319 Aluminum Alloy", *AFS Transactions*, 1992, vol. 100, pp. 383-91.
10. Narayanan, F.H. Samuel and J.E. Gruzleski, "Crystallization Behavior of Iron-Containing Intermetallic Compounds in 319 Aluminum Alloy", *Metallurgical Transactions A*, 1994, vol. 25A, pp. 1761-73.
11. S. Tang and T. Sritharan, "Morphology of β-AlFeSi Intermetallic in Al-7Si Alloy Castings", *Materials Science and Technology*, 1998, vol. 14, pp. 738-42.

12. Y. Choi, J. Lee, W. Kim, and H. Ra, "Solidification Behavior of Al-Si-Fe Alloys and Phase Transformation of Metastable Intermetallic Compound by Heat Treatment", *Journal of Materials Science*, 1999, vol. 34, pp. 2163-68.

13. A. Lakshmanan, S. Shabestari and J. Gruzleski, "Microstructure Control of Iron Intermetallics in Al-Si Casting Alloys", *Z. Metallkunde*, 1995, vol. 86, pp.457-64.

14. H. Tanihata, T. Sugawara, K. Matsuda, and S. Ikeno, "Effect of Casting and Homogenizing Treatment Condition on the Formation of Al-Fe-Si Intermetallic Compounds in 6063 Al-Mg-Si Alloys", *Journal of Materials Science*, 1999, vol. 34, pp. 1205-10.

15. A. M. Samuel and F.H. Samuel, "Modification of Iron Intermetallics by Magnesium and Strontium in Al-Si Alloys", *International Journal of Cast Metals Research*, 1997, vol. 10, pp 147-54.

16. A. L. Dons, "AlFeSi-Particles in Industrially Cast Aluminium Alloy", *Z. Metallkunde*, 1985, vol 76, pp. 609-12.

17. P. Liu, T. Thorvaldsson, and G. L. Dunlop, "Formation of Intermetallic Compounds During Solidification of Dilute Al-Fe-Si Alloys", *Materials Science and Technology*, 1986, vol. 2, pp. 1009-18.

18. Y. Awano and Y. Shimizu, "Non-Equilibrium Crystallization of AlFeSi Compound in Melt-Superheated Al-Si Alloy Castings", *AFS Transactions*, 1990, vol. 98, pp. 889-95.

19. M. W. Meredith, A. L. Greer, and P. V. Evans, "The Effect of Grain Refining Additions on Intermetallic Selection in Dilute Aluminum Alloys", *Int. Conf. on Light Metals 1998*, B. Welch (Ed.), The Minerals, Metals and Materials Society, Warrendale, PA, 1998, pp. 977-82.

20. P. S. Mohanty, "Studies on the Mechanisms of Heterogeneous Nucleation of Grains and Pores in Aluminum Castings", *Ph.D. thesis*, McGill University, Montreal, 1994.

21. M. C. Flemings, *Solidification Processing*, McGraw-Hill, New York, 1974.

22. I. Miki, H. Kosuge, and K. Nagahama, "Supersaturation and Decomposition of Al-Fe Alloys During Solidification", *Journal of Japan Institute of Light Metals*, 1975, vol. 25, pp. 1-9.

23. R. M. Young and T. Clyne, "An Al-Fe Intermetallic Phase Formed During Controlled Solidification", *Scripta Metallurgica*, 1981, vol. 15, pp. 1211-16.

24. V. G. Rilvin and G. V. Raynor, "Critical Evaluation of Constitution of Aluminium-Iron-Silicon System", *International Metals Reviews*, 1981, vol. 3, pp. 133-52.

25. C.M. Allen, K.A.Q. O'Reilly, B. Cantor, and P.V. Evans, "Intermetallic Phase Selection in 1XXX Al Alloys", *Progress in Materials Science*, 1998, vol. 43, pp. 89-170.

26. D. Munson, "A Clarification of the Phases Occurring in Aluminium-Rich Aluminium-Iron-Silicon Alloys, with Particular Reference to the Ternary Phase α-AlFeSi", *Journal of Institute of Metals*, 1967, vol. 95, pp.217-19.

27. V. Stefaniay, A. Griger, and T. Turmezey, "Intermetallic Phase in Aluminum-Side Corner of the Al-Fe-Si Alloy System", *Journal of Materials Science*, 1987, vol. 22, pp. 539-46.

28. C. Y. Sun and Mondolfo, "A Clarification of the Phases Occurring in Aluminium-Rich Aluminium-Iron-Silicon Alloys", *Journal of Institute of Metals*, 1967, vol. 95, p. 384.

29. P. J. Black, "The Structure of $FeAl_3$", *Acta Crystallographica*, 1955, vol. 8, pp. 43-8.

30. D. Porter and H Westengen, "STEM Microanalysis of Intermetallic Phases in an Al-Fe-Si Alloy", *Quantitative Microanalysis with High Spatial Resolution*, Institute of Physics (Great Britain), Electron Microscopy and Analysis Group, The Metals Society Publications, 1981, pp. 94-100.

31. H. Kosuge and I. Mizukami, "Behavior of Fir-Tree Structure in Al-Fe-Si Alloy Ingots Soaking at Elevated Temperatures", *Journal of Japan Institute of Light Metals*, 1972, vol. 22, pp. 437-44.

32. H. Westengen, "Formation of Intermetallic Compounds During DC Casting of a Commercial Purity Al-Fe-Si Alloys", *Z. Metallkde*, 1982, vol. 73, pp. 360-8.

33. E. H. Hoolingsworth, G. R. Frank, and R. E. Willett, "Identification of a New Al-Fe Constituent, $FeAl_6$", *Transactions of the AIME*, 1962, vol. 224, pp. 188-9.

34. R. C. Hudd and W. H. Taylor, "The Structure of Co_4Al_{13}", *Acta Crystallographica*, 1962, vol. 15, pp. 441-2.

35. K. Robinson and P. J. Black, "An X-Ray Examination of an α(Al-Fe-Si) Ternary Compound", *Philosophical Magazine*, 1953, vol. 44, pp. 1392-97.

36. A. L. Dons, "Superstructure in α-Al(Mn,Fe,Cr)Si", *Z. Metallkunde.*, 1985, vol. 76, pp. 151-58.

37. P. Skjerpe, "Structure of Al_mFe", *Acta Crystallographica*, 1988, vol. B44, pp. 480-86.

38. J. Gjonnes, V. Hansen, B. Berg, P. Runde, Y. Cheng, K. Gjonnes, D. Dorset, and C. Gilmore, "Structure Model for the Phase Al_mFe Derived from Three-Dimensional Electron Diffraction Intensity Data Collected By a Precession Technique. Comparison with Convergent-Beam Diffraction", *Acta Crystallographica*, 1998, vol. A54, pp. 306-19.

39. J. Hatch, *Aluminum: Properties and Physical Metallurgy*, American Society for Metals Inc., 1984.

40. P. Crepeau, "Effect of Iron in Al-Si Casting Alloys: A Critical Review", *AFS Transactions*, 1995, vol. 103, pp. 361-66.

41. S. Shebestari and J. E. Gruzleski, "The Kinetics of Formation and Growth of Complex Intermetallic Compounds in Aluminum-Silicon Alloys", *Proc. Int. Symp. on Light Metals Processing and Applications*, 1993, Brickert, M. Bouchard, G. Davies, E.Ghali and E. Jiran, (Eds.), pp.241-52.

42. L. Wang, D. Apelian and M. M. Makhlouf, "Iron-Bearing Compounds in Al-Si Die Casting Alloys: Morphology and Conditions Under Which They Form", *AFS Transactions*, 1999, vol.107, pp.231-38.

43. D.L. Beke, 1987 [cited in Ref (40), P. Crepeau, *AFS Transactions*, 1995, vol. 103, pp. 361-66].

44. A. Griger and V. Stefaniay, "Equilibrium and Non-Equilibrium Intermetallic Phases in Al-Fe and Al-Fe-Si Alloys", *Journal of Materials Science*, 1996, vol. 31, pp. 6645-52.

45. A.L. Dons, "AlFeSi-Particles in Commercial Pure Aluminum", *Z. Metallkd.*, 1984, vol. 75, pp.170-74.

46. L.Bäckreud, G.Chai, and J.Tamminen, *Solidification Characteristics of Aluminum Alloys*, AFS/Akanaluminium, 1990.

47. H. W. Philips, *Annotated Equilibrium Diagrams of Some Aluminum Alloy Systems*, The Institute of Metals, London, 1976.

48. A. Prince, "Comment on "Intermetallic Phase in Aluminum-Side Corner of the Al-Fe-Si Alloy System"", *Journal of Materials Science Letters*, 1987, vol. 6, p.1364.

49. S. Murali, K.S.Raman, and K. Murthy, "Morphology Studies on the β-$FeSiAl_5$ Phase in Al-7Si-0.3Mg Alloys with Trace Additions of Be, Mn, Cr and Co", *Materials Characterization*, 1994, vol. 33, pp. 99-112.

50. H. Kosuge and I. Mizukami, "Formation of "Fir-Tree" Structure in D.C. Cast Ingots of Al-0.6%Fe Alloys", *Journal of Japan Institute of Light Metals,* 1975, vol. 25, pp. 48-58.

51. R. Mackay and J. E. Gruzleski, "Quantification of Iron in Aluminum-Silicon Foundry Alloys Via Thermal Analysis", *International Journal of Cast Metals Research*, 1997, vol. 10, pp. 131-45.

52. A. Couture, "Iron in Aluminum Casting Alloys: A Literature Survey", *AFS International Cast Metals Journal*, 1981, vol.6, pp. 9-17.

53. B. Xiufang, C. Gouhua and M. Jiaji, "A Master Alloy for the Spheroidisation of Needle-Form Iron Compounds in Aluminium Alloys", *Cast Metals*, 1993, vol. 6, pp. 159-61.

54. Shebestari and J. E. Gruzleski, "Modification of Fe-Intermetallics by Strontium in 413 Aluminum Alloys", *AFS Transactions*, 1995, vol. 103, pp. 285-93.

55. A. Samuel, F. Samuel and H. Doty, "Observations on the Formation of β-Al_5FeSi Phase in 319 Type Al-Si Alloys", *Journal of Materials Science,* 1996, vol. 31, pp. 5529-39.

56. A. M. Samuel and F. H. Samuel, "Modification of Iron Intermetallics by Magnesium and Strontium in Al-Si Alloys", *International Journal of Cast Metals Research*, 1997, vol. 10, pp. 147-57.

57. B. Xiufang, Z. Guohua, Z. Shenxu and M. Jiaji, The Spheroidization of Needle-Form Iron Compounds in an Al-Si Alloy", *Cast Metals*, 1992, vol. 5, pp. 39-41.

58. C.M. Allen, K.A.Q. O'Reilly, B. Cantor, P.V. Evans, "Heterogeneous Nucleation of Solidification of Equilibrium and Metastable Phases in Melt-Spun Al-Fe-Si Alloys", *Materials Science and Engineering*, 1997, vol. A226-228, pp. 784-88.

59. C.M. Allen, K.A.Q. O'Reilly, P.V. Evans, and B. Cantor, "The Effect of Vanadium and Grain Refiner Additions on the Nucleation of Secondary Phases in 1XXX Al Alloys", *Acta Materialia*, 1999, vol. 47, pp. 4387-403.

60. C.M. Allen, K.A.Q. O'Reilly, and B. Cantor, "Effect of Semisolid Microstructure on Solidified Phase Content in 1XXX Al Alloys", *Acta Materialia*, 2001, vol. 49, pp. 1549-63.

61. M.W. Meredith, A. L. Greer, and P.V. Evans, 1997 [cited in Ref (25) C.M. Allen, K.A.Q. O'Reilly, B. Cantor, and P.V. Evans, *Progress in Materials Science*, 1998, vol. 43, pp. 89-170].

62. S. Shabestari and J. E. Gruzleski, "The Effect of Solidification Condition and Chemistry on the Formation and Morphology of Complex Intermetallic Compounds in Aluminum-Silicon Alloys", *Cast Metals*, 1994, vol. 6, pp. 217-24.

63. Y. Osame, K. Toyoda, Y. Tsumura, M. Suzuki, S. Furuya and K. Nagayama, "Sludge Deposition in Molten Aluminum Die Casting Alloys in the Holding Furnace", *Journal of Japan Institute of Light Metals*, 1986, vol.36, pp. 813-18.

64. L. Naraynan, F. H. Samuel and J. E. Gruzleski, "Dissolution of Fe-Intermetallics in Al-Si Alloys Through Nonequilibrium Heat Treatment", *Metallurgical and Materials Transactions*, 1995, vol. 26A, pp. 2161-74.

65. C. Villeneuve and F. H. Samuel, "Fragmentation and Dissolution of β-Al_5FeSi Phase During Solution Heat Treatment of Al-13wt% Si-Fe Alloys", *International Journal of Cast Metals Research*, 1999, vol.12, pp. 145-60.

66. J. Taylor, G. B. Schaffer and D. H. St. John, "The Role of Iron in the Formation of Porosity in Al-Si-Cu-Based Casting Alloys", *Metallurgical and Materials Transactions*, 1999, vol. 30A, pp. 1643-62.

67. D. Sparkman and A. Kearney, "Breakthrough in Aluminum Alloy Thermal Analysis Technology for Process Control", *AFS Transactions*, 1994, vol. 102, pp. 455-60.

68. W. Kurz and D. J. Fisher, *Fundamentals of Solidification*, Trans Tech Publications, Zurich, 1990.

69. I. Maxwell and A. Hellawell, "A Simple Model for Grain Refinement During Solidification", *Acta Metallurgica*, 1975, vol. 23, pp. 229-37.

70. C. V. Thompson and F. Spaepen, "Homogeneous Crystal Nucleation in Binary Metallic Melts", *Acta Metallurgica*, 1983, vol. 31, pp. 2021-27.

71. J. H. Perepezko, "Nucleation Kinetics", *Metals Handbook, vol. 15, Casting*, Ninth Edition, 1988, pp. 101-08.

72. M. B. Veven, *Energetics in Metallurgical Phenomena*, Gordon and Breach Science Publishers 1965.

73. B. Cantor and R. D. Doherty, "Heterogeneous Nucleation in Solidifying Alloys", *Acta Metallurgica*, 1979, vol. 27, pp. 33-46.

74. J. W. Christian, *The Theory of Transformations in Metals and Alloys*, Pergamon Press, Oxford, 2002.

75. I. Minkoff, *Solidification and Cast Structure*, John Wiley & Sons Publishers 1986.

76. C. J. Simensen and G. Berg, "A Survey of Inclusions in Aluminum", *Aluminium*, 1980, vol. 56, pp. 335-40.

77. ABB Bomem, *Metallographic Evaluation Reports for Prefil*, Jan. 2001.

78. I. Maxwell and A. Hellawell, "The Constitution of the System Al-Ti-B with Reference to Aluminum-Base Alloys", *Metallurgical Transactions*, 1972, vol. 3, pp. 1487-93.

79. C. Eckert, "Inclusions in Aluminum Foundry Alloys", *Modern Casting*, April 1991, pp. 28-30.

80. A. Kelly, *Concise Encyclopedia of Composite Materials*, Pergamon Press, Oxford, 1994, pp. 188, 253.

81. R. Brook, *Concise Encyclopedia of Ceramic Materials*, Pergamon Press, Oxford, 1991, p. 393.

82. P. Rohatgi, "Interfacial Phenomenon in Cast Metal-Ceramic Particles Composites", *Interfaces in Metal-Matrix Composites*, A. Dhingra and S. Fishman (Eds.), AIME-ASM, New Orleans, 1986, pp.185-202

83. J. K. Kim, and P. K. Rohatgi, "Nucleation on Ceramic Particles in Cast Metal-Matrix Composites", *Metallurgical and Materials Transactions A,* 2000, vol. 31A, pp. 1295-304.

84. P. K. Rohatgi, R. Asthana and F. Yardi, "Formation of Solidification Microstructures in Cast Metal Matrix Particle Composites", *Solidification of Metal Matrix Composites*, P. Rohatgi (Ed.), The Minerals, Metals, & Materials Society, Warrendale, PA, 1990, pp. 51-75.

85. B. J. Mckay, P. Cizek, P. Schumacher, and A. Q. O'Reilly, "Heterogeneous Nucleation of α-Al in Al-Ni-Si Alloys", *Int. Conf Light Metals 2000*, R. Peterson (Ed.), The Minerals, Metals, & Materials Society, Warrendale, PA, 2000, pp. 833-38.

86. P. K. Rohatgi, R. Asthana and S. Das, "Solidification, Structure, and Properties of Cast Metal-Ceramic Particles Composites", *International Metals Reviews*, 1986, vol. 31, pp. 115-39.

87. P.S. Mohanty, F.H. Samuel, and J. E. Gruzleski, "Studies on Addition of Inclusions to Molten Aluminum Using a Novel Technique", *Metallurgical and Materials Transactions B,* 1995, vol. 26B, pp. 103-09.

88. O.J. Ilegbusi and J. Szekely, "The Engulfment of Particles by an Elecromagnetically Stirred Melt", *Journal of Colloid and Interface Science*, 1988, vol. 125, pp. 567-74.

89. A. Neumann, C. J. Van Oss and J. Szekely, "Thermodynamics of Particle Engulfment: Particle Engulfment by Solidifying Melts and Phagocytosis", *Kolloid-Z.u.Z., Polymere*, 1973, vol. 251, pp. 415-23.

90. P. K. Rohatgi and R. Asthana, "Transfer of Particles and Fibers from Gas to Liquid During Solidification Processing of Composites", *Cast Reinforced Metal Composites*, S. G. Fishman, A. K. Dhingra (Eds), American Society for Metals, Metals Park, Ohio, 1988, pp. 61-66.

91. P. K. Rohatgi, R. Asthana, R. N. Yadav, and S. Ray, "Energetics of Particle Transfer from Gas to Liquid During Solidification Processing of Composites", *Metallurgical and Materials Transactions A,* 1990, vol. 21A, pp. 2073-82.

92. G. P. Jones, "Grain Refinement of Castings Using Inoculants for Nucleation Above Liquidus", *Conf. NPL,* Institute of Metals, London, 1988, pp. 496-99,

93. P. Sahoo and M. Koczak, "Microstructure-Property Relationships of *in Situ* Reacted TiC/Al-Cu Metal Matrix Composites", *Materials Science and Engineering*, 1991, vol. A131, pp. 69-76.

94. P. Sahoo and M. Koczak, "Analysis of *in Situ* Formation of Titanium Carbide in Aluminum Alloys", *Materials Science and Engineering*, 1991, vol. A 144, pp. 37-44.

95. J. E. Perepezko and S. L. LeBeau, "Nucleation of Al During Solidification", *Proc. 2nd Int. Symp. "Al-Transformation Technology and Its Applications"* Buenos Aires, August 1981, pp. 309-46.

96. D. Turnbull and B. Vonnegut, "Nucleation Catalysis", *Industrial and Engineering Chemistry*, 1952, vol. 44, pp. 1292-98.

97. D.L. Zhang and B. Cantor, "The Effect of Dopants on the Heterogeneous Nucleation of the Solidification of Cd and Pb Particles Embedded in an Al Matrix", *Acta Metallurgica and Materialia*, 1992, vol. 40, pp. 2951-60.

98. M. E. Glicksman and W. J. Childs, "Nucleation Catalysis in Supercooled Liquid Tin", *Acta Metallurgica*, 1962, vol. 10, pp. 925-33.

99. D. A. Porter and k. E. Easterling, *Phase Transformations in Metals and Alloys*, Chapman & Hall, London, 1992, pp. 192-97.

100. B. Cantor and K. Q. O'Reilly, "The Nucleation of Solidification in Liquid Droplets Embedded in a Solid Matrix", *Current Opinion in Solid State and Materials Science*, 1997, vol. 2, pp. 318-23.

101. Y. Nakao, T. Kobayashi and A. Okumura, "Effects of TiC, TaC, WC, TaC-WC, NbC and VC on Grain Refining of Pure Aluminum and Its Alloys", *Journal of Japan Institute of Light Metals*, 1970, vol. 20, pp. 163-75.

102. P.S. Mohanty, F. H. Samuel and J. E. Gruzleski, "Mechanism of Grain Refinement in Aluminum", *Int. Conf. Light Metals*, U. Mannweiler (Ed.), The Minerals, Metals & Materials Society, Warrendale, PA, 1994, pp. 1039-46.

103. I. G. Davies, J.M. Dennis and A. Hellawell, "The Nucleation of Aluminum Grains in Alloys of Aluminum with Titanium and Boron", *Metallurgical Transactions*, 1970, vol. 1, pp. 275-80.

104. A. Abdel-Hamid and F. Durand, "Discussion of "The Grain Refining of Aluminum and Phase Relationships in the Al-Ti-B System"", *Metallurgical Transactions A*, 1986, vol. 17A, p. 349.

105. G. K. Sigworth, "The Grain Refining of Aluminum and Phase Relationships in the Al-Ti-B System", *Metallurgical Transactions A*, 1984, vol. 15A, pp. 277-82.

106. J. Gruzleski and B. Closset, *The Treatment of Liquid Aluminum-Silicon Alloys*, The American Foundrymen's Society Inc., 1990, pp. 132-7.

107. M. K. Hoffmeyer and J. H. Perepezko, "Evaluation of Al-Ti-Si Alloys as Grain Refining Agents", *Int. Conf. Light Metals*, E. Rooy (Ed.), The Minerals, Metals & Materials Society, Warrendale, PA, 1991, pp. 1105-14.

108. P.V. Evans, J. Worth, A. Bosland and S.C. Flood, 1997 [cited in Ref (25), C.M. Allen, K.A.Q. O'Reilly, B. Cantor, and P.V. Evans, *Progress in Materials Science*, 1998, vol. 43, pp. 89-170].

109. H. Kosuge, *Journal of Japan Institute of Light Metals*, 1984, vol. 24, pp. 4 [cited in Ref (25), C.M. Allen, K.A.Q. O'Reilly, B. Cantor, and P.V. Evans, *Progress in Materials Science*, 1998, vol. 43, pp. 89-170].

110. A. Griger, V. Stefaniay, Al Lendvai, and T. Turmezey, Aluminium, 1989 [cited in Ref (25), C.M. Allen, K.A.Q. O'Reilly, B. Cantor, and P.V. Evans, *Progress in Materials Science*, 1998, vol. 43, pp. 89-170].

111. H. Tesuka and A. Kamio, 1992 [cited in Ref (25), C.M. Allen, K.A.Q. O'Reilly, B. Cantor, and P.V. Evans, *Progress in Materials Science*, 1998, vol. 43, pp. 89-170].

112. S. J. Maggs, R.F. Cochrance, 1995 [cited in Ref (25), C.M. Allen, K.A.Q. O'Reilly, B. Cantor, and P.V. Evans, *Progress in Materials Science*, 1998, vol. 43, pp. 89-170].

113. A. Flores, M. Sukiennik, A. Castillejos, F. Acosta, and J. Escobedo, "A Kinetic Study on the Nucleation and Growth of the $Al_8FeMnSi_2$ Intermetallic Compound for Aluminum Scrap Purification", *Intermetallics*, 1998, vol. 6, pp. 217-27.

114. J. Wang, J. Lin and H. Hwang, "Studies on the Nucleation Behaviors of Precipitation in Aluminum Metallization", *Materials Research Society Symp. Proc.*, 1992, vol. 260, pp. 679-83.

115. J. Lacaze and G. Lesoult, *E-MRS Conf. Computer Simulation of Solidification*, 1986, pp. 119-127.

116. E. Tromborg, A. Dons, R. Orsund, E. Jensen and L. Arnberg, "Computer Modelling as a Tool for Understanding the Precipitation of Mn in AA3XXX Alloys", *Modelling of Casting, Welding and Advanced Solidification Processes VI*, T. Piwonka, V. Voller, and L. Katgerman (Eds.), The Mineral, Metals and Materials Society, 1993, pp. 103-11.

117. J. Szekely and N. Themelis, *Rate Phenomena in Process Metallurgy*, Wiley-Interscience, New York, 1971.

118. A. Mortensen, L. Masur, J. Cornie and M. Flemings, "Infiltration of Fibrous Preforms by a Pure Metal: Part 1 Theory", *Metallurgical Transactions A*, 1989, vol. 20A, pp. 2535-47.

119. H. Suzuki and M. Kanno, "The Effect of Si or Mg Addition on the Metastable to Stable Phase Changes in an Al-0.5%Fe Alloy", *Journal of Japan Institute of Light Metals*, 1978, vol. 28, pp. 558-65.

120. L. K. Walford, "The Structure of the Intermetallic Phase $FeAl_6$", *Acta Crystallographica*, 1965, vol. 18, pp. 287-91.

123. P. Skjerpe: "Intermetallic Phase Formed During DC-Casting of an Al-0.25 wt pct Fe-0.13 wt pct Si Alloy", *Metallurgical Transactions A,* 1987, vol. 18A, pp. 189-200.

124. L.F. Mondolfo, *Aluminium Alloys: Structure and Properties*, Butterworths, London, 1976.

125. H. Jones, "Observations on a Structural Transition in Aluminum Alloys Hardened by Rapid Solidification", *Materials Science and Engineering*, 1969, vol. 5, pp. 1-18.

126. P. Liu and G. L. Dunlop, *Aluminum Alloys- Physical and Mechanical Properties*, Trans Tech Publications Inc., Zurich Switzerland, 1986, vol. 1, pp. 3-16.

127. W. B. Pearson, *Handbook of Lattice Spacings and Structure of Metals and Alloys*, Pergamon Press, London, 1967.

128. C.J.Simensen and R. Vellasamy, "Determination of Phases Present in Cast Materials of an Al-0.5wt% Fe-0.2wt% Si Alloy", *Z. Metallkunde*, 1977, vol. 68, pp. 426-31.

129. R. Ferro and A. Saccone: *Physical Metallurgy, Vol. 1*, R. Cahn and P. Hansen (Eds.), North-Holland Pub., Amesterdam, 1996, p. 206.

130. B. Yang, D. Stefanescu, and J. Leon-Torres, "Modeling of Microstructural Evolution with Tracking of Equiaxed Grain Movement for Multicomponent Al-Si Alloys", *Metallurgical and Materials Transactions A*, 2001, vol. 32A, pp. 3065-76.

131. ASM Specialty Handbook, *Aluminum and Aluminum Alloys*, J. Davis (Ed.), 1994.

132. H. D. Brody and M. C. Flemings, *Transactions of TMS-AIME*, 1966, vol. 236, pp. 615.

133. T. W. Clyne and W. Kurz, "Solute Redistribution During Solidification with Rapid Solid State Diffusion", *Metallurgical Transactions A,* 1981, vol. 12A, pp. 965-71.

134. C. Potard, G. Bienvenu, and B. Schaub, "A Study of the Distribution of Iron, Copper and Molybdenum Impurities Between the Solid and Liquid Phases in Aluminum-Beryllium Alloys", *Thermodynamics of Nuclear Materials*, Vienna, 4-8 Sept. 1967, The International Atomic Energy Agency, Vienna, 1968, pp. 809-23.

135. I. Miki and H. Warlimont: *Z. Metallkd*, 1968, vol. 59, pp. 254-64 [cited by L.F. Mondolfo, *Aluminium Alloys: Structure and Properties*, Butterworths, London, 1976].

136. D. J. Allen and J. D. Hunt, "Diffusion in the Semi-Solid Region During Dendritic Growth", *Metallurgical Transactions A,* 1979, vol. 10A, pp. 1389-97.

137. M. J. Aziz, "Model for Solute Redistribution During Rapid Solidification", *Journal of Applied Physics*, 1982, vol. 53, pp. 1156-68.

138. H. Iwahori, K. Yonekura, Y. Yamamoto, and M. Nakamura, "Occurring Behavior of Porosity and Feeding Capabilities of Sodium- and Strontium-Modified Al-Si Alloys", *AFS Transactions*, 1990, vol. 98, pp. 167-73.

139. O. Ilegbusi and J. Yang, "Porosity Nucleation in Metal Matrix Composites", *Metallurgical and Materials Transactions A,* 2000, vol. 31A, pp. 2069-74.

140. P. D. Lee and S. Sridhar, "Direct Observation of the Effect of Strontium on Porosity Formation During the Solidification of Aluminum-Silicon Alloys", *International Journal of Cast Metals Research*, 2000, vol. 13, pp. 185-98.

141. P. Mohanty, F. Samuel and J. Gruzleski, "Mechanism of Heterogeneous Nucleation of Pores in Metals and Alloys", *Metallurgical Transactions A*, 1993, vol. 24A, pp. 1845-56.

142. R. Mehrabian, R, Riek and M. Flemings, "Preparation and Casting of Metal-Particulate Non-Metal Composites", *Metallurgical Transactions*, 1974, vol. 5, pp. 1899-905.

143. B. Pai, S. Ray, K. Prabhakar and P. Rohatgi, "Fabrication of Aluminium-Alumina (Magnesia) Particulate Composites in Foundries Using Magnesium Additions to the Melts", *Materials Science and Engineering*, 1976, vol. 24, pp. 31-44.

144. C. Levi, G. Abbaschian and R. Mehrabian, "Interface Interactions During Fabrication of Aluminum Alloy-Alumina Fiber Composites", *Metallurgical Transactions A*, 1978, vol. 9A, pp. 697-711.

145. A. Banerji, M. Surappa and P. Rohatgi, "Cast Aluminum Alloys Containing Dispersions of Zircon Particles", *Metallurgical Transactions B*, 1983, vol. 14B, pp. 273-83.

146. L. Masur, A. Mortensen, J. Cornie and M. Flemings, "Pressure Casting of Fiber-Reinforced Metals", *Composite Materials*, R. Mathews (Ed.), Elsevier, London, 1987, pp. 2.320-2.329.

147. C. Milliere and M. Suery, "Fabrication and Properties of Metal Matrix Composites Based on SiC Fiber Reinforced Aluminum Alloys", *Materials Science and Technology*, 1988, vol. 4, pp. 41-51.

148. A. Mortensen, J. Cornie and M. Flemings, "Solidification Processing of Metal Matrix Composites", *Journal of Metals*, Feb. 1988, pp. 12-19.

149. P. Ghosh and S. Ray, "Effect of Mixing Parameters on the Microstructure of Compocast Al(Mg)-Al2O3 Particulate Composite", *Z. Metallkunde*, 1989, vol. 80, pp. 53-59.

150. J. Al-Jarrah, S. Ray and P. Ghosh, "Solidification Processing of Al-Al_2O_3 Composite Using Turbine Stirrer", *Metallurgical and Materials Transactions A,* 1998, vol. 29A, pp. 1711-18.

151. F. Badia and P. Rohatgi, "Dispersion of Graphite Particles in Aluminum Castings Through Injection of the Melt", *AFS Transactions*, 1969, vol. 77, pp. 402-06.

152. *Proc. Int. Confs. Injection Metallurgy (Scaninject)*, Jernkonet and MEFOS, Lulea, Sweden, 1977 and 1986.

153. R. O'Malley, C. Dremann and D. Apelian, "Alloying of Molten Aluminum by Manganese Powder Injection", *Journal of Metals*, Feb.1979, pp. 14-19.

154. M. Surappa and P. Rohatgi, "Melting, Degassing and Casting Characteristics of Al-11.8Si Alloys Containing Dispersion of Copper-Coated Graphite Particles", *Metals Technology*, 1980, vol. 7, pp. 378-83.

155. S. King III and J. Reynolds, "Flux Injection/Rotary Degassing Process Provides Cleaner Aluminum", *Modern Casting*, April 1995, pp. 37-40.

156. C. J. Smithells and E. A. Brandes, *Metals Reference Book*, Fifth Edition., Butterworths, Boston, 1976, p. 944.

157. D. Kunii and O. Levenspiel, *Fluidization Engineering*, Butterworth-Heinemann, Boston, 1991.

158. A. Haider and O. Levenspiel, *Powder Technology*, 1989, vol. 58, pp. 63-70 [cited by D. Kunii and O. Levenspiel, *Fluidization Engineering*, Butterworth-Heinemann, Boston, 1991].

159. M. Sano and K. Mori, "Size of Bubbles in Energetic Gas Injection into Liquid Metal", *Transactions of the Iron and Steel Institute of Japan*, 1980, vol. 25, pp. 675-81.

160. D. R. Poirier and G. H. Geiger, *Transport Phenomena in Materials Processing*, TMS Publications, Warrendale, PA, 1994.

161. K. Russell, J. Cornie and S. Oh, "Particulate Wetting and Particle/Solid Interface Phenomena in Casting Metal Matrix Composites", *Interfaces in Metal Matrix Composites*, A. Dhingra (Ed.), The Minerals, Metals & Materials Society, Warrendale, PA, 1986, pp. 61-91.

162. S. Oh, J. Cornie and K. Russell, "Wetting of Ceramic Particulates with Liquid Aluminum Alloys: Part II. Study of Wettability", *Metallurgical and Materials Transactions A,* 1989, vol. 20A, pp. 533-41.

163. D. M. Stefanescu, F. Rana, A. Moitra and Kacar, "Kinetics of Gas-to-Liquid and Liquid-to-Solid Transfer of Particles in Metal-Matrix Composites", *Solidification of Metal Matrix Composites*, P. Rohatgi (Ed.), The Minerals, Metals & Materials Society, Warrendale, PA, 1990, pp. 77-89.

164. L. Murr, *Interfacial Phenomena in Metals and Alloys*, Addison-Wesley Publishing Company, Massachusetts, 1975, pp.90-100.

165. S. Oh, J. Cornie and K. Russell, "Wetting of Ceramic Particulates with Liquid Aluminum Alloys: Part I. Experimental Techniques", *Metallurgical and Materials Transactions A,* 1989, vol. 20A, pp. 527-32.

166. L. Darken and R. Gurry, *Physical Chemistry of Metals*, McGraw-Hill, New York, 1953, p. 349.

167. L. Martins and G. Sigworth, "Inclusion Removal by Flotation and Stirring", *2nd Int. Conf. on Molten Aluminum Processing*, American Foundrymen's Society, Nov. 6-7, Florida, 1989, pp. 16-1 to 16-28.

168. J. Meredith, "Metal Treatment of Aluminum Alloys", *Metal Asia*, Dec. 1999, pp. 28-30.

169. C. Loper and J. Cho, "Influence of Trace Amounts of Calcium in Aluminum Casting Alloys: Review of Literature", *AFS Transactions*, 2000, vol. 108, pp. 585-92.

170. G. Jones and J. Pearson, "Factors Affecting the Grain-Refinement of Aluminum Using Titanium and Boron Additives", *Metallurgical Transactions B*, 1976, vol. 7B, pp. 223-34.

171. L. Arnberg, L. Bäckreud and H. Klang, "Grain Refinement of Aluminium, 2: Intermetallic Particles in Al-Ti-B Type Master Alloys for Grain Refinement of Aluminium", *Metals Technology*, 1982, vol. 9, pp. 7-13.

172. L. Mondolfo, "Grain Refinement in the Casting of Non-Ferrous Alloys", *Grain Refinement in Castings and Welds*, G. Abbaschain and S. David (Eds.), The Metallurgical Society of AIME, St. Louis, Missouri, 1983, pp. 3-51.

173. D. Lee and M. Basaran, "Size Effect in Grain Refinement of Al Ingots", *Grain Refinement in Castings and Welds*, G. Abbaschain and S. David (Eds.), The Metallurgical Society of AIME, St. Louis, Missouri, 1983, pp. 183-95.

174. T. Wang, M. Guo, S. Chen and C. Liao, "On the Fade of Grain Refinement of Aluminum Alloys by the Al-Ti-B Grain Refiners", *Light Metals 1998*, B. Welch (Ed.), The Minerals, Metals & Materials Society, Warrendale, PA, 1998, pp. 969-75.

175. L. Marechal, N. El-Kaddah, and P. Menet, "Influence of Convection on Agglomeration and Removal of Non-Metallic Inclusions in Molten Aluminum", *Int. Conf. Light Metals 1993*, S. Das (Ed.), The Minerals, Metals & Materials Society, Warrendale, PA, 1993, pp. 907-13.

176. G. Boudreault, A. Samuel, F. Samuel and H. Doty, "Porosity Formation in 319 Aluminum Alloy Sand Castings in Relation to Product Quality for Automotive Applications", *Proc. Int. Symp. Light Metals 1997*, The Canadian Institute of Mining, Metallurgy & Petroleum, Montreal, Canada, 1997, pp. 369-84.

177. A. Mortensen and I. Jin, "Solidification Processing of Metal Matrix Composites", *International Materials Reviews*, 1992, vol. 37, pp. 101-28.

178. D. Uhlmann, B. Chalmers and K. Jackson, "Interaction Between Particles and a Solid Liquid Interface", *Journal of Applied Physics*, vol. 35, 1964, pp. 2986-93.

179. J. Pötschke and V. Rogge, "On the Behaviour of Foreign Particles at an Advancing Solid-Liquid Interface", *Journal of Crystal Growth*, 1989, vol. 94, pp. 726-38.

180. S. Omenyi and A. Neumann, "Thermodynamic Aspects of Particle Engulfment by Solidifying Melts", *Journal of Applied Physics*, 1976, vol. 47, pp. 3956-62.

181. G. Wilde, M. Byrnes and J. Perepezko, "Particles-Dendrite Interaction During Undercooled Liquid Solidification of Metal-Matrix Composites", *Journal of Non-Crystalline Solids*, 1999, vol. 250-252, pp. 626-31.

182. Y. Wu, H. Liu and E. Lavernia, "Solidification Behavior of Al-Si/SiC MMCs During Wedge-Mold Castings", *Acta Metallurgica and Materialia*, 1994, vol. 42, pp. 825-37.

183. J. Cissé, G. Boling and H. Kerr, "Crystallographic Orientations Between Aluminum Grown from the Melt and Various Titanium Compounds", *Journal of Crystal Growth*, 1972, vol. 13-14, pp. 777-81.

184. P. Mohanty and J. Gruzleski, "Mechanism of Grain Refinement in Aluminium", *Acta Metallurgica and Materialia*, 1995, vol. 43, pp. 2001-12.

185. I. Jin and D. Lloyd, "Solidification of SiC Particulate Reinforced Al-Si Alloy Composites", *Int. Conf. "Fabrication of Particulate Reinforced Metal Composites"*, J. Masounave and F. Hamel (eds.), ASM International, Materials Park, Ohio, 1990, pp. 47-52.

186. G. Wilde and J. Perepezko, "Experimental Study of Particle Incorporation During Dendritic Solidification", *Materials Science and Engineering*, 2000, vol. A283, pp. 25-37.

187. H. Toshihiro, K. Toshiro, N. Mitsuo and S. Yuichi, *Journal of Japan Institute of Light Metals*, vol. 84, 1993, pp. 133-4.

188. T. Kobayashi, H. Jim and M. Niinomi, *Materials Science and Technology*, vol. 13, 1997, pp. 497-502.

189. D. Kubaschewski, C. Alcock and P. Spencer, *Materials Thermochemistry*, Sixth Edition, Pergamon Press, Oxford, 1993.

190. S. El Hadad, A. Samuel, F. Samuel, H. Doty and S. Valtierra, "Effects of Bi and Ca Addition on the Characteristics of Eutectic Si Particles in Sr-modified 319 Alloys", *International Journal of Cast Metals Research*, 2003, vol. 15, pp. 551-64.

191. W. Weyl, "Wetting of Solids as Influenced by the Polarizability of Surface Ions", Conf. Proc. "*Structure and Properties of Solid Surfaces*" R. Gomer, and C. Smith, (Eds.), The National Research Council, Wisconsin, Sept 1952, The University of Chicago Press, Chicago, 1952, pp. 147-84.

192. W. Kingery, H. Bowen and D. Uhlmann, *Introduction to Ceramics*, Second Edition, John Wiley & Sons, New York, 1976, pp. 205-6.

193. G. Levi and W. Kaplan, "Oxygen Induced Interfacial Phenomena During Wetting of Alumina by Liquid Aluminum", *Acta Materialia*, 2002, vol. 50, pp. 75-88.

194. E. Pippel, J. Woltersdorf, J. Genger and R. Kirchheim, "Evidence of Oxygen Segregation at Ag/MgO Interfaces", *Acta Materialia*, 2000, vol. 48, pp. 2571-8.

195. M. Backhaus-Ricoult, "A Model of Oxygen-Activity-Dependent Adsorption (Desorption) to Metal-Oxide Interfaces", *Acta Materialia*, 2000, vol. 48, pp. 4365-74.

196. P. S. Mohanty, J. E. Gruzleski, "Grain Refinement of Aluminum by TiC", *Scripta Metallurgica et Materialia*, 1994, vol. 31, pp. 179-84.

197. R. C. Dorward, "Discussion of "Comments on the Solubility of Carbon in Molten Aluminum"" *Metallurgical Transactions*, 1990, vol. 21A, pp. 255-7.

198. J. Campbell, *Castings*, Butterworth-Heinmann, 1991, p.11.

199. G. Sigworth, "Communication on the Mechanism of Grain Refinement in Aluminum", *Scripta Materialia*, 1996, vol 34, pp. 919-22.

200. A. Cibula, *Journal of Institute of Metals*, 1951, vol. 80, pp. 1-16.

201. M. Johnsson, L. Bäckreud, and G. Sigworth, "Study of the Mechanism of Grain Refinement of Aluminum After Additions of Ti- and B-Containing Master Alloys", *Metallurgical and Materials Transactions. A*, 1993, vol. 24A, pp. 481-91.

202. K. Kashyap and T. Chandrashekar, "Effects and Mechanisms of Grain Refinement in Aluminum Alloys", *Bulletin of Materials Science*, 2001, vol. 24, Indian Academy of Sciences, pp. 345-53.

203. E. Hondros, M. Seah, S. Hofmann and P. Lejcek, *Physical Metallurgy*, R. Cahn and P. Haasen (Eds.), 1996, North-Holland, Amsterdam, pp. 1202-89.

204. J. Howe, "Bonding, Structure, and Properties of Metal/Ceramic Interfaces: Part 1 Chemical Bonding, Chemical Reaction, and Interfacial Structure", *International Materials Reviews*, 1993, vol. 38, pp. 233-56.

205. P. Hou and G. Ackerman, "Chemical State of Segregants at Al_2O_3/Alloy Interfaces Studied Using μXPS", *Applied Surface Science*, 2001, vol. 178, pp. 156-64.

206. D. Ragone, *Thermodynamics of Materials*, John Wiley & Sons Inc., New York, 1995, pp.116-9.

207. J. Sebastian, J. Rusing, O. Hellman, D. Seidman, W. Vriesendrop, B. Kooi and J. Hosson, "Subnanometer Three-Dimensional Atom-Probe Investigation of Segregation at MgO/Cu Ceramic/Metal Heterophase Interfaces", *Ultramicroscopy*, 2001, vol. 89, pp. 203-13.

208. L. Bäckreud, P. Gustafson and M. Johnsson, "Grain Refining Mechanisms in Aluminum as a Result of Additions of Titanium and Boron, Part II", *Aluminium*, 1991, vol. 67, pp. 910-15.

209. M. Johnsson, "Grain Refinement of Aluminum Studied by Use of a Thermal Analysis Technique", *Thermochimica Acta*, 1995, vol. 256, pp. 107-21.

210. K. Sohlberg, S. J. Pennycook and S. T. Pantelides, "Hydrogen and the Structure of Gamma Alumina", *web page, http://www.accelrys.com/cases/ornl.html.*

211. S. Blonski and S. Garofalini, "Molecular Dynamics Simulations of α-Alumina and γ-Alumina Surfaces", *Surface Science*, 1993, vol. 295, pp. 263-74.

212. C. Hsu, K.A.Q. O'Reilly, B. Cantor, and P.V. Evans [cited in Ref (25), C.M. Allen, K.A.Q. O'Reilly, B. Cantor, and P.V. Evans, *Progress in Materials Science*, 1998, vol. 43, pp. 89-170].

213. D. G. McCartney, "Grain Refining of Aluminium and Its Alloys Using Inoculants", *International Materials Reviews*, 1989, vol. 34, pp. 247-60.

214. W.D. Donnelly and M.L. Rudee, 1964, [cited in Ref (25), C.M. Allen, K.A.Q. O'Reilly, B. Cantor, and P.V. Evans, *Progress in Materials Science*, 1998, vol. 43, pp. 89-170].

215. L. Ping and G.L. Dunlop, 1988, [cited in Ref (25), C.M. Allen, K.A.Q. O'Reilly, B. Cantor, and P.V. Evans, *Progress in Materials Science*, 1998, vol. 43, pp. 89-170].

216. C.L. Adam and L.M. Hogan, 1972, [cited in Ref (25), C.M. Allen, K.A.Q. O'Reilly, B. Cantor, and P.V. Evans, *Progress in Materials Science*, 1998, vol. 43, pp. 89-170].

217. G. Sha, K. Q. O'Reilly, B. Cantor, J.M. Titchmarch and R.G. Hamerton, "Quasi-Peritectic Solidification Reactions in 6XXX Series Wrought Al Alloys", *Acta Materilaia*, 2003, vol 51, pp. 1883-97.